INDENTIFICATION OF CRACKS ON ORTHOGONALLY STIFFENED SHIP PLATE PANELS USING ON-LINE MONITORING

AGUNG BUDIPRIYANTO

IDENTIFICATION OF CRACKS ON ORTHOGONALLY STIFFENED SHIP PLATE PANELS USING ON-LINE MONITORING

by

© Agung Budipriyanto

A thesis submitted to the School of Graduate Studies in partial fulfillment of the requirements for the degree of Doctor of Philosophy

Faculty of Engineering and Applied Science
Memorial University of Newfoundland
April 2006

St. John's **Newfoundland** **Canada**

Your file Votre référence
ISBN: 978-0-494-19617-5
Our file Notre référence
ISBN: 978-0-494-19617-5

Abstract

Due to wave and other loadings, the connections between longitudinals and transverse members of ship's side shell structure become vulnerable to cracking. The main objective of the studies carried out in this thesis was to identify the occurrence of cracks in a stiffened plate model representing the ship's side shell structure.

Based on analysis using a finite element program package, a one-twentieth aluminum stiffened plate model of a tanker ship's side shell structure was designed. Three models were fabricated; the models were tested using random excitation forces whose dominant frequency was far separated ($\approx$ 2Hz) from the first natural frequency of the models ($\approx$ 580Hz) under intact and 8 (eight) damaged conditions. These damages occurred at flange(s) and web(s) of the model's longitudinal(s). In damage cases #1 to #4, the damage occurred at a longitudinal in the connections between the longitudinal and bulkheads while in damage cases #5 to #8, damage the intersections of longitudinals and a web frame. Using the model's responses obtained from finite element analysis the best accelerometer and strain gage locations were determined. Output-only modal analysis was implemented in the experimental investigations; random decrement method and Ibrahim time domain

identification technique were employed to extract modal parameters.

Natural frequencies, root mean square (rms) of acceleration and strain response and amplitudes of a function of the natural frequency, the damping ratio and free response (which was called D_n in this study) obtained from numerical and experimental investigations were compared. Although natural frequencies, the rms and the D_n amplitude values computed from the results of numerical investigations were different from those obtained from the experimental investigations, most of them had similar trends due to increasing crack lengths.

Damage identification schemes for on-line and off-line identification of cracks, using the rms of acceleration and strain response and the amplitude of D_n function, were presented. Using these values a damage indicator was proposed. It was demonstrated that the schemes could identify the crack locations and lengths. In the first scheme, a damage indicator was computed from the rms of acceleration and strain response obtained from numerical and experimental investigations. To estimate the damage indicator values as cracks increased in length an algebraic function was developed and used. It was observed that the difference between the actual and extrapolated damage indicator values was a maximum of 18.63%. Crack lengths could also be estimated by employing the function along with an iteration procedure using assumed damage indicator value as initial value and defined error tolerance. Very good results were obtained; a maximum error of 3% was observed. Another damage identification scheme using numerically computed rms response to obtain crack length and location was also presented. This scheme can be categorized as a nomogram technique. It is shown that the scheme can be

used to identify accurately the extent and the location of cracks occurring in the horizontal's flange and web with maximum error of 2%.

The amplitude of D_n function was also examined to assess damage in the investigated model. The function was obtained utilizing a neural network technique. While the modal frequencies decreased and modal damping ratios did not have definable trend as the crack lengths grew, the D_n amplitudes changed consistently as a results of cracks occurring at one location. A damage indicator was also computed from the amplitudes of D_n function, for different damage cases. The algebraic function developed earlier was also employed to extrapolate the damage indicator values for subsequent damage cases with assumed crack lengths and locations. In addition, the function was also employed to estimate the crack sizes for known damage indicator values. The scheme produced promising results with a maximum error of about 11%.

Acknowledgments

I would like to express my sincere gratitude to my supervisor Dr. A.S.J. Swamidas and my co supervisor Dr. M.R. Haddara for their guidance and untiring support throughout my program at Memorial University. Without their encouragement and expert advice, this thesis might not have been completed successfully. I also would like to thank Dr. S.M.R. Adluri, my supervisory committee member, for his comments. Many thanks also go to everyone in Technical services (Jim Andrew, Charlie Carter and their friends) and technicians in the Structural laboratory (Austin Bursey, Shawn Organ and Tom Pike) for their help.

I am grateful to my family members for giving me continued support and encouragement to finish my Ph.D program. Special thanks are also due to all the An Noor Mosque cleaning members. It was one of the most wonderful activities I had during my stay in St. John's.

Last but not least, I would like to thank God for allowing me to complete my Ph.D program. Without His will it would not have been possible.

Contents

List of Figures

List of Tables

List of Symbols

a	Lower level triggering condition
a_{i1}	Crack length at first damage location
a_{i2}	Crack length at second damage location
a_n	Real part of eigenvalue
A	The system matrix
$[A]$	State transition matrix
b	Upper level triggering condition
$b^{(1)}, b^{(2)}$	Biases in input and output network layer
b_n	Imaginary part of eigenvalue at n^{th} mode
c	Parameter of autoregressive model with external input
c_1	Distance measured from the bottom side of the side shell to first damage location
c_2	Distance measured from the bottom side of the side shell to second damage location
$[C]$	Matrix containing C_{i1} and C_{i2}
C_i	Coefficients of autoregressive model with external input method
C_{i1}, C_{i2}	Coefficients containing dimensionless crack locations and lengths, as per Equation 6.3

d	Parameter of autoregressive model with external input method
d_1	Maximum possible crack length at first damage location
d_2	Maximum possible crack length at second damage location
D_j	Coefficients of autoregressive model with external input method
D_n	Function of the natural frequency, the damping ratio and free response, as per Equation 3.39
$D_{r,k}$	Damage indicator computed using D_n amplitudes
e	Exponential function
$\{e\}$	Vector containing damage indicator values
e_i	Damage indicator obtained using numerical and experimental rms response
e_{ij}	Damage indicator obtained using numerical rms response
e_Q	Curve of equi-value of the damage indicator, e_{ij}
E	Modulus of elasticity
E_m, E_p	Modulus of elasticity of model and prototype, respectively
f	Natural frequency in Hz
f_m, f_p	Natural frequency of model and prototype in Hz
$f(a)$	The activation function
$f(\tau)$	Random excitation force
F	Cumulative distribution function
g	Acceleration due to gravity
h_w	Web height
$h(t-\tau)$	Impulse response function

i	Integer number, Location number
i_m	Imaginary number
j	Integer
K	The number of points at which the response is computed within the frequency range considered
l	Number of sensor locations
l_m, l_p	Structure's characteristic dimension of model and prototype, respectively
L	Side shell length
m	Number of degrees of freedom
n	Number of eigenvectors
$n_r^{(1)}$	Number of neurons in input layer
$n_r^{(2)}$	Number of neurons in output layer
N	Number of data points in a time response
N_{av}	Number of averages used in random decrement function
$p_r(.)$	Probability density function
$r(t)$	Random signals or response
$\dot{r}(t)$	The first derivative of random time response at triggering points
rms	Root mean square
$R(f)$	Fourier transform of $r(t)$
RD_{rr}	Auto random decrement function
RD_{rs}	Cross random decrement function

$s(t)$	Random signal or response
$s_d(t)$	Time response of a damaged structure
S_f	Wave spectrum at frequency f
S_i	Autospectral density at a frequency f_i
S_K	Autospectral density at frequency f_K, the upper limit of the user's defined frequency range
S_l	Auto spectral density at frequency f_l, the lower limit of the user's defined frequency range
S_{rr}	Autospectral density
SD	Statistical distance of two cumulative distribution functions
t	Time
t_f	Flange thickness
t_p	Plate thickness
t_w	Web thickness
T	Maximum time lag value
U	Wind speed at 19.5 m above the sea surface
$w^{(1)}, w^{(2)}$	Weights of the network input and output layer
w_f	Flange width
x	Free decay response
$\dot{x}$	First time derivative of a free decay response
$\ddot{x}$	Second time derivative of a free decay response
$x(t)$	Dynamic system response

$\hat{x(t)}$	Dynamic system response, which delayed at time shift Δt $\hat{x}(t) = x(t) + \Delta t$
x	Input of neural networks
y	Output of neural networks
α	Matrix containing exponential values of eigenvalue and time shift Δt
α_0, α_1, α_2	Coefficients of the equation for estimating a damage indicator
$\{\alpha\}$	Vector containing coefficients α_0, α_1, α_2
β_n	Real part of eigenvalue at n^{th} mode
ε_r, ε_{sd}	Residual error in autoregressive model with the external input method for intact and damaged structure, respectively
$\hat{\varepsilon}_r, \hat{\varepsilon}_{sd}$	Error of time response estimation using autoregressive model with the external input method for intact and damaged structure, respectively
ϕ_{ij}	Modal vector computed at i^{th} location for j^{th} mode
$\hat{\phi_{ij}}$	Modal vector, ϕ_{ij}, which delayed at Δt
$[\varphi]$	Matrix whose columns are the system's eigenvector
$[\hat{\varphi}]$	Matrix of system eigenvector, $[\varphi]$, which delayed at Δt
${}_n\varphi_i$	Eigenvector of a system at i^{th} sensor location for n^{th} mode
γ_n	Imaginary part of eigenvalue at n^{th} mode
λ_n	Eigenvalue at n^{th} mode
μ	Mean value
ν	Poisson's ratio

ν_m, ν_p	Poisson's ratio of model and prototype
ρ	Mass density of material
ρ_m, ρ_p	Mass density of material of model and prototype
ρ_0	Triggering level vector
ρ_{rr}	Auto correlation function
ρ_{rs}	Cross correlation function
σ_r	Standard deviation of a random response
σ_r^2	Variance of a random response
τ	Time lag
ψ_r	The root mean square (rms) response
ω_n	Angular natural frequency in radian per second
ω_d	Damped angular natural frequency in radian per second
ψ_{fr}	The rms response, ψ_r, over a frequency range
ζ_n	Damping ratio at n^{th} mode
Δt	Sampling time interval
Γ	Triggering condition
K	Kolmogorov-Smirnov function
Λ	Matrix of complex exponentials

To Liha, Putri, Reza and Mutiara...

Chapter 1

Introduction

1.1 General

Early identification of the occurrence of cracks in complex structures is desirable for the safe operation and the economic maintenance of the structure. Structures experiencing ambient excitation due to waves, wind or ice loadings become vulnerable to fatigue cracking. To avoid the occurrence of severe damage to a structure as a result of cracking, cracks should be identified at the earliest stage. In locations where the structure is not readily accessible for inspection, it would be more profitable to employ a damage monitoring technique based on the vibration characteristics of the structure. Throughout this thesis the term "damage" and "crack" were used interchangeably.

Many damage identification methodologies are available today, e.g., alternating current field methods, eddy current methods, laser-based and conventional vibration methods and ultrasonic methods. However in many of these techniques, the equipment used for sensing should be close to crack location and the structural member should be accessible. The last three decades have witnessed a growth in vibration based monitoring methods. These methods, unlike the conventional

nondestructive evaluation techniques, do not require that the equipment used for sensing the vibration response be placed close to the crack location.

Various vibration based monitoring methods have been reported for assessing damages in civil, mechanical and aerospace structures, such as beams, plates, bridges, offshore platforms, air conditioning equipment, steam turbines, aircraft wings and space shuttle orbiters. Vibration based monitoring methods utilize the changes of the structure's dynamic characteristics to identify damage occurrence, location, and extent. Changes in modal frequencies, damping ratios, and mode shapes can be used to indicate the presence of a crack. In many situations, natural or environmental excitations are employed especially when the damage inspection is performed while the structure is under its operating conditions. In this thesis, identification of damage occurring on stiffened plate models of a tanker ship's side shell structure using a simulated wave excitation is presented.

In tanker ship structures, studies have shown (Schulte-Strathhaus (1991) and Sucharski (1995)) that most cracks were found in the side shell structures, especially in the connection between longitudinals and heavy transverse members. Most cracks observed in the side shell structures occurred in the region between laden and ballast waterlines at mid-ship region, see Figures 1.1 (a) and (b). Very little cracking was observed in the regions "in-between" the joints of the longitudinals and heavy transverses, mainly due to the fact of lower stress concentration factor. Several conditions that could bring about cracking in tanker ships are high local stress and the consequent fatigue cracking, extensive use of high tensile strength materials and structural degradation for instance, corrosion and wear (Liu and

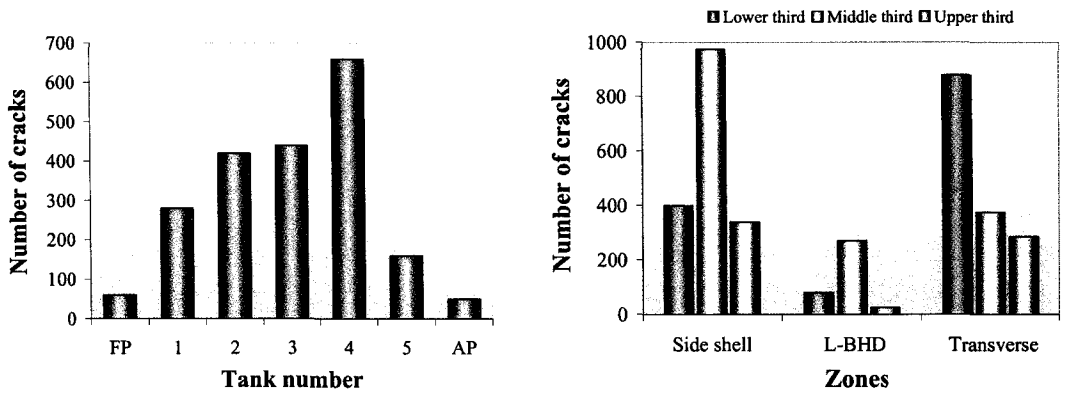

(a) Crack distribution

(b) Number of cracks

Figure 1.1: Crack distributions and number of cracks found in tanker ships (Schulte-Strathhaus, 1991)

Thayamballi, 1997). Sucharski (1995) also pointed out that at least forty percent of these cracks were located at the intersections of longitudinals with bulkhead and web frame. The crack initiated at a region of high stress concentration in the longitudinal connection to a bulkhead or a web frame; then it propagated across the flange and the web of the longitudinal (Dexter and Gentilcore, 1997). If it reached the shell plate it would bring about leaking. Although cracks occurring during normal operating conditions might not lead to a catastrophic failure of the ship structure, it could lead to leakage of tanker's cargo which would be devastating to the environment.

For a large structure such as a ship, it would be difficult to measure the external excitation. Therefore methods based on frequency response function were not used in this study since the methods require both excitation force and response be measured. From the structural response, modal parameters of the structure were extracted and damages occurring in the structure were identified.

1.2 Objective and Scope of Study

The investigations undertaken for this thesis were primarily aimed at studying the effects of cracks on the response of orthogonally stiffened aluminum plates under narrow band random forces, simulating random wave forces. The prototype of ocean wave excitation forces was computed based on Pierson-Moskowitz wave amplitude spectrum model. Three modeled structures were tested under intact and different damaged conditions. Time domain output-only modal analysis was employed during the experimental investigations and schemes for identifying cracks have been proposed.

Prior to undertaking numerical investigations, a side shell prototype of a ship structure was designed using American Bureau of Shipping Rules for steel ships ABS (2003). The ship considered for modeling was 209.9 m in length, 14.3 m in depth, 27.4 m in breadth, and had a draft of 10.7 m, see Taggart (1980). Modal characteristics of the prototype were computed using finite element package program ABAQUS (2004). The finite element program was also employed to obtain a model having similar modes of vibrations. By considering facilities available in the structures laboratory for experimental investigations, one-twentieth aluminum models of the structure, were designed and fabricated. Three aluminum models were tested in air using the random force excitations under intact and eight different damage cases.

Schemes suitable for on-line, i.e, when a structure is in operating conditions, and off-line damage identifications are presented in this thesis. These schemes employed a damage indicator, obtained from numerical and experimental root mean

square response, for assessing the damage location and extent. In addition damage identification using a damage indicator, obtained using neural network simulations, is also presented.

1.3 Organization of Thesis

The contents of different chapters in this thesis are compiled according to the following format: Chapter 2 presents the literature review as pertaining to this thesis. Chapter 3 deals with the relevant theoretical background for random processes, random decrement technique, Ibrahim time domain technique and finite element method. Chapter 4 describes the development and fabrication of stiffened plate models of a side shell of ship structure. Steps carried out to obtain model dimension and sizes are discussed. Chapter 5 gives details of the numerical and experimental investigations carried out for the model. Comparisons of numerical and experimental investigation results are also given in this chapter. Chapter 6 describes schemes proposed for off-line and on-line damage identification. Finally conclusions and suggestions for future work are presented in Chapter 7.

Chapter 2

Literature Review

2.1 Introduction

One of the challenging problems in nondestructive testing and evaluation is to identify the location of a structural crack and to quantify its extent. Identification becomes difficult when there is no easy access available for investigators to utilize conventional nondestructive evaluation techniques. In the last three decades a number of research studies on structural damage identification using vibration response have been reported. Significant efforts have been made to identity the damage locations and their extent on large structures such as bridges, high rise buildings, as well as offshore, ship and aircraft structures. The basic assumption in using this methodology is that when damage occurs the mass, stiffness and damping of the structure will change; and they result in changes in modal response.

Popular techniques reported in the last few years were based on changes in modal frequencies, mode shapes and mode shape derivatives. In addition techniques using neural networks have also attracted the attention of a number of researchers. In few cases, first few modal frequencies were not sensitive to damage. Changes in modal frequencies were usually significant for higher modes, see

Budipriyanto (1993), Budipriyanto and Swamidas (1994), Zubaydi et al. (2000b), Farrar and Jauregui (1996). Therefore other damage indicators, i.e. quantities that can reveal damage locations and extents, were introduced. Mode shapes and mode shape derivatives were found to be sensitive to damage. However especially for experimental investigations, many sensors are needed to obtain mode shapes and their derivatives. In utilizing neural networks for damage identification, multi-layer back propagation neural networks were mostly employed. Numerical and/or experimental data were normally obtained and used as input given to the networks. A review of these techniques were presented earlier by Doebling et al. (1996).

For large structures such as bridge and ship structures where it would be difficult to measure the input excitations, techniques using the structure's response were extensively investigated. Among others, stochastic subspace identification, and the random decrement method and Ibrahim time domain technique have been given considerable attention by many researchers, see for instance Bodeux and Golinval (2003), Mevel and Goursat (2003), Pridham and Wilson (2002), Cole (1973), Bolton et al. (2002). Recently, investigations on damage identification were carried out utilizing time domain response of structures. These were conducted without prior knowledge of structure's modal parameters, see for instance Andrade et al. (2001), Choi and Stubbs (2004), Kullaa (2003), Lee et al. (1996a), Worden et al. (2000), Sohn and Farrar (2001).

The investigation presented in this thesis will focus on crack identification of tanker ship hull structures, which are primarily composed of stiffened plates joined

together by welding. The procedure will utilize the change in the root mean square of acceleration and strain amplitude response. A neural network technique will also be employed for crack identification using natural frequencies, damping and response of healthy and damaged structures. The literature survey has been carried out in areas which are related to the thesis topic; these are damage investigation on ship hull structures, damage detection using vibration response and artificial neural networks.

2.2 Damage on Ship Hull Structure

Schulte-Strathhaus (1991) and Sucharski (1995) reported that in tanker ship hull structures most cracks were found in the side shell structures, especially in the connections between longitudinals and heavy transverse members. Having conducted investigation on 10 tanker ships with a total number of 3600 cracks, Schulte-Strathhaus (1991) reported that: (a) More cracks were found at midship region than at forward or aft; and (b) Most cracks occurred at side shell longitudinals located at middle third zone of the hull depth. Sucharski (1995) conducted investigation on fractures occurring in tankers. He pointed out that at least forty percent of these cracks were located at the intersections of longitudinals with a bulkhead and a web frame. The crack starts at a region of high stress concentration in the longitudinal connection to a bulkhead or a web frame, see Figure 2.1. It then propagates across the flange and the web of the longitudinal. Even though under normal operating conditions the cracks rarely lead to a catastrophic failure of the

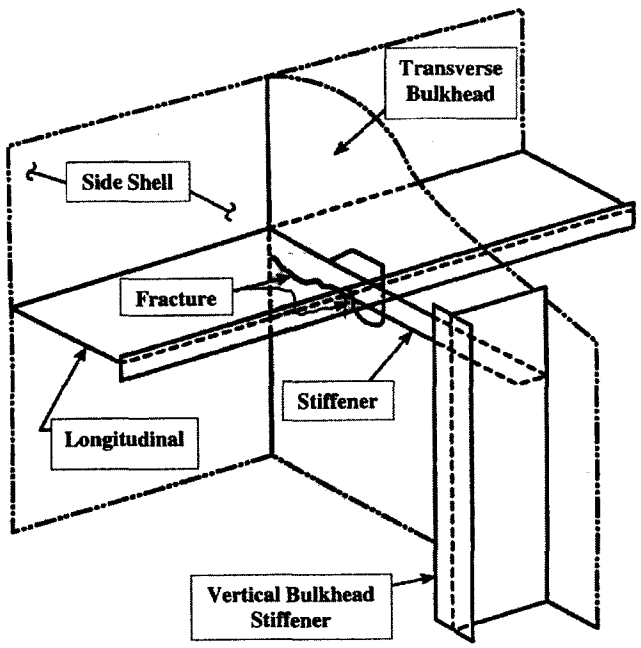

Figure 2.1: Cracking in side shell of ship (Dexter and Gentilcore, 1997)

ship structure, if the crack reached the side shell plate it might lead to leakage of tanker ship contents. The spillage would prove to be harmful to the environment. Cramer et al. (1993) developed a methodology to predict fatigue crack initiation and growth due to water wave loading in side shell longitudinals of ship structures. Numerical studies were carried out to investigate the type of damage. They concluded that most fatigue damages took place at stiffeners located at mean water line region. DeKat et al. (1995) employed finite element analysis for predicting crack growth and hull strength of tankers under wave and other dynamic loads.

Experimental study on a fast patrol boat using fiber optic sensors for structural health monitoring were reported by Wang et al. (2001). The boat was 47 m long and 13.5 m wide. More than 20 fiber optic sensors were mounted. Six of the sensors were located amidships of the boat for global wave load monitoring, see Figure 2.2.

For comparison, strain gages were also used to monitor the boat response during its operations. Time response data were collected for 20 minutes. They stated that the agreement between results obtained from data measured using fiber optics and strain gages was very good. Kiddy et al. (2002) reported the application of optical fiber strain sensors to monitor the response of a British Research Vessel (RV) at rough sea. Response of the ship due to main bending and wave slamming impact load were examined in this investigation. To measure the ship's response, 51 (fifty one) sensors were installed. The strain time response was recorded and converted to frequency domain utilizing a fast Fourier transform technique. They stated that using the measured response data, the ship's first and second bending frequencies were determined. In addition, wave slamming impact load striking the ship hull was detected.

2.3 Damage Detection Using Vibration Response

In damage detection of large structures such as a bridge or ship, the modal parameters, i.e., natural frequencies, damping ratios and mode shapes, are generally estimated from output response only, without observing or measuring the input excitation, since measuring the input of these structures would be a difficult task. In this section, literature survey of studies on damage detection of bridges, building models, truss structures and side shell panel of ships are presented. Recently, damage identification of structures in time domain using statistical approaches has become an important research topic. Studies published in this area of study

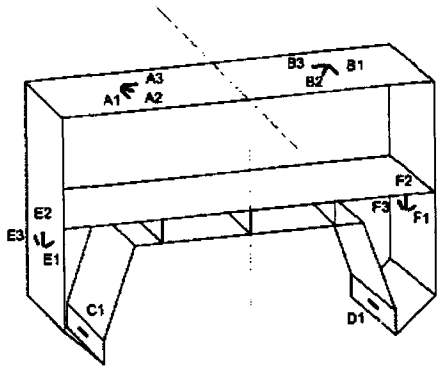

(a) Sensors at midship

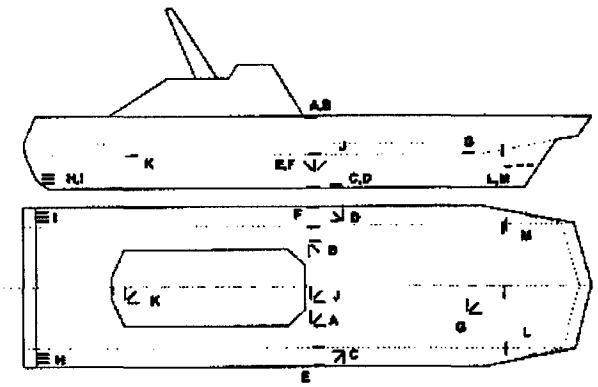

(b) Locations of sensors on the boat

Figure 2.2: Sensor locations mounted on the fast patrol boat (Wang et al., 2001)

are also reviewed in the next subsection.

Damage identification in a bridge was conducted by Farrar and Jauregui (1996); they compared five damage identification methods, viz., damage index, mode shape curvature, change in flexibility, change in uniform flexibility shape curvature and change in stiffness methods from experimental and numerical response data of I-40 Bridge, across the Rio Grande river in New Mexico, under healthy and damaged conditions. In their experimental investigations, the bridge was excited by random inputs having a prescribed frequency range of 2Hz - 12 Hz. Eight damage cases were investigated. These damages were introduced in the bridge by cutting the

structure's girder flange and/or web. To measure the response of damaged structures, 26 accelerometers were installed in the first set and then an additional 11 accelerometers were mounted in the second set. In the analytical investigations a finite element model was developed to predict the bridge response. Five damage identification methods were applied and compared to examine their performances in identifying and estimating damage location. The authors stated that damage index method gave better performance in localizing damage than others.

On-line monitoring of damage identification using the random decrement (RD) technique was initiated by Cole (1973). Random decrement function was obtained by averaging random response of structures and making the use of level crossing triggering conditions. He examined the change of RD signature of a truss structure before and after several connection bolts were loosened. By zooming over desired frequency ranges, he found that the signatures, obtained from acceleration response, slightly changed due to the loosened bolts. He hypothesized that by setting a certain frequency range and transducer location, a particular damage can be detected. A flutter wing model, on which a strain gage was mounted, was also tested. He reported that random decrement signatures experienced gradual changes as the damage became more severe. From his numerical and experimental studies, the author concluded that the random decrement signature was equivalent to free decay response of a structure and was stable in shape and amplitude for a wide range of frequencies. In addition, random decrement signature could also be used as a damage indicator and for damping measurement. Since Cole's work, extensive studies on random decrement had been reported, see for example

Ibrahim (1986), Vandiver et al. (1982), Haddara (1992), Asmussen et al. (1996). Their studies were not reviewed in this chapter since they do not belong to damage identification.

Studies investigating the response of a unidirectionally stiffened plate model representing the ship hull structure were reported by Zubaydi et al. (2000a,b). Numerical and experimental studies were carried out to determine the proper finite element model. They stated that the impulse response computed, using the finite element analysis models, were similar to the measured random decrement response; and the contribution of the non-structural modes generated from the test bed, were negligible. Zubaydi et al. (2002) used a function having the damping force and the non-linear restoring force terms as damage indicator. Very good agreement between the autocorrelation function obtained from the experiment and that obtained from the finite element model was reported.

Structural health monitoring on bridge structures were carried out by Bolton et al. (2001, 2002), Reynolds and Pavic (2001) and Peeters and Ventura (2002). Bolton et al. (2001) compared the modal frequencies and modal vectors extracted from measurements conducted on a reinforced concrete highway bridge. The bridge was excited by using two types of excitation, i.e., a drop weight impactor and the ambient traffic excitation. Frequency response functions, obtained from the impact measurement response data, were utilized to compute modal parameters. Ibrahim time domain (ITD) and transmissibility methods were applied to extract modal frequencies as well as modal vectors from ambient response data. The authors found that these methods gave similar results for both modal frequencies and mode

shapes. Both the methods indicated modal assurance criterion (MAC) values to be close to 1. Later Bolton et al. (2002) extended their studies to a two span reinforced concrete bridge on which 42 accelerometers were permanently mounted. The bridge was excited by impact loading before it was opened and thereafter by ambient traffic excitations. They pointed out that natural frequencies extracted from data measured from impact and traffic loadings were significantly different (up to 15%). The natural frequencies obtained from traffic loading were lower than those computed from impact loading. They stated that the difference might be due to: (a) the effect of vehicle traffic mass on the bridge response; and (b) change in the structural system since there was "several month gap" between these two investigations. Mode shapes computed from those two types of loading also differed; this was indicated by low values of MAC. One of the problems encountered in their investigation was that of accurately and consistently identifying several closely spaced modes. They stated that more data might be required to get better results.

Reynolds and Pavic (2001) carried out investigations on Z24 pre-stressed concrete bridge response due to a drop weight forced exciter and ambient excitation, see Figure 2.3 for the bridge view, elevation and cross sections. Signal processing was carried out in a MATLAB environment and the DIAMOND computer software developed by structural health monitoring group at Los Alamos National Laboratory was employed to extract modal parameters. The authors concluded that the measured response from forced excitation were less noisy so that it gave more reliable modal parameters. They also suggested taking longer acquisition time in order to get better results when ambient excitation was used. Comparative study

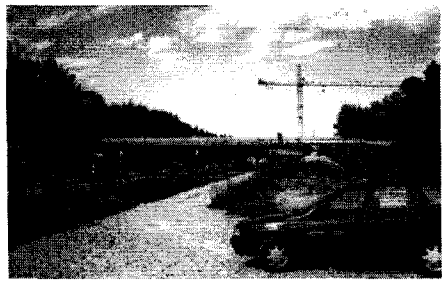

(a) view

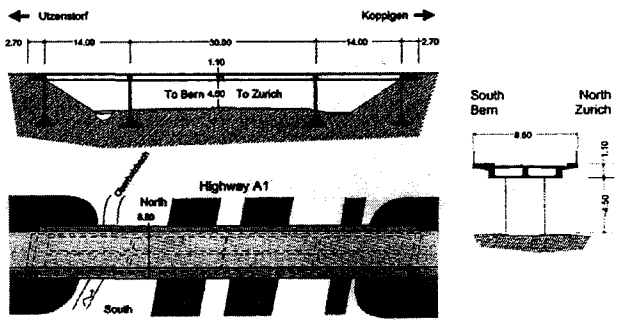

(b) elevation and cross sections

Figure 2.3: The Z24 Bridge (Reynolds and Pavic, 2001)

of modal identification methods for Z24 bridge was conducted by Peeters and Ventura (2002). Frequency and time domain methods including, the pick-picking, the rational fraction polynomial (RFP), autoregressive moving average and subspace identification methods, were compared. The authors concluded that among methods investigated in the study, the RFP and subspace identification methods gave most consistent results. They also pointed out that the development and use of relevant sensor technology, data acquisition system technology and identification techniques were essential for output-only system.

Kharrazi et al. (2002) implemented a study on a one-third-scale model of a four story steel building frame. Fourteen sensors were installed at all the structure's floors in three possible displacement directions. The structure was excited

by forced vibration and ambient vibration with white noise signals of frequency (within 0.1 Hz to 50 Hz band). The model was tested for nine different conditions including undamaged condition and damaged conditions in which several of structure's bracings were removed or beam-column bolted connections were loosened. Natural frequencies and mode shapes were extracted from response data. An analytical study using finite element analysis was also implemented. A finite element model of the steel frame model was developed to obtain modal parameters of the frame model under intact and damaged conditions. In the finite element analysis, damage was simulated by changing moment of inertias of the frame members and cross sectional areas of the braces. The finite element analysis results were then correlated with experimental results, to evaluate the correlation of several parameters, e.g., modal assurance criterion and mode shape pairing. They reported that: (a) using ambient vibration, the modes of the frame model could be well defined, especially the lower ones; and (b) most of damage locations and extent also could be identified. They also noted that more accurate results would have been obtained if more modes were considered in the analysis.

Pridham and Wilson (2002) applied a stochastic subspace identification technique to estimate the natural frequency and the damping coefficient of a steel suspension bridge. The bridge was 766 m long and 16 m wide. 26 (twenty six) sensors were installed on both sides of the truss deck, located at the middle span of the bridge and at the pylons (at the top of pylon, at deck level and at the bottom level). The bridge response, due to the ambient (traffic, wind and other) excitations, were recorded at 0.01 second resolution for 1000 seconds. Prior to carrying out detailed

analysis, the recorded data were preprocessed to reduce the effects of noise and computational errors. The raw data were bandpass filtered so that the data fell into a Nyquist frequency range of 2.5 Hz to 6.25 Hz. To distinguish between the noise and the true computational modes, modal assurance criterion (MAC) and modal amplitude coherence were utilized. There were 24 (twenty four) vertical modes of vibration in the range between 0.2 Hz to 6 Hz; 25 (twenty five) lateral modes in the range between 0.1 Hz to 3 Hz; and 28 (twenty eight) transitional modes in the range between 0.5 Hz to 6 Hz. Computed vertical and transitional modal damping values were observed to be consistent while transverse modal damping ratios were inconsistent.

A study on the vibration characteristics of undamaged and damaged free-free aluminum beams were conducted (Ramsagar and Pardue, 2001). The authors utilized autocorrelation of frequency response functions measured at different nodes to examine the possible change in dynamic properties. They showed that additional peaks in autocorrelation of frequency response functions could be used as damage indicators. Verboven et al. (2002) introduced a modal parameter identification method using frequency response functions data. To distinguish between structural and computational modes a fuzzy algorithm was proposed. The modal parameter identification method was verified for applications by conducting experimental tests on a slat track of a commercial aircraft wing, see Figure 2.4. The structure was excited using sinusoidal signals ranging from 0 Hz to 4096 Hz. Seven accelerometers were mounted and a laser doppler vibrometer was utilized to measure the structure's dynamic response. Results of the tests showed that the method

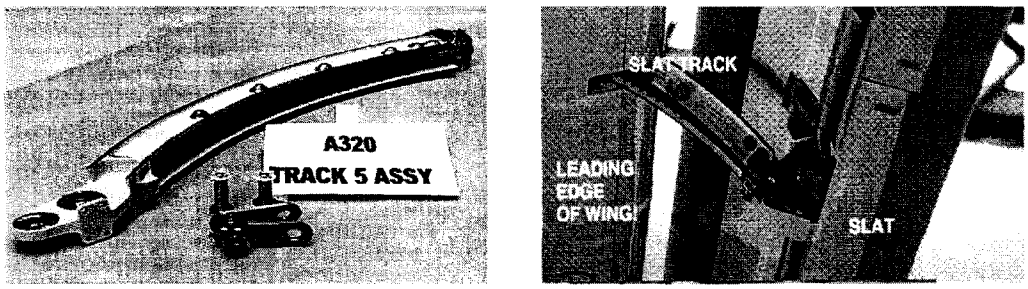

(a) A slat track (b) A slat tract attached on an aircraft wing

Figure 2.4: A slat track of an commercial aircraft (Verboven et al., 2002)

was able to estimate modal parameters correctly although several of them were closely spaced modes. Later Parloo et al. (2002) proposed sensitivity based methods for computing mass normalized mode shapes for damage identification using output-only measurements. The methods were verified using a slat track of an aircraft wing experimental data described in Verboven et al. (2002). The structure was tested under different damage cases which were simulated by attaching different masses on the structure by means of magnets. They demonstrated that the attached masses were well estimated using the proposed mass normalization method and modal parameter identification presented in Verboven et al. (2002).

2.3.1 Damage Identification in Time Domain

Lee et al. (1996a) proposed a scheme for detection of faults in heating, ventilating and air-conditioning (HVAC) systems using residuals and changes in model parameters as damage indicators. The residual values were computed by subtracting measured values under fault conditions to their values under normal conditions. The parameters examined in the study were supply air temperature, cooling coil control signals, supply of duct static pressure and flow difference between fans.

To investigate the change in model parameters the systems were modeled using Autoregressive moving average with external input (ARMAX) and Autoregressive with external input (ARX) models; then the model parameters were calculated using a Kalman filter. It was assumed that physical changes in the systems would result in changes of model parameters. The systems were considered to be damaged when the damage indicators were exceeded by three standard deviations of undamaged model response. They reported that the scheme worked successfully when it was applied to laboratory experimental data obtained from systems under damaged and healthy conditions.

Cattarius and Inman (1997) utilized the beat phenomenon for identifying damage of structures. The authors proposed a method that required free decay response of structures to be available. It was assumed that the phases of single frequency free response under intact and damaged conditions were shifted by small values. For frequency changes less than 30%, the signal obtained from subtracting intact and damage response showed the beat phenomenon. Changes in half time period of the signal were employed to indicate the presence of damage. Numerical studies on a beam and experimental investigations on plate and rotor blade structures were performed for verifying the proposed method. Worden et al. (2000) carried out numerical simulations and experimental investigations on damaged and undamaged structures. A statistical analysis called outlier analysis was proposed for damage detection using Mahalanobis squared distance as a damage indicator. The method was applied on numerical response data obtained from a three degree of freedom system and experimental data measured from composite plates.

It was demonstrated that the proposed damage indicator was able to discriminate between damaged and undamaged structures.

Seibold and Weinert (1996) introduced a method using of extended Kalman filter for determining a crack location and its extent. The proposed method required displacement time history data as input. Simulation study using the finite element analysis and experimental investigation on rotor shafts were carried out to verify the method. The results showed that method was capable to determine correctly the crack location and extent. Andrade et al. (2001) presented a crack identification technique using the Kolmogorov-Smirnov test. The technique was based on the assumption that time signatures of a structure under cracked and uncracked conditions have different probability density functions. The authors determined the statistical distance (SD) of two cumulative distribution functions, $F(r_1)$ and $F(r_2)$ using,

$$SD = max|F(r_1) - F(r_2)| \tag{2.1}$$

where r_1 and r_2 are structure's random time response. The probability density of SD [$p(SD)$] was assumed to follow the Kolmogorov-Smirnov probability density function $f(\kappa)$ as,

$$\begin{aligned} p(SD) &= f(\kappa) \\ &= 2\sum_{j=1}^{\infty}(-)^{j-1}\, e^{-2j^2\kappa^2} \\ \kappa &= \sqrt{N_e} + 0.12 + \frac{0.11}{\sqrt{N_e}} \\ N_e &= \frac{N_1 N_2}{N_1 + N_2} \end{aligned} \tag{2.2}$$

where N_1 and N_2 are the number points in the first and second time domain response data respectively. An experimental study on gears under intact and cracked conditions was conducted to examine the performance of the proposed technique. The gears under investigation were operated at a rotational speed of 5 Hz. An accelerometer was used to monitor the response which was recorded at 5.12 kHz frequency sampling rate. It was reported that the technique was able to distinguish the integrity of gears.

Sohn and Farrar (2001) used the standard deviation of an error as a damage indicator. The error was computed from the difference between the measured response data and the predicted values computed using a combination of the auto-regressive (AR) and auto-regressive with external input (ARX) models. Considering $r(t)$ to be a reference time response of a healthy system, $s_d(t)$ to be the time response of the system under damaged condition, $\hat{\varepsilon}_r(t)$ and $\hat{\varepsilon}_{sd}(t)$ to be the error obtained from the estimation of $r(t)$ and $s_d(t)$ using autoregressive (AR) model, the residual error, $\varepsilon_r(t)$, obtained by employing ARX (c,d) model on $r(t)$ and $\hat{\varepsilon}_r(t)$, was given as,

$$\varepsilon_r(t) = r(t) - \sum_{i=1}^{c} C_i\, r(t-i) - \sum_{j=0}^{d} D_j\, \hat{\varepsilon}_r(t-j) \tag{2.3}$$

where the values of c and d were taken equal to 5. Using the value of coefficients C_i and D_j determined from Equation (2.3), the ARX residual error for time response $s_d(t)$ and $\hat{\varepsilon}_{sd}(t)$ was given as,

$$\varepsilon_{sd}(t) = s_d(t) - \sum_{i=1}^{c} C_i\, s_d(t-i) - \sum_{j=0}^{d} D_j\, \hat{\varepsilon}_{sd}(t-j) \tag{2.4}$$

The authors defined a damage indicator as the ratio of standard deviation of $\varepsilon_r(t)$ and standard deviation of $\varepsilon_{sd}(t)$. An eight degrees-of-freedom system was tested in laboratory. The system was excited using random force. Its acceleration response for several damage cases were recorded. The experimental results showed that the damage indicator changed significantly at the location close to where damage was introduced. In a later study, Sohn et al. (2001) applied the above technique for identifying structural changes that occurred in a fast patrol boat investigated by Wang et al. (2001), see Figure 2.2. Outlier analysis method proposed by Worden et al. (2000) was also used for comparison. Using three strain time measurements obtained from two structural boat conditions, they pointed out that these techniques successfully identified the two structural damage conditions.

Bodeux and Golinval (2003) investigated the effect of damage on a steel space frame. The modal parameters of a two story steel space frame structure were estimated using the autoregressive moving average vector (ARMAV) and stochastic subspace methods by assuming the excitation to be a stationary Gaussian white noise. It was reported that the uncertainties on the estimated natural frequencies were small compared to those on the damping ratios. Moreover the natural frequencies decreased due to damages occurring in the structure. Therefore the natural frequency changes were used as a damage indicator. Choi and Stubbs (2004) developed a nondestructive evaluation methodology using the mean strain energy computed from displacement response. A damage indicator defined as the ratio of the element stiffness of intact and cracked elements was proposed. The methodology was verified by employing numerical data obtained from response of

a continuous I beam subjected to impact excitation. They stated that the methodology was able to detect the damage location and quantify its size. The use of control charts of assessing damage was introduced by Kullaa (2003). The modal parameters of the bridge structure were estimated using the stochastic subspace identification. The bridge response was recorded under undamaged conditions and under the pier settlements of 40 mm and 95 mm. The author noted that the damping ratios were not sensitive to damage whereas the natural frequencies and mode shapes changed considerably due to damage.

2.4 Damage Detection Using Neural Networks

Artificial neural networks are an attempt at modeling information capabilities of a human brain, which contains millions of interconnected cells, called neural cells or neurons (Bishop, 1995). Diagram of two biological neurons is shown in Figure 2.5. Neurons receive signals and produce response. The branches that function as transmission channels for incoming information (input) are called dendrites. Communication between neurons occurs at synapses. The cell body produces output signals that can be transmitted by axons. Artificial neural networks have input channels, cell body and output channels. Synapse is simulated by a weight, which relates cell body to inputs or outputs. Researchers have shown growing interest on neural networks. Two major neural network techniques that are extensively used at present for damage identification are multilayer perceptron technique and the radial basis function technique. Studies on damage identification utilizing neural

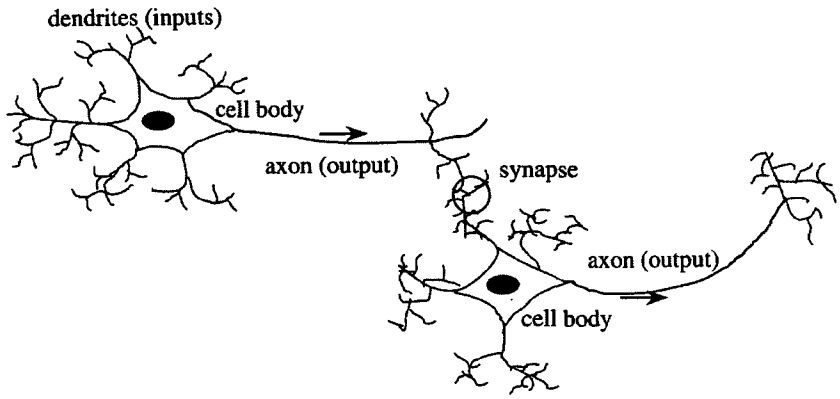

Figure 2.5: Diagram of bioneural neurons

networks are reviewed below.

Neural network approach has been used to identify cracks or damages in civil engineering structures in studies reported Barai and Pandey (1995, 1997). They proposed the use of back propagation multilayer perceptron neural networks for identifying changes of the cross sectional area of a truss member. To predict the changes of the member area, nodal time history was employed as input to the networks. Both experimental and analytical studies were carried out. The authors stated that: (a) The neural network was a suitable method for damage identification of structures; and (b) It was necessary that the transducer location be properly selected so that accurate results could be obtained. Later they proposed a time delay neural network for damage identification of truss structures (Barai and Pandey, 1997). The difference between multilayer perceptron neural networks and time delay neural networks is that the latter receives both the input signal and delayed signals; its output depends upon present and previous inputs. To test the performance of these two methods, they were applied to identify damages of rail-

way truss bridges. The training patterns were generated using a finite element computer program package. They concluded that the time delay neural networks produced less average error than the multilayer perceptron neural networks for all cases investigated.

Study on damage detection and identification of composite cantilever beams by using neural networks was proposed by Rim and Lee (1995). Three damage cases with different lengths of delamination occurring in the beam were investigated. A finite element program package was used to simulate the beam response in undamaged and delaminated conditions. The inputs were applied to the beam and the response was recorded. Auto-regressive model with exogenous input system identification technique was employed to extract structure's transfer functions that were then used as inputs into a multilayer perceptron neural network. They reported that the proposed method could be used to identify correctly all damage cases.

To identify the existence of damage on an offshore platform model, Mangal et al. (1996) used adaptive resonance theory and back propagation neural network with modal frequencies and modal vectors as input data. Lim et al. (1996) presented a neural network based method for on-line identification of modal parameters. They assumed that modes were known so that a Butterworth band pass filter could be applied to a mode of interest. The filtered signals were then used as inputs to a neural network algorithm capable of identifying response transfer functions from which the natural frequency, the damping ratio and mode shape could be extracted. The proposed method could only be applied to identify one mode at a frequency bandwidth. Therefore filtering should be carried out at several frequency ranges

in which a natural frequency existed. To demonstrate performance of the proposed method, simulation study and experimental investigation on a circular aluminum plate were carried out. The plate was fixed around its circumference. Impact hammer load was applied and the first two modes were investigated. They found that measured and predicted acceleration response were slightly different. Natural frequencies were accurate within 2% when they were compared with those computed using a fast Fourier transform technique.

Atalla and Inman (1998) proposed a modal updating approach using radial basis function neural network that required real and imaginary parts of frequency response as input data. The motivation for developing the method was to obtain updated parameters quickly and to avoid the use of time consuming minimization procedures so that it can be applied to response controlled structures. Numerical and experimental investigations were performed to examine the performance of the proposed method.

Zubaydi et al. (2002) presented the use of artificial neural networks with autocorrelation function and its derivative obtained from numerical study as input data for identifying the existence and location of cracks. They used the maximum value of a function having damping force and nonlinear restoring force terms to identify the extent and locate cracks. They pointed out that the results were encouraging and more data might be required to give better results. They also suggested comparing results obtained from numerical and experimental studies for future research investigations. Samman (2001) combined artificial neural network and recognition techniques to identify the damage existence and extent in concrete

cylinders. Two neural networks were used; one was for identifying the damage existence and the other was for predicting the extent of damage. He reported that the proposed technique successfully detected the defect existence and extent present in the cylinders. In addition he noted that the proposed technique required less training patterns than those needed by using artificial neural networks alone.

Tsai and Hsu (2002) reported that neural network method could successfully identify simulated damage in a reinforced concrete rectangular simply supported beam. Numerical studies and experimental investigations were conducted. Damage in concrete was simulated by reducing concrete compressive strength by 25%, 50% and 75% of undamaged value while damage in steel reinforcement was simulated by reducing 30% of undamaged steel diameter. Damage scenarios studied considered damage occurring in concrete or steel or both. A total of 200 cases were analyzed in the numerical study. Finite element analysis was used to obtain vertical displacement time histories at three locations on a beam subjected to an impact load. The displacement response were then employed to train an artificial neural network. In the experimental study, 10 sets of beams were tested under impact load. Linear-variable differential transformers (LVDTs) were used to monitor displacement response, which were then recorded in a computer. They concluded that using the proposed method material damages, due to concrete, steel or both, could be identified. Moreover damage (extent and location) occurring in the beam can also be located.

Zhang and Imregun (2001a,b) proposed a method to detect the existence of damage by using artificial neural network with measured frequency response function

as input data. To avoid very large input data given to artificial neural network and to remove noise presents in the data, the frequency response function data were reduced by using principle component analysis technique. Later Zhang et al. (2004) implemented a technique using independent component analysis to condense time history response data. Mixing matrix method produced from the component analysis, was employed as input to multilayer perceptron networks for damage detection of structures. The proposed method was applied to numerical displacement data of a truss structure and experimental data measured from response of a three story building model. It was demonstrated that the method was able to identify intact and damaged conditions of the structures.

Lopes et al. (2002) proposed the use of electrical impedance technique to detect and locate damage and back propagation artificial neural network and optimization technique to estimate the damage severity. An aluminum frame structure with piezoelectric (PZT) actuators/sensors attached to it was excited at a very high sweep frequency range of 18 kHz - 28 kHz. The electrical impedance signals, i.e., the ratio of input voltage to output current was recorded. Undamaged and damaged structures in which saw cuts were introduced to simulate damage, were tested. Their hypotheses were that: (a) Small defects can be detected at high frequencies by closely examining electrical impedance curves; and (b) PZT sensors measure a limited area of the structure so that damage occurring away from the sensor would not affect the response obtained from it; in other words, only local changes were measured. Using electrical impedance curves, several damage indicators were computed, e.g., root mean square of electrical impedance and

correlation coefficient between undamaged and damaged curves. These damage indicators were then utilized as inputs to an artificial neural network. This technique was shown to be able to locate as well as quantify damages introduced on the structure. There were two steps in the optimization technique for damage detection. The first was to establish a model representing the dynamical behavior of undamaged structure. The second was to compute stiffness changes from a damaged model. It was reported that damage could be identified by using the proposed methodology.

Lee et al. (2002) presented a damage identification method of a bridge excited by traffic loadings. Numerical investigation using finite element method and experimental investigation were carried out to obtain the bridge's response under traffic excitations. From the measured response, modal parameters were estimated using random decrement method. A damage identification method using a multilayer perceptron neural network was proposed. The networks required ratios of modal frequencies under damaged and intact conditions and mode shapes under damaged conditions as inputs. They showed that the method can be used to detect and localize damage. However the damage extent was slightly overestimated. Numerical and experimental studies for damage identification of honeycomb sandwich structure were reported by Yam et al. (2003). In the numerical study, finite element method was used to model the investigated structure. In the experimental study, piezoelectric sensors were attached on the structure to monitor its dynamic response. Since large response data were obtained, a wavelet analysis was employed to reduce the large amount of data and to transform the original response data.

Using the transformed response data, energy spectra were calculated and utilized as inputs for a back propagation neural network. They concluded that the methodology was not capable of identifying all damage cases investigated, especially when small damages occurred.

From the above review, it is obvious that vibration based monitoring methods have been used extensively to examine the existence and extent of damage in structures. The approaches reviewed in this chapter consider output-only measurement techniques in time and frequency domain in conjunction with neural network techniques. The studies presented in this thesis are aimed at obtaining damage indicators and investigating the use of time domain structural damage identification methods and a neural network technique for off-line and on-line damage detection.

Chapter 3

Theoretical Background

3.1 Introduction

Numerical investigations and experimental testing of three orthogonally stiffened plate models, representing the side shell of a ship structure, were carried out. The models were excited using random forces simulating wave forces under intact and damaged conditions. The natural frequencies and damping ratios were identified from the measured response using the random decrement and Ibrahim time domain techniques.

In analyzing the random response of a structure, the root mean square (rms) of amplitude response is usually utilized to quantify the strength of the response, since it is a measure of the energy in the signal. This thesis presents the use of the rms of amplitude response for identifying damages occurring in orthogonally stiffened plate panels. In addition, neural network techniques were also utilized for damage identification. In this chapter basic theories relating to these studies are discussed. These include the random process, random decrement technique, Ibrahim time domain technique, neural networks, and the finite element method.

3.2 Random Processes

Ships and offshore structures are subjected to random forces due to ocean waves and current. Responses obtained from random inputs are also random. This means that any given measurement will produce a unique time history; the measurement will represent only one of many possible results that might have happened. To investigate random response, a collection of sample functions called ensembles as shown in Figure 3.1 are required. The mean and the mean square value of the random process at a time say t_1 can be computed using (Bendat and Piersol, 2000),

$$\mu(t_1) = \lim_{N\to\infty} \frac{1}{N} \sum_{i=1}^{N} r_i(t_1) \tag{3.1}$$

$$\psi_r^2(t_1) = \lim_{N\to\infty} \frac{1}{N} \sum_{i=1}^{N} r_i^2(t_1) \tag{3.2}$$

The autocorrelation function is a measure of the correlation between the values of random signal, $r(t)$ obtained at two different times, t and $t+\tau$. The autocorrelation function is calculated as,

$$\rho_{rr}(t,\tau) = \lim_{N\to\infty} \frac{1}{N} \sum_{i=1}^{N} r_i(t_1)\, r_i(t_1+\tau) \tag{3.3}$$

A process is said to be stationary when the mean, mean square and the autocorrelation computed by Equations (3.1), (3.2) and (3.3) do not vary with time. In other words, the mean and the mean square values are constants and the auto correlation function depends only on the time lag τ. If the process is stationary, the random process is said to be ergodic when the mean value as well as the au-

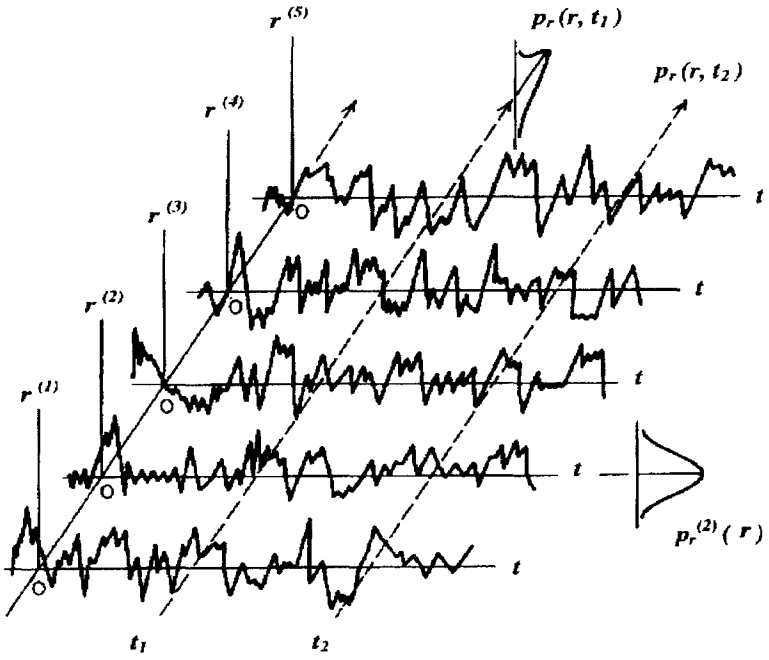

Figure 3.1: Ensemble of time history responses forming a random process (Hughes, 1988)

tocorrelation function computed over a particular sample function is equal to the corresponding ensemble values.

Consider measured response data $\{r_i\}$ $i = 1,2,3,\ldots N$, where N is the total number of points in the measurement. The time response is sampled at a time interval Δt ; the mean (μ), mean square (ψ^2) and autocorrelation function (ρ_{rr}) can be calculated using expressions below,

$$\mu = \frac{1}{N}\sum_{i=1}^{N} r(t) \tag{3.4}$$

$$\psi^2 = \frac{1}{N}\sum_{i=1}^{N} [r(t)]^2 \tag{3.5}$$

$$\rho_{rr}(\tau) = \frac{1}{N-\tau}\sum_{i=1}^{N-\tau} (r_i - \mu)(r_{i+\tau} - \mu) \qquad \tau = 0,1,2,\ldots T \tag{3.6}$$

where μ is the mean, τ is the time lag for which a maximum value T is usually taken to be not larger than $\frac{N}{4}$ (Box et. al, 1994).

The autospectral density function is a Fourier transform of the autocorrelation function. It can also be efficiently calculated using a fast Fourier transform technique. The autospectral density as a function of frequency f can be obtained through Fourier transform of r_j [or $R_i(f)$] using,

$$\begin{aligned} S_{rr}(f) &= \frac{1}{n_d N \Delta t} \sum_{i=1}^{n_d} |R_i(f)|^2 \\ R_i(f) &= \frac{1}{N} \sum_{j=1}^{N} r_j \, e^{-\mathrm{i_m}(2\pi i f)}, \quad i_m = \sqrt{-1} \end{aligned} \tag{3.7}$$

where n_d is the number of time histories. The above mentioned procedure is called the periodogram technique (MATLAB, 1997). Other spectral estimation techniques such as Welch's, Multitaper, Yule-Walker autoregressive, Burg and Multiple signal classification techniques are elaborated in MATLAB (1997). Throughout this study, the periodogram was utilized for computing the power spectral density since this technique was simple and not time consuming. Crossspectral density functions can be determined from cross correlation functions using a similar procedure.

In this study, the rms, (ψ_{fr}), in a frequency range between f_l (lower frequency) and f_h (upper frequency), is obtained through numerical integration of the spectral density,

$$\psi_{fr} = \sqrt{\int_{f_l}^{f_h} S_{rr}(f)\, df} \tag{3.8}$$

As mentioned earlier, numerical investigation for this thesis was conducted utilizing ABAQUS computer package program. ABAQUS assumes the response to have

a zero mean. It computes the rms (ψ_{fr}) by performing numerical integration of the one sided autospectral density function over a frequency range of f_l and f_h as,

$$\psi_{fr} \approx \sqrt{0.5 \left[S_1 (f_h - f_l) + \sum_{i=1}^{K-1} S_i (f_{i+1} - f_{i-1}) + S_K (f_K - f_{K-1}) \right]} \tag{3.9}$$

where S_l denotes autospectral density at, f_l, the lower limit of the user's defined frequency range, S_i is the autospectral density at f_i, S_K is the autospectral density at the frequency f_K , the upper limit of the user's defined frequency range, and K is the number of points at which the response is computed within the frequency range considered.

3.3 Random Decrement Function

The random decrement concept and applications were initially introduced by Cole (1973). Since then the random decrement has been widely used for testing civil and aerospace engineering structures. The relationship between the autocorrelation and the random decrement functions for linear systems was first established by Vandiver et al. (1982). The relationship between the random decrement and the cross correlation functions was introduced by Brincker et al. (1991). Spanos and Zeldin (1998) estimated autocorrelation function using the random decrement. Ibrahim (1986) showed that for zero mean, stationary excitation, the application of the random decrement to the response of a system results in the free decay signals when the response is filtered at a triggering level.

The response of a linear system subjected to a random excitation can be written

as,

$$r(t) = e^{[A(t-t_0)]}\, r(t_0) + \int_{t_0}^{t} h(t-\tau) f(\tau) d\tau \tag{3.10}$$

in which $[A]$ is the state transition matrix which contains the system's properties (mass, damping and stiffness), $r(t_0)$ represents the response at $t = t_0$, $h(t-\tau)$ is the system's response due to a unit amplitude impulse at $t = \tau$ and $f(\tau)$ is the random excitation force. The first term on the right hand side of Equation (3.10) is the homogeneous free decay response, which does not depend on the type of excitation used but depends only on the structure's vibration characteristics. The second term on the right hand side of Equation (3.10), representing the particular response, depends upon the type of excitation exerted on the structures. By assuming the number of averages (N_{av}) used in the estimation to be large and the excitation to be random, the second term of the equation will become zero. In order that the first term does not vanish, the so called triggering condition should be applied (Ibrahim et al., 1998). Auto and cross random decrement function can be written as,

$$RD_{rr} = \frac{1}{N_{av}} \sum_{i=1}^{N_{av}} r(t_i + \tau) | \Gamma_{r(t_i)} \tag{3.11}$$

$$RD_{sr} = \frac{1}{N_{av}} \sum_{i=1}^{N_{av}} s(t_i + \tau) | \Gamma_{r(t_i)} \tag{3.12}$$

where N_{av} is the number of averages, Γ_r denotes the triggering condition, $r(t_i)$ and $s(t_i)$ are random responses, t_i is the discrete time (triggering point) and τ is the time lag. Four types of triggering conditions are often used in practice, viz., local crossing, zero crossing with positive slope, positive point triggering and local extremum (Asmussen et al., 1997).

- Level crossing

  $r(t_i) = a;\ 0 < a < \sigma_r$

- Zero crossing with positive slope

  $r(t_i) = 0;\ \dot{r}(t_i) > 0$

- Positive point

  $a \leq r(t_i) < b;\ -\infty \leq \dot{r}(t_i) < \infty; [a,b] = [\sigma_r, \infty]$

- Local extremum

  $a \leq r(t_i) < b;\ \dot{r}(t_i) = 0;\ [a,b] = [\sigma_r, \infty]$

where a and b are triggering levels and σ_r denotes standard deviation of the response. For level crossing and positive point triggering conditions the relationship between the random decrement and the correlation functions is (Brincker et al., 1991)

$$RD_{sr} = \frac{\rho_{rs}}{\sigma_r^2}\rho_0 \tag{3.13}$$

$$\rho_0 = \frac{\int_a^b r\, p_r(r)\, dr}{\int_a^b p_r(r)\, dr} \tag{3.14}$$

where a and b are lower and upper triggering levels respectively, ρ_{rs} is correlation function between time responses r and s, and $p_r(r)$ is the probability density function of response. Equation 3.13 will be used for damage identification which will be presented in Chapter 6.

3.4 Ibrahim Time Domain Method

Ibrahim time domain method (ITD) estimates the modal parameters from the free decay response of a system in cases where the excitation force is either measured or not measured (Ewins, 2000). In the ITD method the response is assumed to be in the form,

$$x_i(t_j) = \sum_{n=1}^{2m} {}_n\varphi_i \, e^{\lambda_n t_j} \tag{3.15}$$

where $x_i(t_j)$ is the measured free decay response. λ_n is the n^{th} eigenvalue or characteristic root of the system and ${}_n\varphi_i$ is n^{th} eigenvector of the system at i^{th} location and m is the number of degrees of freedom identified from a structure's response.

For response measured at l locations on the structure for N number of sample data, Equation 3.15 can be written in matrix form as,

$$\begin{bmatrix} x_1(t_1) & x_1(t_2) & \cdots & x_1(t_N) \\ x_2(t_1) & x_2(t_2) & \cdots & x_2(t_N) \\ \vdots & \vdots & \vdots & \vdots \\ x_1(t_1) & x_1(t_2) & \cdots & x_l(t_N) \end{bmatrix} = \begin{bmatrix} {}_1\varphi_1 & {}_2\varphi_1 & \cdots & {}_{2m}\varphi_1 \\ {}_1\varphi_2 & {}_2\varphi_2 & \cdots & {}_{2m}\varphi_2 \\ \vdots & \vdots & \vdots & \vdots \\ {}_1\varphi_l & {}_2\varphi_l & \cdots & {}_{2m}\varphi_l \end{bmatrix} \begin{bmatrix} e^{\lambda_1 t_1} & e^{\lambda_1 t_2} & \ldots & e^{\lambda_1 t_s} \\ e^{\lambda_2 t_1} & e^{\lambda_2 t_2} & \ldots & e^{\lambda_2 t_s} \\ \vdots & \vdots & \vdots & \vdots \\ e^{\lambda_{2m} t_1} & e^{\lambda_{2m} t_2} & \ldots & e^{\lambda_{2m} t_s} \end{bmatrix} \tag{3.16}$$

or in a compact form

$$[x] = [\varphi][\Lambda] \tag{3.17}$$

where $[x]$ is a lxN matrix, $[\varphi]$ is a $lx2m$ matrix and $[\Lambda]$ is a mxN matrix. The response

with respect to a time shift of Δt of the first response is given by,

$$\begin{aligned} x_i(t_j+\Delta t) &= \sum_{n=1}^{2m} {}_n\varphi_i \, e^{\lambda_n (t_j+\Delta t)} \\ &= \sum_{n=1}^{2m} {}_n\varphi_i \, e^{\lambda_n t_j} \, e^{\lambda_n \Delta t} \\ &= \sum_{n=1}^{2m} {}_n\hat{\varphi}_i \, e^{\lambda_n t_j} \end{aligned} \tag{3.18}$$

where $[\hat{\varphi}] = e^{\lambda_n \Delta t}[\varphi]$ or in matrix from can be written as,

$$[\hat{x}] = [\hat{\varphi}][\Lambda] \tag{3.19}$$

From (3.17) and (3.19), $[\Lambda]$ can be eliminated to obtain,

$$\begin{aligned} [\hat{x}] &= [\hat{\varphi}]\,[\varphi]^{-1}[x] \\ [\hat{x}]\,[x]^{-1} &= [\hat{\varphi}]\,[\varphi]^{-1} \\ [\hat{x}]\,[x]^{-1}[\varphi] &= [\hat{\varphi}] \end{aligned} \tag{3.20}$$

Since $[\hat{\varphi}] = \alpha[\varphi]$ where $\alpha = e^{\lambda_n \Delta t}$, Equation (3.20) can be rewritten in form of a standard eigenvalue problem as,

$$[A][\varphi] = \alpha[\varphi] \tag{3.21}$$

in which $[A]$ has to satisfy the relation,

$$[A]\,[x] = [\hat{x}] \tag{3.22}$$

Since N, number of sample data, is customarily taken to be greater than l, number of sensor location, $[A]$ can be computed using a least square technique. In this case $[A]$ can be obtained from the expression given below,

$$[A] = [\hat{x}][x]^{\mathrm{T}}([x][x]^{\mathrm{T}})^{-1} \tag{3.23}$$

or by post multiplying Equation (3.22) by $[\hat{x}]^{\mathrm{T}}$, $[A]$ can be expressed as,

$$[A] = [\hat{x}][\hat{x}]^{\mathrm{T}}([x][\hat{x}]^{\mathrm{T}})^{-1} \tag{3.24}$$

Combining solutions given in Equations (3.23) and (3.24),

$$[A] = \frac{1}{2}\left\{[\hat{x}]\,[x]^{\mathrm{T}}\,([x][x]^{\mathrm{T}})^{-1} + [\hat{x}]\,[\hat{x}]^{\mathrm{T}}\,([x]\,[\hat{x}]^{\mathrm{T}})^{-1}\right\} \tag{3.25}$$

Once $[A]$ is computed, the eigenproblem (Equation 3.21) can be solved for modal vectors $[\varphi]$ and eigenvalues from which the modal frequency (ω_n) and the damping ratio (ζ) can be obtained. The complex eigenvalue (α), computed from Equation (3.21) for n^{th} mode, can be written as $\beta_n + i_m\,\gamma_n$. The structure's modal frequency and damping ratio can be written in the form $\lambda_n = a_n + i_m\,b_n$ in which, $a_n = -\zeta_n\,\omega_{nn}$, $b_n = \omega_{nn}\sqrt{(1-\zeta_n^2)}$. Further a_n, b_n, β_n and γ_n can be related through a relationship, viz.,

$$\begin{aligned} \beta_n + i_m\,\gamma_n &= e^{(a_n + i_m b_n)\,\Delta t} \\ &= e^{a_n \Delta t}\,(\cos b_n\,\Delta t + i_m \sin b_n\,\Delta t) \end{aligned} \tag{3.26}$$

Then β_n and γ_n can be expressed as,

$$\beta_n = e^{a_n \Delta t} \cos(b_n \Delta t) \tag{3.27}$$

$$\gamma_n = e^{a_n \Delta t} \sin(b_n \Delta t) \tag{3.28}$$

Squaring β_n and γ_n , and summing them up will give,

$$\beta_n^2 + \gamma_n^2 = e^{2 a_n \Delta t} \tag{3.29}$$

From Equation (3.29), a_n can be rewritten as

$$a_n = \frac{1}{2\Delta t} \ln (\beta_n^2 + \gamma_n^2) \tag{3.30}$$

Using Equations (3.27) and (3.28), b_n can be obtained using the relationship,

$$\begin{aligned} \frac{\gamma_n}{\beta_n} &= \tan (b_n \Delta t) \\ b_n &= \frac{1}{\Delta t} \arctan \left(\frac{\gamma_n}{\beta_n} \right) \end{aligned} \tag{3.31}$$

Finally the natural frequency (ω_{nn}) and the damping ratio (ζ_n) can be obtained via Equations (3.32) and (3.33) given below,

$$\omega_{nn} = \sqrt{a_n^2 + b_n^2} \tag{3.32}$$

$$\zeta_n = \sqrt{\frac{1}{1 + \left[\frac{b_n}{a_n} \right]^2}} \tag{3.33}$$

Ibrahim (1987) utilized upper Hessenberg matrix to improve the damping ratio estimation in the modal parameter identification technique. In the present study, the procedure described above was employed for structural parameter identification.

The modal parameters obtained from the procedure contain true modal parameters of the system and noise related modal parameters. Therefore modal confidence factor (MCF) is computed for every eigenmode to distinguish between structural modal parameters and those related to noise measurement. Modal confidence factor is a complex quantity; the value close to one can be judged as a structural mode. Modal confidence factor computed for n^{th} mode at i^{th} measurement location is,

$$MCF_i = \frac{\hat{\phi}_{in}}{\phi_{in}\, e^{\lambda_j \Delta t}} \tag{3.34}$$

ϕ_{ij} is modal vector identified at a location and $\hat{\phi}_{ij}$ is modal vector identified at a location with time delay Δt which should be chosen, $\Delta t < \frac{1}{2f_{max}}$; f_{max} is maximum frequency of interest. The effect of sampling frequency on natural frequencies extracted using the random decrement and Ibrahim time domain techniques is presented in Chapter 5.

3.5 Neural Networks

An artificial neural network is an information processing system which mimics the processing system in the human brain. The network consists of a large number of interconnected neurons. The network needs to be trained to learn the behavior of the system. There are two kind of learning processes: a supervised learning and

unsupervised learning. In supervised learning scheme, a neural network output is matched with a target output by minimizing the difference (or error) between the computed output and the target output. No target is given in artificial neural networks system with unsupervised learning (MATLAB, 1997).

An artificial neural network processing system is composed of input, weights, activation function, learning process and output. A sufficient number of input data shall be provided to a neural network (Bishop, 1995). Each input has its own coefficient named weight. Weight values can be adjusted in a learning process. An input and its weight are multiplied and then added to obtain the weighted sum of the inputs. The result can also be considered as the inner product of the input and the weight vectors. A special weight called bias is normally added to the result. The weighted sum of the inputs is then passed through an activation function. The activation functions can be linear or non linear functions. S-shaped (sigmoidal) functions, e.g., the logistic functions or hyperbolic tangent, are often used in multilayer perceptron neural network. In a supervised learning process, the computed outputs obtained from the application of the activation function on the weighted sum of inputs are compared to the target or the desired input. In the training or learning process, the weights are changed to minimize the error (the difference between the computed output and the target) so that suitable weights associated with minimum error can be determined. For back propagation neural networks, gradient descent, conjugate gradient, quasi newton algorithms are among the available techniques used for minimizing the error.

Studies undertaken for this thesis utilized neural network codes available in

Haddara and Hinchey (1995). Neural network presented in Haddara and Hinchey (1995) consisted of input, hidden and output layer and the relationship between the input x and the output y as,

$$\begin{aligned} \mathbf{y} &= \sum_{j=1}^{n_r^{(2)}} w_j^{(2)} f\left(\sum_{i=1}^{n_r^{(1)}} w_i^{(1)} \mathbf{x} + b^{(1)}\right) + b^{(2)} \\ f(a) &= \frac{1-e^{-a}}{1+e^{-a}} \end{aligned} \tag{3.35}$$

where $w^{(1)}$ and $w^{(2)}$ are matrices containing the weights of the input and output layers respectively; $b^{(1)}$ and $b^{(2)}$ are biases in input and output layer of the network, and $n_r^{(1)}$ and $n_r^{(2)}$ are the number of neuron in the input and output layers.

The artificial neural network was employed to obtain a damage indicator. The D_n function is obtained from the free decay response of the structure, as

$$\ddot{x}_n + 2\,\zeta_n\,\omega_{nn}\,\dot{x}_n + \omega_{nn}^2\,x_n = 0 \tag{3.36}$$

$$\ddot{x}_n + 2\,\zeta_n\,\omega_{nn}\,\dot{x}_n + (\omega_{dn}^2 + \zeta_n^2\,\omega_{nn}^2)\,x_n = 0 \tag{3.37}$$

$$\ddot{x}_n + \omega_{dn}^2\,x_n + D_n(x_n, \dot{x}_n) = 0 \tag{3.38}$$

where $\ddot{x}_n$ is the acceleration of free decay response and ω_{dn} is damped natural frequency at n^{th} mode. where x_n and $\dot{x}_n$ are the free decay response and its derivative at the n^{th} mode, respectively, ω_{nn} is the natural frequency and ζ_n is the damping ratio. The damage indicator is a function having the damping force and nonlinear

restoring force terms. The function (D_n) is expressed as,

$$D_n(x_n, \dot{x}_n) = 2\,\zeta_n\,\omega_{nn}\,\dot{x}_n + \zeta_n^2\,\omega_{nn}^2\,x_n \tag{3.39}$$

3.6 Finite Element Method

Numerical investigations for obtaining dynamic response of orthogonally stiffened plate of the side shell of a ship structure were undertaken using a finite element method. In this method, a structure is discretized into a number of elements which are interconnected by nodes whose relative geometric positions in space or coordinates are clearly defined. To obtain approximate expressions for dependent variables within the element (e.g, displacement), shape or interpolation functions are commonly utilized. Mass, damping and stiffness matrices of each element as well as load matrix are computed and then the element mass, damping, stiffness and load matrices are assembled into corresponding global matrices. Damping matrix is normally taken proportional to mass and stiffness matrices or given in term of ratio of critical damping. The equation of motion is obtained (e.g., by minimizing the potential energy) and is then solved after boundary conditions are applied to the structure.

The orthogonally stiffened plate structure was discretized using eight-noded quadrilateral (S8R5) and six-noded triangular (STRI65) shell elements available in ABAQUS (2004). In these elements, transverse shear flexibility is negligible and Kirchhoff constraints are satisfied. The eight noded quadrilateral element can

be collapsed into a triangle for linear elastic fracture mechanics modeling.

In ABAQUS, dynamic response can be obtained using direct integration method or modal based method. Direct integration method is suitable for studying nonlinear dynamic response. For linear dynamic system, however, modal based method is generally used. In this method, the eigenmodes are necessarily calculated first before structure's response computation is performed. The modal based method was utilized in the numerical results presented in Chapter 5 because it was less time consuming than the direct integration method. Two modal based methods were employed in this study, i.e., mode based steady state analysis and random response analysis. In mode based steady state dynamic analysis, the input excitation frequencies can be varied. The amplitude and the phase of output response are given as functions of frequency. In random response analysis, the input excitation is the power density function of the excitation forces and the output response are given in term of rms values.

3.7 Summary

This chapter has presented basic theories related to the numerical and experimental studies conducted for this thesis. Theory of random vibration including the relation between correlation function and spectral density function and computation of the rms through spectral density function have been discussed. The use of rms of random response as damage indicator is demonstrated in Chapter 6. Random decrement function and Ibrahim time domain methods have also been

summarized. These techniques were applied for extracting modal parameters from random response measured during experimental study performed for this thesis, see Chapter 5. In addition a brief review of finite element analysis has also been presented.

Chapter 4

Model Development and Fabrication

4.1 Introduction

As mentioned in the previous chapters, investigations carried out in this study were mainly aimed to examine changes in vibration characteristics (e.g., natural frequency and response) that occur due to the presence of damage on the side shell of a ship structure when it is excited by a narrow band noise, simulating wave excitation. For the above mentioned purpose, a one-twentieth model was developed for fabrication. This chapter discusses a procedure for obtaining the model dimension and sizes of a ship side shell structure. Part of results of the study discussed in this chapter have been reported in Budipriyanto et al. (2004a).

4.2 Side Shell of Prototype and Model

The physical model used in this study consists of a stiffened plate; the stiffeners run in two orthogonal directions. It is similar to the stiffened plate structure that is commonly found in the construction of the side of the hull of an oil tanker. The

ship considered for modeling was 209.9 m in length, 14.3 m in depth, 27.4 m in breadth, and had a draft of 10.7 m, see Taggart (1980). The side shell prototype panel size which was located at midship was 12.0 m long by 12.0 m wide. The prototype had two web frames between the transverse bulkheads and fourteen equally spaced (at 0.8 m) longitudinals (horizontal stiffeners). The prototype panel was designed using American Bureau of Shipping Rules for steel ships (ABS, 2003). In the present study, the two web frames were kept the same while only four types of longitudinals, each having a different cross section, were used. Furthermore, brackets were ignored in the analytical calculations and the structure was fixed along its four sides. No attempt was made to minimize the structure's weight in this study. Detailed plate dimensions, web frame and longitudinals of the structure are given in Table 4.1. Figure 4.1 gives the notations used in side shell dimension.

By considering the facilities available in the structural laboratory for testing, a one-twentieth-scale aluminum model of the structure was designed. Three physical aluminum models were fabricated and tested. In order to determine the dimensions of the model, several steps were undertaken. First, the finite element computer package program, ABAQUS (2004), was utilized to calculate the modal parameters (the natural frequencies and mode shapes) of the prototype. Then the modal parameters of a one-twentieth geosim model, a model whose dimension was exactly one-twentieth of the prototype, were calculated. Next, the modal parameters of several models with different plate sizes and various combinations of web frames and longitudinals (size and number) were computed. Finally, the scaled

Table 4.1: Prototype dimensions

Plate thickness t_p = 19.05mm

No	Web frame dimension			
	h_w (mm)	t_w (mm)	w_f (mm)	t_f (mm)
	1850	25.40	525	31.75
	1850	25.40	525	31.75

No	Longitudinal dimension			
	h_w (mm)	t_w (mm)	w_f (mm)	t_f (mm)
1	300	12.7	100	19.05
2	300	12.7	100	19.05
3	300	12.7	100	19.05
4	300	12.7	100	19.05
5	320	12.7	100	19.05
6	320	12.7	100	19.05
7	320	12.7	100	19.05
8	320	12.7	100	19.05
9	415	12.7	125	25.40
10	415	12.7	125	25.40
11	415	12.7	125	25.40
12	450	12.7	125	25.40
13	450	12.7	125	25.40
14	450	12.7	125	25.40

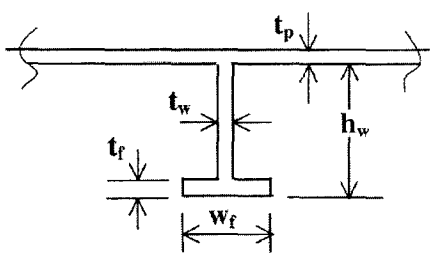

Figure 4.1: Notations for plate dimension

model that had modal parameters closest to the geosim model was selected, taking into consideration the availability of material and the feasibility of fabrication. The model consisted of a hull plate with two transverse T-plate web frames of equal size and four T-shaped longitudinals (horizontal stiffeners) having three different cross sections. In this numerical investigation, the prototype and model were discretized utilizing the S8R5 eight noded shell element. Figure 4.2 shows the finite element mesh of the prototype structure. The material properties used for the analysis purposes are presented in Table 4.2.

In determining the model sizes and dimensions, the relationship of prototype and model natural frequencies for plate in bending given in Harris and Sabnis (1999) was used as a crosscheck so that the results obtained from the package program could be compared. This relationship was employed since model and prototype relationship for orthogonally stiffened plate could not be found. The prototype's and model's natural frequencies were related as (Harris and Sabnis, 1999),

$$f_p = f_m \frac{l_m}{l_p} \sqrt{\frac{E_p \rho_m}{E_m \rho_p}} \sqrt{\frac{1-\nu_m{}^2}{1-\nu_p{}^2}} \tag{4.1}$$

where the subscript p and m denotes prototype and model respectively. f is the natural frequency, l is a structure's characteristic dimension (plan or thickness dimension), E is modulus of elasticity, ρ is mass density of structure materials and ν is the Poisson's ratio. By considering Equation 4.1, the natural frequencies of one-twentieth geosim model of steel were expected to be 20 times of the prototype natural frequencies and about 19.99 times for one-twentieth geosim model of aluminum. Table 4.3 gives the model dimensions for web frames and longitudinals.

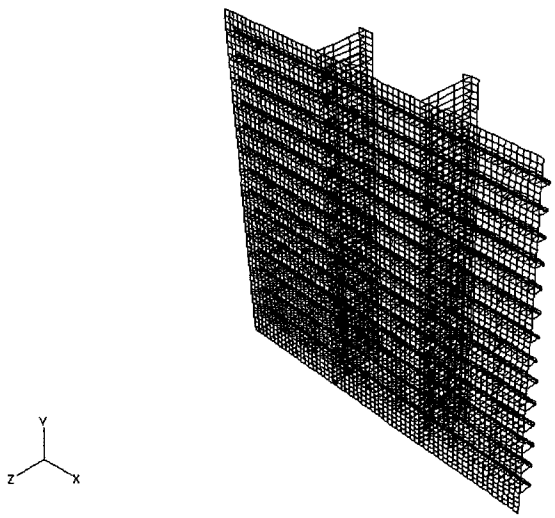

Figure 4.2: Finite element mesh of the prototype

Table 4.2: Material properties

Material	Modulus of elasticity (E) (GPa)	Mass density (ρ) (kg/cm^3)	Poisson's ratio (ν)
Steel	207	7800	0.30
Aluminum	70	2700	0.33

The model was discretized using two different meshes, finite element model (a) and (b). Both finite element models (a) and (b) were meshed using S8R5 shell element. Meshing in model (b) was intended to refine the mesh in model (a). In finite element model (a) all longitudinal flanges were discretized using 2 elements along their widths while in finite element model (b) width of flanges of longitudinals #3 and #4 were discretized using four elements. Moreover the web frames in model (a) were discretized using six elements along their web heights whereas in model (b) eleven elements were employed. The modal frequencies of these model were computed and the results are presented in Table 4.4. The first five natural frequencies of these two model were different by less than 1%. No further finite element convergence analysis was carried out. In this study model (b) was employed for the subsequent numerical investigations. The finite element mesh of model (b) is shown in Figure 4.3.

The first five natural frequencies of the model and the corresponding frequencies of the prototype were computed and are presented in Table 4.4. The error observed between the physical model used in this study and the geosim model, for the lowest five natural frequencies were, respectively, -10.90%, -19.53%, 22.36%, 13.67% and 15.72%. The reasons for this discrepancy may be attributed to the fact that the stiffener sizes in the physical model were chosen based on market availability of structural members and the feasibility of fabrication. The first five modes of vibration of the model and the prototype are shown in Figure 4.4. It can be seen that the model's modes are similar to the prototype's modes. The first four modes are due to the response of transverse web frames and the fifth mode is the first

Table 4.3: Model dimensions

Plate thickness t_p = 6.35 mm

No	Web frame dimension			
	h_w (mm)	t_w (mm)	w_f (mm)	t_f (mm)
1	116.84	6.35	31.75	6.35
2	116.84	6.35	31.75	6.35

No	Longitudinal dimension			
	h_w (mm)	t_w (mm)	w_f (mm)	t_f (mm)
1	31.75	4.76	20.00	4.76
2	31.75	4.76	20.00	4.76
3	38.10	4.76	31.75	4.76
4	50.80	6.35	38.10	6.35

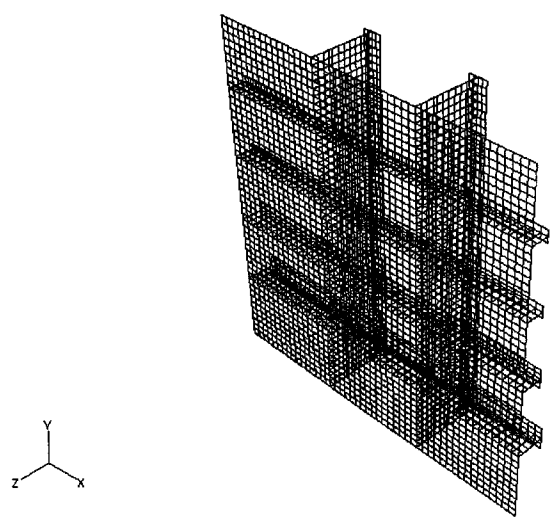

Figure 4.3: Finite element mesh of the model

Table 4.4: First five natural frequencies of prototype and model

Natural Frequencies (Hz)					
Mode	Prototype	1/20 geosim		1/20 Model	
		steel	aluminum	FE mesh (a)	FE mesh (b)*)
1	33.088	661.42	655.77	589.6	584.3
2	36.579	734.74	728.55	591.6	586.3
3	45.777	914.49	906.49	1110.4	1109.2
4	49.362	986.06	977.78	1113.2	1111.4
5	49.734	994.53	982.32	1138.3	1136.7

Note: *) model used for analysis in this study

bending mode of the overall othogonally stiffened plate.

After the model dimensions and sizes were obtained, the next steps were to design the fixed support of the one twentieth fabricated model and to design test bed including connection between test bed and the one twentieth model. To implement fixed support modeled in the analytical study, a 750 mm by 750 mm aluminum plate with 6.35 mm in thickness was used for the side shell plate; the additional 150 mm was intended to provide space for the fixed supports (75 mm left and right or upper and lower sides). Two aluminum plates (600 mm x 115 mm x 9.5 mm) and two aluminum plates (600 mm x 65 mm x 9.5 mm) were welded perpendicularly to the side shell plate at 75 mm measured from the edge of the side shell plate. The end sides of web frames and longitudinals were welded on this plate. At these locations triangular plates with the same thickness were also welded on the side shell plate and the 9.5 mm thick plates to prevent web frames and longitudinals from rotating about the y-axis. Figures 4.5 and 4.6 show the dimensions and sizes of the fabricated physical model. Since there were three model specimens to be tested, it was not possible to weld the model permanently into the test bed. There-

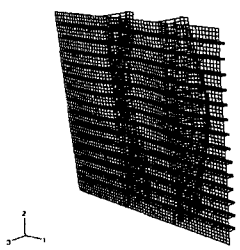

Mode 1 - Prototype (33.09 Hz)

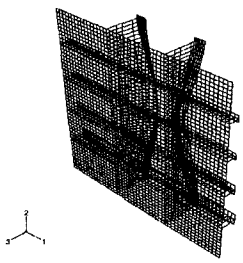

Mode 1 - Model (584.3 Hz)

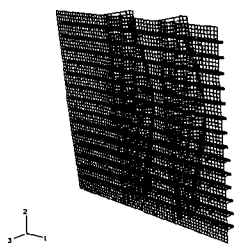

Mode 2 - Prototype (36.76 Hz)

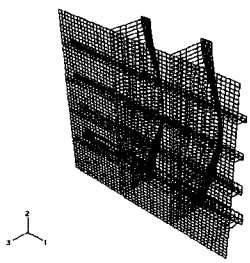

Mode 2 - Model (586.3 Hz)

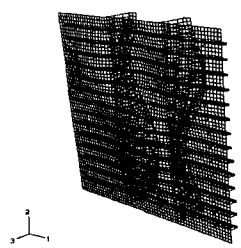

Mode 3 - Prototype (45.78 Hz)

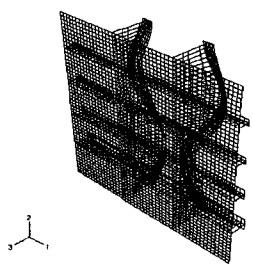

Mode 3 - Model (1109.2 Hz)

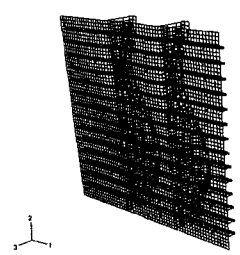

Mode 4 - Prototype (49.36 Hz)

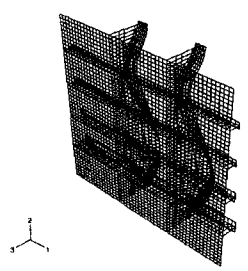

Mode 4 - Model (1111.4 Hz)

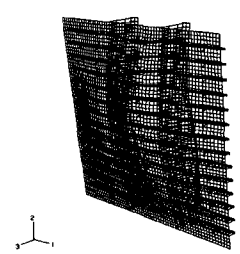

Mode 5 - Prototype (49.73 Hz)

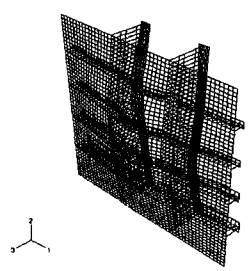

Mode 5 - Model (1136.7 Hz)

Figure 4.4: First five modes of prototype and model

fore the model and the test bed were connected by bolts. Figure 4.6 (b) shows the connection between the model and the test bed.

The test bed consisted of a rigid steel table and a frame with four WF section and two hollow section steel columns; these columns were connected to steel C sections where the model was mounted in the horizontal position for testing, see Figure 4.7 (a). Figure 4.7 (b) shows C section and column section dimensions. The frame columns were welded to a 1218 mm long 1110 mm wide and 12.7 mm thick steel base plate which was connected to the ribbed steel table by 15.9 mm diameter bolts. Rubber mat was placed between the base plate and the table so that the plate was fully in contact with the ribbed steel table and the effect of vibration that would come from the lab floor could be damped out. The ribbed steel table was 1840 mm long 1110 mm wide and 920 mm high. The steel table was available in the structural laboratory and it was built for dynamic testing. Plan view of test bed frame and base plate to steel table bolt connection are shown in Figure 4.7 (c); a square of 390 mm by 390 mm shown in the figure was the provision for mounting the exciter. Exciter used in experimental investigation stood on the base plate, see Figure 4.8. It was bolted to the steel table through the base plate.

4.3 Summary

In this chapter a procedure to determine the one twentieth model of sizes and dimensions are discussed. To determine the one twentieth model dimensions, the first five modes of prototype and the model were computed and compared. It was

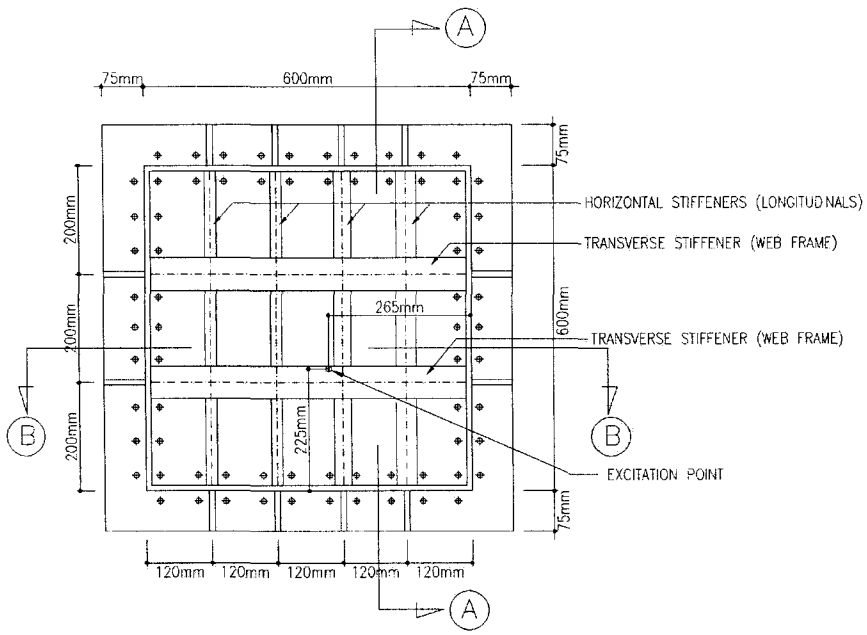

(a) plan view

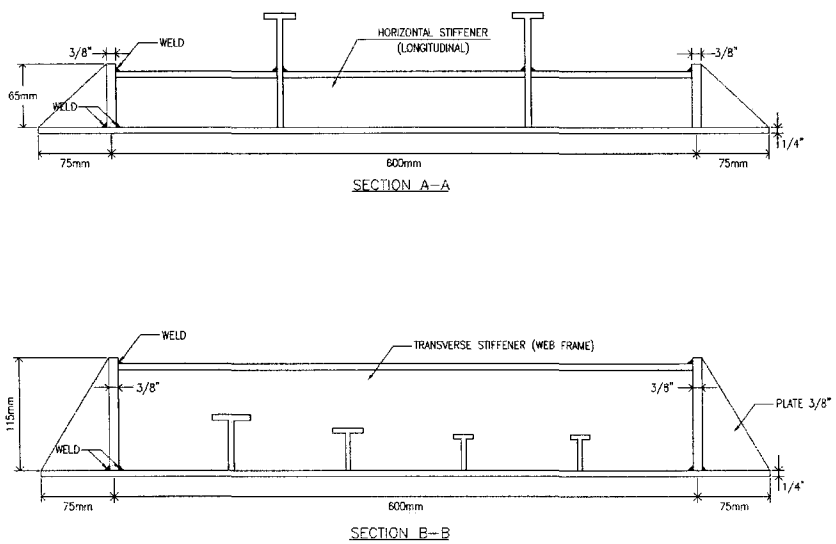

(b) section A-A and B-B

Figure 4.5: Plan view and sections of the fabricated model

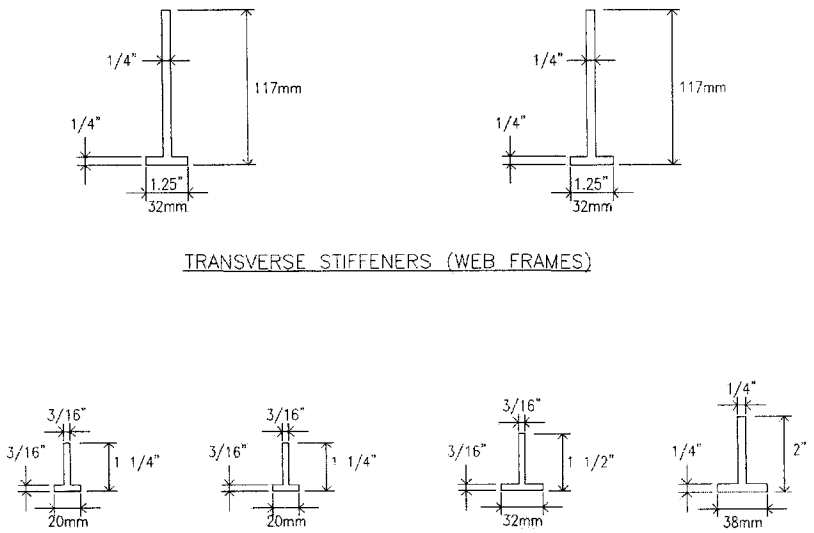

(a) web frame and longitudinals sizes

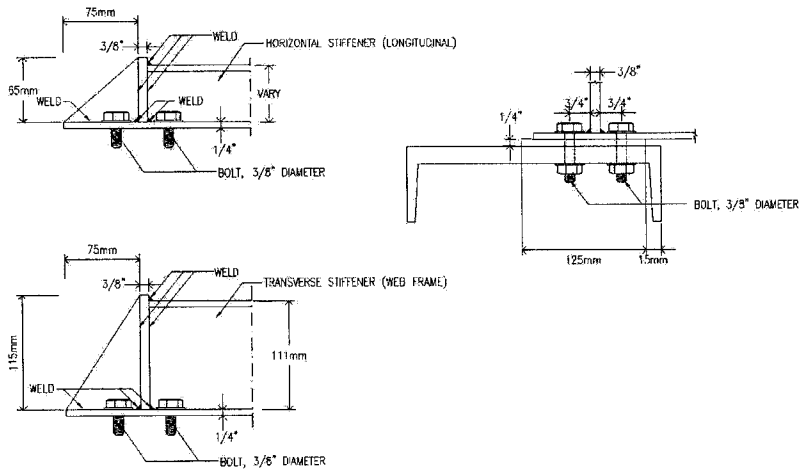

(b) model and test bed bolt connection

Figure 4.6: Dimensions and sizes of the fabricated model

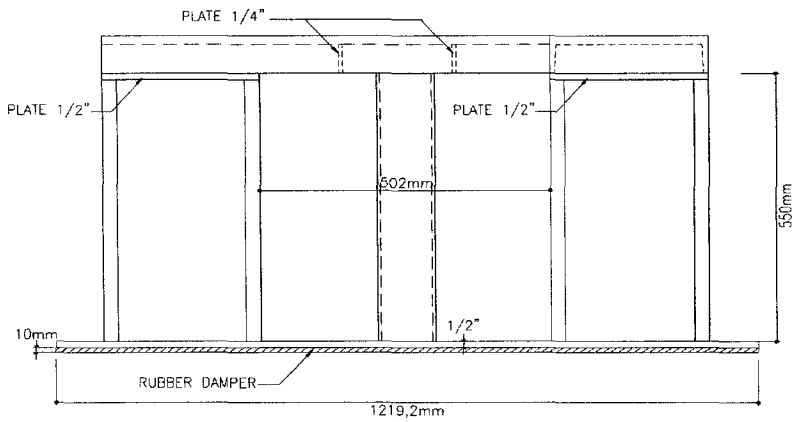

VIEW – B

(a) side view

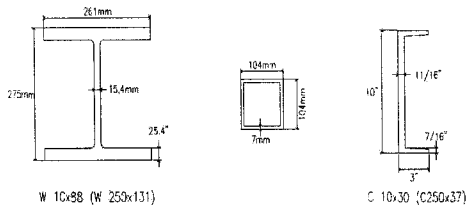

(b) cross sections

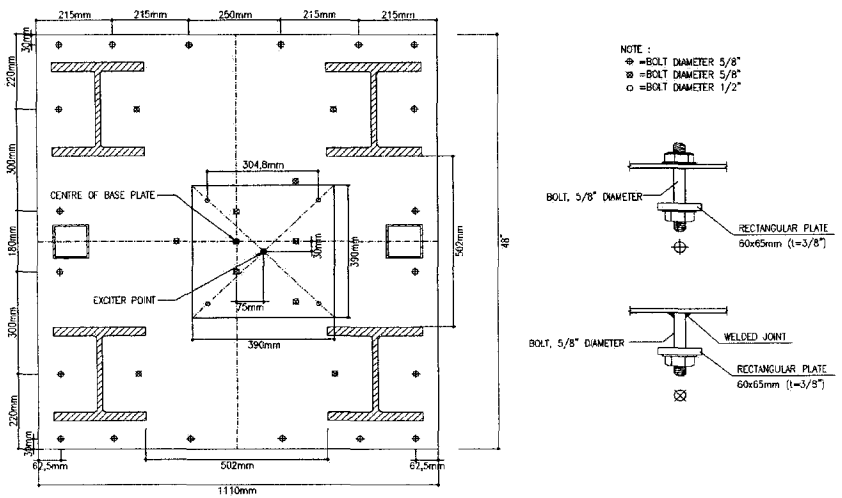

(c) plan view (left) and base plate to steel table bolt connection (right)

Figure 4.7: Dimensions and sizes of test bed frame

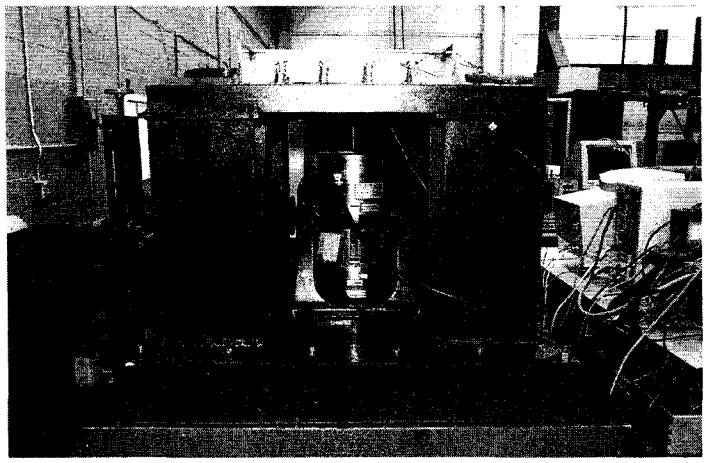

Figure 4.8: The one twentieth model mounted on test bed

observed that the first four modes were flexural-torsional modes of the web frame and the fifth mode was the first bending mode of the structure. The modes of one twentieth model and prototype were similar. However the first five natural frequencies of the model and one twentieth geosim model (the model having dimension exactly one twentieth of the prototype) differed by a maximum value of 22.36%. In addition dimensions of the test bed are also presented. The test bed constisted of a steel table and a frame which was designed especially for this investigation.

Chapter 5

Numerical and Experimental Investigations

5.1 Introduction

Numerical and experimental studies carried out on orthogonally stiffened plate models of ship's side shell structure under intact and damaged conditions, are presented and the results are discussed in this chapter. Three models were fabricated; these were called model #1, model #2 and model #3. The orthogonally stiffened plate model was excited by a random load whose dominant frequency was about 2 Hz. The random excitation force simulated the excitation force exerted on the modelled structure due to Pierson-Moskowitz wave spectrum. The excitation frequency was far separated from the model's fundamental natural frequency. The model's fundamental frequency computed by ABAQUS (2004) was 584.3 Hz; it was a flexural-torsional frequency of web frames, whereas the fist overall bending frequency of the orthogonally stiffened plate system was 1136.7 Hz. In the experimental investigation, output-only experimental modal analysis was implemented. It means that the structural modal parameters were extracted from model's response

only, without measuring excitation forces. In addition, the effect of sampling frequencies on the model's modal parameters identified from measured response was investigated. In this chapter preliminary numerical investigations for determining the sensor locations in the model are discussed. These include various damage cases considered and finite element procedures implemented in these investigations. Then experimental procedures are discussed, and experimental results are presented. Later the results of the numerical and experimental investigations carried out concerning the effect of damages on modal frequencies, root mean square (rms) of amplitude response and the D_n function (given in Equation 3.39) are addressed. Some of the investigation results presented in this chapter were reported earlier in Budipriyanto et al. (2004b) and Budipriyanto et al. (2006a).

5.2 Preliminary Numerical Investigations

Preliminary numerical investigations were carried out to establish sensor location in experiments and also to conduct a sensitivity analysis of the model dynamic response due to cracks. The effect of one or more crack(s) occurring in the longitudinal (horizontal stiffeners) on the response of the orthogonally stiffened plate model was investigated. As mentioned earlier, the term "damage" and "crack" are used interchangeably in this thesis. In addition, intact condition and damage case #0 also referred to the same condition.

5.2.1 Damage Cases

Damage cases considered in this investigation were determined from previous studies reported by Schulte-Strathhaus (1991) and Sucharski (1995). They reported that at least forty percent of damage in side shell tanker ship occurred in the intersections of horizontals and bulkhead or web frame. Table 5.1 gives the locations and size of cracks for eight damage cases investigated in this study. In the first four cases, the cracks occurred on the second longitudinal at locations 1 and 2, see Figure 5.1. These cracks will allow one to examine the structural behavior when cracks occur at the connection between a longitudinal and bulkheads. In damage cases #5 to #8, cracks were present only at locations 3 and 4. These cracks will allow one to investigate the scenarios of crack growth at the intersections of the longitudinals and a web frame. In damage case #1, a crack was introduced across half the width of the longitudinal's flange width (about 10 mm wide) at location 1 and there was no crack at location 2. In the second case, the crack in location 1 was made to run across the whole width of the longitudinal's flange while in location 2 the crack depth was through one half of the flange width. Effect of cracks on response of the orthogonally stiffened plate model were investigated when cracks were introduced according to the damage scenarios listed in Table 5.1. In the experimental investigations, in order to utilize the same three models fabricated for the purpose, cracks were introduced first at locations 1 and 2 and then the cracks at these locations were welded back before introducing cracks at locations 3 and 4, respectively. The condition after the crack locations 1 and 2 were welded was called damage case #0*.

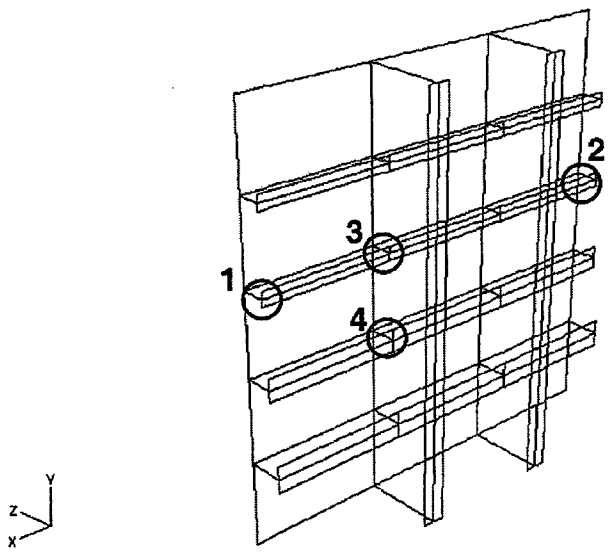

Figure 5.1: Crack locations

Table 5.1: Crack length for eight damage cases

Case #	Crack length at location			
	1	2	3	4
1	10.0 mm	none	none	none
2	20.0 mm	10.0 mm	none	none
3	20.0 mm	20.0 mm	none	none
4	25.4 mm	30.8 mm	none	none
5	none	none	10.0 mm	none
6	none	none	20.0 mm	16.0 mm
7	none	none	20.0 mm	32.0 mm
8	none	none	30.8 mm	41.7 mm

5.2.2 Finite Element Modeling Procedures

In the finite element analysis, the structure was discretized, using eight-noded S8R5 and six-noded STRI65 shell elements. The latter elements were located in the "transition" regions only, between the coarser and the finer meshes (for detailed description of these elements, see ABAQUS (2004)). In element mesh for the analysis carried out in this thesis element aspect ratio, the ratio between the longest and the shortest side of the element, in region away from the crack was maintained below 2.5 or above 0.4. In the regions where cracks were located, the maximum aspect ratio was varied between 0.5 to 1.5.

In order to model the crack tip properly, the eight-noded shell element was collapsed to a six-noded triangle having 3 nodes at the same coordinate crack tip location. In addition the nodes at the mid-side of the two sides joining at the crack tip were moved to the quarter points closest to the crack tip to obtain a square root singularity. It is called the quarter point technique.

The finite element model was examined under intact and damaged conditions. In these investigations, the model was excited at the corresponding resonant frequency and the same damping ratio of 0.01 was chosen for all modes. In this investigation, the model was assumed to have fixed boundary conditions along its sides.

5.2.3 Determination of Locations for the Sensors

In experimental studies involving vibration measurements, the location of the measuring sensor has to be decided carefully. A bad choice of the sensor's location af-

fects the measured response. The data obtained may not show the required characteristics necessary for crack identification. Since the structure under consideration is complex and the change in the modal parameters due to the presence of cracks was not known prior to the tests, a finite element model was utilized to identify the best sensor locations. In addition the location of the excitation point was also investigated. This is also important since it facilitates the excitation of proper modes. The exact location of the excitation point selected for these numerical and experimental investigations has been given earlier in Figure 4.5.

Figure 5.2 shows node numbering, web frame and longitudinal number. The acceleration and strain response at the nodes on longitudinal #2 and at the nodes of the transverse web frames #1 and #2 were normalized using the largest response value which was selected from response data under intact and the four damage cases (cases #1 to #4 or #5 to #8). The normalized response at the nodes on the longitudinal and web frames were plotted. These plots are presented in Appendix B.

Figures 5.3 and 5.4 show the first and second modes acceleration response of horizontal #2 along the y- direction in cases #1 to #4 and #5 to #8, respectively. As seen from these figures, appreciable changes occurred in the responses due to the presence of cracks for all damage cases. Figures 5.5 and 5.6 show the first and second mode acceleration response of the flange nodes on the web frame along the x- direction. These results show that, as damage extent increased, the response changed significantly from one sensor location to the other. For instance, the acceleration response in the y- direction (A_y) at nodes 6 and 92 changed considerably

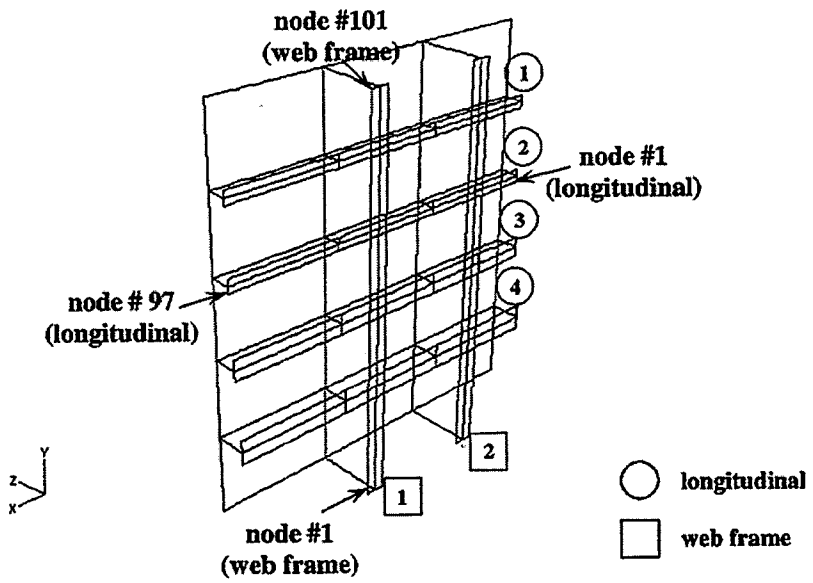

Figure 5.2: Longitudinal number, web frame number and node numbering

from one damage case to the other, see Figure 5.3. However the response did not show much change in Figure 5.5, since the local deformations of the transverse web frame in mode 2 were not influenced by the cracks occurring at the end support of the longitudinal for damage cases #1 to #4. As seen in Figures 5.3 and 5.4, a small asymmetric crack at an end support or on the flange at an intermediate support seems to introduce a very large change in the acceleration of the longitudinal's flange in the y- direction. Moreover when the flange and the web of an intermediate support developed cracks (damage cases #5 to #8), the acceleration of the longitudinal in the y- direction and the transverse's flange in the x- direction showed consistent and highly noticeable changes due to cracking, see Figures 5.4 and 5.6.

The modal strain response for modes 1 and 5, for the damage cases #1 to #4 in the x- direction for the nodes on the side shell plate, are shown in Figure 5.7.

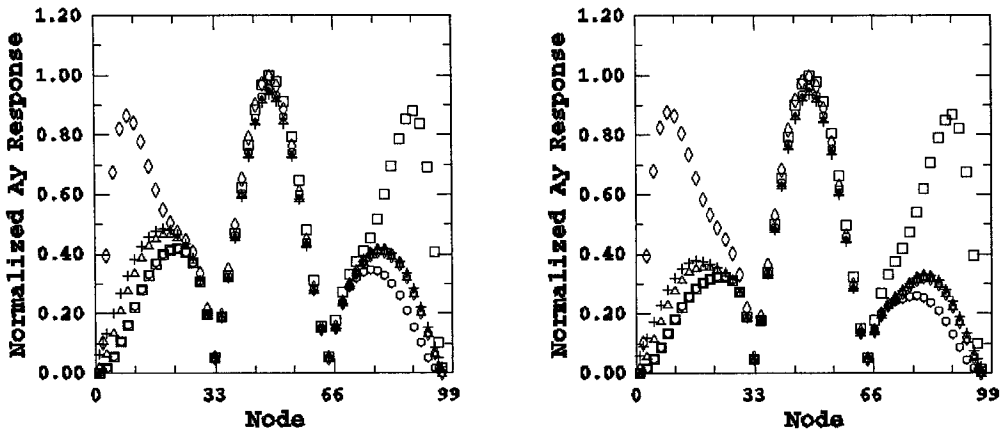

(a) Mode 1 (b) Mode 2

Figure 5.3: Normalized acceleration response of longitudinal #2 in the y- direction for damage cases #1 to #4: O: intact, □: case #1, ◇: case #2, △: case #3, +: case #4

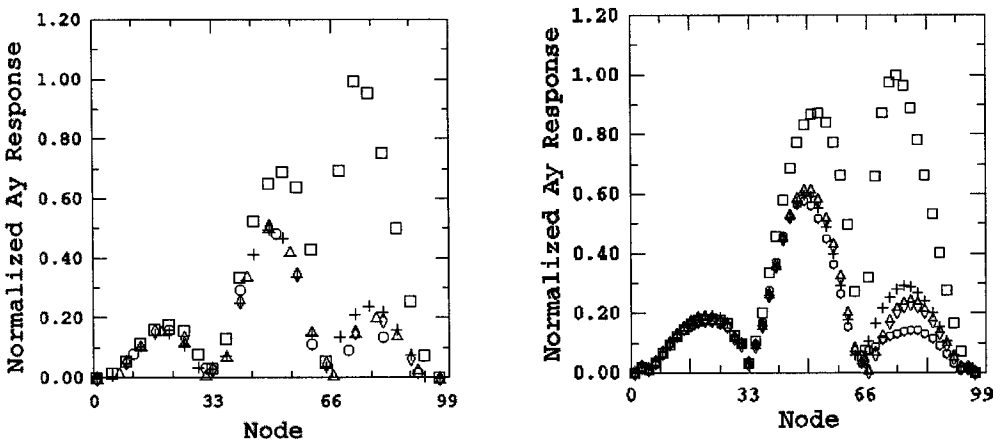

(a) Mode 1 (b) Mode 2

Figure 5.4: Normalized acceleration response of longitudinal #2 in the y- direction for damage cases #5 to #8: O: intact, □: case #5, ◇: case #6, △: case #7, +: case #8

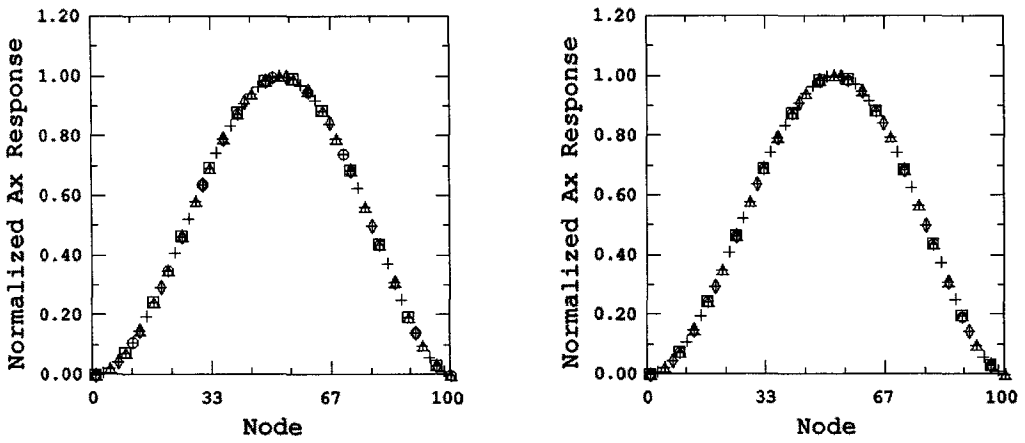

(a) Mode 1 (b) Mode 2

Figure 5.5: Normalized acceleration response of transverse web frame #1 in the x-direction for damage cases #1 to #4: O: intact, □: case #1, ◇: case #2, △: case #3, +: case #4

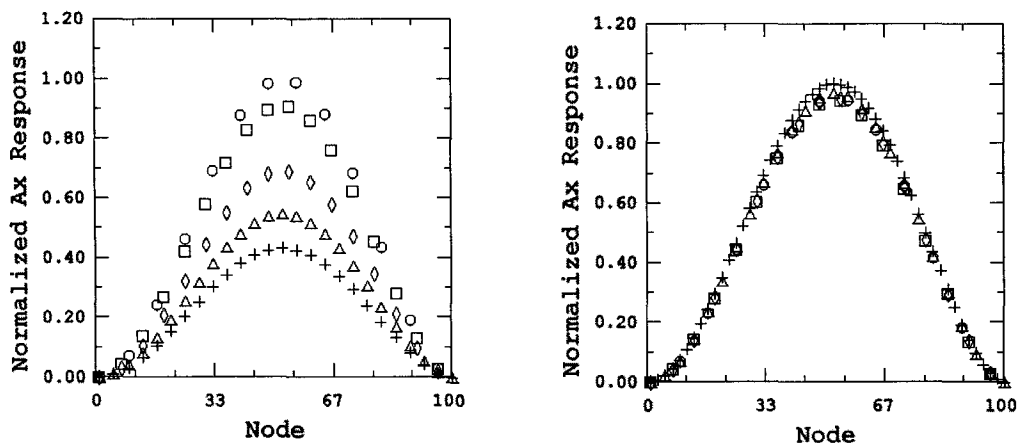

(a) Mode 1 (b) Mode 2

Figure 5.6: Normalized acceleration response of transverse web frame #1 in the x-direction for damage cases #5 to #8: O: intact, □: case #5, ◇: case #6, △: case #7, +: case #8

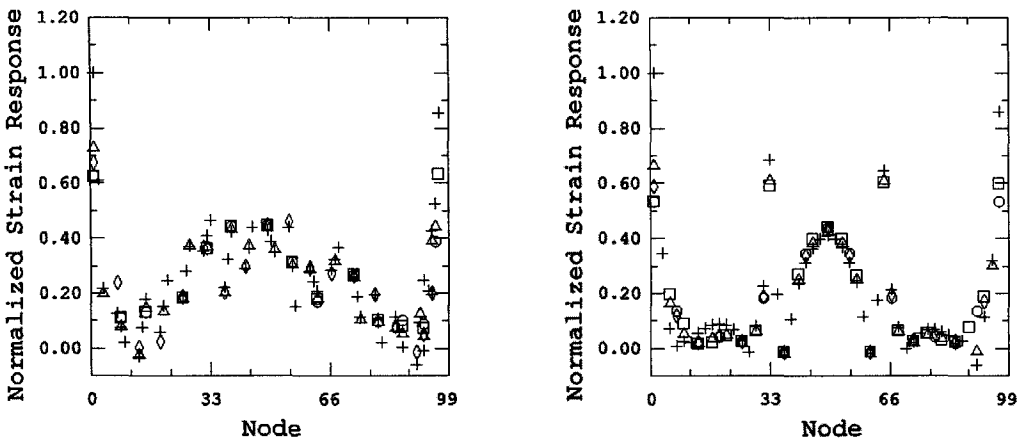

(a) Mode 1

(b) Mode 5

Figure 5.7: Normalized strain response of side shell plate along longitudinal #2 in the x- direction for damage cases #1 to #4: O: intact, □: case #1, ◇: case #2, △: case #3, +: case #4

Figure 5.8 shows the strain response for damage cases #5 to #8. Strain response in the x- direction for the nodes on the side shell plate changed significantly in the fixed support (nodes 1 and 97) and on nodes where the longitudinal and the transverse web frame intersected. The change in the strain over the whole length of the longitudinal was not consistent. However near the supports (nodes 1 and 97) and at the intersection between the longitudinal and the transverse web (node 35) strains changed significantly due to cracks, see Figures 5.7 and 5.8.

Accelerometer and strain gage locations were determined based on the above mentioned considerations and the possibility of mounting them on the model. Accelerometers #1, #2 and #3 were mounted on longitudinal #2, at the tip of flanges, to measure the acceleration modal response in the y-axis direction while accelerome-

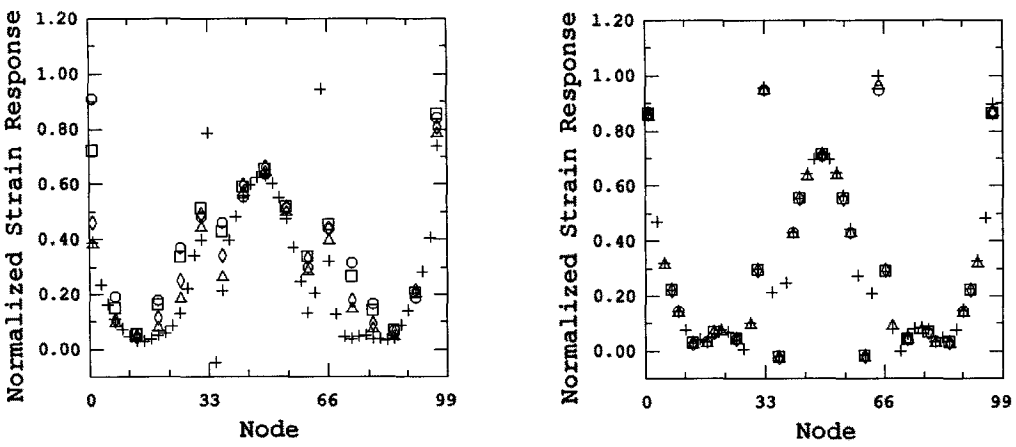

(a) Mode 1

(b) Mode 5

Figure 5.8: Normalized strain response of side shell plate along longitudinal #2 in the x- direction for damage cases #5 to #8: O: intact, □: case #5, ◇: case #6, △: case #7, +: case #8

ters #4, #5 and #6 were mounted on transverse web frames at the tip of the flanges to record the response in the x-axis direction (accelerometers #4 and #5 were located on transverse web frame #1 and accelerometer #6 was located on transverse web frame #2). The strain gages were mounted to monitor the local strain in the side shell plate in the x-axis direction. Figures 5.9 show the location of the accelerometers and the strain gages. The excitation point is shown in Figure 5.9 (b), see also Figure 4.5 for exact location of the excitation point.

5.3 Numerical Investigations

To predict the modal parameters (natural frequencies and mode shapes), and the acceleration and strain response of the orthogonally stiffened plate model under in-

tact and damaged conditions, ABAQUS finite element computer package program was utilized. By computing the model's modal parameters and response under damaged and intact conditions, the changes in the modal parameters and response due to the presence of cracks were determined. This step is very important since it will enhance greatly the possibility of identifying the modal parameters which characterize the damage occurring in the structure.

Simulations using neural network technique described in Chapter 3 was also implemented to obtain the D_n function given in Equation 3.39. The inputs of the networks were the free decay response generated using ABAQUS and its derivative. Amplitude of D_n functions for different damage cases were compared to assess the sensitivity of the amplitude to damage.

In the subsequent subsections, numerical investigations to study the effect of crack on the natural frequency, response, the rms of response amplitudes and the D_n amplitude are discussed.

5.3.1 Effect of Crack on the Natural Frequency

The natural frequencies of the ship's side shell model were computed under intact and damaged conditions. In several cases the frequencies did undergo a change in magnitude due to the presence of cracks while in other cases the effect on the frequencies was very small and in some cases no change occurred. The natural frequencies for the intact (damage case #0) and damaged conditions are shown in Figure 5.10. The natural frequencies of modes 1 to 4 (in cases #1 to #4) did not change as a result of changing crack length and location; while for mode 5,

appreciable frequency changes occurred. In cases #5 to #8, the natural frequencies changed significantly for modes 1 to 4 and no changes were observed for mode 5. This is due to the fact that the first four frequencies correspond to the local torsional-flexural modes for the two web frames and in these modes (modes 1 to 4) the side plate does not suffer any bending, see Figure 4.4. The ship's side plate undergoes flexural bending only in mode 5. These results show that using the magnitude of the natural frequency alone as a damage indicator (a quantity that can reveal the occurrence of damage on a structure) can lead to false conclusions.

5.3.2 Effect of Crack on Mode Shape

The mode shapes of the model under intact and damaged conditions were also computed. The purpose of doing this analysis was to examine the effect of cracking on the mode shapes and to compare them with the mode shapes obtained when the model was excited at a single point. Moreover, the results could be used as a rough guide to indicate the best location to place the accelerometers during experimental investigations.

The modal displacement response for each natural frequency at a number of points on the web frame and the longitudinal of interest were calculated and then normalized using the largest displacement (for node numbering, web frame and longitudinal number, see Figure 5.2). In this investigation, acceleration response were computed on nodes of transverse web frames and longitudinal (horizontal stiffener) #2 and bending strain response were calculated on nodes of side shell plate along longitudinals #2 and #3. In addition only the first two modes (web

frame torsional-flexural modes, modes 1 and 2) and the first bending mode (mode 5) of the model were reported in this study.

In order to investigate the effect of cracking on displacement shapes along the different coordinate axes (the x-, y-, and z- axes) on the longitudinal (horizontal stiffener), displacements in the y- and z- directions were calculated while displacements in the x- and z- direction were computed and examined for the transverse web frame. The results of this investigation are presented in Appendix A. It can be seen from Figures 5.11 and 5.12 that for damage cases #1 to #4, the displacement shapes of the longitudinal along the y- axis were more sensitive to the presence of cracks while for damage cases #5 to #8 significant changes in modal displacement occurred in both directions. However the change in the y- direction was more appreciable, see also Figures A.3 (c) and A.4 (c) for the changes in mode 5.

Modal displacement of transverse web frame #1 for damage cases #1 to #4 and #5 to #8 for modes 1 and 2 are shown in Figures 5.13 and 5.14. It can be seen in Figures 5.13 (c), 5.13 (d), 5.14 (c), and 5.14 (d) that the modal displacements in mode 2 decreased consistently along the x- and z- directions for damage cases #5 to #8. In mode 1 the modal displacement did not change due to cracks, see Figures 5.13 (a), 5.13 (b), 5.14 (a), and 5.14 (b). However modal displacements of the transverse web frame changed more significantly along the x- direction than those along the z- direction in mode 5, see Figures A.5 to A.8 in Appendix A.

5.3.3 Effect of Crack on the rms of Response

A numerical investigation using the finite element program ABAQUS was carried out to obtain the rms values of the model's random response for eight different possible damage cases presented Table 5.1. The random force used to excite the model simulated the model of an ocean wave having a Pierson-Moskowitz spectrum with a dominant spectral wave frequency of 2 Hz. This corresponds to a prototype dominant wave frequency of 0.1 Hz (or a period of 10 seconds). Detailed description of the technique to determine the excitation frequency range is presented in Appendix C. Random force spectrum similar to the wave force spectrum, which is a peaked spectrum in the frequency ranges, was employed as input in this investigation. The spectrum was extended beyond this range and it was assumed that the spectrum was flat (have the same value) within the frequency range where the first five model's natural frequencies existed (20 Hz to 1200 Hz).

The rms values of response were computed at the twelve sensor locations shown in Figure 5.9 for all the eight damage cases. The rms values of response, obtained from one type of sensor (accelerometer or strain gage) were then normalized by dividing them by the largest rms value present at the location of that sensor; the results are shown in Figures 5.15 to 5.18. Figures 5.15 and 5.16 show the normalized acceleration rms values, while Figures 5.17 and 5.18 show the normalized strain rms values for frequencies ranging from 200 Hz to 1200 Hz, for the eight cases considered. For all cases considered (damage cases #1 to #8 shown in Figures 5.15 and 5.16), appreciable changes occurred in the rms values of the response at the location of accelerometers #1, #2, #4 and #5. In damage cases #1 to #4, rms response at

all accelerometer locations, except at location of accelerometer #6, showed changes in mode 5 (at frequency of 1200 Hz), see Figure 5.15. Nevertheless no changes in modes 1 and 2 (at frequency of 600 Hz) were observed. In damage cases #5 to #8, at locations of accelerometers #1 and #2 the rms response changed appreciably in mode 5 while at locations of accelerometers #4 and #5 the rms showed significant changes in modes 1, 2, and 5, see Figure 5.16. With the exception of strain gage #2, all strain rms values showed appreciable changes for cases #1 to #4. Consistent changes at locations of strain gages #3, #4 and #6 were observed. Changes in the strain rms values of strain gages #1, #4 and #5, were observed in cases #5 to #8 in mode 5. However, changes in these damage cases were insignificant. Therefore strain response in cases #5 to #8 were not further investigated and were not used for damage identification presented in Chapter 6.

5.3.4 Effect of Crack on the D_n Amplitude

Amplitude of D_n function given in Equation 3.39 was computed using a neural network technique for various damage cases that occurred in the orthogonally stiffened plate model to assess its sensitivity under different damaged conditions. The D_n function included not only the modal frequency and the damping ratio, but also the response amplitude. By including these three parameters in the function the amplitude would be more sensitive to damage occurring on the model.

The effect of cracks, occurring at a single location (damage cases #1a to #1 and #5a to #5, see Table 5.2) and at two simultaneous different locations (damage cases #2 to #4 and #6 to #8, see Table 5.1), on the D_n amplitude was examined in this

Table 5.2: Crack length for single crack cases

Case #	Crack length at crack location				% of flange width
	1	2	3	4	
0	none	none	none	none	0.0
1a	2.5 mm	none	none	none	12.5
1b	5.0 mm	none	none	none	25.0
1c	7.5 mm	none	none	none	37.5
1	10.0 mm	none	none	none	50.0
5a	none	none	2.5 mm	none	12.5
5b	none	none	5.0 mm	none	25.0
5c	none	none	7.5 mm	none	37.5
5	none	none	10.0 mm	none	50.0

investigation. For cracks occurring at a single location, cracks with an increment of 2.5 mm in length (12.5% of flange width) at location 1 or 3 were investigated. In Table 5.2, the crack length is also presented as a percentage of flange width.

In this investigation the D_n function was obtained from simulations utilizing the neural network technique whose inputs were the model's free response and its derivative. The free response was numerically computed by ABAQUS using modal damping ratio obtained from the experiment. The average values of the damping ratios measured from model #2 and #3 were employed as input in this numerical investigation, see subsection 5.4.5 for the damping ratio measured from experiments. Neural network simulations using the experimental response of model #1 could not be carried out since the model's response in the damage cases as given in Table 5.2 were not measured. Neural network simulations were performed till the minimum difference between the simulated and the input response was reached. Typically the network required as many as 10000 iterations for these cases.

Numerically computed natural frequencies of the first two modes and the fifth

Table 5.3: Modal frequency and damping ratio for single crack cases

Case #		0	1a	1b	1c	1
Natural frequency (Hz)	Mode 1	584.30	584.30	584.30	584.30	583.61
	Mode 2	586.30	586.30	586.30	586.30	586.30
	Mode 5	1136.70	1136.60	1136.50	1136.30	1136.00
Damping ratio*) (%)	Mode 1	0.504	0.503	0.504	0.506	0.503
Case #		0	5a	5b	5c	5
Natural frequency (Hz)	Mode 1	584.30	583.61	583.35	582.95	582.59
	Mode 2	586.30	585.89	585.81	585.72	585.67
	Mode 5	1136.70	1136.60	1136.60	1136.60	1136.60
Damping ratio*) (%)	Mode 1	0.504	0.392	0.339	0.350	0.395

*)the average of values measured from response of model #2 and #3

mode for intact (damage case #0) and single crack cases (where cracks occurred at one location) are presented in Table 5.3. Average modal damping ratios of mode 1 measured from the experiment are also given in the same table. Natural frequencies of the first two modes did not decrease as a result of cracks occurring at location 1 (damage cases #1a to #1) while the modal frequencies of mode 5 decreased slightly. For damage cases #5a to #5 where cracks occurred at location 3 natural frequencies of mode 1 decreased. Natural frequencies of mode 2 did not change significantly whereas there was no change in natural frequencies of mode 5 in these damage cases. The damping ratio changed considerably from intact to damage case #1a. The damping ratio values did not have any trend due to increasing crack lengths.

The neural network simulations were performed for the response of accelerometers #1 and #4. These accelerometers were chosen since one was mounted on the

longitudinal (horizontal stiffener) and the other was mounted on the web frame, see Figure 5.9. In addition, only response of mode 1 were used as inputs for the simulations. The reason was that the natural frequencies of this mode did not change for damage cases #1a to #1 (see Table 5.3) and damage cases #2 to #4 (see Figure 5.10) while for damage cases #5a to #5 (see Table 5.3) and damage cases #5 to #8 (see Figure 5.10) the modal frequencies decreased consistently. Moreover damping ratios of this mode under these damage cases did not have any trend (see Table 5.3) and experimental results presented in section 5.4.5. Therefore mode 1 was chosen in this investigation to determine the sensitivity of D_n under these damage cases. Simulation for other accelerometers and modes could be carried out in a similar manner.

The D_n amplitudes obtained from the neural network simulations for different damage cases were divided by the largest value to examine the relative change of these amplitudes. Figures 5.19 (a) and (b) show the normalized D_n amplitudes of the first mode response computed from accelerometer #1 and #4 response for the fourteen damage cases. It can be seen from these figures that the D_n amplitude was sensitive to the damage; it changed as a result of cracks occurring in the model. Figure 5.19 also shows that the D_n amplitudes of both accelerometers produced similar trends. For single crack cases (cases #1a to #1 and #5a to #5) the amplitudes increased consistently although there was no change in the modal frequencies for damage cases #1a to #1. It was also shown earlier that no trend was observed in the modal damping ratios for all these damage cases. For cracks occurring simultaneously at two locations D_n amplitudes did not show any predominant

trend as crack lengths increased. This was due to the interaction of responses at these two locations that tended to cancel the effect of each other. In the experimental investigation presented in the next section D_n amplitudes were examined especially under the damage cases where the amplitudes showed a trend.

5.4 Experimental Investigations

Experimental investigations on the orthogonally stiffened aluminum models of the side shell of a ship structure were carried out in the structural laboratory of Memorial University. Three models were tested under different damage conditions using random excitation forces having dominant frequency of 2 Hz. The excitation dominant frequency of 2 Hz was separated by a large frequency range from the numerically computed model's fundamental frequency of 584.3 Hz. Prior to performing the experimental testing sensors employed in the testing were calibrated to obtain the calibration factor of every sensor mounted in the model. The model's responses were acquired using a data acquisition system and recorded in a computer for further analysis. The modal frequency, the damping ratio and rms of amplitude were extracted from the acquired response. Moreover the effect of cracks on amplitudes of the D_n function was examined. The neural network technique was employed to calculate D_n amplitudes under different damage cases using measured response as input. Mode shapes were not extracted from the measured response since it would require many sensors (accelerometer and strain gage) to obtain the mode shapes of the horizontal and web frames. Therefore it was decided that mode shapes would

not be used as an indicator of damage in this part of the investigation.

This section discusses the experimental set up and sensor calibration and locations, study on sampling frequency used in the experiment and excitation force amplitudes, and experimental results including the modal parameters and the rms values of response for different damage cases. The change of D_n amplitudes obtained from neural network simulations using the experimental response data as input is also addressed.

5.4.1 Experimental Set up

The one twentieth orthogonally stiffened aluminum plate model was fabricated and tested to examine the model response changes under intact and damaged conditions. As mentioned earlier in this chapter three models were tested in this investigation; they were named model #1, #2 and #3. During the experiment the tested model was attached properly by bolted connections to a steel frame test rig which was specially designed and fabricated for this experimental investigation. The schematic diagram of experimental set up is shown in Figure 5.20 and a photograph of the set up is shown in Figure 5.21. The model was excited by random forces generated from a Wavetek 132 signal generator. The input signal was filtered by a low pass Krohn-Hite filter model 3323 to simulate wave force dominant frequency regime. The signal was amplified to drive a B&K model 4812 vibration exciter, which was connected to the model thorough a stinger. To monitor the excitation force, a Kistler model 912 load cell was attached to the stinger and it was connected to the plate of the tested model. The dynamic response of the model was

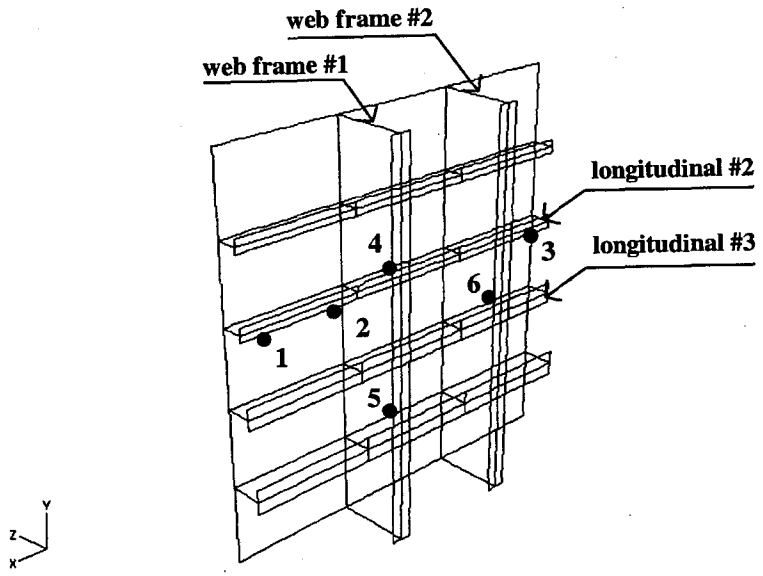

(a) Accelerometer locations

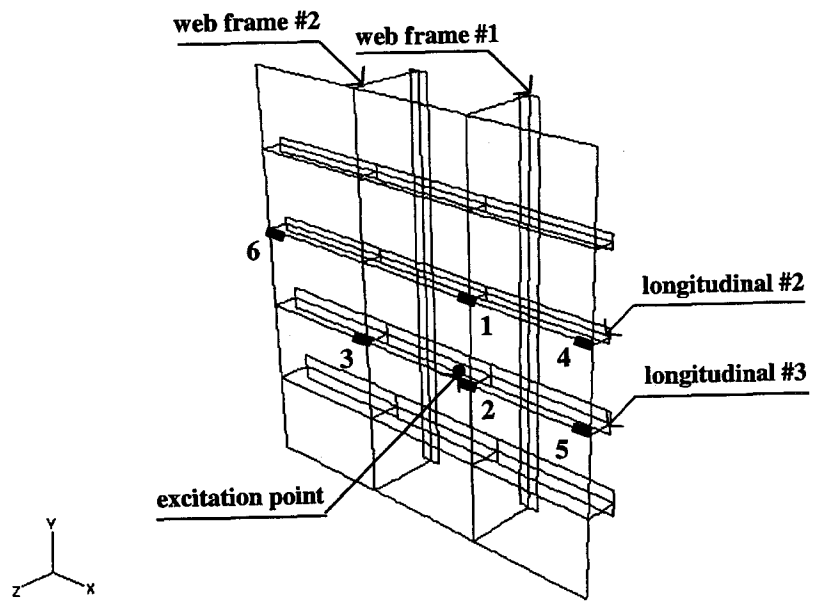

(b) Strain gage locations

Figure 5.9: Accelerometer and strain locations

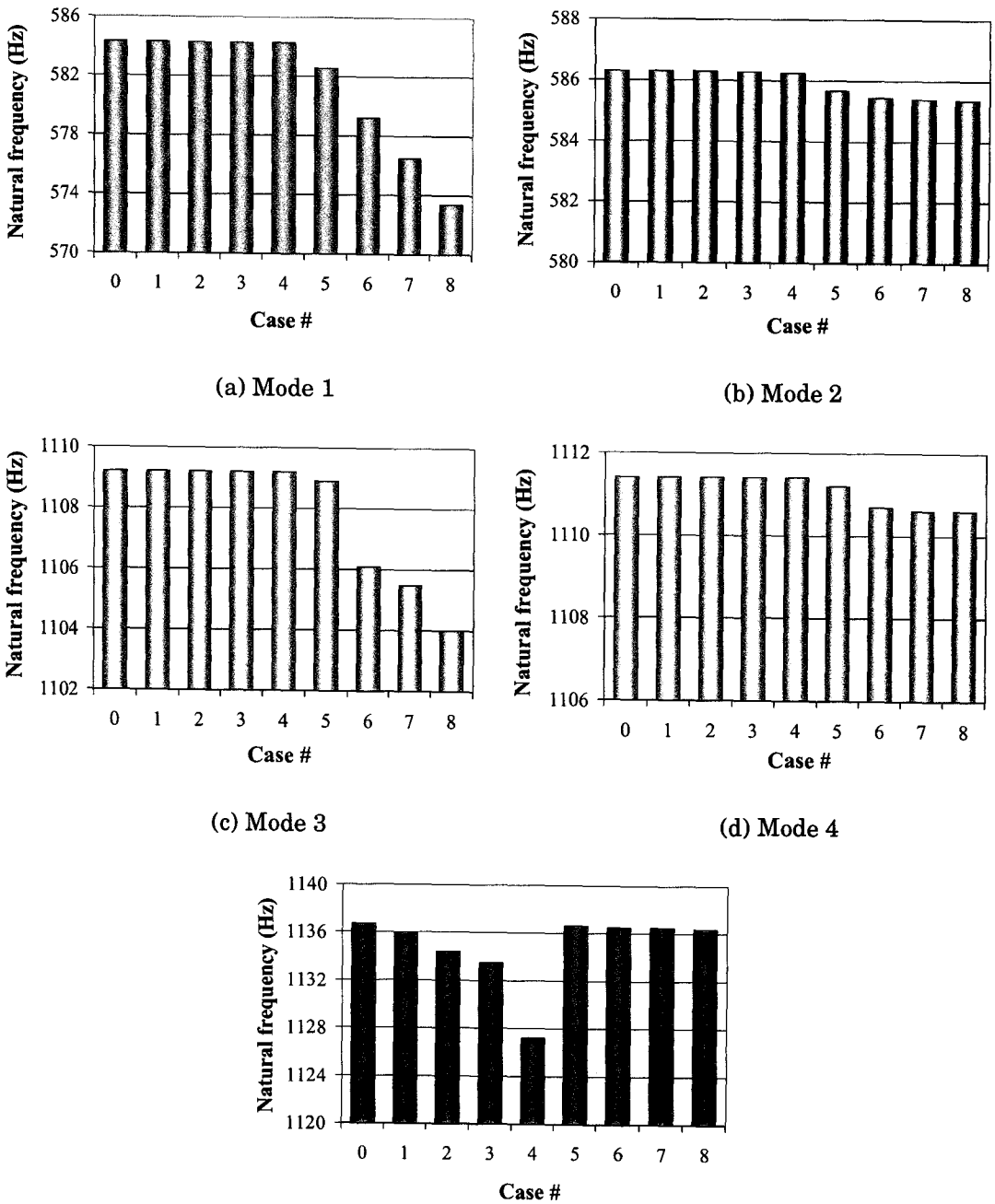

Figure 5.10: Changes in natural frequencies due to cracks for the first five modes

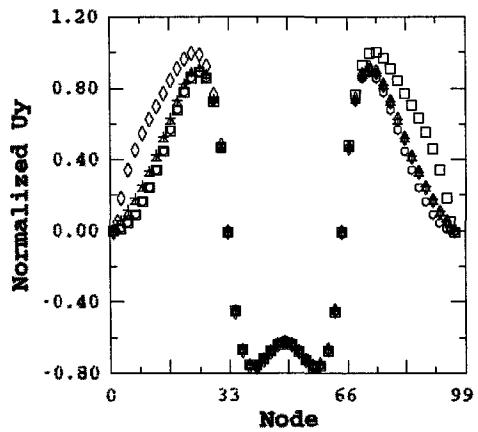

(a) Mode 1 the y-direction

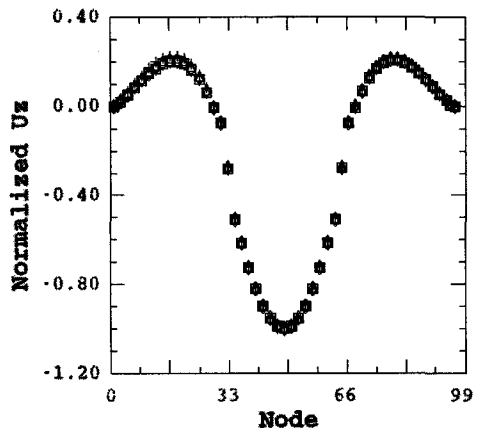

(b) Mode 1 the z-direction

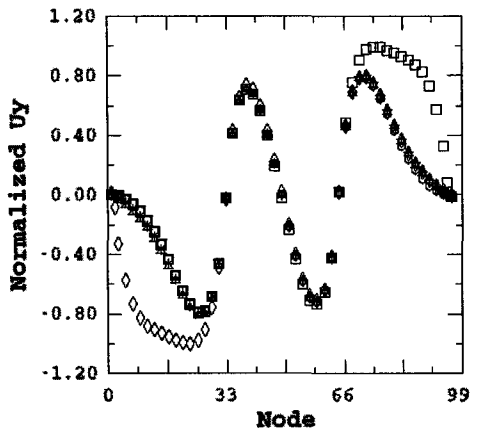

(c) Mode 2 the y-direction

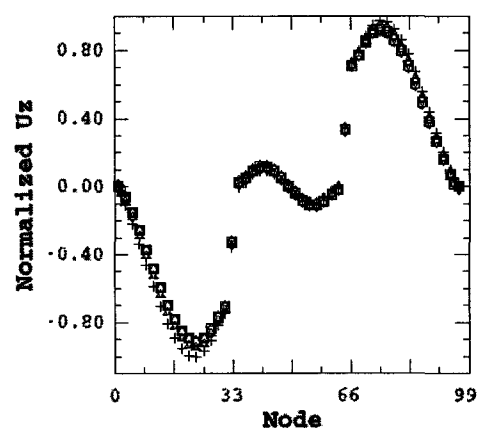

(d) Mode 2 the z-direction

Figure 5.11: Displacement shapes of longitudinal #2 in y- and z- directions for modes 1 and 2 for damage cases #1 to #4: O: intact, □: case #1, ◇: case #2, △: case #3, +: case #4

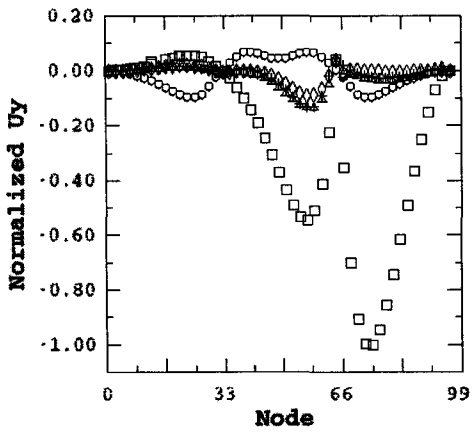

(a) Mode 1 the y- direction

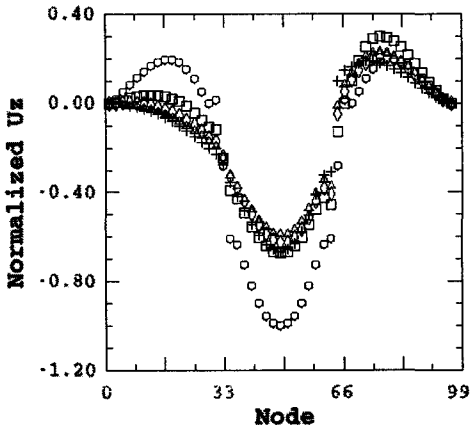

(b) Mode 1 the z- direction

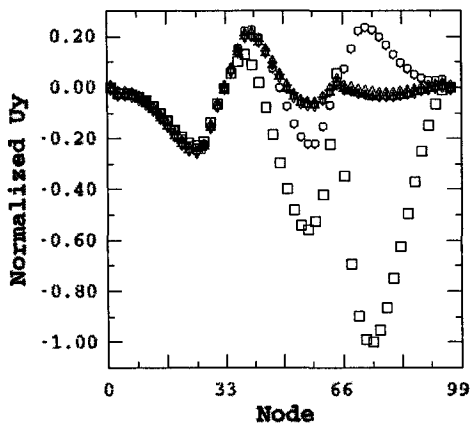

(c) Mode 2 the y- direction

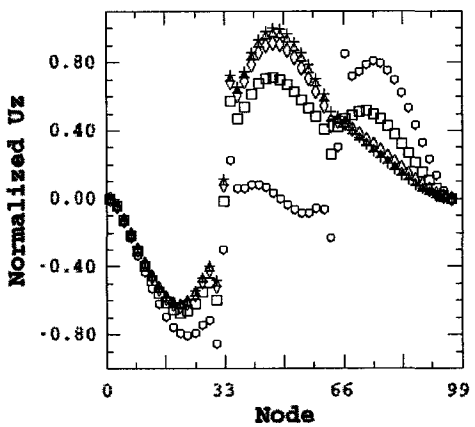

(d) Mode 2 the z- direction

Figure 5.12: Displacement shapes of longitudinal #2 in y- and z- directions for modes 1 and 2 for damage cases #5 to #8: O: intact, □: case #5, ◇: case #6, △: case #7, +: case #8

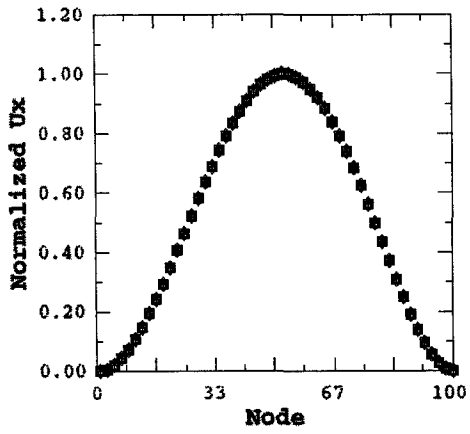

(a) Mode 1 the x- direction

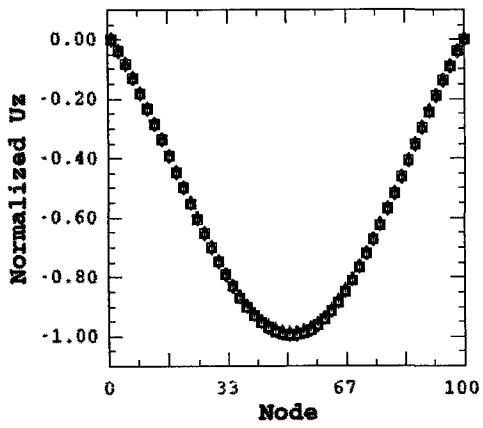

(b) Mode 1 the z- direction

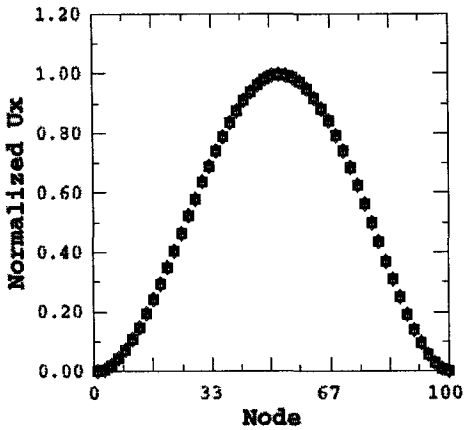

(c) Mode 2 the x- direction

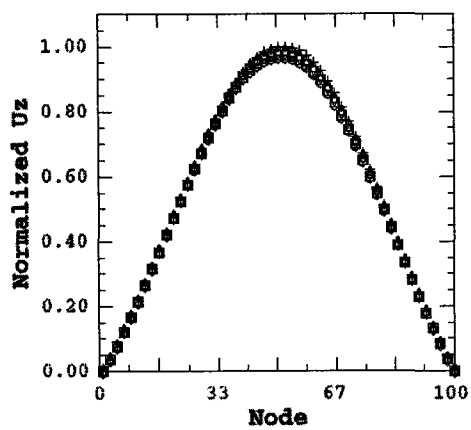

(d) Mode 2 the z- direction

Figure 5.13: Displacement shapes of transverse web frame #1 in x- and z- directions for modes 1 and 2 for damage cases #1 to #4: O: intact, □: case #1, ◇: case #2, △: case #3, +: case #4

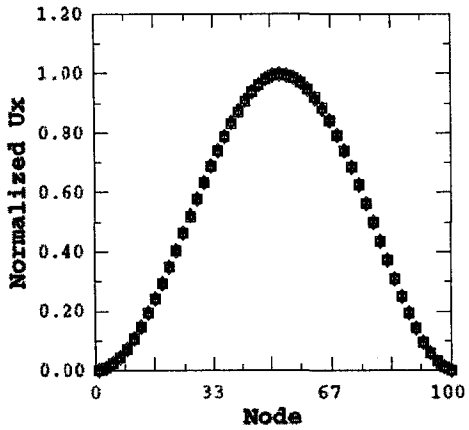

(a) Mode 1 the x- direction

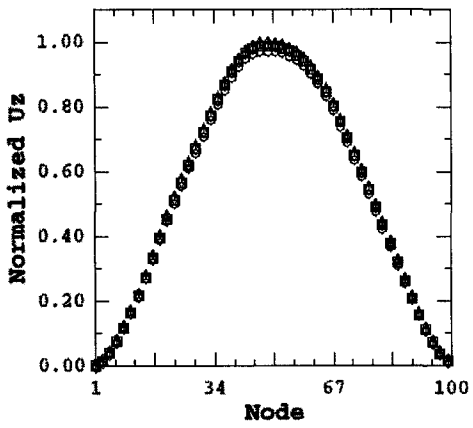

(b) Mode 1 the z- direction

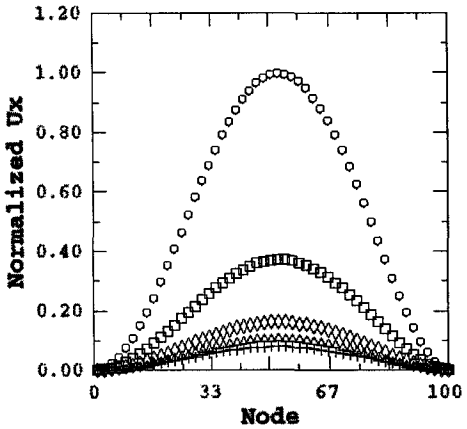

(c) Mode 2 the x- direction

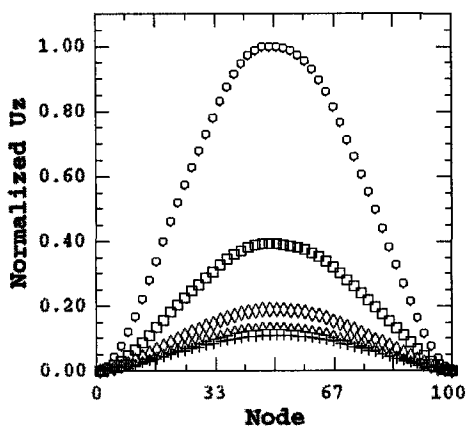

(d) Mode 2 the z- direction

Figure 5.14: Displacement shapes of transverse web frame #1 in x- and z- directions for modes 1 and 2 for damage cases #5 to #8: O: intact, □: case #5, ◇: case #6, △: case #7, +: case #8

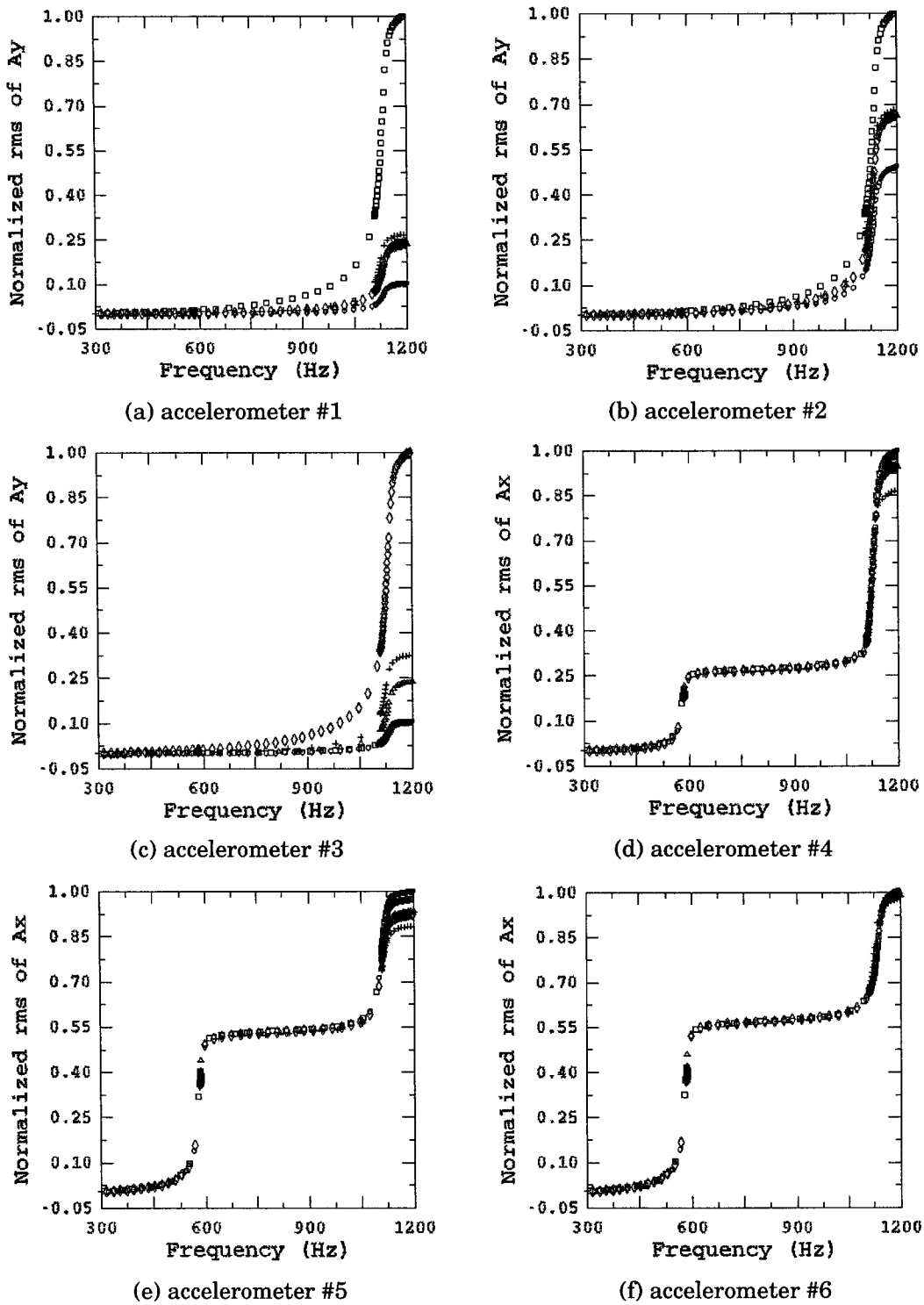

(a) accelerometer #1 (b) accelerometer #2

(c) accelerometer #3 (d) accelerometer #4

(e) accelerometer #5 (f) accelerometer #6

Figure 5.15: Normalized rms of acceleration as a function of frequency for damage cases #1 to #4: O: intact, □: case #1, ◇: case #2, △: case #3, +: case #4

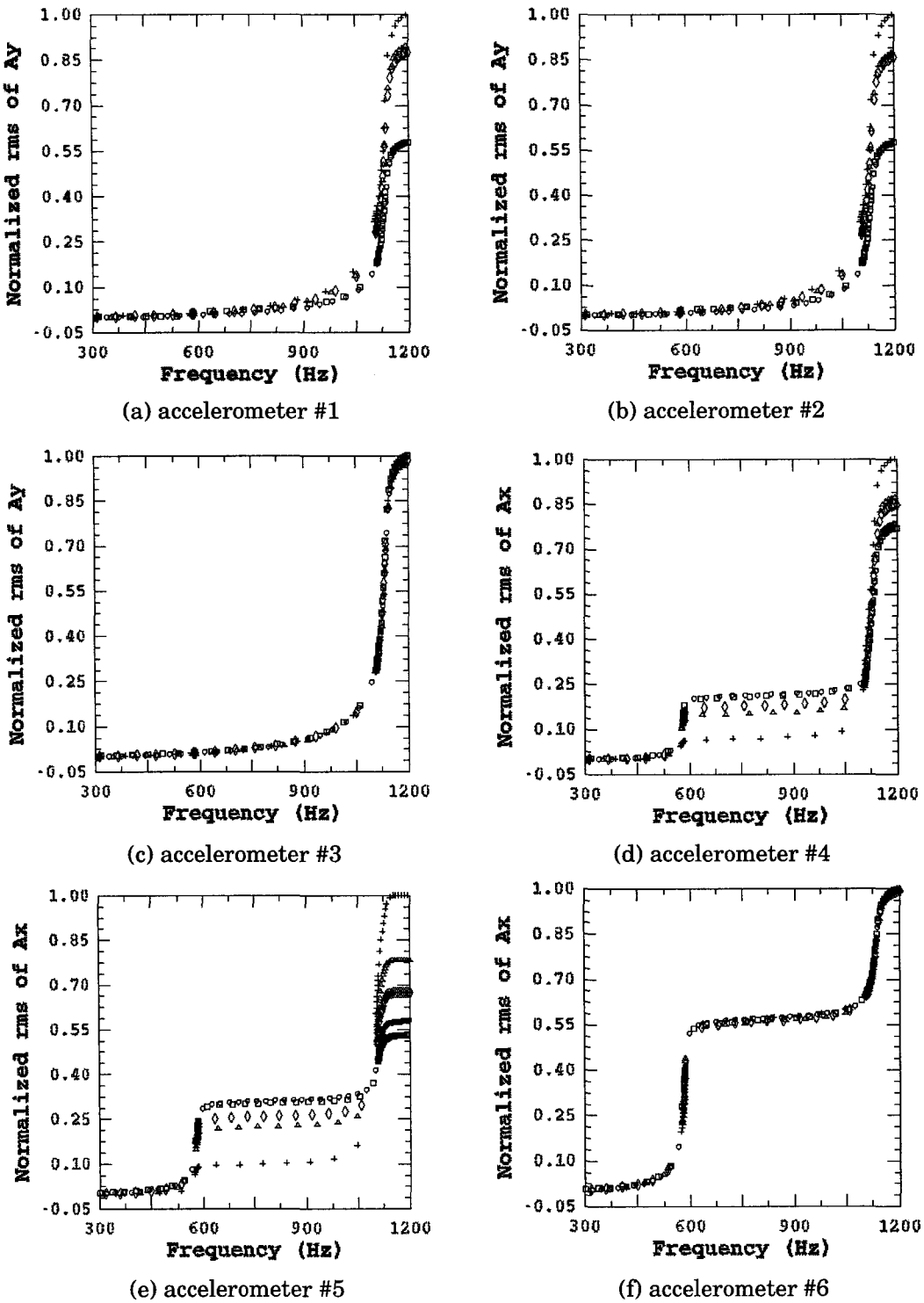

(a) accelerometer #1

(b) accelerometer #2

(c) accelerometer #3

(d) accelerometer #4

(e) accelerometer #5

(f) accelerometer #6

Figure 5.16: Normalized rms of acceleration as a function of frequency for damage cases #5 to #8: O: intact, □: case #5, ◇: case #6, △: case #7, +: case #8

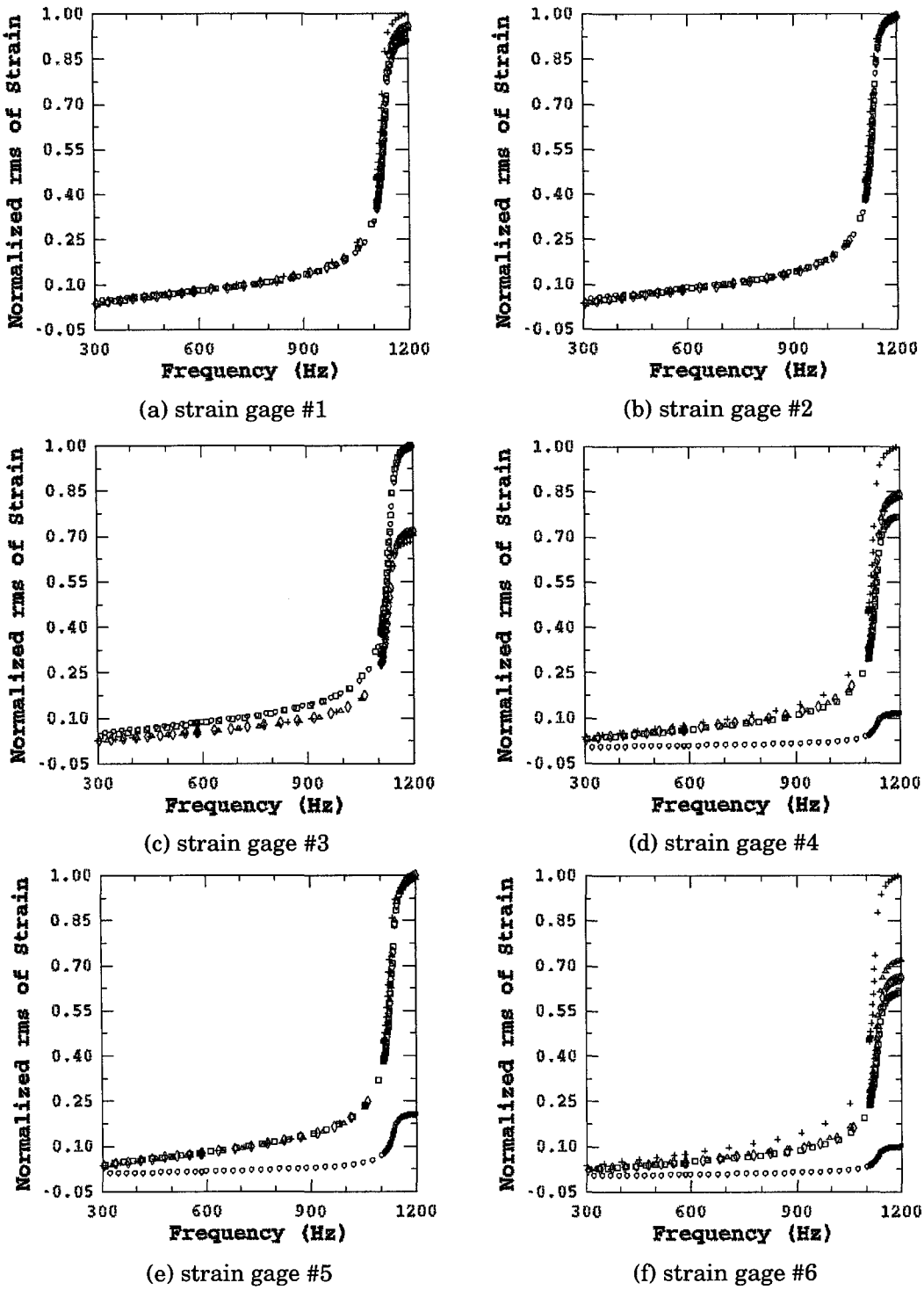

(a) strain gage #1

(b) strain gage #2

(c) strain gage #3

(d) strain gage #4

(e) strain gage #5

(f) strain gage #6

Figure 5.17: Normalized rms of strain as a function of frequency for damage cases #1 to #4: O: intact, □: case #1, ◇: case #2, △: case #3, +: case #4

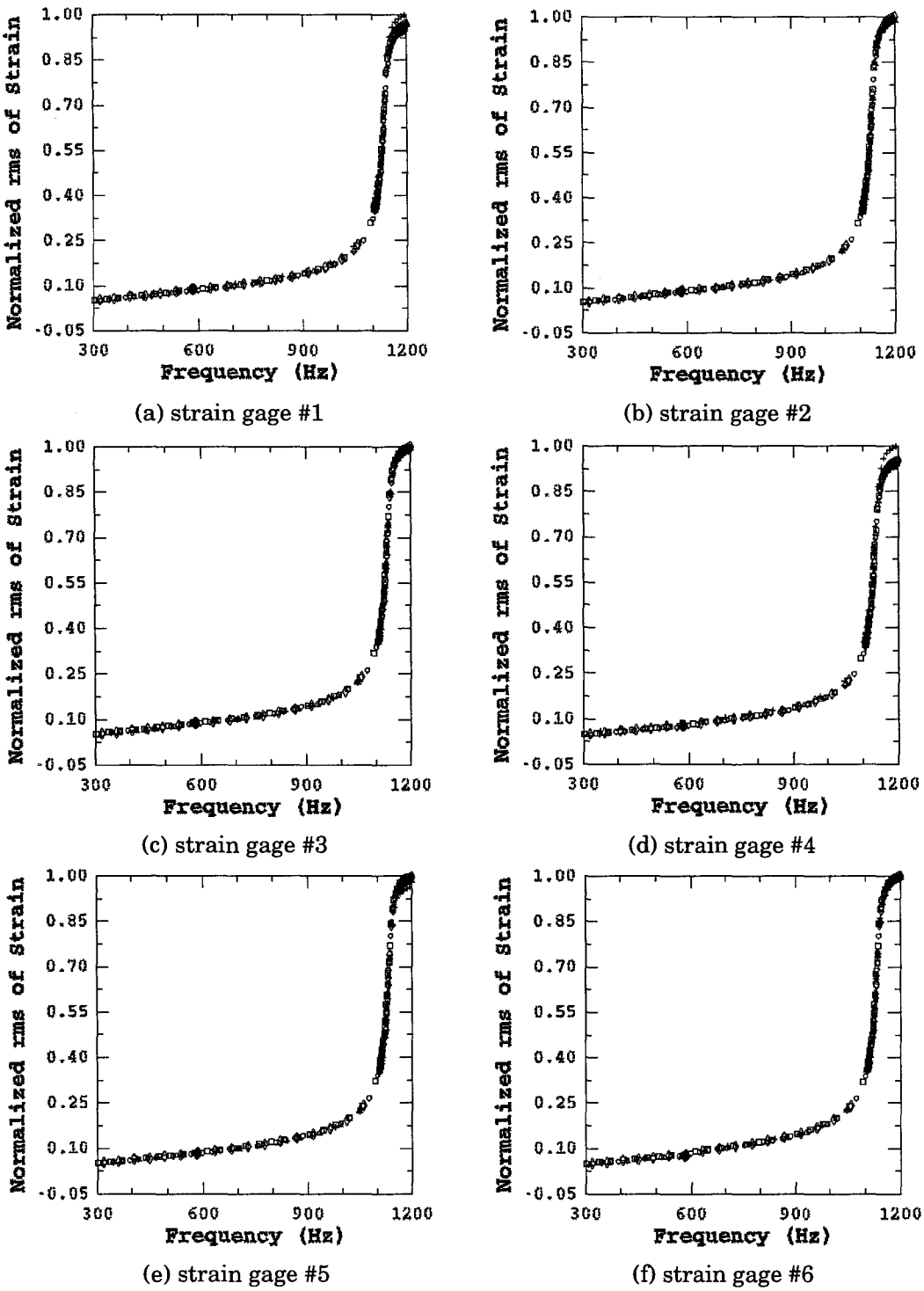

(a) strain gage #1

(b) strain gage #2

(c) strain gage #3

(d) strain gage #4

(e) strain gage #5

(f) strain gage #6

Figure 5.18: Normalized rms of strain as a function of frequency for damage cases #5 to #8: O: intact, □: case #5, ◇: case #6, △: case #7, +: case #8

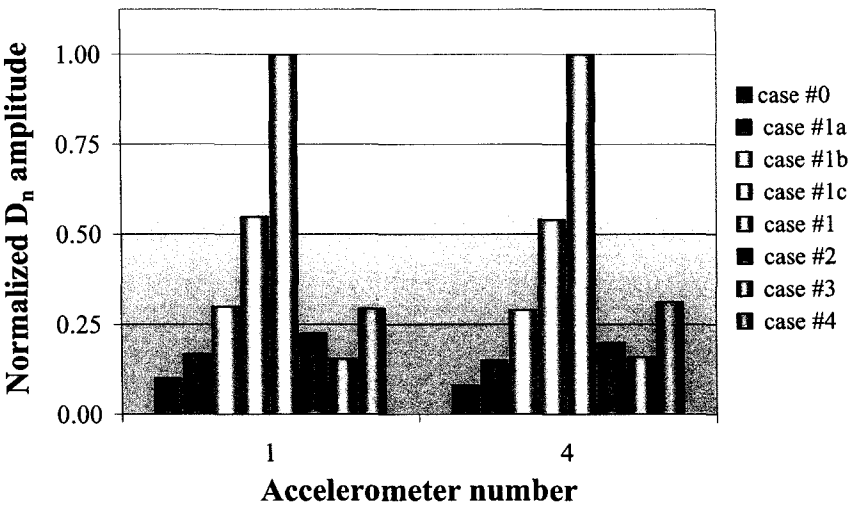

(a) Damage cases #1 to #4

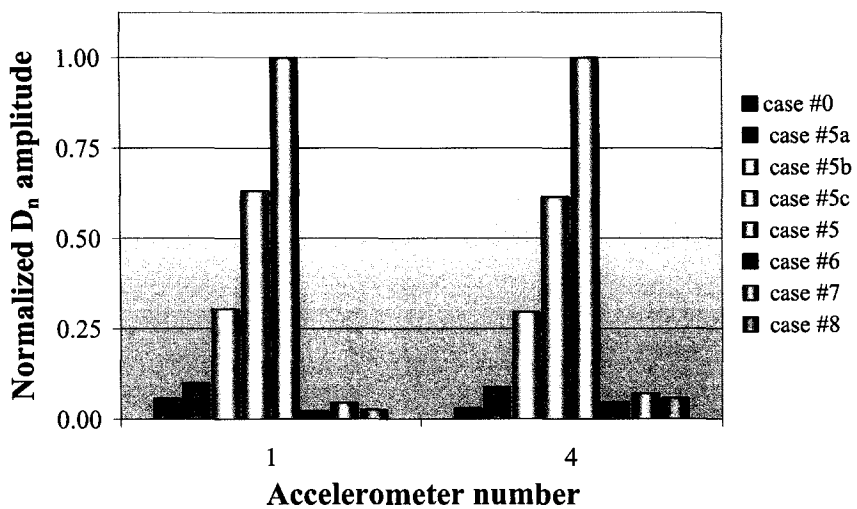

(b) Damage cases #5 to #8

Figure 5.19: D_n amplitudes obtained from response of the first mode of accelerometers #1 and #4 for fourteen damage cases

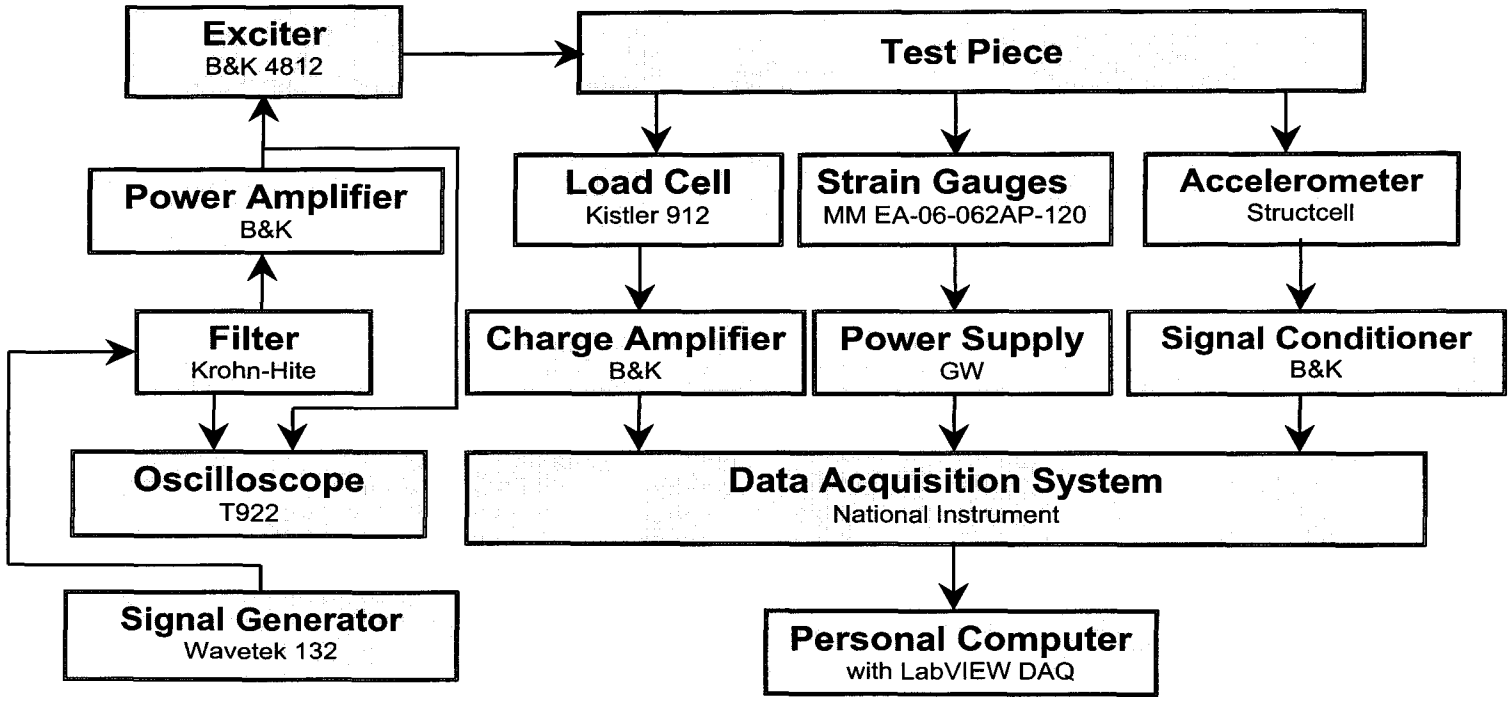

Figure 5.20: Diagram of experimental set up

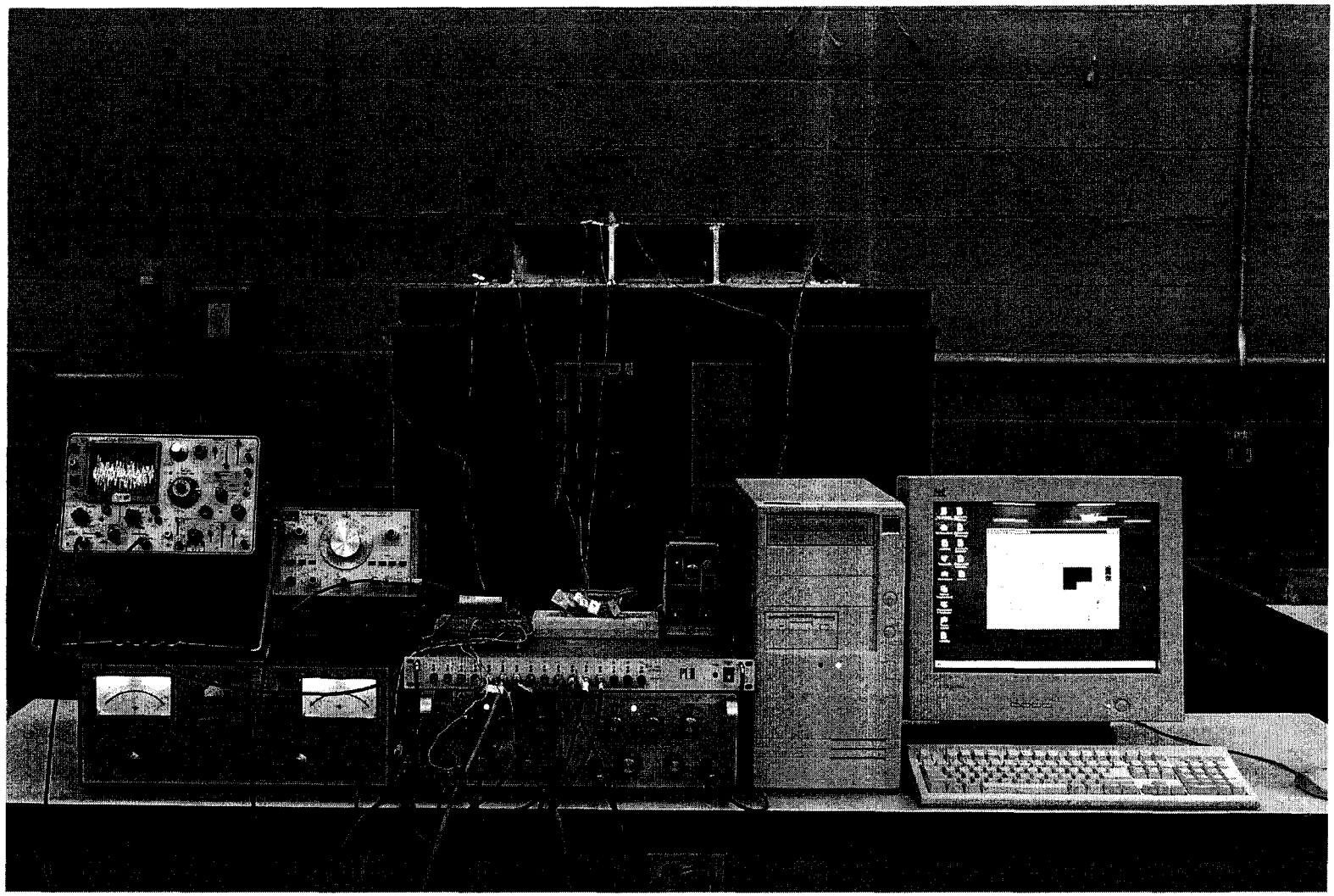

Figure 5.21: Experimental set up

measured using MM EA-06-062AP-120 strain gages and Structcel accelerometers (Model No. 330A). The accelerometers used in the model were low weight acceleration measuring devices (about 2 grams each). The strain gages had resistance of 120 Ohms $\pm$ 15%, gage factor of 2.065 $\pm$ 0.5% and transverse sensitivity of (0.9 $\pm$ 0.2)%. The transducer signals (load cell, strain gages and accelerometers) were passed through amplifiers prior to acquiring data using LabVIEW (1998) data acquisition system which recorded data at a sampling frequency of 12 kHz (12000 samples per second per channel) for about 8 to 10 seconds for one measurement. Ten measurements were carried out for each case and model. The recorded data were stored in a personal computer for further analysis.

Measured time response was preprocessed using a procedure that will be described later in this chapter. The response was then digitally band pass filtered. The center frequency of the filter was taken as the natural frequency of the model. From the filtered response, the random decrement function was calculated and utilized to extract the natural frequency and the damping ratio, using Ibrahim time domain procedures.

In this study, the changes in the modal parameters in the first two torsional-flexural modes and the first bending mode (mode 5) were investigated. It was decided to ignore the third and forth modes since no new information could be gained from these two modes. The rms of response in the frequency range of the first two modes were also computed.

5.4.2 Sensor Calibration and Location

Prior to performing the experiment, the accelerometers, strain gages and load cell were calibrated. All accelerometers were calibrated using PCB 394B05 hand-held calibrator, which produced output at the level of 1g. Response signals from the accelerometer due to the calibrator excitation were recorded by LabVIEW data acquisition system and the average acceleration amplitude of signals was then computed. Figure 5.22 shows the response of accelerometer #1 excited by PCB 394B05 calibrator for the first 0.1 second. During this study investigation, accelerometer calibrations were performed three times, i.e., once before each of the orthogonally stiffened models was tested. Calibration factors for six accelerometers used in the experiments are presented in Appendix D. Six accelerometers were mounted on the model. Three accelerometers were located on the horizontal flange and others were located on web frame flanges. These accelerometers were attached on the model using bees wax and their positions and connections to the model were checked before each measurement was taken.

Strain gage calibration were carried out using calibration box which excites the strain gage at 1000 μ strain. The strain gage response before and after being excited by the calibration box were recorded through LabVIEW data acquisition system. The average amplitude of the strain response were obtained. The strain gages were calibrated two times for each model, i.e, prior to carrying out test and before performing tests for damage cases #5 to #8. Calibration factors of six strain gages mounted in the model for this experimental investigation are presented in Appendix D. These strain gages were mounted on the side shell plate in the x-

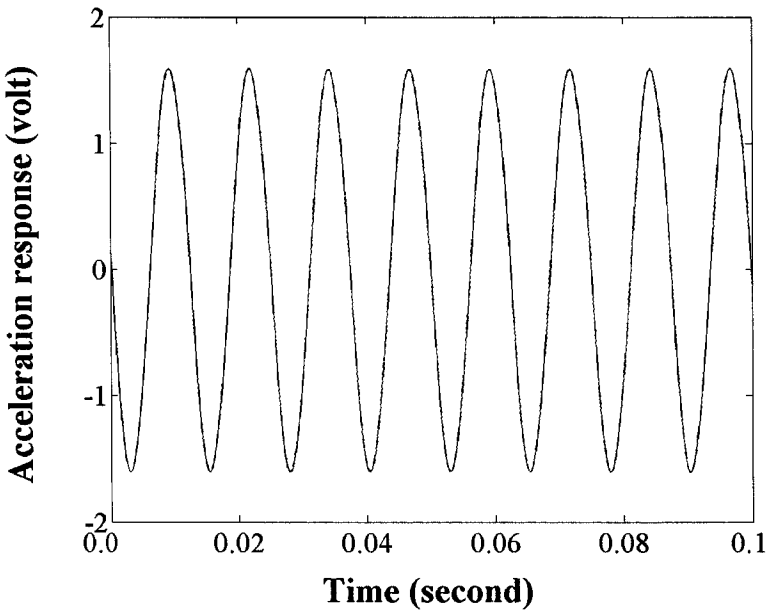

Figure 5.22: Response of accelerometer #1 excited by PCB 394B05 calibrator direction.

In calibrating the load cell PCB 394B05 hand-held calibrator was again employed. Several known weights were applied to the load cell and the voltages were measured. Due to the lack of apparatus for this calibration purpose only four weights were applied to the load cell viz., 1 gram, 2 grams, 5 grams and 10 grams and it was assumed that the load cell output varied linearly over the range mentioned in the specification. In this investigation the excitation force signal was recorded to examine whether force changed from one measurement to other measurements during the experiment. However the excitation force signal was not employed for obtaining modal parameters since output-only modal analysis was conducted in this experimental investigation. Relationship between the force and output voltage measured from the load cell is shown in Figure D.1 in Appendix D.

5.4.3 Study Parameters

The effect of sampling frequency on the identified modal frequency and the effects of excitations from one measurement to the other on force amplitudes were investigated. These investigations were important to determine sampling frequency used in the experiments to obtain the correct modal frequencies without significant error when they were compared to the numerical values. Investigation on random force amplitudes exerted on the model from one measurement to other measurements was also necessary since rms amplitude response obtained from the experiments were employed for damage identification scheme presented in Chapter 6.

Sampling Frequency

The response experimental data were sampled at high frequencies. The reason was that the fifth mode natural frequency extracted from a response with sampling frequency (sampling rate) lower than 10000 Hz differed significantly from the computed one. The effect of sampling frequency on identified frequencies for the first two modes and the first bending mode (mode 5) of the model for the intact condition was investigated and the results are shown in Figure 5.23. By sampling the model response at the rate of 5000 samples per second, the first two modes of the model matched the numerical ones without significant errors. However the calculated natural frequency for mode 5 did not match the numerical value. Only when the sampling frequency was higher than 10000 samples per second, mode 5 was properly identified. In this experimental investigation, it was decided to use a sampling frequency of 12000 samples per second.

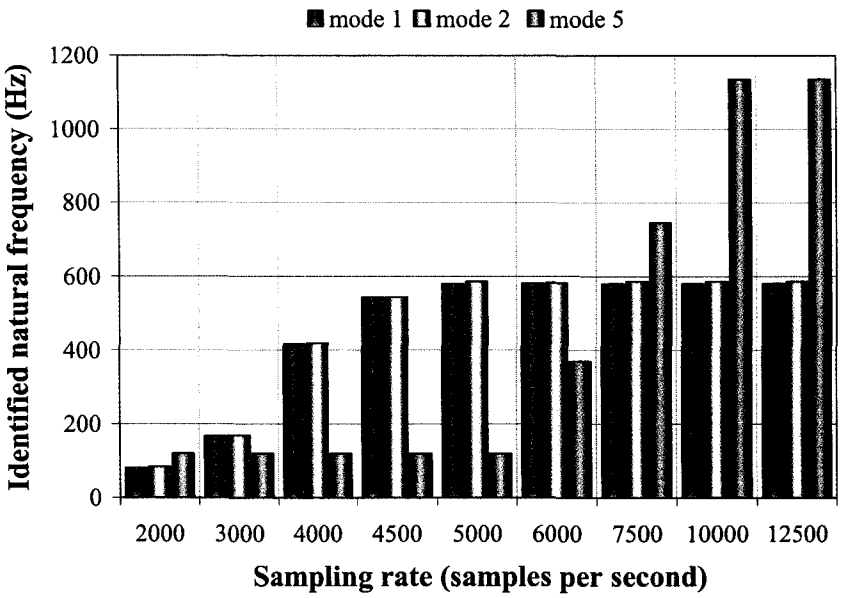

Figure 5.23: Identified natural frequency and sampling rate

The Excitation Amplitude for Different Measurements

In the experimental investigation carried out in this study output-only modal analysis was implemented. It means that the excitation force was not used for obtaining structural modal parameters. To investigate whether excitation force amplitudes changed in different measurements, the force applied to model #1 under intact condition for ten measurements were recorded and the autospectra of the excitation forces were computed. Figure 5.24 shows autospectral density of the excitation forces. As seen in the figure the amplitudes of the force were not constant from one measurement to other measurements. Therefore a response signal preprocessing procedure was performed. The preprocessing procedure is discussed later in subsection 5.4.4.

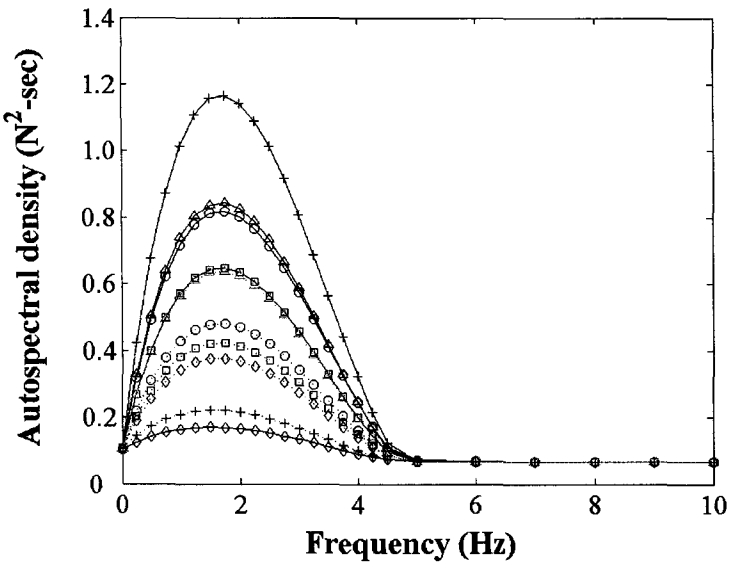

Figure 5.24: Autospectral density of excitation forces obtained from ten different measurements under intact condition

5.4.4 Procedures

To utilize three orthogonally stiffened models available for testing, the model was first tested for damage cases #1 to #4 and then the model was carefully welded at locations where cracks were located (locations 1 and 2). The model was not taken from the test rig when welding was carried out to minimize discrepancies in experimental results due to experimental set up. The model condition after being welded was considered to be undamaged and it was used as benchmark for the damage cases #5 to #8. All accelerometers along with cables were removed from the model during welding. Since strain gages were attached to the model when it was welded, calibrations for all strain gages were conducted once again after the model was welded to check whether the strain gages were affected by the welding procedures. In this experimental investigation damage was simulated by a cut

made using a hacksaw. Damage cases #1 to #4 (where cracks occurred at locations 1 and 2) were carried out before damage cases #5 to #8 since it would be easier to weld at these locations than at locations 3 and 4, where the space availability was less.

The random excitation forces were different from one measurement to the other, see Figure 5.24. Therefore a preprocessing of the response signals was carried out prior to computing modal parameters and the rms of response at frequency range of interest. Figure 5.25 shows a diagram of response signal preprocessing procedure implemented in this experimental investigation. In the signal preprocessing procedure, after the response were calibrated, the trend and the mean were removed from the response and then they were normalized by the chosen rms value of amplitude response within the frequency excitation band. The response mean was zeroed because it was observed that the mean was different from one measurement to the other. In addition, random decrement and Ibrahim time domain methods required the mean to be zero. In this investigation, the mean of rms values obtained within the dominant frequency excitation for response measured by a sensor (accelerometers or strain gages) was computed. The rms chosen for normalizing the model's responses was the one which had closest value to the mean of the rms computed from six different sensor locations. Since two types of sensors were used to measure the model's responses, viz., accelerometer and strain gage, the rms value utilized was selected from the same type of sensor.

As mentioned previously in this chapter, the modal parameters (natural frequencies and damping ratios) for the first two modes, which were torsion-bending

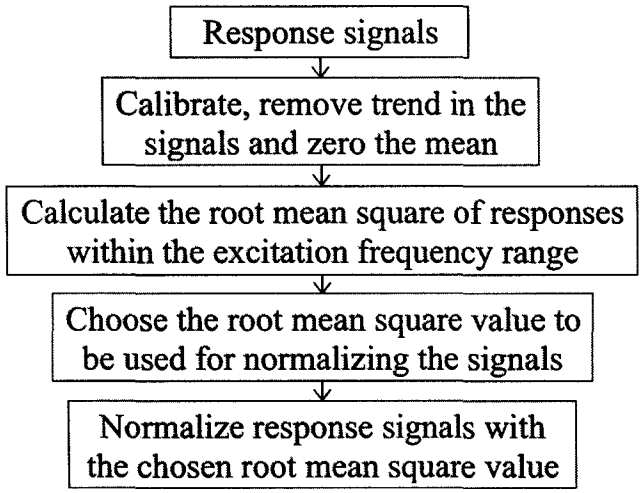

Figure 5.25: Preprocessing procedure implemented for experimental response data

modes of the web frames, and the first bending mode (mode 5) were extracted from measured response using the random decrement and Ibrahim time domain techniques. The modal parameter estimations of modes 1 and 2 were undertaken twice for each measurements. First, these modes were estimated at the same time and then to refine the estimation, these two modes were extracted individually by zooming at smaller frequency bands. The modal parameters were computed for ten measurements recorded in the experiments for each damage case. A total of one hundred and twenty modal parameters were obtained for each damage case for one model; sixty data were extracted from six strain gage response and the rest were obtained from the response of six accelerometers.

5.4.5 Experimental Results

Using responses measured from the experiment, modal parameters (the natural frequency and damping ratio) were extracted and rms response and the amplitude D_n function were obtained. These experimental results are presented in this subsection and are compared with the numerical investigation results in section 5.5.

Measured Natural Frequency and Damping Ratio

Tables 5.4 to 5.6 show the mean and standard deviation of natural frequencies and damping ratios obtained from model #1 to model #3 for modes #1, #2 and #5 for the eight damage cases. Modal frequencies of mode 1 for damage cases #1 to #4 did not change significantly due to the presence of crack for all models tested in the experiment. However for damage cases #5 to #8 the modal frequency changed significantly. For mode 2, no significant change in the natural frequencies were obtained for damage cases #1 to #4 while for damage cases #5 to #8 the natural frequencies decreased slightly. This was due to the fact that the damage cases #1 to #4 were located at the ends of the longitudinal (horizontal stiffener) which did not influence the local bending of modes 1 and 2. The damage cases #5 and #8 were located at the junctions of transverse web frame #1 and the longitudinals #2 and #3; these damage locations influenced the local bending of modes 1 and 2.

The modal frequencies in mode 5 decreased appreciably for damage cases #1 to #4 while for damage case #5 to #8 these changes were not significant. This effect was due to the fact that the damage cases #1 and #4 were located at the end of longitudinal #2 which affected the global bending of the whole ship panel model.

The standard deviation of modal frequency data were less than 0.1 Hz for the first and second modal frequencies and 0.4 Hz for the fifth frequency. It means the modal frequency estimation did not vary significantly from one measurement to other for the same damage case. Due to fabrication, the web frames of model #1 seemed to be less stiff than those of model #2 and #3. Therefore the first two modal frequencies of model #1, which were torsion-bending modes of the web frames, were about 1% less than than modal frequencies of models #2 and #3.

The damping ratios calculated from response acquired using accelerometers and strain gages, did not differ significantly. Modal damping ratios estimated from three investigated models increased and decreased due to the increase of crack lengths. The damping ratios ranged from 0.28% to 0.65% for mode 1. It ranged from 0.2% to 0.55% for mode 2 and the ratios was nearly 0.01% to 0.12% for mode 5. These damping ratios cannot be used as a damage indicator since their values under different damage cases did not show any definable trend.

It appears that modal parameters, especially damping ratios, were not sensitive to crack for all damage cases considered in the investigation. Therefore the rms of response and D_n amplitudes were also computed from the measured response to examine their sensitivities to cracks occurring at various locations and lengths.

The rms of Response

The rms of response under intact and damaged conditions were obtained by the use of response autospectrum. For this purpose, the model's time response was converted into frequency domain to calculate the response autospectrum and then

the rms was obtained by integrating the autospectrum of response in the frequency band of 400 Hz to 600 Hz. The frequency band or range was selected since in that band the analytical rms values showed appreciable changes. It could be seen from Figures 5.15 to 5.17 that the change in normalized rms response for accelerometers #4, #5 and #6 and strain gages #4, #5 and #6 below 400 Hz were small compared to that between 400 Hz and 600 Hz. This large change was due to the fact that there were two dominant frequencies in this frequency band. In addition, by integrating the spectrum over the frequency band the effect of noise, which would be present in the measured response data, could be minimized. Although the frequency range selected was different from the range used in the numerical investigations, it would not matter since only relative values of the rms were used (those rms values were normalized by the largest value).

In this investigation, prior to calculating the rms the response preprocessing procedure shown in Figure 5.25 was also performed. The rms of accelerometer response for all damage cases investigated were computed in this study whereas the rms of response of strain gages for damage cases #5 to #8 were not computed due to insignificant changes observed in the numerical results as shown in Figure 5.18. Moreover the rms within the frequency range of first overall bending mode frequency (1120 Hz to 1200 Hz) was not computed because of low response signal to noise ratio. In this case it was difficult to minimize the effect of noise amplitude from the structural response amplitude. The noisy response signals in this frequency range might be due to the fact that there were three frequencies (two local bending modes - 3 and 4 - and one global bending mode 5 within a frequency

Table 5.4: Measured natural frequencies and damping ratios obtained from response of model #1

Case #	Sensor	Natural frequency (Hz)						Damping ratio (%)					
		Mode 1		Mode 2		Mode 5		Mode 1		Mode 2		Mode 5	
		mean	sd	mean	sd	mean	sd	mean	sd	mean	sd	mean	sd
0	str	580.734	0.085	586.449	0.043	1136.707	0.376	0.642	0.009	0.478	0.005	0.012	0.002
	acc	580.726	0.072	586.453	0.039	1135.902	0.367	0.644	0.009	0.477	0.005	0.011	0.002
1	str	580.725	0.088	586.458	0.042	1135.860	0.330	0.645	0.009	0.476	0.004	0.010	0.002
	acc	580.734	0.087	586.449	0.039	1135.676	0.410	0.645	0.008	0.477	0.005	0.010	0.001
2	str	580.733	0.079	586.456	0.034	1133.945	0.293	0.644	0.009	0.478	0.004	0.011	0.002
	acc	580.693	0.073	586.454	0.045	1133.611	0.299	0.643	0.009	0.476	0.005	0.010	0.002
3	str	580.736	0.095	586.447	0.042	1133.475	0.356	0.644	0.008	0.477	0.005	0.011	0.001
	acc	580.725	0.092	586.467	0.047	1133.415	0.313	0.646	0.009	0.477	0.005	0.010	0.001
4	str	580.728	0.079	586.456	0.044	1127.193	0.183	0.644	0.010	0.476	0.004	0.010	0.002
	acc	580.719	0.086	586.462	0.048	1127.262	0.267	0.644	0.010	0.477	0.005	0.010	0.002
0*	str	580.616	0.166	586.888	0.268	1136.817	0.559	0.433	0.015	0.370	0.012	0.013	0.003
	acc	580.613	0.173	586.888	0.266	1136.030	0.348	0.432	0.015	0.368	0.012	0.010	0.003
5	str	578.790	0.088	585.607	0.050	1136.778	0.463	0.278	0.005	0.193	0.005	0.014	0.002
	acc	578.776	0.097	585.362	0.045	1136.038	0.365	0.276	0.006	0.191	0.006	0.014	0.001
6	str	576.691	0.049	584.662	0.042	1136.435	0.496	0.646	0.006	0.193	0.005	0.014	0.003
	acc	576.695	0.039	584.659	0.043	1136.045	0.301	0.647	0.005	0.192	0.009	0.014	0.001
7	str	573.807	0.042	584.407	0.042	1136.240	0.351	0.609	0.005	0.196	0.010	0.012	0.001
	acc	573.811	0.042	584.414	0.046	1135.718	0.282	0.609	0.007	0.194	0.009	0.011	0.001
8	str	568.714	0.062	584.365	0.046	1135.890	0.309	0.440	0.014	0.195	0.011	0.012	0.001
	acc	568.714	0.060	584.351	0.049	1135.742	0.409	0.439	0.016	0.193	0.010	0.011	0.001

acc : accelerometers; str : strain gages; sd: standard deviation; 0*: the condition after cracks at locations 1 and 2 were welded

Table 5.5: Measured natural frequencies and damping ratios obtained from response of model # 2

Case #	Sensor	Natural frequency (Hz)						Damping ratio (%)					
		Mode 1		Mode 2		Mode 5		Mode 1		Mode 2		Mode 5	
		mean	sd	mean	sd	mean	sd	mean	sd	mean	sd	mean	sd
0	str	586.164	0.039	591.533	0.037	1136.576	0.154	0.548	0.006	0.326	0.008	0.011	0.002
	acc	586.169	0.031	591.527	0.036	1136.681	0.340	0.546	0.006	0.327	0.006	0.013	0.002
1	str	586.150	0.030	591.521	0.040	1135.026	0.138	0.546	0.005	0.328	0.006	0.010	0.002
	acc	586.153	0.038	591.522	0.040	1135.064	0.174	0.546	0.006	0.329	0.007	0.010	0.002
2	str	586.151	0.030	591.524	0.038	1134.988	0.313	0.547	0.006	0.329	0.007	0.016	0.001
	acc	586.146	0.032	591.521	0.041	1134.644	0.337	0.546	0.006	0.327	0.007	0.016	0.001
3	str	586.154	0.036	591.521	0.040	1133.445	0.308	0.546	0.006	0.326	0.007	0.009	0.009
	acc	586.146	0.034	591.522	0.038	1133.252	0.353	0.546	0.005	0.328	0.006	0.009	0.010
4	str	586.154	0.039	591.473	0.022	1127.634	0.011	0.547	0.006	0.334	0.007	0.015	0.001
	acc	586.145	0.030	591.470	0.025	1127.636	0.011	0.546	0.006	0.336	0.008	0.015	0.001
0*	stg	586.159	0.038	591.522	0.038	1136.584	0.190	0.546	0.006	0.427	0.006	0.011	0.001
	acm	586.161	0.037	591.525	0.029	1136.315	0.355	0.547	0.007	0.425	0.007	0.012	0.001
5	stg	583.963	0.037	590.719	0.049	1135.870	0.264	0.370	0.006	0.341	0.001	0.011	0.001
	acm	583.966	0.044	590.792	0.129	1135.859	0.240	0.369	0.005	0.368	0.002	0.011	0.001
6	stg	581.343	0.029	589.381	0.060	1135.705	0.274	0.374	0.006	0.301	0.002	0.008	0.001
	acm	581.334	0.033	589.544	0.160	1135.729	0.304	0.373	0.007	0.342	0.002	0.009	0.001
7	stg	577.779	0.013	589.098	0.014	1135.697	0.255	0.273	0.003	0.273	0.002	0.008	0.002
	acm	577.780	0.016	589.100	0.017	1135.658	0.382	0.275	0.003	0.266	0.002	0.009	0.002
8	stg	574.332	0.021	589.096	0.022	1135.070	0.330	0.181	0.005	0.258	0.007	0.011	0.002
	acm	574.340	0.020	589.101	0.015	1135.008	0.481	0.180	0.005	0.268	0.002	0.011	0.002

acc : accelerometers; str : strain gages; sd: standard deviation; 0*: the condition after cracks at locations 1 and 2 were welded

Table 5.6: Measured natural frequencies and damping ratios obtained from response of model #3

Case #	Sensor	Natural frequency (Hz)						Damping ratio (%)					
		Mode 1		Mode 2		Mode 5		Mode 1		Mode 2		Mode 5	
		mean	sd	mean	sd	mean	sd	mean	sd	mean	sd	mean	sd
0	str	585.622	0.051	591.540	0.040	1136.597	0.419	0.461	0.011	0.507	0.010	0.021	0.002
	acc	585.629	0.051	591.542	0.047	1136.313	0.412	0.460	0.012	0.506	0.009	0.020	0.005
1	str	585.591	0.062	591.537	0.039	1135.258	0.141	0.462	0.011	0.506	0.009	0.005	0.001
	acc	585.604	0.050	591.531	0.043	1135.227	0.224	0.460	0.008	0.507	0.008	0.006	0.002
2	str	585.583	0.069	591.532	0.042	1134.272	0.191	0.460	0.011	0.506	0.007	0.015	0.002
	acc	585.600	0.048	591.522	0.045	1134.318	0.472	0.461	0.011	0.507	0.010	0.016	0.002
3	str	585.589	0.043	591.277	0.094	1133.360	0.258	0.464	0.009	0.416	0.019	0.011	0.001
	acc	585.595	0.056	591.290	0.085	1133.329	0.266	0.463	0.011	0.417	0.020	0.012	0.001
4	str	585.580	0.051	591.235	0.042	1125.798	0.017	0.462	0.012	0.546	0.008	0.123	0.001
	acc	585.586	0.056	591.241	0.046	1125.793	0.046	0.462	0.010	0.542	0.009	0.123	0.001
0*	str	585.634	0.054	591.538	0.044	1136.689	0.282	0.462	0.010	0.507	0.008	0.021	0.002
	acc	585.633	0.052	591.551	0.048	1136.483	0.345	0.462	0.011	0.507	0.009	0.022	0.002
5	str	583.969	0.049	590.162	0.057	1135.651	0.314	0.420	0.006	0.299	0.009	0.016	0.002
	acc	583.957	0.053	590.170	0.056	1135.698	0.366	0.420	0.006	0.302	0.010	0.016	0.002
6	str	581.172	0.044	589.433	0.038	1134.879	0.403	0.412	0.005	0.337	0.009	0.014	0.002
	acc	581.170	0.039	589.429	0.035	1134.867	0.547	0.412	0.005	0.337	0.008	0.014	0.002
7	str	577.926	0.038	589.174	0.040	1134.808	0.332	0.515	0.008	0.548	0.007	0.014	0.002
	acc	577.928	0.037	589.180	0.036	1134.890	0.501	0.514	0.008	0.549	0.007	0.014	0.002
8	str	574.940	0.040	589.175	0.036	1134.894	0.288	0.308	0.010	0.545	0.007	0.015	0.002
	acc	574.928	0.035	589.162	0.042	1134.787	0.404	0.308	0.009	0.547	0.007	0.015	0.002

acc : accelerometers; str : strain gages; sd: standard deviation; 0*: the condition after cracks at locations 1 and 2 were welded

range of 30 Hz (1109.2 Hz to 1136.7 Hz) and that the whole supporting structure also had a natural frequency in the range of 1050 Hz. The normalized experimental rms values were plotted along with the numerical rms values and presented in Appendix E.

Figures 5.26 and 5.27 shows the normalized rms of acceleration and strain response obtained from model #2. The rms computed from models #1 and #3 were similar to that of model #2. Therefore only the rms of response of model #2 was presented in this chapter. The rms values for models #1 to #3 are presented in Appendix E along with the rms values obtained from numerical investigation. As seen from Figures 5.26 and 5.27, for cases where cracks occurred at one location only (damage cases #1 and #5), the rms showed significant changes in accelerometers #1 and #2 while for cases where cracks occurred at two locations (cases #2 to #4 and #6 to #8) the rms did not change significantly. The rms values obtained for accelerometer #3 consistently increased for damage cases #1 to #2. However they did not show a significant change for other damage cases. The rms computed from the response of accelerometers #4 and #5 decreased for all damage cases. The rms response of accelerometer #6 did not change significantly for all damage cases. For damage cases #1 to #4, the rms of amplitude response of strain gages #3 and #5 did not show significant changes while appreciable changes were observed in the rms of strain gages #4 and #6. The rms obtained from experimental and numerical investigation will be compared later in this chapter.

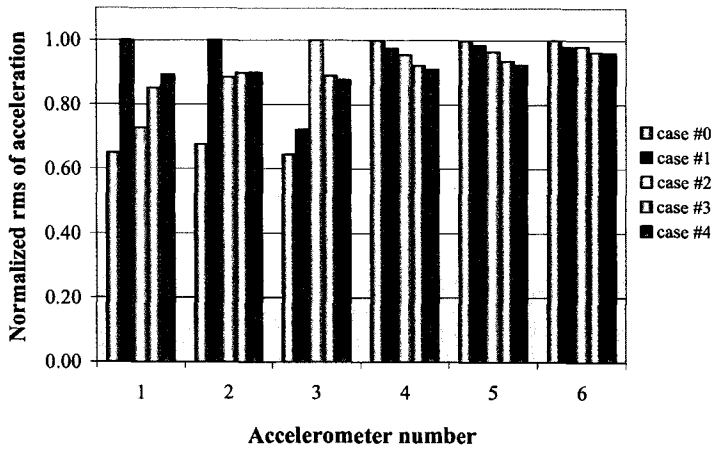

(a) acceleration response

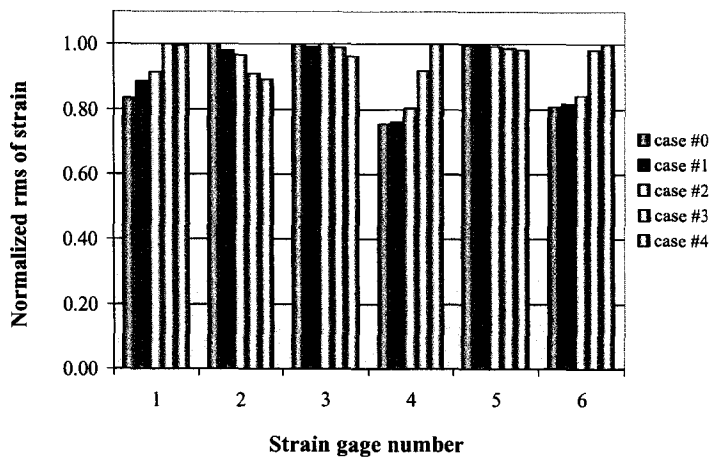

(b) strain response

Figure 5.26: Normalized rms acceleration and strain gage response obtained from model #2 for damage cases #1 to #4

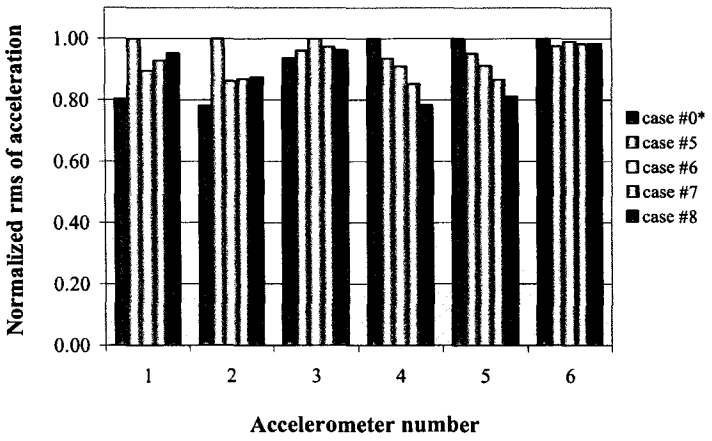

Figure 5.27: Normalized rms of acceleration response obtained from model #2 for damage cases #5 to #8

Experimental D_n Amplitude

The D_n function was obtained from simulations using neural network technique with random decrement function and its derivative as input. The random decrement function was employed in this investigation since it is analogous to the free decay response function and the response measured in the experimental tests were random.

The random decrement function was computed from the response autocorrelation using Equation 3.13. Using lower triggering level, a, of 0.5 σ and the upper triggering level, b, of ∞ for all damage cases investigated, the value of ρ_0 in Equation 3.14 for Gaussian distributed response was 1.14 σ. σ is the standard deviation or the rms for response having zero mean.

Since acceleration response was obtained in the experiment the autocorrelation of measured response was numerically integrated using MATLAB before it was in-

put to the neural networks. For one damage case the simulation normally required 10000 iterations to reach minimum error, viz. the difference between input and simulated response. The simulation result was then scaled by the rms computed from the average of the rms obtained from ten measurements carried out in the experimental investigation.

D_n functions of response from accelerometers #1 and #4 in mode 1 were simulated using the networks. In addition only cases where cracks occurred at a single location were examined to investigate the similarity in trend between numerical and experimental results for increasing crack lengths. Figure 5.28 shows the D_n time histories of accelerometers #1 and #4 for cracks occurring at location 1 (damage cases #1a to #1) using response of model #2. Normalized D_n amplitude for these damage cases is shown in Figure 5.29 (a). From this figure it is clear that D_n amplitudes show an increasing trend as a result of increasing crack lengths, although there was no change in natural frequencies and no definable trend in damping ratios for these damage cases.

Figure 5.29 (b) shows the normalized amplitudes for cracks occurring at location 3 (damage cases #5a to #5). In these damage cases modal frequencies decreased and the damping ratio either decreased or increased. However the D_n amplitudes obtained from the simulations increased consistently as the crack length increased. This might be an advantage in using the random decrement functions as inputs of the networks. Similar trends were also observed from the output of the simulation using inputs obtained from response of model #3. Figure 5.30 shows the normalized D_n amplitudes simulated using input from response measured from model #3. In

the next section these experimental investigation results will be compared with the results obtained from numerical investigation.

5.5 Comparison of Results

The natural frequencies, the rms of amplitude response and D_n amplitudes obtained from the numerical and experimental investigations for different damage cases are compared in this section to examine the trend of values for these damage cases. These results are further discussed in Chapter 6 for damage identification of the model.

5.5.1 Numerical and Experimental Natural Frequencies

Since the natural frequencies obtained from accelerometer and strain gage response did not differ significantly, natural frequencies measured from twelve transducers (six accelerometers and six strain gages) for each damage case were averaged and the results were compared with natural frequencies computed numerically using the finite element package program ABAQUS. In general the experimental and computed natural frequencies agreed well; the difference ranged from -0.83% to +0.89%. Moreover the measured natural frequencies had the same trend as the numerical ones. These results provided the required reliability to the computed and measured values that the same data were used subsequently in the damage identification, discussed in the next chapter.

The difference between numerical and experimental natural frequencies com-

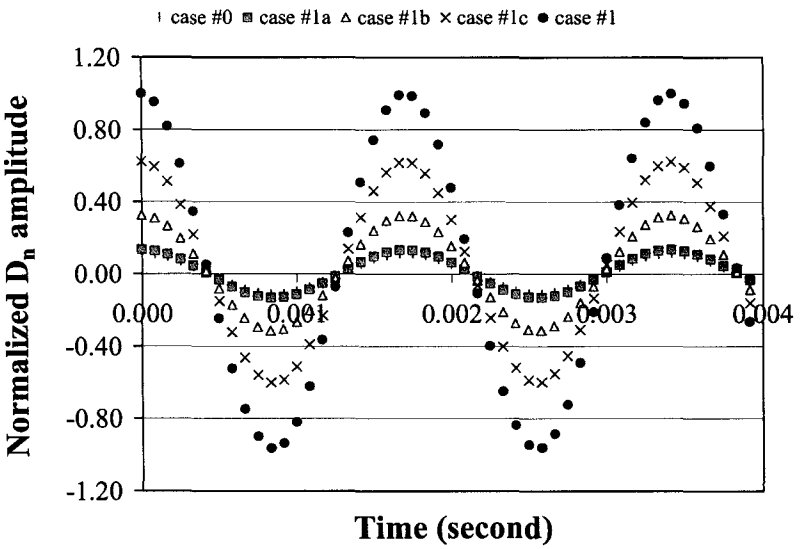

(a) accelerometer #1

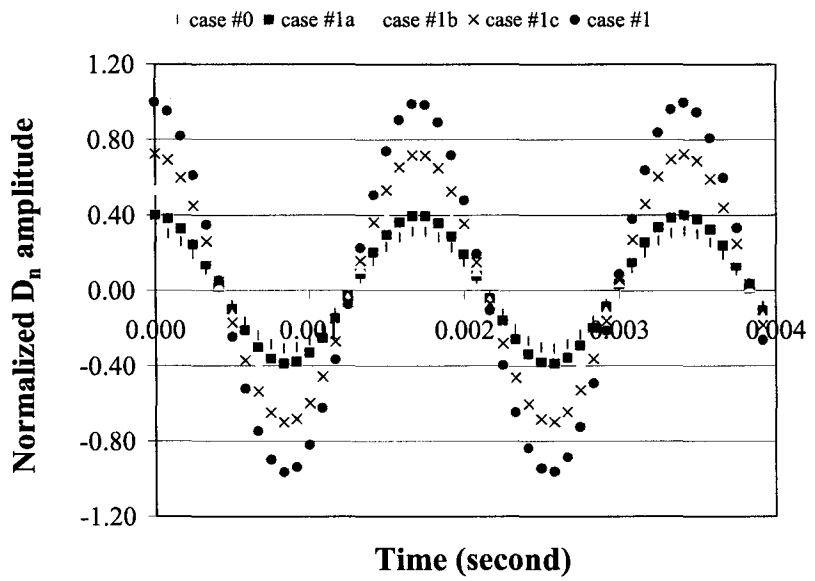

(b) accelerometer #4

Figure 5.28: D_n time history obtained from response of model #2 for cracks occurring at location 1

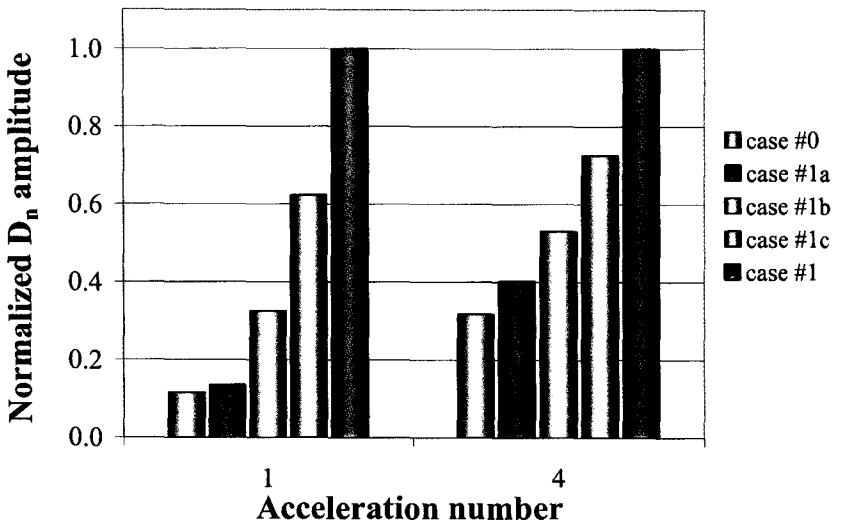

(a) cracks occurred at location 1

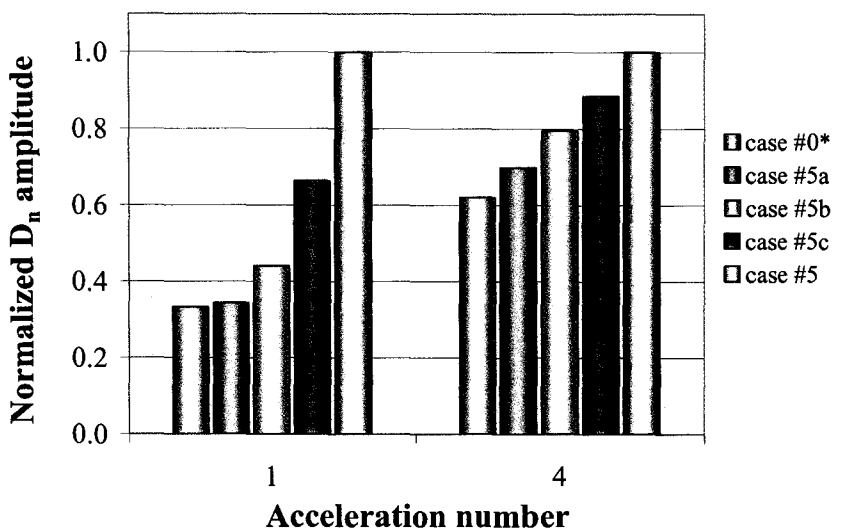

(b) cracks occurred at location 3

Figure 5.29: Normalized D_n amplitude of model #2 for cracks occurred at locations 1 and 3

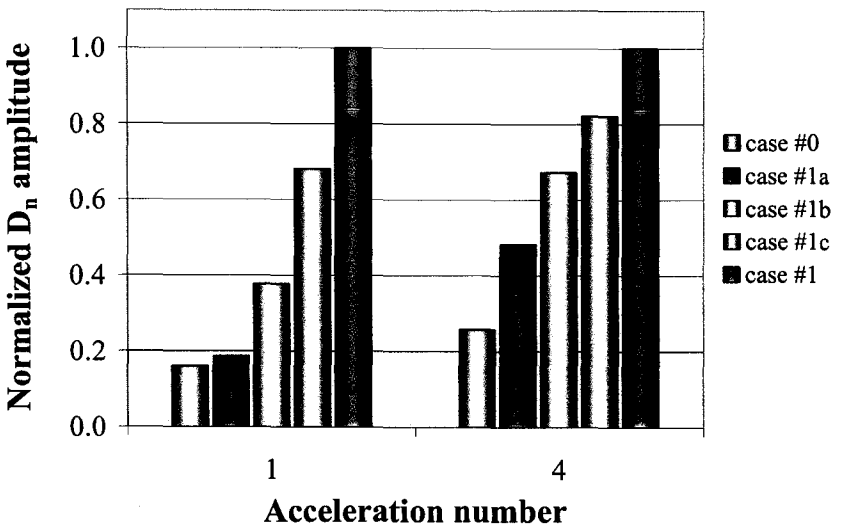

(a) cracks occurred at location 1

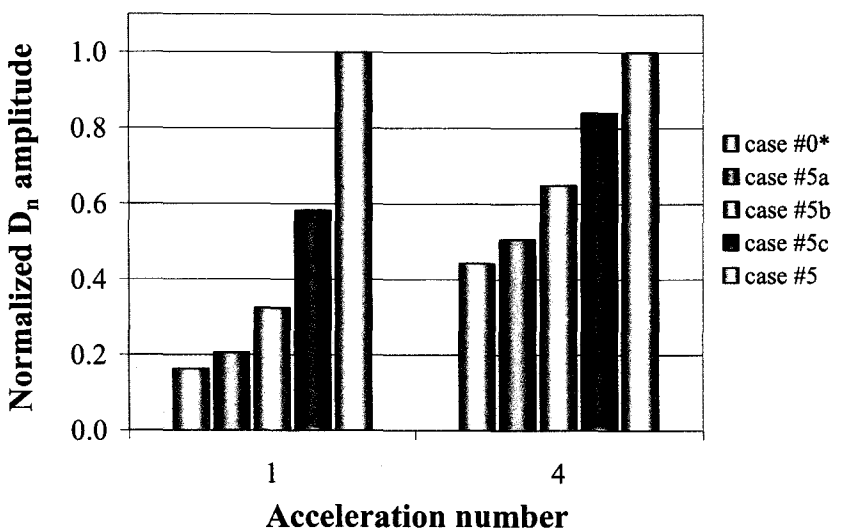

(b) cracks occurred at location 3

Figure 5.30: Normalized D_n amplitude of model #3 for cracks occurred at locations 1 and 3

puted from response of model #1 ranged from -0.83% to 0.2 %; the maximum difference in percentage occurred at mode 1 for damage case #8. However the difference was not significant in mode #5. For models #2 and #3 the difference between numerically computed and measured natural frequencies ranged from -0.01% to 0.89%. Maximum difference was observed at mode 2 for damage case #0 (intact), and the minimum difference occured at mode 5 for damage case #1.

Plots of natural frequencies obtained from numerical and experimental investigations for all damage cases and models are presented in Appendix E. Figure 5.31 shows a comparison between computed and measured natural frequencies for the first two modes of model #2 for damage cases #1 to #4 and #5 to #8, respectively. Although the numerical and experimental natural frequencies for damage cases #5 to #8 did not decrease to the same extent (in Hz) as damage cases #1 to #4, yet they had a similar trend for all damage cases investigated.

5.5.2 Numerical and Experimental rms of Response

Figure 5.32 shows normalized rms response of accelerometers #1 and #4 for damage cases #1 to #8. Plots of the normalized rms of amplitude response obtained from numerical analysis and experimental investigation for all accelerometers and damage cases are presented in Appendix E. From these plots it can be seen that the normalized rms of accelerations #1, #2 , #4, #5 and strain gages #1, #4, #6 had increasing trends even though the normalized experimental and numerical values of the rms were different. The difference between numerical and experimental results may be attributed to local stiffness of the horizontal or web frame in the

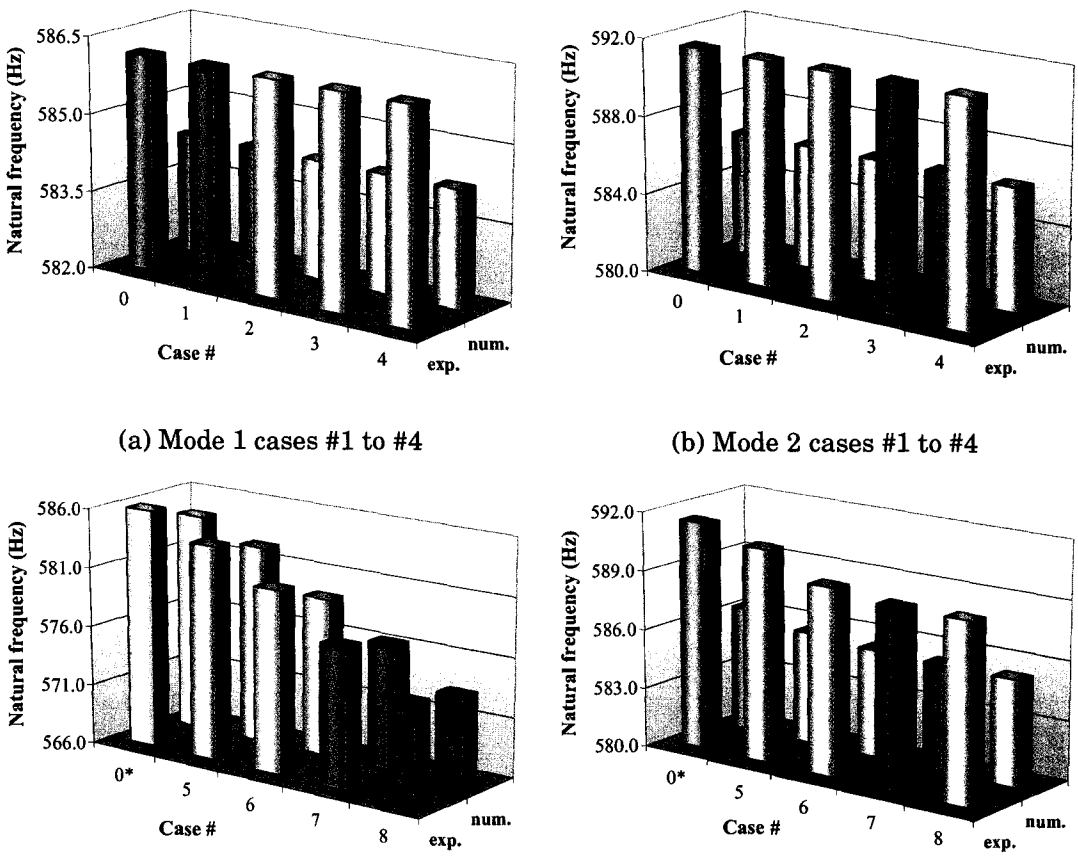

(a) Mode 1 cases #1 to #4

(b) Mode 2 cases #1 to #4

(c) Mode 1 cases #5 to #8

(d) Mode 2 cases #5 to #8

Figure 5.31: Comparison of numerical and experimental natural frequencies for modes 1 and 2 of model #2. num.= numerical values; exp.= experimental values

accelerometer directions being different from that of the numerical model due to fabrication details. For instance the numerical rms obtained from response of accelerometer #1 for case #0 (intact) and case #1 changed by almost 10 times while the experimental rms of response measured for the same accelerometer under the same damaged conditions was only larger by 1.6 times, see Figure 5.32 (a). For accelerometers #4 the numerical response of acceleration values for damage cases #5 to #8 decreased by 70% while the experimental values decreased approximately by 20% only, see Figure 5.32 (d). However the above mentioned transducers gave consistent and similar trends for increasing crack sizes introduced in the models. These experimental and numerical results will be employed for damage identification procedure presented in Chapter 6.

5.5.3 Numerical and Experimental D_n Amplitudes

Normalized D_n amplitudes obtained from numerical and experimental investigations are shown in Figures 5.33 and 5.34 for models #2 and #3, respectively. As seen in these figures, D_n amplitudes obtained from the response of accelerometer #4 produced slightly better results than accelerometer #1. The normalized values from measured response of accelerometer #4 were close to the values obtained from numerical investigations. This might be due to the location of accelerometer #4 which was mounted on the web frame. In addition, the modal response investigated was in flexure torsional mode of the web frames. However the numerical and experimental D_n amplitudes simulated from response of accelerometers #1 and #4 had the same in trend due to increasing in crack length. These results corroborated

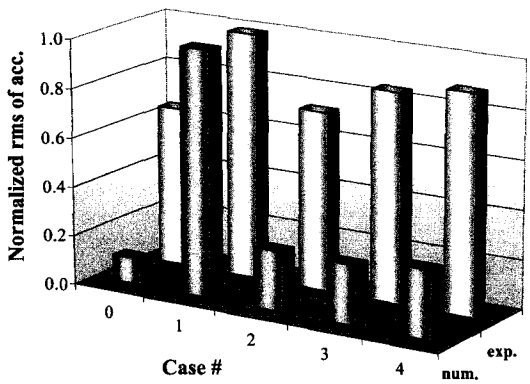

(a) accelerometer #1 for cases #1 to #4

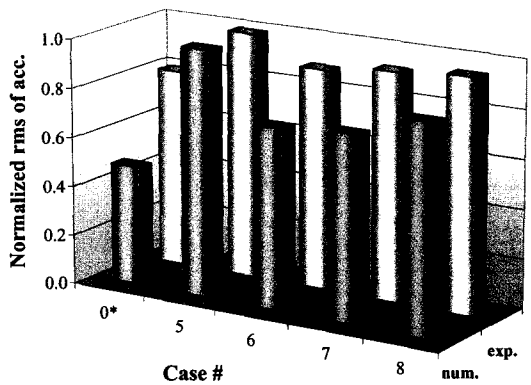

(b) accelerometer #1 for cases #5 to #8

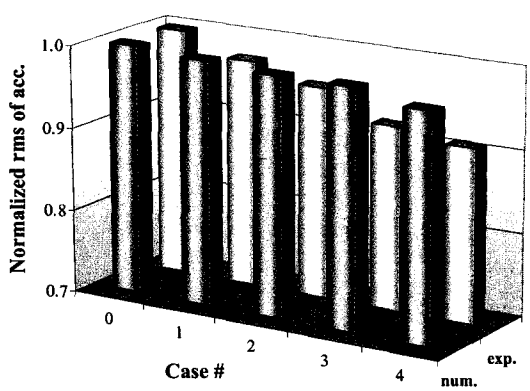

(c) accelerometer #4 cases #1 to #4

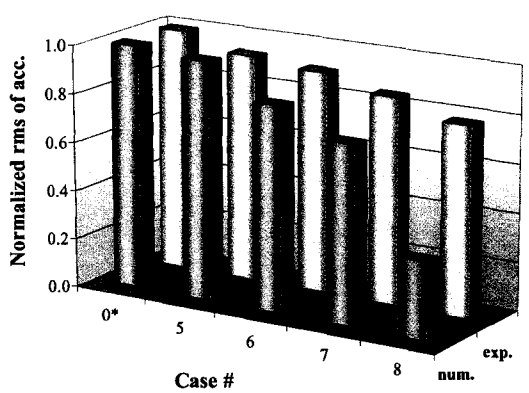

(d) accelerometer #4 cases #5 to #8

Figure 5.32: Comparison of normalized numerical and experimental rms response of model #2 for accelerometers #1 and #4. num.= numerical values; exp.= experimental values

the sensitivity of D_n to small cracks.

5.6 Summary

Numerical and experimental investigations on orthogonally stiffened plate of a ship's side shell model have been discussed in this chapter. Numerical investigations were carried out to obtain the modal parameters (natural frequency and mode shape), and acceleration and strain response of the model under intact and eight damaged conditions. The cracks occurred at a longitudinal in the connection between the longitudinal and bulkheads for damage cases #1 to #4 and at the intersection of the longitudinals and a tranverse web frame for damage cases #5 to #8. From the acceleration and strain response obtained in this investigation the best sensor locations were determined. Thereafter a total of twelve sensors (six accelerometers and six strain gages) were mounted on the model at these identified locations.

The three fabricated models were tested under random excitation forces whose dominant frequency ($\approx$ 2 Hz) was separated far away from the first natural frequency of the model ($\approx$ 580 Hz). The experimental tests were performed under nine conditions, i.e., intact and eight different damage cases. For each damage case the model's responses were measured ten times to investigate the variation of estimated modal parameters from one measurement to the other. Output-only modal analysis was conducted in this experimental investigation. The modal frequency, the damping ratio and the rms of response were extracted from the model

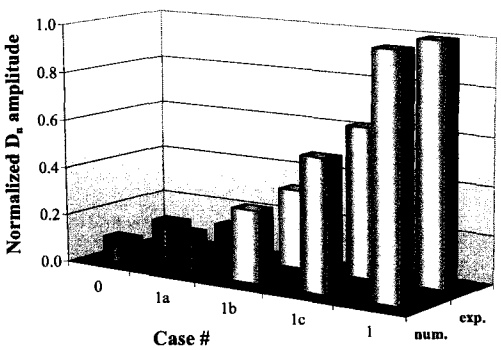

(a) accelerometer #1 for cases #1a to #1

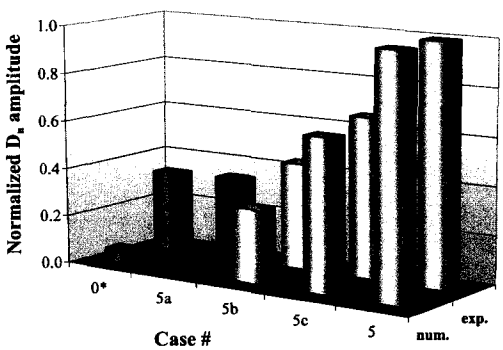

(b) accelerometer #1 for cases #5a to #5

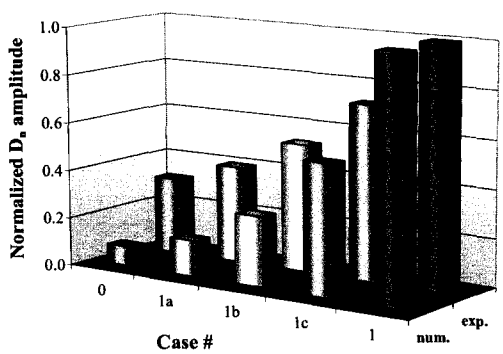

(c) accelerometer #4 for cases #1a to #1

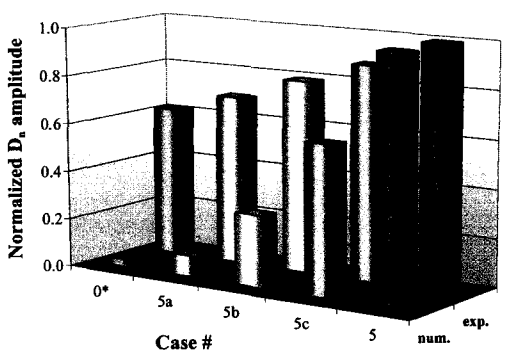

(d) accelerometer #4 for cases #5a to #5

Figure 5.33: Comparison of normalized numerical and experimental D_n values obtained from response of model #2. num.= numerical values; exp.= experimental values

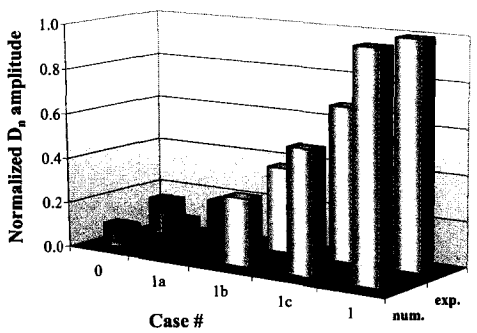

(a) accelerometer #1 for cases #1a to #1

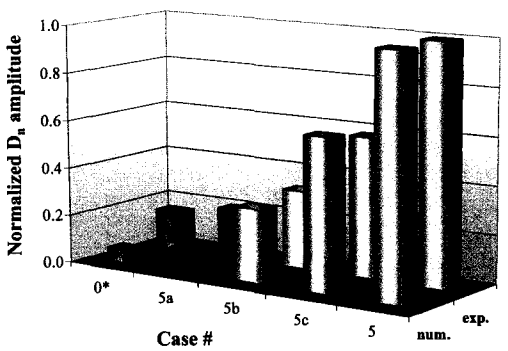

(b) accelerometer #1 for cases #5a to #5

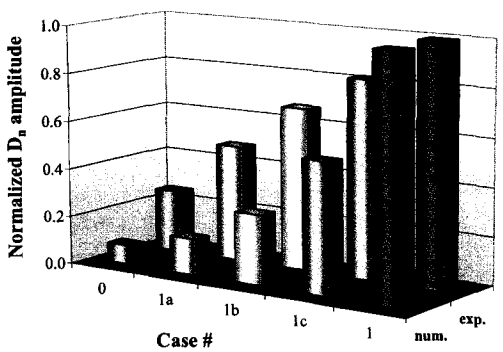

(c) accelerometer #4 for cases #1a to #1

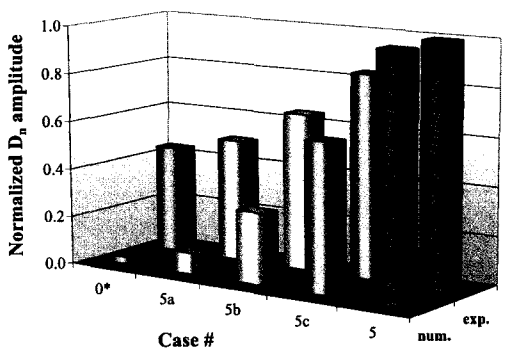

(d) accelerometer #4 for cases #5a to #5

Figure 5.34: Comparison of normalized numerical and experimental D_n values obtained from response of model #3. num.= numerical values; exp.= experimental values

response, without measuring of the excitation forces.

Natural frequencies and the rms response obtained from numerical and experimental investigations were compared. The numerical and experimental natural frequencies differed by a maximum of 0.9%. Although the rms response computed from the results of numerical investigations were different from those computed from the experimental investigations, most of them had similar trends due to increasing crack lengths.

Numerical and experimental D_n amplitudes showed increasing trends for all cases where cracks occurred at a single location. Even for cases where natural frequencies did not decrease, and no trend was noticeable in modal damping ratios, the D_n amplitudes showed consistently increasing trends. This confirmed the sensitivity of the D_n amplitudes to small cracking occurring at single location.

The experimental and numerical investigation results discussed in this chapter was used for the damage identification procedure presented in the next chapter.

Chapter 6

Damage Identification

6.1 Introduction

On-line and off-line damage identification schemes suitable for determining crack location and its extent, on orthogonally stiffened plate models excited by simulated wave forces, are proposed and presented in this chapter. These schemes use the root mean square (rms) of structural response and the amplitude of D_n function described in the previous chapters for identifying damage location and length in the modeled structure.

Numerical and experimental results presented in Chapter 5 indicated that the presence of damage occurring in the model could be identified from the change in natural frequency, rms response and amplitude of D_n function. For cases where damage occurred at the intersection between longitudinals and the transverse web frame, the first and second modal frequencies of the model decreased consistently and appreciably while for cases where cracks occurred in the connection of a longitudinal and bulkheads significant modal frequency changes occurred for the fifth mode, which was the overall bending mode. This was due to the fact that the first

two modal frequencies of the model were associated with local bending-torsional modes of the web frames. Consequently damage related to the web frame fixity would result in decrease of the modal frequencies. Since in this investigation, modal frequencies were extracted without knowledge of the excitation forces, natural frequencies could be used for on-line damage monitoring, although the crack length cannot not be properly determined from the change of the modal frequencies.

Numerical and experimental investigation results presented in Chapter 5 also showed that the rms of acceleration and strain response changed as cracks increased in length. In addition, the amplitudes of D_n function increased consistently as cracks at a location grew larger in length. Therefore by examining the rms of response and the amplitude of D_n function under normal operational conditions, the presence of a crack occurring in the structure could be identified.

In the proposed schemes presented in this chapter, cracks are identified using the rms of response and the amplitude of D_n function obtained from the results of investigations reported in Chapter 5. Moreover a scheme using the rms response obtained from finite element simulations is also presented. These investigation results were reported earlier in Budipiyanto et al. (2005a), Budipriyanto et al. (2006b) and Budipriyanto et al. (2006c).

6.2 Damage Identification Using rms Response

In this section, damage identification schemes using the rms response obtained from numerical and experimental investigations reported in Chapter 5 are discussed. The first scheme uses an algebraic function obtained from numerical/experimental measurements for assessing damage occurrence and extent. The second scheme employs the rms response data obtained from numerical simulation to determine the damage locations and quantifying damage size. The latter scheme can be categorized as a nomogram technique which could estimate accurately damage locations and extents. Schemes presented in this section were implemented in MATLAB environment.

6.2.1 Numerical and Experimental rms Response

A damage identification scheme using the rms of acceleration and strain response is discussed.The scheme uses the results of numerical and experimental investigations reported in Chapter 5 to obtain a damage indicator. Unlike the rms values, the damage indicator has a definable trend as cracks increased in lengths. Using the values of the proposed damage indicator, an algebraic function was developed to estimate the damage indicator values for different crack lengths and locations. In addition, a graphical scheme (based on nomogram procedure) was also developed to identify the crack length and location, using the damage indicator.

The Damage Indicator

The rms values obtained from the numerical and experimental investigations suggested the use of a damage indicator, e_i, that can be expressed as

$$e_i = e_{i-1} + |\psi_i - \psi_{i-1}| \qquad i = 2,3,4,5 \tag{6.1}$$

where | | denotes the absolute value and e_1 is taken equal to ψ_1 which denotes the rms value for intact condition, ψ_i is rms values under i^{th} case; the value of i for damage cases studied in this investigation is given in Table 6.1. For damage cases #1 to #4, i is equal to 2 for case #1 and i is equal to 3 for case #2 etc. For damage cases #5 to #8, i is equal to 2 for damage case #5, i is equal to 3 for damage case #6 and so forth. Equation 6.1 transforms the rms values that had no trend to that with an increasing trend. In cases where the complete set of rms values have an increasing trend, the e_i values would be the same as the rms values.

The e_i values computed from numerical and experimental response of accelerometers #1, #4 and #5 and strain gages #1, #4 and #6 under intact and eight damage cases were employed in this investigation. Using the damage indicator, a damage identification scheme was developed to identify the present and future damage scenario that can occur and the damage size and location.

Table 6.1: i for different damage case number

case	#0	#1	#2	#3	#4	#5	#6	#7	#8
i	1	2	3	4	5	2	3	4	5

Damage Identification Scheme

The scheme presented in this section assumes that the damage indicators e_i are known beforehand from the earlier simulated calculation. This is done by carrying out finite element analysis for a number of crack growth scenarios. Also these results are calibrated or benchmarked using data from experiments. Then for certain measured values of the damage indicator e_i, the method outlined herein seeks to quantify the crack size and determine crack location.

For representing the e_i values for different damage cases, an algebraic function was employed. In the function, crack location and crack length values were included since e_i seemed to be dependent on them. Several algebraic functions were used to estimate numerical e_i values before it was employed to interpolate/extrapolate the experimental e_i values. The one that appeared to give results close to the actual numerical e_i values (less than $\pm$ 20% error) is given below. The algebraic function can be written as,

$$e_i \approx \alpha_0 + \alpha_1 \left[\left(\frac{c_1}{L}\right)\left(\frac{a_{i1}}{d_1}\right)^2 + \left(\frac{c_2}{L}\right)\left(\frac{a_{i2}}{d_2}\right)^2 \right]^{1/2} + \alpha_2 \left[\left(\frac{c_1}{L}\right)\left(\frac{a_{i1}}{d_1}\right)^2 + \left(\frac{c_2}{L}\right)\left(\frac{a_{i2}}{d_2}\right)^2 \right] \tag{6.2}$$

where a_{i1} and a_{i2} are crack lengths at first and second damage locations (crack locations 1 and 2 for damage cases #1 to #4 or crack locations 3 and 4 for damage cases #5 to #8, see Table 5.1 for the crack lengths), c_1 and c_2 are distances measured from the bottom side of the side shell to the longitudinal where cracks are assumed to be occurring (in the present case, c_1 = c_2 = 360 mm for damage cases #1 to #4, c_1 = 360 mm and c_2 = 240 mm for damage cases #5 to #8), d_1 and d_2 are the

maximum possible crack lengths at two damage locations, respectively; the values of d_1 and d_2 were used for normalizing crack lengths so that Equation 6.2 becomes dimensionless. Total possible crack lengths in this investigation were taken as the longitudinal's flange width plus the horizontal's web depth for the values of d_1 and d_2 ($d_1 = d_2 = 49.4$ mm for damage cases #1 to #4, $d_1 = 49.4$ mm and $d_2 = 67.5$ mm for damage cases #5 to #8), L is the side shell plate length ($L = 600$ mm) and α_0, α_1, α_2 are coefficients that would be determined from the equation. A similar algebraic equation could also be developed when three damage indicator values, e_i, obtained from three different sensors (accelerometers or strain gages) from three different locations are utilized for identifying the crack lengths and locations.

For three different damage cases from the same sensor, Equation 6.2 can be expressed in matrix form as,

$$\begin{Bmatrix} e_1 \\ e_2 \\ e_3 \end{Bmatrix} = \begin{bmatrix} 1 & \sqrt{C_{11}+C_{12}} & (C_{11}+C_{12}) \\ 1 & \sqrt{C_{21}+C_{22}} & (C_{21}+C_{22}) \\ 1 & \sqrt{C_{31}+C_{32}} & (C_{31}+C_{32}) \end{bmatrix} \begin{Bmatrix} \alpha_0 \\ \alpha_1 \\ \alpha_2 \end{Bmatrix} \tag{6.3}$$

where

$$\begin{aligned} C_{i1} &= \left(\frac{c_1}{L}\right)\left(\frac{a_{i1}}{d_1}\right)^2 \\ C_{i2} &= \left(\frac{c_2}{L}\right)\left(\frac{a_{i2}}{d_2}\right)^2 \quad i = 1,2,3 \end{aligned}$$

or in a compact form

$$\{e\} = [C]\{\alpha\} \tag{6.4}$$

where $\{e\}$ is a vector containing the damage indicator values, $[C]$ is a ix3 matrix containing information about crack lengths and locations and $\{\alpha\}$ is a vector containing the coefficients.

Steps utilized to estimate the damage indicator amplitudes, e_i, using Equation 6.2 were: (a) using the known values of c_1, c_2, d_1, d_2, L, a_{i1}, a_{i2} and e_i under already known three damage cases (e_1, e_2, and e_3) the coefficients α were determined; (b) for assumed (or known) values of cracks length, values of e_4 and e_5 could be extrapolated using the constants α's obtained from step (a); e_5 could also be extrapolated using the values of e_2, e_3, and e_4, the one that gives better correlation with the measured damage indicator is used. Tables 6.2 to 6.4 present the damage indicator amplitudes along with the error obtained from the above mentioned extrapolation procedure.

The procedure produced good results for damage cases #1 to #4 especially for numerical values of accelerometers #4 and #5; the absolute error was less than 6% maximum. For numerical e_i extrapolated from response of accelerometer #1 (located on the flange of longitudinal #2) a maximum error of 18.6 % was observed whereas the error for the experimental values were between -5.9% to 9.2%. From Table 6.2 it appears that applying the scheme most of the e_4 values were underestimated while most of the e_5 values were overestimated. The error in extrapolated e_i values using strain gage response (given in Table 6.3) ranged from -12.6% to 17.7%. Unlike the values estimated from acceleration response, most of e_i estimated from strain gage response data were underestimated, see Table 6.3. As seen in Table 6.4 for damage cases #5 to #8, error in extraplotated value for e_4 ranged from -5.7% to

5.8% whereas the error for e_5 ranged from -7.7% to 18.3%. In all sensors and damage cases examined, maximum error occured in extrapolating the value of e_5. This scheme would have given better results if it was applied to smaller crack growth in each incremental step.

An attempt was also made to estimate crack lengths at two locations for known value of e_i (actual e_4 or e_5 value given in Table 6.2). Equation 6.2 with computed α's was solved for the crack lengths by using an iteration technique. In this study initial crack values were chosen and iterations were carried out using an incremental crack length until the difference between the known e_i value and the one obtained from the iteration were within the prescribed error tolerance. The actual and estimated crack lengths for e_i values of accelerometers #1, #4, and #5 are presented in Table 6.5. The crack lengths obtained using the technique were very close to the actual crack lengths (they had a maximum error of -3%). However it was observed that the technique was sensitive to initial values chosen for the iteration. If the initial values were chosen away from the actual crack lengths, employing this technique would result in erroneous results. It would be due to the fact that the crack growth (crack length difference from one damage case to other) was rather large (the largest crack growth investigated was 10 mm for damage cases #1 to #4 and 16 mm for damage cases #5 to #8). Another crack identification scheme using the rms values is also proposed and its capability to determine crack lengths and locations is demonstrated in the next subsection.

Table 6.2: Comparison of simulated/measured damage indicator (e_i) values with extrapolated values based on acceleration response data for cases #1 to #4

e_i	i	The damage indicator (e_i) values obtained using response of											
		accelerometer #1				accelerometer #4				accelerometer #5			
		num.	exp. of model			num.	exp. of model			num.	exp. of model		
			#1	#2	#3		#1	#2	#3		#1	#2	#3
actual	4	1.758	1.225	1.397	1.421	1.011	1.089	1.078	1.073	1.011	1.082	1.064	1.078
	5	1.793	1.247	1.438	1.439	1.025	1.104	1.089	1.094	1.025	1.106	1.076	1.101
extrp.	4	1.948	1.185	1.340	1.417	1.013	1.102	1.049	1.038	1.013	1.053	1.044	1.065
	5	2.127	1.261	1.353	1.512	1.016	1.133	1.189	1.184	1.016	1.165	1.158	1.118
error	4	10.808	-3.265	-4.080	-0.281	0.193	1.194	-2.690	-3.262	0.194	-2.680	-1.880	-1.206
(%)	5	18.628	1.123	-5.911	5.073	-0.843	2.627	9.183	8.227	-0.830	5.335	7.621	1.544

num.: numerical values; exp.: experimental values; extrp.: extrapolated values using Equation 6.2

Table 6.3: Comparison of simulated/measured damage indicator (e_i) values with extrapolated values based on strain response data for cases #1 to #4

e_i	i	The damage indicator (e_i) values obtained using response of											
		strain gage #1				strain gage #4				strain gage #6			
		num.	exp. of model			num.	exp. of model			num.	exp. of model		
			#1	#2	#3		#1	#2	#3		#1	#2	#3
actual	4	0.959	0.775	1.000	0.979	0.835	0.754	0.918	0.902	0.718	0.726	0.983	0.838
	5	1.000	1.000	1.004	1.000	1.000	1.000	1.000	1.000	1.001	1.000	1.000	1.000
extrp.	4	0.960	0.750	0.914	0.935	0.868	0.678	0.838	0.879	0.698	0.719	0.859	0.776
	5	0.974	1.044	0.917	0.973	0.931	1.065	0.929	1.054	0.916	1.154	0.903	1.177
error	4	0.104	-3.226	-8.600	-4.494	3.952	-10.080	-8.715	-2.550	-2.786	-0.964	-12.614	-7.399
(%)	5	-2.600	4.400	-8.665	-2.700	-6.900	6.500	-7.100	5.400	-8.492	15.400	-9.700	17.700

num.: numerical values; exp.: experimental values; extrp.: extrapolated values using Equation 6.2

Table 6.4: Comparison of simulated/measured damage indicator (e_i) values with extrapolated values based on acceleration response data for cases #5 to #8

e_i	i	The damage indicator (e_i) values obtained using response of											
		accelerometer #1				accelerometer #4				accelerometer #5			
		num.	exp. of model			num.	exp. of model			num.	exp. of model		
			#1	#2	#3		#1	#2	#3		#1	#2	#3
actual	4	1.291	1.133	1.138	1.136	1.263	1.230	1.148	1.169	1.262	1.227	1.133	1.138
	5	1.385	1.155	1.162	1.157	1.680	1.253	1.216	1.204	1.681	1.255	1.188	1.189
extrp.	4	1.269	1.103	1.105	1.132	1.257	1.268	1.083	1.149	1.255	1.298	1.100	1.120
	5	1.278	1.105	1.114	1.176	1.593	1.336	1.373	1.279	1.583	1.484	1.290	1.295
error	4	-1.704	-2.648	-2.900	-0.352	-0.475	3.089	-5.662	-1.711	-0.555	5.786	-2.913	-1.582
(%)	5	-7.726	-4.329	-4.131	1.642	-5.179	6.624	12.911	6.229	-5.830	18.247	8.586	8.915

num.: numerical values; exp.: experimental values; extrp.: extrapolated values using Equation 6.2

Table 6.5: Actual and estimated crack lengths from accelerometer response and the error

Damage case	Crack location	Crack lengths obtained from response of accelerometer								
		#1			#4			#5		
		actual	estm.	error (%)	actual	estm.	error (%)	actual	estm.	error (%)
3	1	20.00	20.13	0.625	20.00	20.05	0.250	20.0	20.0	-0.250
	2	20.00	20.21	1.037	20.00	20.15	0.750	20.0	20.1	0.250
4	1	25.40	24.98	-1.646	25.40	25.55	0.591	25.4	25.5	0.197
	2	30.80	30.32	-1.567	30.80	30.90	0.325	30.8	30.5	-0.974
7	3	20.00	19.80	-1.000	20.00	19.95	-0.250	20.00	20.10	0.500
	4	32.00	31.25	-2.344	32.00	32.25	0.781	32.00	32.25	0.781
8	3	30.80	30.05	-2.435	30.80	30.20	-1.948	30.80	30.20	-1.948
	4	41.70	42.30	1.439	41.70	42.45	1.799	41.70	42.45	1.799

estm.: estimated crack length using Equation 6.2

6.2.2 The rms Obtained from Numerical Simulations

As mentioned earlier, the rms of structural response will change by different amounts when a crack occurs. The changes may be insignificant at some locations while it may be significant at others. At locations where the response changed significantly, the rms values of the response of a cracked structure will be different from its value for the intact structure. Since changes in response may not be significant at all locations, the sensor locations where response changes appreciably, due to the presence of cracks in the structure, were investigated earlier and the results reported in Chapter 5.

Results of simulations using ABAQUS reported in this investigation were based on the assumption that the response had zero mean. For response having non-zero mean (for instance response data measured from an experimental test), a preprocessing procedure as described in the previous chapter is needed to obtain zero mean response.

The proposed scheme aims at identifying the crack location and length without prior knowledge of excitations applied on the structure and its modal characteristics. The use of the rms values of the vibration response is demonstrated. Two types of response are employed: acceleration, and strain. Numerical simulations, using the finite element computer program ABAQUS, were carried out to obtain the rms values of the response at the locations of the sensors, see Figure 5.9. In this investigation two frequency ranges were considered independently. The first range spanned frequency values from 200 Hz to 600 Hz, and the second range spanned frequency values from 200 Hz to 1200 Hz. In the following discussion,

the first range will be referred as the 600 Hz range and the second range will be referred as the 1200 Hz range. The rms response values in the two ranges were computed and utilized to validate the crack identification scheme. These values were selected because the rms response values changed near these two frequencies. Within these frequency ranges, the rms values were sensitive to damage. Within the 600 Hz range, the sensitivity of rms response values to damage was rather limited, whereas within the 1200 Hz range the rms response values changed appreciably especially for rms of acceleration response, see Figures 5.15 and 5.16.

Tables 6.6 and 6.7 show the locations and lengths of the cracks used to obtain the simulations for different cases. The row number i and column number j in Tables 6.6 and 6.7 relate the simulated crack cases. Thus, in simulations #1 to #4, there was no crack at location 2, and the crack length at location 1 progressed from 0.0 to 25.4 mm in four stages (0.0 mm, 10.0 mm, 20.0 mm and 25.4 mm). The corresponding rms values can be found in Table 6.8, by using the row and column numbers given in Table 6.6. Thus, the rms values for the response at accelerometer #1, obtained from simulations #1 to #4, between frequency ranges from 200 Hz to 600 Hz were 0.105584, 1.000000, 0.245303, and 0.290959, respectively, see Table 6.8 (a). Values of the rms response in Tables 6.8 (b), (c), (d) and (e) can be related to other simulations given in Table 6.6 in the same way.

Tables 6.9 (a), (b), (c), (d) and (e) show the rms values obtained at the locations of accelerometers #1, #2 and #4 for damage cases #5 to #8, for the two frequency ranges of 200 Hz to 600 Hz (the 600 Hz range) and 200 Hz to 1200 Hz (the 1200 Hz range), respectively. The rms values tabulated in Table 6.9 were related to

simulations given in Table 6.7. The rms values for all damage cases and frequency ranges are presented in Tables F.1 to F.18 in Appendix F.

Damage Identification Scheme

This section discusses the damage identification scheme developed in this study. The scheme uses the rms of response obtained from ABAQUS after normalizing the values. The method described below is for computing the damage indicator, e_{ij}, obtained from normalized rms values. The computation is necessary for identifying the definable trend present in the rms values when the crack length increases since the rms response values did not increase consistently due to increasing crack length. After computing the damage indicator values, the values are plotted (along the z- axis) in a three dimensional plot, plotting the crack lengths at two different locations along the x- and y- axes, respectively. A horizontal plane along any of the damage indicator magnitude will give a curve along which the damage indicator will have the same value (called as equi-value, in this study) for various crack lengths and two different locations. This proposed scheme was performed by employing MATLAB scripts.

The results of the analysis using the rms values suggest the use of a quantity denoted by e_{ij}, as a damage indicator, which can be expressed as

$$e_{ij} = e_{i,j-1} + |\psi_{ij} - \psi_{i,j-1}| \quad i = 1,2,...nrow, \quad j = 2,...ncol \tag{6.5}$$

Table 6.6: Numerical simulations carried out for damage cases #1 to #4

No	row no.	column no.	Crack lengths (in mm) at crack locations			
			location 1	location 2	location 3	location 4
1	1	1	0.00	0.00	none	none
2	1	2	10.0	0.00	none	none
3	1	3	20.0	0.00	none	none
4	1	4	25.4	0.00	none	none
5	2	1	0.00	10.0	none	none
6	2	2	10.0	10.0	none	none
7	2	3	20.0	10.0	none	none
8	2	4	25.4	10.0	none	none
9	3	1	0.00	20.0	none	none
10	3	2	10.0	20.0	none	none
11	3	3	20.0	20.0	none	none
12	3	4	25.4	20.0	none	none
13	4	1	0.00	30.8	none	none
14	4	2	10.0	30.8	none	none
15	4	3	20.0	30.8	none	none
16	4	4	25.4	30.8	none	none

Table 6.7: Numerical simulations carried out for damage cases #5 to #8

No	row no.	column no.	Crack lengths (in mm) at crack locations			
			location 1	location 2	location 3	location 4
1	1	1	none	none	0.00	0.00
2	1	2	none	none	10.0	0.00
3	1	3	none	none	20.0	0.00
4	1	4	none	none	30.8	0.00
5	2	1	none	none	0.00	16.0
6	2	2	none	none	10.0	16.0
7	2	3	none	none	20.0	16.0
8	2	4	none	none	30.8	16.0
9	3	1	none	none	0.00	32.0
10	3	2	none	none	10.0	32.0
11	3	3	none	none	20.0	32.0
12	3	4	none	none	30.8	32.0
13	4	1	none	none	0.00	41.7
14	4	2	none	none	10.0	41.7
15	4	3	none	none	20.0	41.7
16	4	4	none	none	30.8	41.7

Table 6.8: The rms of accelerometers #1, #2 and #4 for damage cases #1 to #4

(a) accelerometer #1 for frequency range of 200 Hz to 600 Hz				
Crack length at location 2 (mm)	Crack length at location 1 (mm)			
	0.0	10.0	20.0	25.4
0.0	0.105584	1.000000	0.245303	0.290959
10.0	0.104110	0.995261	0.242488	0.287847
20.0	0.104261	0.986744	0.242265	0.287413
30.8	0.100556	0.951480	0.233846	0.277608
(b) accelerometer #1 for frequency range of 200 Hz to 1200 Hz				
Crack length at location 2 (mm)	Crack length at location 1 (mm)			
	0.0	10.0	20.0	25.4
0.0	0.103818	1.000000	0.240596	0.283886
10.0	0.102187	0.993850	0.237445	0.280406
20.0	0.102185	0.983620	0.236847	0.279534
30.8	0.097625	0.940259	0.226511	0.267575
(c) accelerometers #2 for frequency range of 200 Hz to 600 Hz				
Crack length at location 2 (mm)	Crack length at location 1 (mm)			
	1(0.0)	2(10.0)	3(20.0)	4(25.4)
0.0	0.501359	1.000000	0.688031	0.742983
10.0	0.494783	0.998037	0.679659	0.734324
20.0	0.495496	0.985786	0.679851	0.734278
30.8	0.478974	0.948753	0.656963	0.709952
(d) accelerometer #4 for frequency range of 200 Hz to 600 Hz				
Crack length at location 2 (mm)	Crack length at location 1 (mm)			
	0.0	10.0	20.0	25.4
0.0	0.998752	0.993378	0.987731	0.972806
10.0	0.998768	0.993565	0.987920	0.972992
20.0	0.998972	0.993769	0.988121	0.973189
30.8	1.000000	0.994791	0.989137	0.974187
(e) accelerometer #4 for frequency range of 200 Hz to 1200 Hz				
Crack length at location 2 (mm)	Crack length at location 1 (mm)			
	0.0	10.0	20.0	25.4
0.0	1.000000	0.982223	0.948839	0.874970
10.0	0.999199	0.981353	0.947818	0.873754
20.0	0.999450	0.981499	0.947735	0.873329
30.8	0.994341	0.975746	0.940885	0.864989

Table 6.9: The rms of accelerometers #1, #2 and #4 for damage cases #5 to #8

(a) accelerometer #1 for frequency range of 200 Hz to 600 Hz				
Crack length at location 4 (mm)	Crack length at location 3 (mm)			
	0.0	10.0	20.0	30.8
0.0	0.483036	1.000000	0.734159	0.816648
16.0	0.478977	0.909558	0.731732	0.815722
32.0	0.480675	0.871124	0.754886	0.841974
41.7	0.469188	0.719192	0.759070	0.848456
(b) accelerometer #1 for frequency range of 200 Hz to 1200 Hz				
Crack length at location 4 (mm)	Crack length at location 3 (mm)			
	0.0	10.0	20.0	30.8
0.0	0.582147	0.577807	0.885799	0.978960
16.0	0.575034	0.571568	0.876037	0.971673
32.0	0.590234	0.600039	0.902352	1.000000
41.7	0.591009	0.605092	0.900563	0.999717
(c) accelerometer #2 for frequency range of 200 Hz to 600 Hz				
Crack length at location 4 (mm)	Crack length at location 3 (mm)			
	0.0	10.0	20.0	30.8
0.0	0.471210	1.000000	0.701730	0.803186
16.0	0.466431	0.919879	0.700682	0.803293
32.0	0.465378	0.869844	0.717328	0.823508
41.7	0.451394	0.717964	0.721247	0.829722
(d) accelerometer #4 for frequency range of 200 Hz to 600 Hz				
Crack length at location 4 (mm)	Crack length at location 3 (mm)			
	0.0	10.0	20.0	30.8
0.0	1.000000	0.978761	0.924088	0.719817
16.0	0.934999	0.904899	0.843783	0.631160
32.0	0.885427	0.803055	0.736945	0.515378
41.7	0.666299	0.617627	0.548360	0.319802
(e) accelerometer #4 for frequency range of 200 Hz to 1200 Hz				
Crack length at location 4 (mm)	Crack length at location 3 (mm)			
	0.0	10.0	20.0	30.8
0.0	0.786780	0.769185	0.823992	0.920877
16.0	0.817335	0.796920	0.848333	0.936817
32.0	0.836828	0.825072	0.875290	0.959432
41.7	0.902625	0.876868	0.923842	1.000000

or

$$e_{ij} = e_{i-1,j} + |\psi_{ij} - \psi_{i-1,j}| \quad i = 2, ...nrow, \quad j = 1, 2, ...ncol \tag{6.6}$$

where the value of e_{11} is taken equal to ψ_{11} which denotes the rms value for intact condition, i and j indicate the simulated damage case considered. The values of i and j are given in the second and third columns of Tables 6.6 and 6.7.

The damage indicator, e_{ij}, values given in Equation 6.5 satisfy the following condition:

$$\|e_{i-1,j}\|_2 < \|e_{ij}\|_2 \quad \text{or} \quad \|e_{i-1,j}\|_2 > \|e_{ij}\|_2 \tag{6.7}$$

where $\|e_{i-1,j}\|_2 = \sqrt{e_{i-1,1}^2 + e_{i-1,2}^2 + \ldots + e_{i-1,ncol}^2}$ and $\|e_{ij}\|_2 = \sqrt{e_{i,1}^2 + e_{i,2}^2 + \ldots + e_{i,ncol}^2}$

whereas e_{ij}, values given in Equation 6.6 satisfy the condition:

$$\|e_{i,j-1}\|_2 < \|e_{ij}\|_2 \quad \text{or} \quad \|e_{i,j-1}\|_2 > \|e_{ij}\|_2 \tag{6.8}$$

where $\|e_{i,j-1}\|_2 = \sqrt{e_{1,j-1}^2 + e_{2,j-1}^2 + \ldots + e_{nrow,j-1}^2}$ and $\|e_{ij}\|_2 = \sqrt{e_{i,1}^2 + e_{i,2}^2 + \ldots + e_{nrow,j}^2}$

It can be seen from Tables 6.8, 6.9 and the rms values presented in Appendix F that the rms values do not follow a definable trend (decreasing or increasing) when the crack length increases. Applying Equations 6.5 and 6.7 or Equations 6.6 and 6.8 the rms values were transformed into values that have an increasing trend due to the increase of crack lengths. This trend is a requisite step for the damage identification scheme developed in this section. Values for the damage indicator calculated for various cases are given in Tables 6.10 and 6.11. The same scheme

that relates Table 6.8 to Table 6.6 and Table 6.9 to Table 6.7 can be used to relate the values of the damage indicator in Tables 6.10 and 6.11 for the different simulations shown in Tables 6.6 and 6.7. The e_{ij} values obtained using accelerometer and strain gage response for all damage cases are given in Tables G.1 to G.18 in Appendix G.

Figures 6.1 (a, b, c and d) show the three dimensional plots for the rms values and the values of the crack indicator, e_{ij}, for the 600 Hz frequency range plotted as a function of crack lengths at crack locations 1 and 2. The four plots are for the accelerometers #1 and #4, for the damage cases #1 to #4 (shown in Table 5.1). Figures 6.2 (a, b, c and d) show the plots of the rms and e_{ij} as a function of crack lengths at locations 3 and 4 (for accelerometers #1 and #4) for damage cases #5 to #8 (shown in Table 5.1).

The fact that magnitude of e_{ij} is a function of crack length and location indicates that a horizontal plane through a certain magnitude of e_{ij} will give a curve (in the horizontal plane) that relates the crack sizes at the two locations (1 and 2 or 3 and 4). This curve is called the equi-value curve, denoted by e_Q, and has the same e_{ij} magnitude for different combinations of crack sizes at two locations for a particular sensor. To obtain the unknown values of crack length (at the two locations) at least two such curves are needed. The crack length and location would be given from the intersection of the curves. In practice, however, three curves were sometimes required to obtain the correct intersection point since two curves of equi-value of e_{ij} intersect at more than one point. Curves of equi-value of the damage indicator (e_Q) for the two frequency ranges are shown in Figures 6.3 to 6.5. Each curve in

Table 6.10: The e_{ij} values of accelerometers #1, #2 and #4 for damage cases #1 to #4 (crack size in mm for various of i, j values are given within the brackets)

(a) accelerometers #1 for frequency range of 200 Hz to 600 Hz				
Crack length at location 2 (mm)	Crack length at location 1 (mm)			
	1(0.0)	2(10.0)	3(20.0)	4(25.4)
1(0.0)	0.105584	1.000000	1.754697	1.800353
2(10.0)	0.104110	0.995261	1.748035	1.793394
3(20.0)	0.104261	0.986744	1.731223	1.776370
4(30.8)	0.100556	0.951480	1.669114	1.712876
(b) accelerometers #1 for frequency range of 200 Hz to 1200 Hz				
Crack length at location 2 (mm)	Crack length at location 1 (mm)			
	1(0.0)	2(10.0)	3(20.0)	4(25.4)
1(0.0)	0.103818	1.000000	1.759404	1.802695
2(10.0)	0.102187	0.993850	1.750255	1.793215
3(20.0)	0.102185	0.983620	1.730393	1.773080
4(30.8)	0.097625	0.940259	1.654008	1.695071
(c) accelerometers #2 for frequency range of 200 Hz to 600 Hz				
Crack length at location 2 (mm)	Crack length at location 1 (mm)			
	1(0.0)	2(10.0)	3(20.0)	4(25.4)
1(0.0)	0.501359	1.000000	1.311969	1.366921
2(10.0)	0.494783	0.998037	1.316415	1.371080
3(20.0)	0.495496	0.985786	1.291721	1.346148
4(30.8)	0.478974	0.948753	1.240542	1.293531
(d) accelerometers #4 for frequency range of 200 Hz to 600 Hz				
Crack length at location 2 (mm)	Crack length at location 1 (mm)			
	1(0.0)	2(10.0)	3(20.0)	4(25.4)
1(0.0)	0.998752	0.993378	0.987731	0.972806
2(10.0)	0.998768	0.993565	0.987920	0.972992
3(20.0)	0.998972	0.993769	0.988121	0.973189
4(30.8)	1.000000	0.994791	0.989137	0.974187
(e) accelerometers #4 for frequency range of 200 Hz to 1200 Hz				
Crack length at location 2 (mm)	Crack length at location 1 (mm)			
	1(0.0)	2(10.0)	3(20.0)	4(25.4)
1(0.0)	1.000000	0.982223	0.948839	0.874970
2(10.0)	1.000801	0.983094	0.949859	0.876185
3(20.0)	1.001052	0.983240	0.949943	0.876610
4(30.8)	1.006160	0.988993	0.956792	0.884950

Table 6.11: The e_{ij} values of accelerometers #1, #2 and #4 for damage cases #5 to #8 (crack size in mm for various of i, j values are given within the brackets)

(a) accelerometers #1 for frequency range of 200 Hz to 600 Hz				
Crack length at location 4 (mm)	Crack length at location 3 (mm)			
	1(0.0)	2(10.0)	3(20.0)	4(30.8)
1(0.0)	0.483036	1.000000	1.265841	1.348331
2(16.0)	0.478977	0.909558	1.087385	1.171375
3(32.0)	0.480675	0.871124	0.987363	1.074451
4(41.7)	0.469188	0.719192	0.759070	0.848456
(b) accelerometers #1 for frequency range of 200 Hz to 1200 Hz				
Crack length at location 4 (mm)	Crack length at location 3 (mm)			
	1(0.0)	2(10.0)	3(20.0)	4(30.8)
1(0.0)	0.582147	0.577807	0.885799	0.978960
2(16.0)	0.589261	0.584047	0.895562	0.986247
3(32.0)	0.604461	0.612517	0.921877	1.014575
4(41.7)	0.605236	0.617570	0.923666	1.014857
(c) accelerometers #2 for frequency range of 200 Hz to 600 Hz				
Crack length at location 4 (mm)	Crack length at location 3 (mm)			
	1(0.0)	2(10.0)	3(20.0)	4(30.8)
1(0.0)	0.471210	1.000000	1.298270	1.399727
2(16.0)	0.466431	0.919879	1.139077	1.241688
3(32.0)	0.465378	0.869844	1.022361	1.128541
4(41.7)	0.451394	0.717964	0.721247	0.829722
(d) accelerometers #4 for frequency range of 200 Hz to 600 Hz				
Crack length at location 4 (mm)	Crack length at location 3 (mm)			
	1(0.0)	2(10.0)	3(20.0)	4(30.8)
1(0.0)	1.000000	1.021239	1.075912	1.280183
2(16.0)	0.934999	0.965098	1.026214	1.238837
3(32.0)	0.885427	0.967800	1.033909	1.255476
4(41.7)	0.666299	0.714972	0.784238	1.012796
(e) accelerometers #4 for frequency range of 200 Hz to 1200 Hz				
Crack length at location 4 (mm)	Crack length at location 3 (mm)			
	1(0.0)	2(10.0)	3(20.0)	4(30.8)
1(0.0)	0.786780	0.804375	0.859182	0.956067
2(16.0)	0.817335	0.837749	0.889161	0.977646
3(32.0)	0.836828	0.848585	0.898803	0.982945
4(41.7)	0.902625	0.928382	0.975355	1.051514

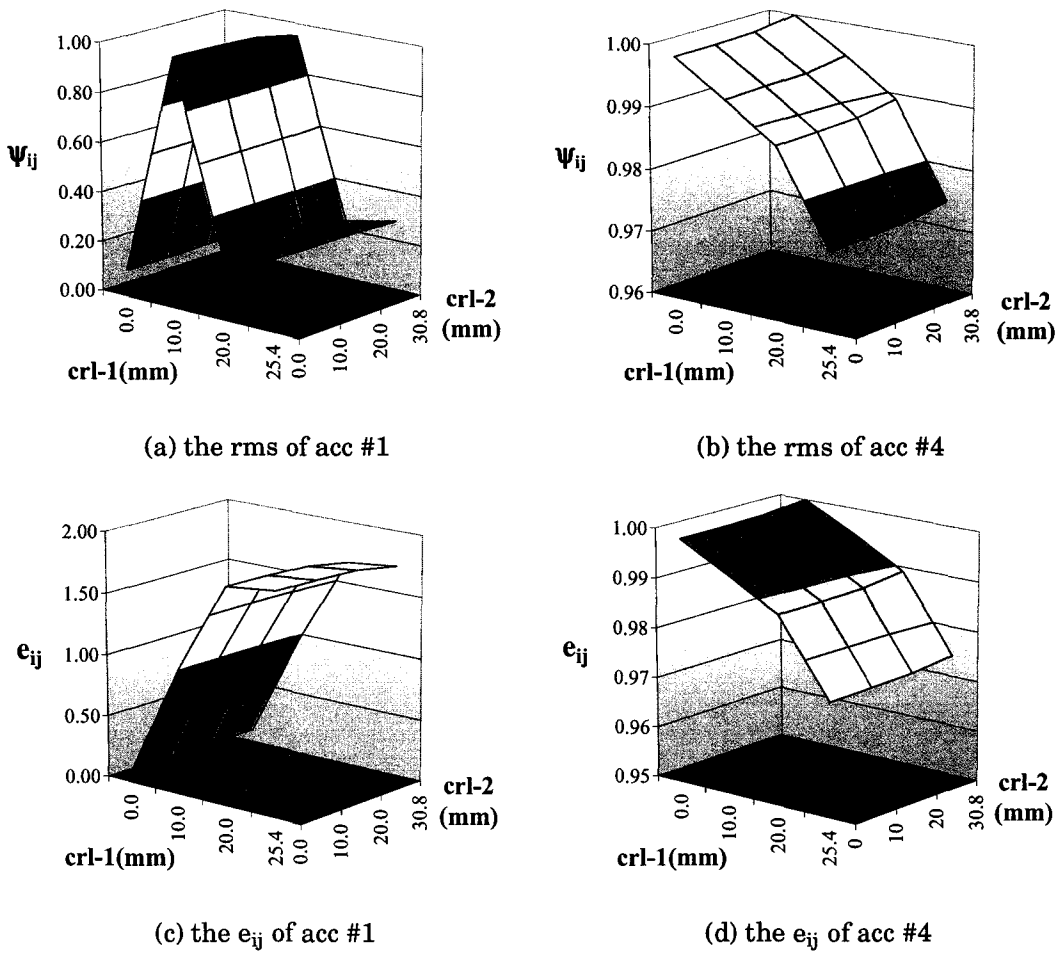

(a) the rms of acc #1

(b) the rms of acc #4

(c) the e_{ij} of acc #1

(d) the e_{ij} of acc #4

Figure 6.1: Three-dimensional plot of the normalized rms and e_{ij} computed from response of acceleration #1 and #4 for the 600 Hz frequency range for damage cases #1 to #4

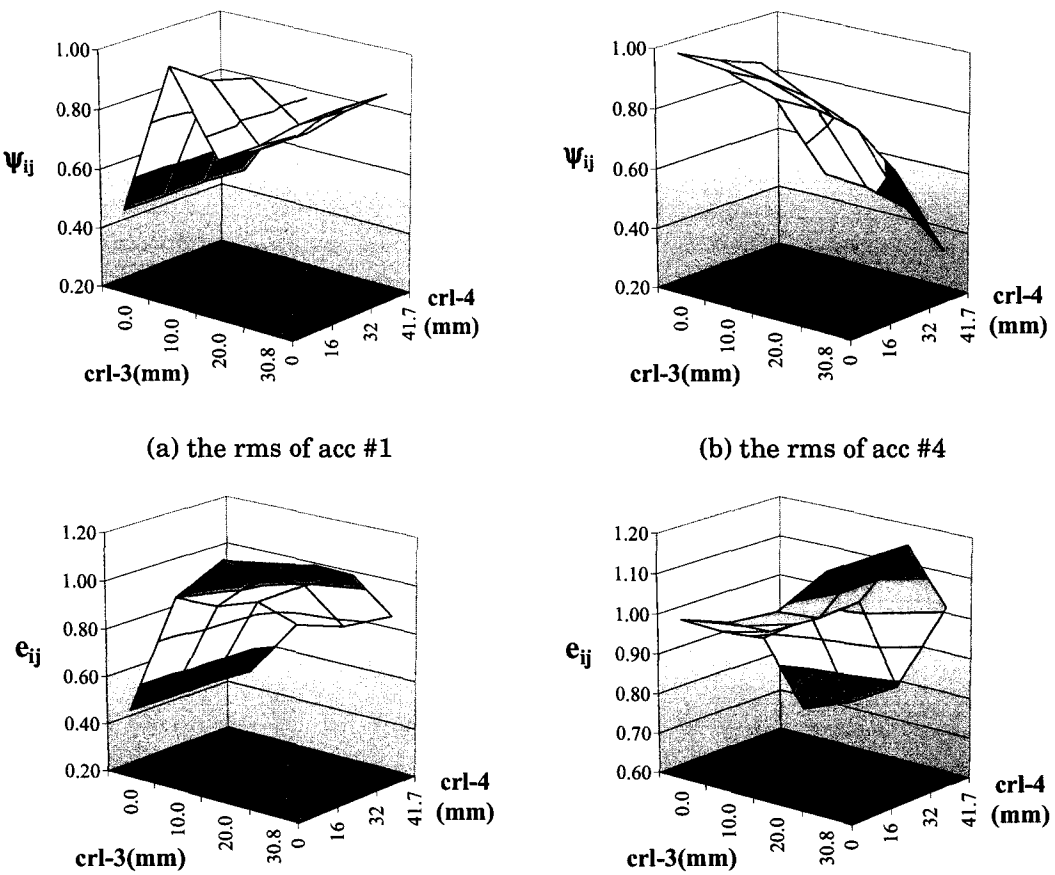

(a) the rms of acc #1

(b) the rms of acc #4

(c) the e_{ij} of acc #1

(d) the e_{ij} of acc #4

Figure 6.2: Three-dimensional plot of the normalized rms and e_{ij} computed from response of acceleration #1 and #4 for the 600 Hz frequency range for damage cases #5 to #8

these figures has the same value of e_{ij} for the given frequency range. For instance, the three curves shown in Figure 6.3 (a) are drawn for: (i) Amplitudes of 0.105584 and 0.103818 for e_{ij}, for the two frequency ranges between 200 Hz to 600 Hz and 200 Hz to 1200 Hz., of accelerometer #1; and (ii) An amplitude of 0.501359 for e_{ij}, for the frequency range between 200 Hz to 600 Hz, for accelerometer #2. These amplitudes were obtained from the values of e_{ij} shown in Tables 6.10 (a), (b) and (c) when the 0.0 mm crack occurred at location 1 and no crack occurred at location 2. By plotting these three curves at a single plot, crack sizes and locations can be determined from the point of intersection of the e_Q curves. In Figure 6.3 (a) the intersection point indicates that there is a crack of length 0.0 mm at location 1, and 0.0 mm at location 2.

In a similar manner, Figure 6.3 (b) was plotted using the values in Table G.4 (or Tables 6.10 (d) and (e)) and Table G.5 in Appendix G (equi-values for the three intersecting e_Q curves are 0.993378, 0.982223 and 0.875832, respectively). The common intersection location in Figure 6.3 (b) indicates that there are cracks at locations 1 and 2, whose lengths are 9.8 mm, and 0.0 mm, respectively. It is seen from Figure 6.3 that by using a minimum of two curves of e_Q, the equi-value of the damage indicator, the crack sizes and locations can be identified; use of the third curve gives better certainty for the point of intersection.

Similarly Figures 6.4 (a), (b), (c) and (d) were obtained by using the corresponding tables computed for strain gages, see Tables G.7 to G.12. In Figure 6.4 (d), e_Q curves at amplitudes of 0.813171 and 0.986866 (computed from response of strain gages #4 and #5) for damage case #3 were employed to obtain the crack lengths

and locations. It can be diagnosed from Figure 6.4 (d) that crack size at location 1 was 20.2 mm and crack length at location 2 was 20.0 mm. Figures 6.5 show similar plots for damage cases #5 to #8. Once again the crack lengths are determined from the intersection of these e_Q curves.

Tables 6.12 (a) and (b) present identified crack lengths at locations using e_Q values obtained acceleration and strain response for all damage cases. Excellent results were obtained. The error between identified and the actual crack length was within $\pm$ 2%. These results showed that the method can be used to identifiy acurately crack length and location.

A preliminary investigation on the sensitivity of the identified crack lengths and location when an error occurs in e_{ij} value, was also carried out. It was found that by introducing a 2.5 % difference on crack lengths, the difference in the damage indicator was nearly 5%. For instance using response of accelerometers #4 and #5, see Figure 6.3 (c), when the crack lengths at locations 1 and 2 were 19.5 mm and 10.2 mm a -5% error in was found in the damage indicator. Also when crack lengths of 20.5 mm and 9.7 mm occurred at crack locations 1 and 2 a +5% error in e_{ij} was observed. Similar computation can be made for other sensors and locations.

6.3 The Amplitude of D_n Function

As stated earlier in this chapter amplitudes of D_n functions could also be used to identify the occurrence of crack in the stiffened plate model since the amplitudes increased consistently as crack lengths at a location grew larger, see section 5.5.3

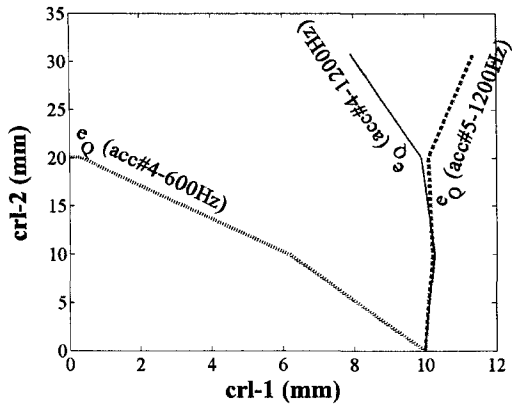

(a) e_Q plots of two different accelerometers #4 and #5 (accelerometer #4 at two frequency ranges) for damage case #1 (e_Q = 0.993378, 0.982223 and 0.875832). Diagnosis: crack size at location 1 $\approx$ 9.8 mm and crack size at location 2 $\approx$ 0.0 mm

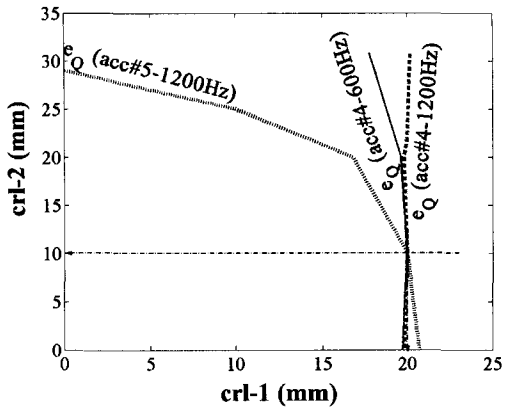

(b) e_Q plots of two different accelerometers #4 and #5 (accelerometer #4 at two frequency ranges) for damage case #2 (e_Q = 0.987920, 0.949859 and 0.832525). Diagnosis: crack size at location 1 $\approx$ 19.9 mm and crack size at location 2 $\approx$ 10.2 mm

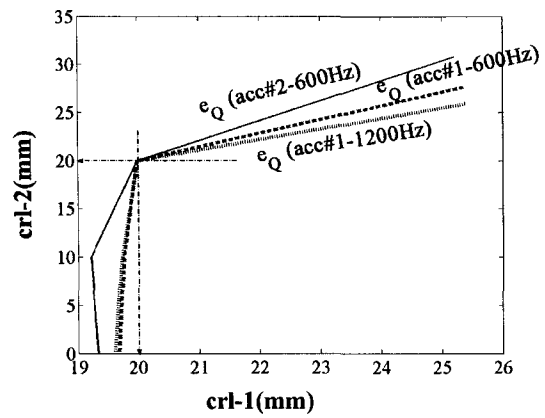

(c) e_Q plots of two different accelerometers #1 and #2 (accelerometer #1 at two frequency ranges) for damage case #3 (e_Q = 1.731223, 1.730393 and 1.291721). Diagnosis: crack size at location 1 $\approx$ 20.2 mm and crack size at location 2 $\approx$ 20.0 mm

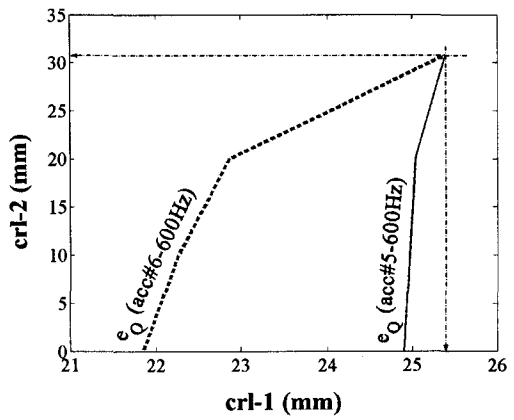

(d) e_Q plots of two different accelerometers #5 and #6 for damage case #4 (e_Q = 0.974402 and 0.995104). Diagnosis: crack size at location 1 $\approx$ 24.3 mm and crack size at location 2 $\approx$ 31.0 mm

Figure 6.3: Crack identifications using equi-value of e_{ij} (e_Q) obtained from acceleration response for damage cases #1, #2, #3 and #4

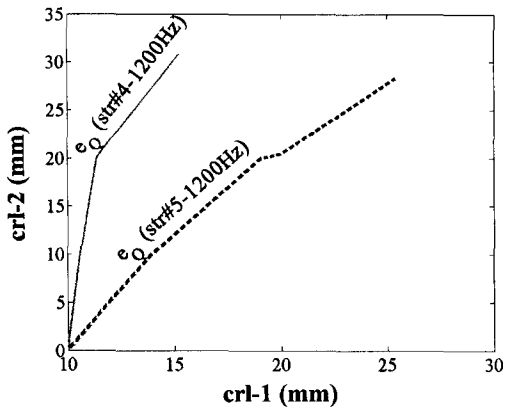

(a) e_Q plots of two different strain gages #4 and #5 for damage case #1 (e_Q = 0.728618 and 0.960557). Diagnosis: crack size at location 1 $\approx$ 10.1 mm and crack size at location 2 $\approx$ 0.0 mm

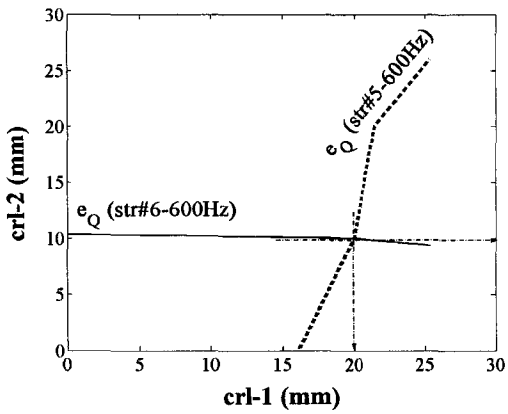

(b) e_Q plots of two different strain gages #5 and #6 for damage case #2 (e_Q = 0.979810 and 0.653599). Diagnosis: crack size at location 1 $\approx$ 20.0 mm and crack size at location 2 $\approx$ 9.8 mm

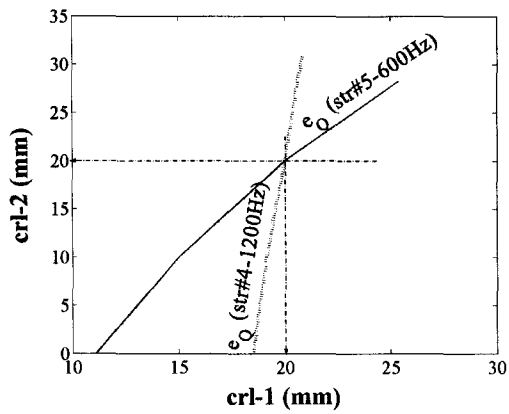

(c) e_Q plots of two different strain gages #4 and #5 for damage case #3 (e_Q = 0.813171 and 0.986866). Diagnosis: crack size at location 1 $\approx$ 20.2 mm and crack size at location 2 $\approx$ 20.0 mm

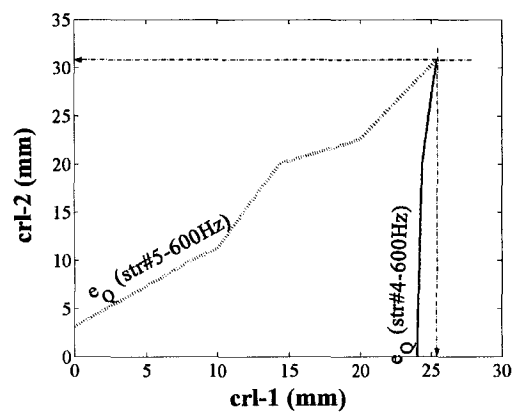

(d) e_Q plots of two different strain gages #4 and #5 for damage case #4 (e_Q = 1.048878 and 1.046320). Diagnosis: crack size at location 1 $\approx$ 25.8 mm and crack size at location 2 $\approx$ 30.2 mm

Figure 6.4: Crack identifications using equi-value of e_{ij} (e_Q) obtained from strain response for damage cases #1, #2, #3 and #4

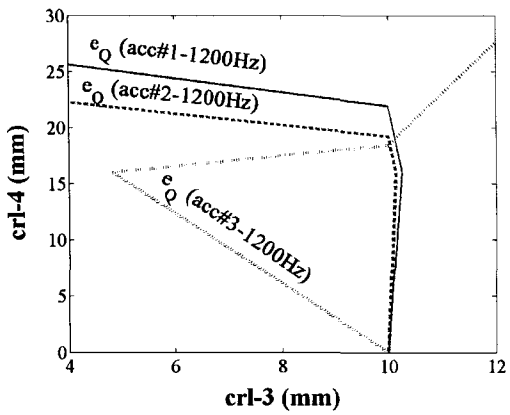

(a) e_Q plots of three different accelerometers #1, #2 and #3 for damage case #5 (e_Q = 0.577807 , 0.572178 and 0.998133). Diagnosis: crack size at location 3 $\approx$ 10.0 mm and crack size at location 4 $\approx$ 0.0 mm

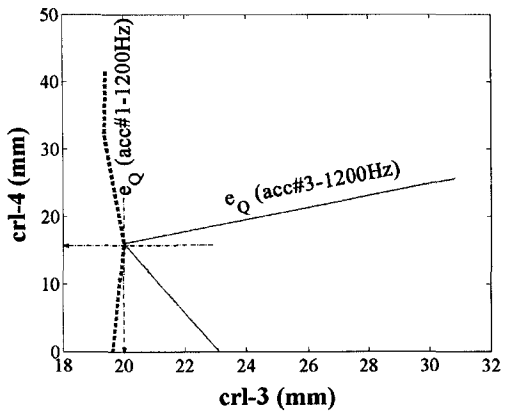

(b) e_Q plots of two different accelerometers #1 and #3 for damage case #6 (e_Q = 0.895562 and 0.986124). Diagnosis: crack size at location 3 $\approx$ 19.9 mm and crack size at location 2 $\approx$ 16.2 mm

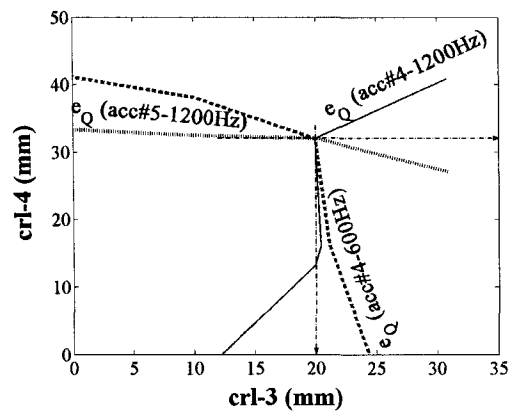

(c) e_Q plots of two different accelerometers #4 and #5 (accelerometer #4 at two frequency ranges) for damage case #7 (e_Q = 1.033909, 0.898803 and 0.794654). Diagnosis: crack size at location 3 $\approx$ 20.0 mm and crack size at location 4 $\approx$ 32.2 mm

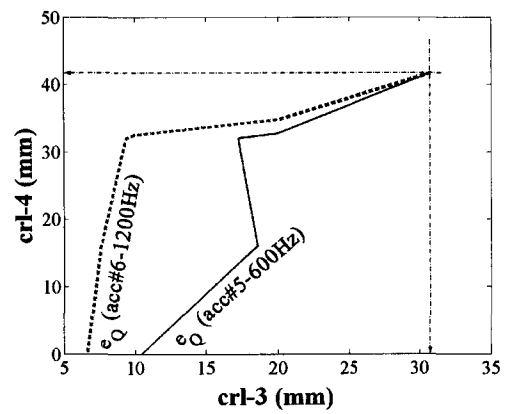

(d) e_Q plots of two different accelerometers #5 and #6 for damage case #8 (e_Q = 1.027404 and 0.994211). Diagnosis: crack size at location 3 $\approx$ 30.9 mm and crack size at location 4 $\approx$ 42.0 mm

Figure 6.5: Crack identifications using equi-value of e_{ij} (e_Q) obtained from acceleration response for damage cases #5, #6, #7 and #8

Table 6.12: Identified crack length using e_Q of acceleration and strain response and the error

(a) Damage cases #1 to #4

Damage case #	e_Q obtained from acceleration				e_Q obtained from strain			
	location 1		location 2		location 1		location 2	
1	9.8	(-2.0%)	0.0	(0.0%)	10.1	(1.0%)	0.0	(0.0%)
2	19.9	(-0.5%)	10.2	(2.0%)	20.0	(0.0%)	9.8	(-2.0%)
3	20.0	(0.0%)	20.2	(1.0%)	20.2	(1.0%)	20.0	(0.0%)
4	25.3	(-0.4%)	31.0	(0.6%)	25.8	(1.6%)	30.2	(-1.9%)

Note: values given within the brackets are the error

(b) Damage cases #5 to #8

Damage case #	e_Q obtained from acceleration			
	location 3		location 4	
5	10.0	(0.0%)	0.0	(0.0%)
6	19.9	(-0.5%)	16.2	(1.3%)
7	20.0	(0.0%)	32.2	(0.6%)
8	30.9	(0.3%)	42.0	(0.7%)

Note: values given within the brackets are the error

in Chapter 5. In this section similar procedure presented in section 6.2.1 is implemented. A damage indicator, which is akin to Equation 6.1, was used and then an algebraic function was employed to estimate the amplitude and crack sizes. The damage indicator was computed using the expression given below,

$$D_{r,k} = D_{r,k-1} + |D_{n,k} - D_{n,k-1}| \qquad k = 2,3,4 \tag{6.9}$$

where $D_{n,1}$ is taken equal to $D_{r,1}$. It can be recognized easily that Equation 6.9 is similar to Equation 6.1; only the variable is different. To extrapolate the amplitude of D_r Equation 6.2 was utilized. For cracks occurring at one location, the equation

can be written as,

$$D_{r,k} \approx \alpha_0 + \alpha_1 \sqrt{\left(\frac{c}{L}\right)} \left(\frac{a_k}{d}\right) + \alpha_2 \left(\frac{c}{L}\right) \left(\frac{a_k}{d}\right)^2 \tag{6.10}$$

where a_k is crack length d the maximum possible crack lengths at a damage location.

The scheme implemented for damage assessment in this section is similar to the damage identification scheme described section 6.2.1. In this study eight damage cases were investigated. In the first four cases cracks occurred at location 1 and cracks occurred at location 3 in last four cases, see Table 5.2. Damage indicator values obtained from Equation 6.9 for intact and the first two damage cases (cases #1a, #1b for cracks occurred at location 1 or cases #5a, #5b for cracks at location 3) were fitted to obtain the coefficients, α's. Using coefficients (α), Equation 6.10 was employed to extrapolate the damage indicator for damage case #1c for cracks occurring at location 1 or damage case #5c for cracks at location 3. To estimate the crack size for known values of the damage indicator for damage case #1c or #5c, the Equation 6.10 was solved for the crack length, a_k, using an iteration method with initial crack length value of a_{k-1}. Damage indicator value and crack size for case #1 and #5 were estimated in the same way.

Table 6.13 shows the actual and extrapolated values of the amplitude of D_r and crack sizes for damage cases #1c and #1 (crack occurred at location 1) and for damage cases #5c and #5 (crack occurred at location 3) for response of accelerometers #1 and #4. Good results are obtained. A maximum error (difference between ac-

tual and extrapolated values) of 11% was observed in this investigation. The error for numerical damage indicator ranged from -10.2% to 8.4 % whereas for experimental damage indicator the error was nearly 11 % (plus and minus). The error in estimated crack length was less than 10%. It was observed that the error was 8% maximum for numerical values while for experimental values the error ranged from -9.3% to 8%. There was no trend in error as crack length increased. In damage cases #1c to #1, the error of numerical D_r values of accelerometer #1 decreased, see Table 6.13 (a), and the error of experimental D_r values of accelerometer#1 of model #2 also decreased. However the error of experimental D_r values of accelerometer#1 of model #3 increased. Problems in choosing initial values of crack lengths were not encountered in this investigation since the crack growth was relatively small, viz. 2.5 mm.

6.4 Summary

Damage identification schemes for on-line and off-line identification of cracks occurring on orthogonally stiffened plate structure of a side shell model using the rms and the amplitude of D_n function have been presented in this chapter. A damage indicator was proposed. It was demonstrated that the schemes could identify the crack locations and sizes.

In the first scheme presented in this chapter, a damage indicator was computed from the rms of response obtained from numerical and experimental investigations. To estimate the damage indicator values as cracks increased in lengths an

algebraic function was developed and used. It was observed that the difference between the actual values and extrapolated values was a maximum of 18.6%. Crack sizes could also be estimated by employing the function along with an iteration procedure. Very good results were obtained; a maximum error of 3% was observed. However the method required that the initial (as guessed) crack values be close to the actual crack sizes. This requirement might be attributed that to relatively large crack growth used in this study.

A damage identification scheme using numerically computed rms response to obtain crack length and location was also presented. This scheme can be categorized as a nomogram technique. The scheme requires no knowledge of excitation forces applied to the model and its modal frequencies. It was shown that the scheme can be used to identify accurately the extent and the location of small cracks occurring in the longitudinal's flange and web.

The amplitude of the D_n function was examined to assess damage in the investigated model. While the modal frequencies decreased and modal damping ratios decreased and increased as the crack lengths grew, the D_n amplitudes increased consistently as a results of cracks occurred at a location. A damage indicator was computed from the amplitudes of the D_n function for different damage cases. An algebraic function computed using the damage indicator values of three different damage cases was employed to extrapolate the damage indicator values for subsequent damage cases with assumed crack sizes and locations. The algebraic function was also utilized to estimate the crack sizes for known damage indicator values. The scheme produced promising results with a maximum error of about 11%.

Table 6.13: Actual and estimated numerical and experimental D_r values of accelerometers #1 and #4 and the error

(a) Numerical values

Case #	Accelerometer #1						Accelerometer #4					
	D_r amplitude			Crack length (mm)			D_r amplitude			Crack length (mm)		
	actual	extrp.	error (%)	actual	estm.	error (%)	actual	extrp.	error (%)	actual	estm.	error (%)
1c	0.549	0.493	-10.200	7.50	7.75	3.333	0.540	0.497	-7.963	7.50	7.75	3.333
1	1.000	0.918	-8.200	10.00	10.25	2.500	1.000	0.903	-9.700	10.00	10.80	8.000
5c	0.632	0.669	5.854	7.50	7.25	-3.333	0.616	0.654	6.169	7.50	7.25	-3.333
5	1.000	1.084	8.400	10.00	9.75	-2.500	1.000	1.048	4.800	10.00	9.75	-2.500

(b) Experimental values of model #2

Case #	Accelerometer #1						Accelerometer #4					
	D_r amplitude			Crack length (mm)			D_r amplitude			Crack length (mm)		
	actual	extrp.	error (%)	actual	estm.	error (%)	actual	extrp.	error (%)	actual	estm.	error (%)
1c	0.623	0.687	10.273	7.50	7.25	-3.333	0.725	0.704	-2.965	7.50	7.75	3.333
1	1.000	1.027	2.700	10.00	9.75	-2.500	1.000	0.986	-1.360	10.00	10.25	2.500
5c	0.664	0.625	-5.873	7.50	7.70	2.667	0.886	0.911	2.901	7.50	6.80	-9.333
5	1.000	1.012	1.200	10.00	9.80	-2.000	1.000	0.968	-3.162	10.00	10.80	8.000

(c) Experimental values of model #3

Case #	Accelerometer #1						Accelerometer #4					
	D_r amplitude			Crack length (mm)			D_r amplitude			Crack length (mm)		
	actual	extrp.	error (%)	actual	estm.	error (%)	actual	extrp.	error (%)	actual	estm.	error (%)
1c	0.681	0.731	7.342	7.50	7.25	-3.333	0.821	0.828	0.777	7.50	7.25	-3.333
1	1.000	1.098	9.800	10.00	9.30	-7.000	1.000	0.928	7.190	10.00	10.25	2.500
5c	0.582	0.519	-10.825	7.50	7.75	3.333	0.841	0.873	3.889	7.50	7.25	-3.333
5	1.000	0.979	-2.100	10.00	9.70	-3.000	1.000	1.081	8.066	10.00	9.30	-7.000

extrp.: extrapolated value; estm.: estimated value using Equation 6.10

Chapter 7

Conclusions, Contributions and Recommendations for Further Investigation

7.1 Conclusions

The main objectives of this study are to study vibration response of orthogonally stiffened plate model of a tanker's side shell structure under intact and damaged conditions and to develop methodologies that would aid in the on-line identification of damage. The prototype ship considered in the investigation was 209.9 m in length, 14.3 m in depth and 27.4 m in breadth. The side shell prototype structure at the midship was 12 m long by 12 m high. The structure had two transverse web frames and fourteen longitudinals of four different types. The side shell prototype was designed using ABS (2003). By considering market availability of structural members, the feasibility of fabrication, and the facilities available in the laboratory for testing and measurement, one-twentieth aluminum models were designed and fabricated. Results of the numerical study showed that the first five modes of the model and the prototype were similar. In addition, the difference in the magnitudes

of natural frequencies of similar modes of the model and prototype was less than 22.5%.

Vibration response of the orthogonally stiffened plate models were investigated under intact and 8 (eight) different damage cases. The models were excited using random forces whose dominant frequency was far separated ($\approx$ 2 Hz) from the first natural frequency of the models ($\approx$ 580 Hz). To the author's knowledge, this is the first time a study of the dynamic response of a stiffened plate modeled structure under simulated wave forces has been attempted. Output-only modal analysis was implemented. Modal parameters were extracted using random decrement and Ibrahim time domain techniques.

Modal frequency, the root mean square (rms) of response and the amplitude of D_n functions (a function of natural frequency, damping ratio and response) obtained from numerical and experimental investigations were examined as possible indicators for damage. Damage identification schemes were developed. The schemes utilized a damage indicator computed using the rms response values. The first proposed scheme employed an algebraic function whereas the second scheme used equi-value of a damage indicator obtained using calibrated finite element simulations for determining the location and extent of cracks. Moreover a scheme using a damage indicator computed from the amplitude of D_n functions was proposed. The D_n functions were obtained utilizing a neural network technique. It was found that the D_n amplitude was sensitive to damage occurred at the horizontal. In addition, crack lengths and locations could be identified accurately using equi-value of the damage indicator obtained from numerical rms response. Based on the numer-

ical and experimental investigations the following conclusions and contributions have been made:

1. Natural frequencies change their magnitudes due to the presence of a damage in a structure. These can be used as a damage indicator. Using the magnitude of natural frequency alone as a damage indicator could lead to false conclusions since natural frequency would not always decrease as crack lengths increase. When cracks occurred at the intersection between a longitudinal and transverse bulkheads (damage cases #1 to #4), modal frequencies of the first four modes (which were torsional-flexure modes) did not change appreciably whereas modal frequency of fifth mode (first bending mode) changed significantly. When cracks occurred at the intersection between longitudinals and a transverse web frame (damage cases #5 to #8) the modal frequencies of the first four modes changed significantly whereas the frequency of the first bending mode (fifth model frequency) did not change.

2. Damping ratios cannot be used as an indicator for damage. The changes in the values of the damping ratio as a result of increasing crack lengths at one or two simultaneous crack locations did not show consistent trends.

3. In order to identify the presence of cracks, it was observed that the sensing accelerometers need not be mounted close to crack locations. Accelerometers mounted on the transverse web frame #1 (or #2) showed changes in response amplitudes as cracks occurred at the intersection between the longitudinal and the bulkhead as well as at the intersection between the longitudinals

and the transverse web frame.

4. Results of the experimental investigation showed that when a structure was excited by random forces having a dominant frequency ($\approx$ 2 Hz), that was far from the first natural frequency of the structure ($\approx$ 580 Hz), it was found necessary to have sampling rates nearly nine to ten times the magnitude of the natural frequency of interest to obtain the correct modal frequencies.

   In addition, a suitable preprocessing procedure for measured response, prior to computation of the rms of response and modal parameters, was found necessary, see section 5.4.5. A normalizing procedure was proposed to address the problem of changes in the force autospectrum of the random excitations from one measurement to the other. Since this difference in excitation force autospectra resulted in different response amplitudes, the normalizing procedure was utilized to standardize all measured response.

   Numerical and experimental investigations carried out for this thesis showed that the numerical and experimental values (natural frequency, the rms of response and D_n amplitude) had similar trends due to increasing crack lengths although these values did not change to the same extent.

5. It was demonstrated that the amplitude of the D_n function is an effective damage indicator, especially for cracks occurring at one location. While natural frequencies did not decrease as a result of cracks (damage cases #1 to #4 for mode 1) and the damping ratios showed no trend, the amplitude of the D_n function showed consistent changes due to the increase of even small

crack lengths. For small cracks occurring at one location, the amplitude of the D_n function increased significantly and consistently. Therefore the amplitude of the D_n function could be used for identifying damage at the horizontal at early stage.

6. The use of an algebraic function for identifying cracks using the damage indicator e_i, obtained from the rms response values was proposed in this study. It was observed that for the various damage cases investigated, the difference between the actual values and extrapolated values were less than 18.5%. Crack sizes could also be estimated by employing the function along with an iteration procedure. Excellent results were obtained. A maximum error of 3% was observed. However the method required that the initial (as guessed) crack values be close to the actual crack lengths. This requirement might be attributed to the relatively large crack growth interval used in this study.

   The algebraic function was also utilized to estimate a damage indicator computed from the amplitudes of the D_n function for different damage cases. The function was also used to estimate the crack sizes for known damage indicator amplitude. The scheme produced promising results with a maximum error of about 11%.

7. A nomogram-based damage identification scheme using the rms response obtained from finite element simulations was also developed. The scheme requires no prior knowledge of the excitation forces applied to the model and its modal frequencies. In this thesis, it was demonstrated that the scheme can

be used to identify accurately the extent and the location of cracks.

Results of a preliminary investigation on the sensitivity of the identified crack lengths using the scheme showed that by introducing a 2.5% difference on crack length the difference in identified damage indicator was nearly 5%.

7.2 Recommendations for Further Investigation

Investigations reported for this thesis were carried out to examine response of orthogonally stiffened plate models of a side shell of tanker ship structure in air under intact and damaged conditions. To obtain better understanding of the structure's response under different damaged and operation conditions it is necessary to carry out more advanced studies.

- Investigating the effects of local cracking on a prototype or modeled ship structure utilizing its response. The research would involve: (i) finite element modeling of ship; (ii) effects of damage at one or more specific location(s) on the overall ship response; (iii) effects of different ship's draft on the response and other types of excitations; and (iv) conducting experimental studies of a scaled model of a tanker ship structure.

- Identifying damage on-line, in a scaled model or prototype of tanker ship structure, during simulated or real operational conditions so that the effect of cracks on the response of a ship can be investigated.

- Investigating the use of the D_n amplitude obtained from response containing two or more modal frequencies with more than one crack location.

References

ABAQUS User's Manual ver. 6.4 , 2004, Hibbitt, Karlsson and Sorensen, Inc.

American Bureau of Shipping, *Rules for Building Classing Steel Vessels*, 2003.

Andrade, F.A., Esat, I. and Badi, M.N., 2001, "A New Approach to Time-domain Vibration Condition Monitoring: Gear Tooth Fatigue Crack Detection and Identification by the Kolmogorov-Smirnov Test," *Journal of Sound and Vibration*, Vol. 240, pp. 909-919.

Asmussen, J.C., Ibrahim, S.R. and Brincker, R., 1996, "Random Decrement and Regression Analysis of Traffic Responses of Bridges," *Proceedings of the 14th International Modal Analysis Conference*, Dearborn, Michigan, pp. 453-458.

Asmussen, J.C., Ibrahim, S.R. and Brincker, R., 1997, "Application of Vector Triggering Random Decrement," *Proceedings of the 15th International Modal Analysis Conference*, pp. 1165-1171.

Atalla, M.J. and Inman, D.J., 1998, "On Model Updating Using Neural Networks," *Mechanical Systems and Signal Processing*, Vol.12, No. 1, pp. 135-161.

Barai, S.V. and Pandey, P.C. , 1995, "Vibration Signature Analysis Using Artificial Neural Networks," ASCE *Journal Computing in Civil Engineering*, Vol. 9, No. 4, pp. 159-265.

Barai, S.V. and Pandey, P.C. , 1997, " Time Delay Neural Networks in Damage Detection of Railway Bridges," *Advances in Engineering Software*, Vol. 28, No.1, pp 1-10.

Bendat, J.S. and Piersol, A.G., 2000, *Random Data Analysis and Measurement Procedures*, 3rd ed., John Wiley and Sons, ISBN 0-471-31733-0.

Bishop, C.M., 1995, *Neural Networks for Pattern Recognition*, Oxford University Press, ISBN 0-19-853849-9.

Bodeux, J.B. and Golinval, J.C., 2003, "Modal Identification and Damage Detection Using the Data-driven Stochastic Subspace and ARMAV Methods , " *Mechanical Systems and Signal Processing*, Vol. 17, No. 1, pp. 83-89.

Bolton, R. Stubbs, N., Sikorsky, C. and Choi, S., 2001, "A Comparison of Modal Properties Derived from Forced and Output-Only Measurements for a Reinforced

Concrete Highway Bridge," *Proceedings of the 19th International Modal Analysis Conference*, Kissimmee, Florida, pp. 857-863.

Bolton, R., Stubb, N. and Sikorsky, C., 2002, "Automation of Modal Property Extraction for A Permanently Instrumented Highway Bridge," *Proceedings of the 20th International Modal Analysis Conference*, Los Angeles, California, pp. 1217-1223.

Box, G.E.P., Jenkins, G. M. and Reinsel, Gregory C. (1994) *Time Series Analysis : Forecasting and Control*, 3rd ed., Prentice Hall, ISBN 0-13-060774-6.

Brincker, R., Krenk, S., and Jensen, J.L., 1991, "Estimation of Correlation Functions by The Random Decrement Technique," *Proceedings of the 9th International Modal Analysis Conference*, pp. 610-615.

Budipriyanto, A., 1993, "Modal Analysis and Testing of Uncracked and Cracked Plates in Air and in Water," Master of Engineering thesis, Memorial University, St. John's, NL, 301 p.

Budipriyanto, A. and Swamidas, A.S.J., 1994, "Experimental and Analytical Verification of Modal Behavior of Uncracked / Cracked Plates in Air and Water," *Proceedings of the 12th International Modal Analysis Conference*, Honolulu, Hawaii, pp. 745-752.

Budipriyanto, A., Haddara, M.R. and Swamidas, A.S.J., 2004a, "Analysis and Testing of Orthogonally Stiffened Plate Panels for Crack Identification," *Proceeding of The 58th Meeting of the Society for Machinery Failure Prevention Technology*, Virginia Beach, April 25-30, pp. 223-232.

Budipriyanto, A., Swamidas, A.S.J. and Haddara, M.R., 2004b, "Crack Identification on a Cross-stiffened Plate Panel," *Proceeding of 23rd International Conference on Offshore Mechanics and Arctic Engineering*, Vancouver, OMAE2004-51109, pp. 1-7.

Budipriyanto, A., Swamidas, A.S.J. and Haddara, M.R., 2005a, "A Time and Frequency Domain On-line Crack Identification of Stiffened Plate Panels," *Proceeding of The 59th Meeting of the Society for Machinery Failure Prevention Technology*, Virginia Beach, Virginia, April 18-21, pp. 231-240.

Budipriyanto, A., Swamidas, A.S.J. and Haddara, M.R., 2006a, "Identification of Small-sized Cracks on Cross-stiffened Plate Structures for Ships," Accepted for publication in ASME *Journal of Engineering Materials and Technology* (January 2006).

Budipriyanto, A., Haddara, M.R. and Swamidas, A.S.J., 2006b, "Crack Identification in Cross Stiffened Plate System Using the Root Mean Square of Time Domain Response," Accepted for publication in *Canadian Journal of Civil Engineering*, CSCE (February 2006).

Budipriyanto, A., Haddara, M.R. and Swamidas, A.S.J., 2006c, "Identification of Damage on Ship's Cross Stiffened Plate Panels Using Vibration Responses," Submitted for publication to *Journal of Ocean Engineering*.

Cattarius, J. and Inman, D.J., 1997, "Time Domain Analysis for Damage Detection in Smart Structures," *Mechanical Systems and Signal Processing*, Vol. 11, pp. 409-423.

Choi, S. and Stubbs, N., 2004, "Damage Identification in Structures Using the Time-domain Response," *Journal of Sound Vibration*, Vol. 275, pp. 577-590.

Cole, H.A., Jr., 1973, "On-line Failure Detection and Damping Measurement of Aerospace Structures by Random Decrement Signatures," *NASA CR-2205*, 75 p.

Cramer, E.H., Loseth, R. and Bitner-Gregersen, E., 1993, "Fatigue in Side Shell Longitudinals due to External Wave Pressure", in Safety and Reliability *Proceedings of The International Conference on Offshore Mechanics and Arctic Engineering*, Vol. 2, pp. 267-272.

De Kat, J.O., Lemmen, P. , Moore, C.S. and Vredeveldt, A.W., 1995, "Dynamic Loading and Strength of a Stranded Double Hull Tanker in Waves," *Proceeding of the 5th International Offshore and Polar Engineering Conference*, Vol. 4, pp. 465-470.

Dexter, R.J., and Gentilcore, M., L., 1997, *Evaluation of Ductile Fracture Models for Ship Structural Details*, Ship Structure Committee, SSC-393, 293 p.

Doebling, S. W., Farrar, C.R., Prime, M.B. and Shevitz, D.W., 1996, "Damage Identification and Health Monitoring of Structural and Mechanical Systems from Changes in Their Vibration Characteristics: A Literature Review," *Technical Report LA-13070-MS*, Los Alamos National Laboratory, Los Alamos, NM, 127 p.

Ewins, D.J., 2000, *Modal Testing: Theory and Practice*, 2nd ed., John Wiley and Sons, ISBN 0-86380-218-4.

Farrar, C. and Jauregui, D., 1996, "Damage Detection Algorithms Applied to Experimental and Numerical Modal Data from I-40 Bridge," *Technical Report LA-13074-MS*, Los Alamos National Laboratory, Los Alamos, NM, 135 p.

Haddara, M.R., 1971, "On the Stability of Ship Motion in Regular Oblique Waves," *International Ship Building Progress*, Vol. 18, No. 207, pp. 416-434.

Haddara, M.R., 1992, "On the Random Decrement for Nolinear Rolling Motion," *Proceeding of the 12th International Conference on Offshore Mechanics and Arctic Engineering*, Calgary, Canada, pp. 283-288.

Haddara, M.R. and Hinchey, M., 1995, "On the Use of Neural Network Techniques in the Analysis of Free Roll Decay Curves," *International Ship Building Progress*, Vol. 42, No. 430, pp. 166-178.

Harris, H.G. and Sabnis, G. M., 1999, *Structural Modeling and Experimental Techniques*, 2nd ed., CRC Press, ISBN 0-8493-2469-6.

Hughes, O.F., 1988, *Ship Structural Design*, The Society of Naval Architects and Marine Engineers, N.J., ISBN 0-939773-04X.

Ibrahim, S.R., 1986, "Incipient Failure Detection from Random Decrement Time Functions," *The International Journal of Analytical and Experimental Modal Analysis*, Vol. 1, No. 2, pp. 1-9.

Ibrahim, S.R., 1987, "An Upper Hessenberg Sparse Matrix Algorithm for Modal Identification on Minicomputers," *Journal of Sound and Vibration*, Vol. 113, No. 1, pp. 47-57.

Ibrahim, S.R., Asmussen, J.C., Brincker, R., 1998, "Vector Random Decrement Technique for High Identification Accuracy," ASME *Journal of Vibration and Acoustics*, Vol. 120, pp. 970-975.

Ibrahim, S.R., 2001, "Efficient Random Decrement Computation for Identification of Ambient Responses," *Proceedings of the 19th International Modal Analysis Conference*, pp. 1-6.

Kharrazi, M.H.K. , Ventura, C.E., Brincker, R. and Dascotte, E., 2002, "A Study on Damage Detection Using Output-Only Modal Data," *Proceeding of the 20th International Modal Analysis Conference*, Los Angeles, California, pp. 1199-1205.

Kiddy, J., Baldwin, C., Salter, T., and Chen, P., 2002, "Structural Load Monitoring of RV Triton Using Fiber Optic Sensors," *Proceedings of Smart Structures and Materials: Industrial and Commercial Applications of Smart Structures Technologies*, SPIE Vol. 4698, pp. 462-472.

Kullaa, J., 2003, "Damage Detection of the Z24 Bridge Using Control Charts," *Mechanical Systems and Signal Processing*, Vol. 17, pp. 163-170.

LabVIEW, 1998, National Instrument.

Lee, J.W., Kim, J.D., Yun, C.B., Yi, J.H. and Shim, J.M., 2002, "Health Monitoring Method for Bridges Under Ordinary Traffic Loading," *Journal of Sound and Vibration*, Vol. 257, No. 2, pp. 247-264.

Lee, W.Y., Park C. and Kelly, G.E., 1996a, "Fault Detection in Air-Handling Unit Using Residual and Recursive Parameter Identification Methods," *ASHRE Transactions*, Vol 102, No. 1, pp. 1-12.

Lee, W.Y., House, J.,M., Park C. and Kelly, G.E.,1996b, "Fault Diagnosis in Air-Handling Unit Using Artificial Neural Networks," *ASHRE Transactions*, Vol 102, No. 1, pp. 540-549.

Lim, T.W., Cabell, R.H. and Silcox, R.J., 1996, "On-Line Identification of Modal Parameters Using Artificial Neural Networks," ASME *Journal of Vibration and Acoustics*, Vol. 118, pp. 649-656.

Liu, D. and Thayamballi, A. K., 1997, "Local Cracking in Ships - Causes, Consequences, and Control," *Symposium and Workshop on The Prevention of Fracture in Ship structure*, Ship Structure Committee, pp. 125-166.

Lopes, V., Turra, A.E., Muller-Slany, H.H., Brunzel, F. and Inman, D.J., 2002, "Structural Health Evaluation by Optimization Technique and Artificial Neural Network," *Proceeding of the 20th International Modal Analysis Conference*, pp. 484-490.

Mangal, L., Idichandy, V. G. and Ganapathy, C., 1996, "ART-Based Multiple Neural Networks for Monitoring Offshore Platforms," *Applied Ocean Research*, Vol. 18, No. 3, pp. 137-143.

MATLAB, 1997, Users Guide, The Mathworks Inc.

Mevel, L. and Goursat, M., 2003, "Stochastic Subspace-based Structural Identification and Damage Detection and Localization - Application to the Z24 Bridge Benchmark," *Mechanical Systems and Signal Processing*, Vol. 17, No. 1, pp. 143-151.

Parloo, E., Verboven, P., Guillaume, P., and Van Overmeire, M., 2002, "Autonomous Structural Health Monitoring - Part II : Vibration-Based In-Operation Damage Assesments," *Mechanical Systems and Signal Processing*, Vol. 16, No. 4, pp. 659-675.

Peeters, B. and Ventura, C.E., 2002, "Comparative Study of Modal Analysis Techniques for Bridge Dynamic Characteristics," *Mechanical Systems and Signal Processing*, Vol. 17, No. 5, pp. 965-988.

Pridham, B.A. and Wilson, J.C., 2002, " Subspace Identification of Vincent Thomas Suspension Bridge Ambient Vibration Data," *Proceeding of the 20th International Modal Analysis Conference*, Los Angeles, California, pp. 134-140.

Ramsagar, P.K. and Pardue, S.J., 2001, "Damage Detection Method Using Autocorrelation," *Proceeding of the 19th International Modal Analysis Conference*, Kissimmee, Florida, pp. 1622-1627.

Reynolds, P. and Pavic, A., 2001, "Comparison of Forced and Ambient Vibration Measurements on A Bridge," *Proceedings of the 19th International Modal Analysis Conference*, Kissimmee, Florida, pp. 846-851.

Rim, J. and Lee, S.W., 1995, "A Neural Network Approach for Damage Detection and Identification of Structures," *Computational Mechanics*, Vol. 16, No. 6, pp. 437-443.

Samman, M.M., 2001, "A Hybrid Analysis Method for Vibration Signals Based on Neural Networks and Pattern Recognition Techniques," ASME *Journal of Vibration and Acoustics*, Vol. 123, pp. 122-124.

Seibold, S., and Weinert, K., 1996, "A Time Domain Method for the Localization of Cracks on Rotors," *Journal of Sound and Vibration*, Vol. 195, pp. 57-73.

Schulte-Strathhaus, R., 1991, "Fatigue Database Development and Analysis," *Report No. SMP-I-1*, Department of Naval Architecture and Offshore Engineering, University of California, Berkeley, 71p.

Sohn, H., and Farrar, C. R., 2001, "Damage Diagnosis Using Time Series Analysis of Vibration Signals," *Smart Materials and Structures*, Vol. 10, pp 1-6.

Sohn, H., Farrar, C. R., Hunter, N.F. and Worden, K., 2001, "Structural Health Monitoring Using Statistical Pattern Recognition Techniques," ASME *Journal of Dynamic Systems, Measurement and Control*, Vol. 123, pp 706-711.

Sorensen, R.M., 1997, *Basic Coastal Engineering*, 2nd Ed., Chapman and Hall, New York, ISBN 0-41-212341-X.

Spanos, P.D., and Zeldin, B.A., 1998, "Generalized Random Decrement Method for Analysis of Vibration Data," ASME *Journal of Vibration and Acoustics*, Vol 120, pp. 806-813.

Sucharski, D., 1995, "Crude Oil Tanker Hull Structure Fracturing: An Operator Perspective," *Prevention of fracture in Ship Structure*, Washington D.C., pp. 87-124.

Taggart, R. (ed), 1980, *Ship Design and Construction*, The Society of Naval Architects and Marine Engineers, N.Y., ISBN 0-9603048-0-0.

Tsai, C. and Hsu, D., 2002, "Diagnosis of Reinforced Concrete Structural Damage Base on Displacement Time History using the Back-Propagation Neural Network Technique," ASCE *Journal of Computing in Civil Engineering*, Vol. 16, No.1, pp. 49-58.

Vandiver, J.K., Dunwoody, A.B. Campbell, R.B. and Cook, M.F., 1982, "A Mathematical Basis for the Random Decrement Vibration Signature Analysis Technique," ASME *Journal of Mechanical Design*, Vol. 104, pp. 307-313.

Verboven, P., Parloo, E., Guillaume, P., and Van Overmeire, M., 2002, "Autonomous Structural Health Monitoring - Part I : Modal Parameter Estimation and Tracking," *Mechanical Systems and Signal Processing*, Vol. 16, No. 4, pp. 637-657.

Wang, G., Pran, K., Sagvolden, G., Havsgard, G.B., Jensen, A.E., Johnson, G.A. and Vohra, S.T., 2001, "Ship Hull Monitoring Using Fibre Optic Sensors," *Smart Material and Structures*, Vol. 10, pp. 472-478.

Worden, W., Manson, G. and Fieller, N.J., 2000, "Damage Detection Using Outlier Analysis," *Journal of Sound and Vibration*, Vol. 229, No. 3, pp. 647-667.

Yam, L.H., Yan, Y.J., Cheng, L., and Jiang, J.S., 2003, "Identification of Complex Crack Damage for Honeycomb Sandwich Plate Using Wavelet Analysis and Neural Networks," *Smart Materials and Structures*, Vol. 12, pp. 661-671.

Zhang, C. and Imregun, M., 2001a, "Structural Damage Detection Using Artificial Neural Networks and Measured FRF Data Reduced via Principal Component Projection," *Journal of Sound and Vibration*, Vol. 242, No. 5, pp. 813 - 827.

Zhang, C. and Imregun, M., 2001b, "Combined Neural Network and Reduced FRF Techniques for Slight Damage Detection Using Measured Response Data," *Archives of Applied Mechanics*, Vol. 71, pp. 525 - 536.

Zhang, C., Friswell, M.I. and Imregun, M., 2004, "Structural Damage Detection Using Independent Component Analysis," *Structural Health Monitoring*, Vol. 3, No. 1, pp. 69-83.

Zubaydi, A., Haddara, M.R. and Swamidas, A.S.J., 2000a, "Damage Identification in Stiffened Plates Using the Random Decrement Technique," *Oceanic Engineering International*, No. 4, pp. 22-30.

Zubaydi, A., Haddara, M.R. and Swamidas, A.S.J., 2000b, "On the Use of the Autocorrelation Function to Identify the Damage in the Side Shell of a Ship's Hull," *Marine Structures*, Vol. 13, pp. 537-551.

Zubaydi, A., Haddara, M.R. and Swamidas, A.S.J., 2002, "Damage Identification in a Ship's Structure Using Neural Networks," *Ocean Engineering*, Vol. 29, No. 10, pp. 1187-1200.

Appendix A

Displacement Shape Changes due to Cracks

Numerical investigations using finite element method were carried out to obtain displacement shapes of the modeled structure under intact and damaged conditions. Displacement shapes of longitudinal #2 and transverse web frame #1 are presented in this appendix. Displacement shapes of the longitudinal in y- and z- axis directions are shown in Figures A.1 to A.2 for damage cases #1 to #4 and in Figures A.3 to A.4 for damage cases #5 to #8. Displacement shapes of transverse web frame #1 in the x- and z- axis directions are presented in Figures A.5 to A.6 and A.7 to A.8 for damage cases #1 to #4 and damage cases #5 to #8 respectively. From these figures, it can be seen that the longitudinal acceleration response changes in the y- axis direction are more significant than the changes in the z- axis direction for all cases, see Figures B.1 to B.4. The changes in the x- and z- axis directions of the web frame #1 for cases #1 to #4 are small for the first two modes, see Figures B.5 and B.6. Responses of the fifth mode show greater changes in the x- axis direction than that in the z- axis direction. For cases #5 to # 8, the acceleration response showed consistent and highly noticeable changes in the x- axis direction

for all modes considered in this investigation for the longitudinal (horizontal stiffener) #2 and the transverse web frame #1, see Figures B.7 and B.8 for the response of transverse web frame #1. The response for transverse web frame #2 show that significant changes occurred in mode 1 in the x- and z- axis directions. However response changes in the x- axis direction was greater than those in the z- axis direction, see Figures B.11 and B.12.

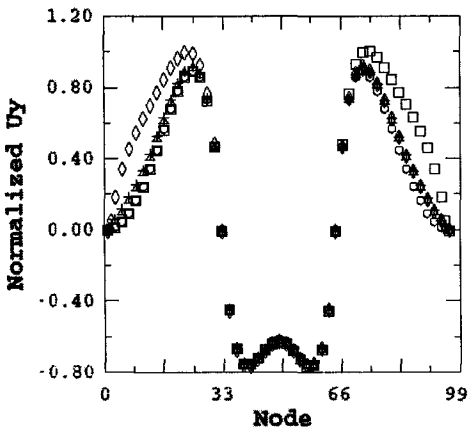

(a) Mode 1

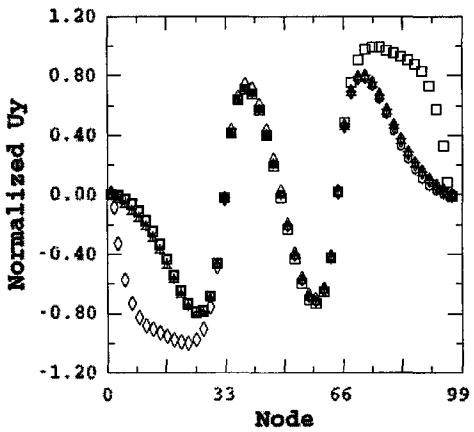

(b) Mode 2

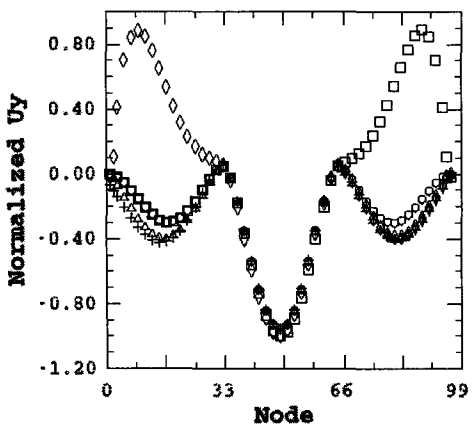

(c) Mode 5

Figure A.1: Displacement shapes of longitudinal #2 in the y- direction for damage cases #1 to #4: O: intact, □: case #1, ◇: case #2, △: case #3, +: case #4

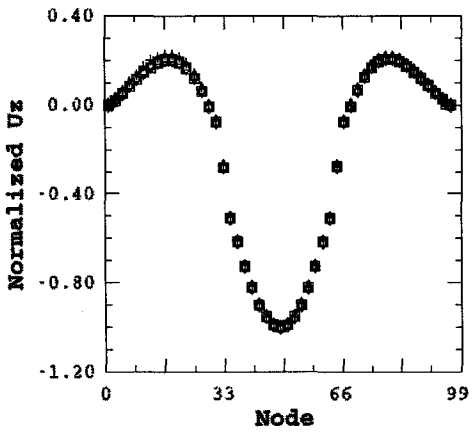

(a) Mode 1

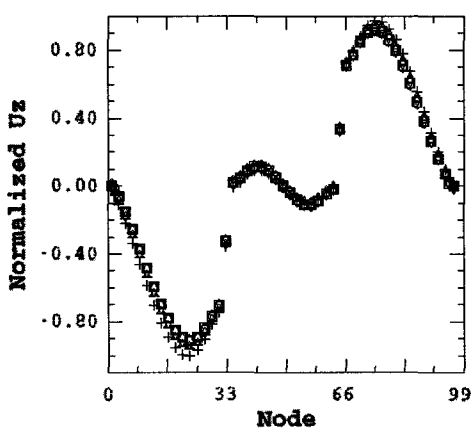

(b) Mode 2

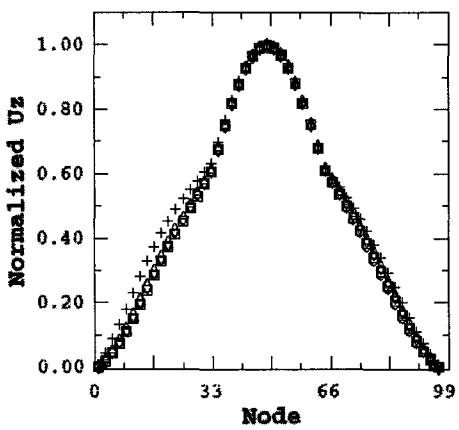

(c) Mode 5

Figure A.2: Displacement shapes of longitudinal #2 in the z- direction for damage cases #1 to #4: O: intact, □: case #1, ◇: case #2, △: case #3, +: case #4

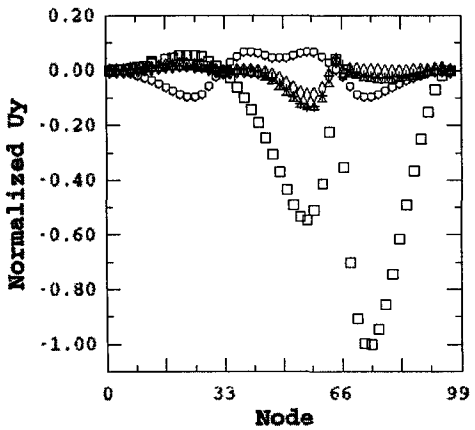

(a) Mode 1

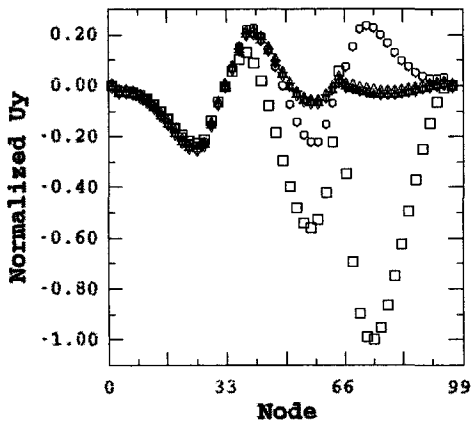

(b) Mode 2

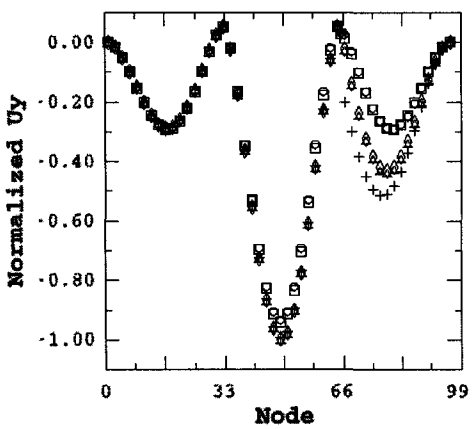

(c) Mode 5

Figure A.3: Displacement shapes of longitudinal #2 in the y- direction for damage cases #5 to #8: O: intact, □: case #5, ◇: case #6, △: case #7, +: case #8

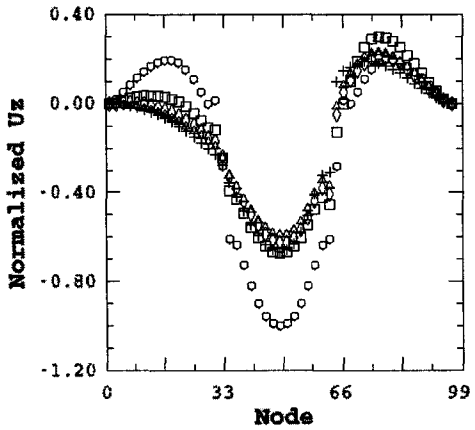

(a) Mode 1

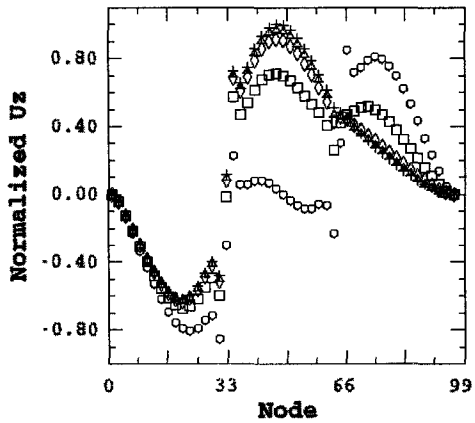

(b) Mode 2

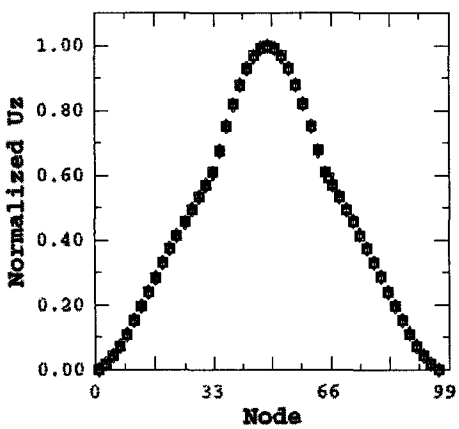

(c) Mode 5

Figure A.4: Displacement shapes of longitudinal #2 in the z- direction for damage cases #5 to #8: O: intact, □: case #5, ◇: case #6, △: case #7, +: case #8

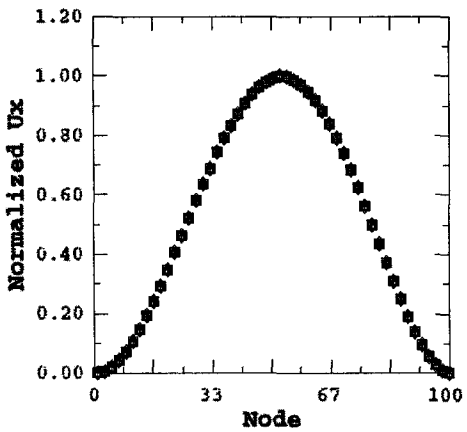

(a) Mode 1

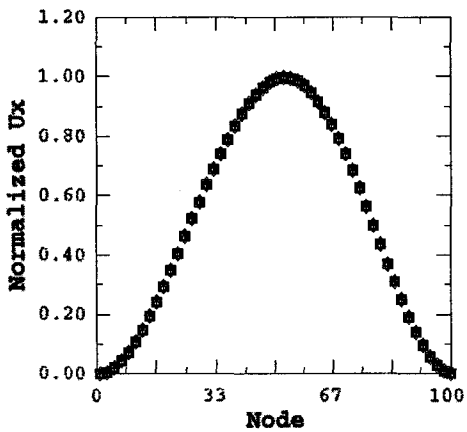

(b) Mode 2

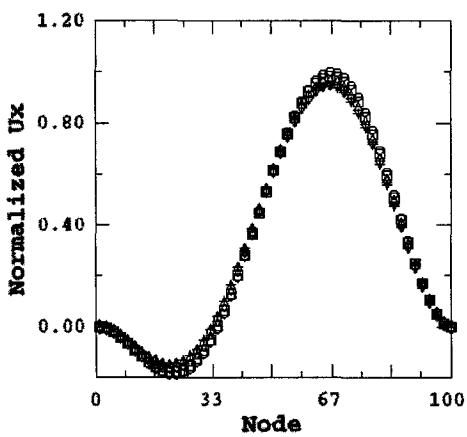

(c) Mode 5

Figure A.5: Displacement shapes of transverse web frame #1 in the x- direction for damage cases #1 to #4: O: intact, □: case #1, ◇: case #2, △: case #3, +: case #4

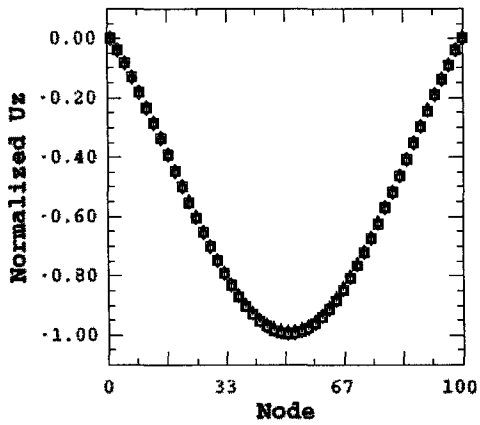

(a) Mode 1

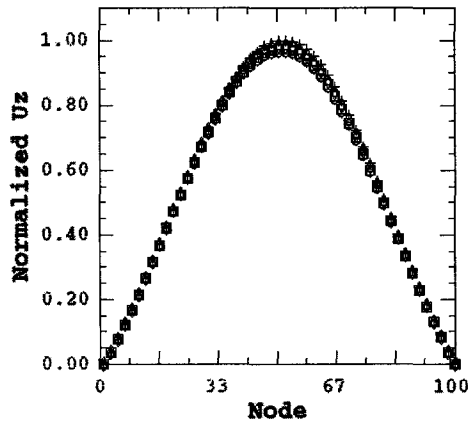

(b) Mode 2

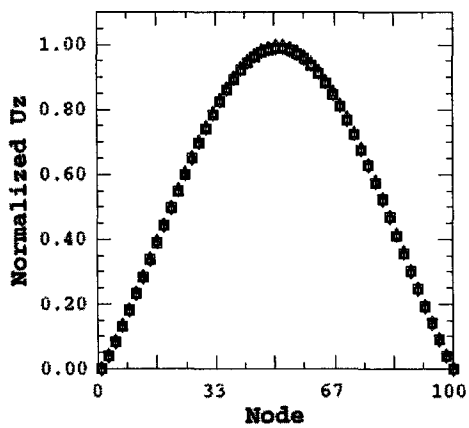

(c) Mode 5

Figure A.6: Displacement shapes of transverse web frame #1 in the z- direction for damage cases #1 to #4: O: intact, □: case #1, ◇: case #2, △: case #3, +: case #4

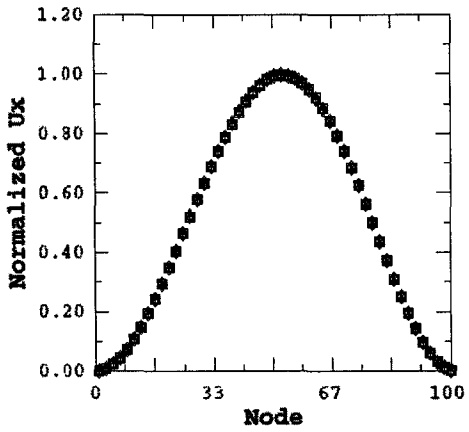

(a) Mode 1

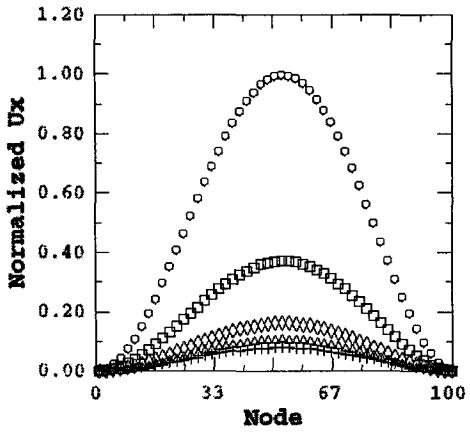

(b) Mode 2

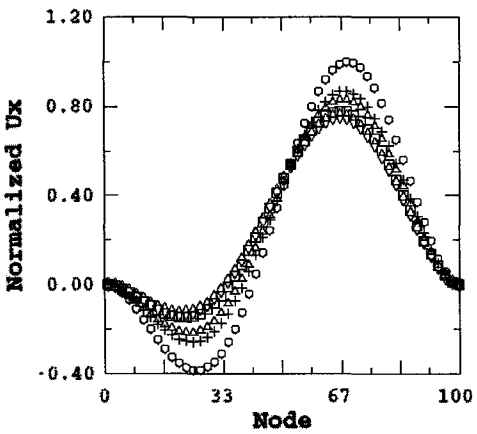

(c) Mode 5

Figure A.7: Displacement shapes of transverse web frame #1 in the x- direction for damage cases #5 to #8: O: intact, □: case #5, ◇: case #6, △: case #7, +: case #8

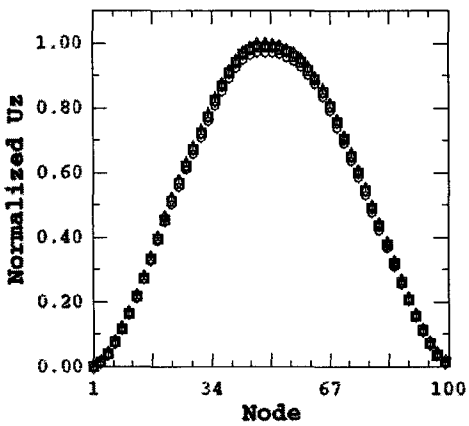

(a) Mode 1

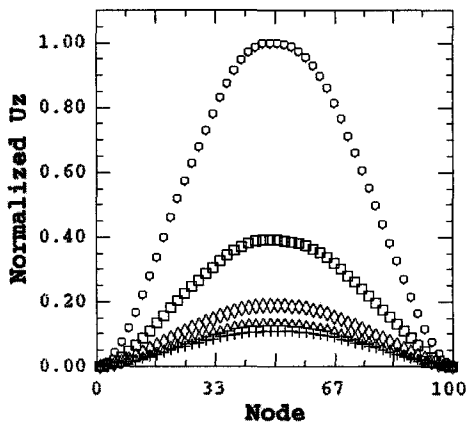

(b) Mode 2

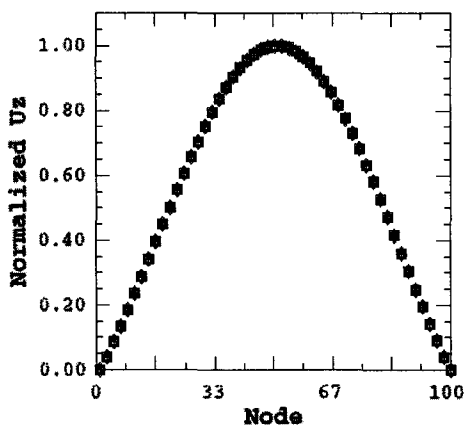

(c) Mode 5

Figure A.8: Displacement shapes of transverse web frame #1 in the z- direction for damage cases #5 to #8: O: intact, □: case #5, ◊: case #6, △: case #7, +: case #8

Appendix B

Numerical Acceleration and Strain Response

Numerical investigations on the modeled structure were carried out to examine the acceleration and strain response of horizontals #2 and #3 and transverse web frames #1 and #2. The results of these investigations were utilized to determine the excitation point, acceleration and strain gage locations. The acceleration and strain response were normalized using the largest response under intact and damaged conditions for different nodes. Figures B.1 to B.4 show normalized acceleration response of horizontal #2 in the y- and z- axis directions for damage cases #1 to #8. Figures B.5 to B.8 and B.9 to B.12 show the response of transverse web frame #1 and #2 respectively in x- and z- axis direction for damage cases #1 to #8. Figures B.13 to B.16 show the normalized strain response of side shell plate along longitudinals #2 and #3 in the x- axis direction for damage cases #1 to #8.

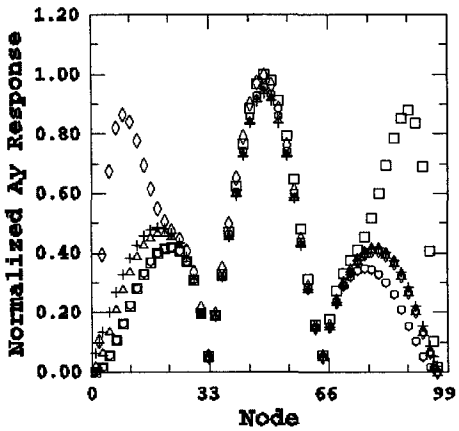

(a) Mode 1

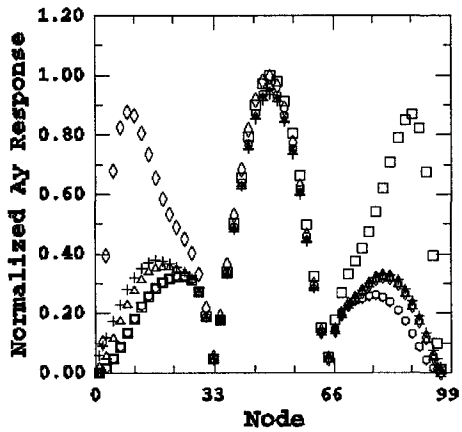

(b) Mode 2

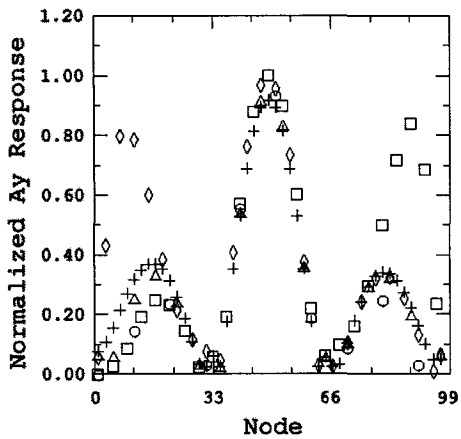

(c) Mode 5

Figure B.1: Normalized acceleration response of longitudinal #2 in the y- direction for damage cases #1 to #4: O: intact, □: case #1, ◇: case #2, △: case #3, +: case #4

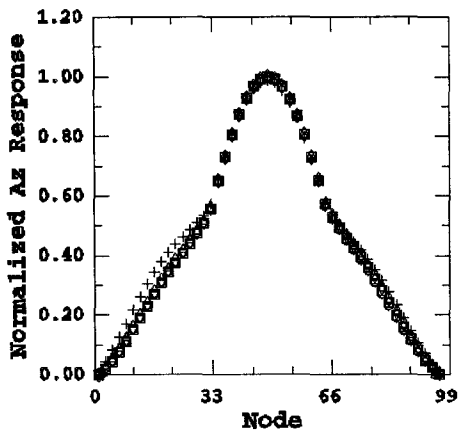

(a) Mode 1

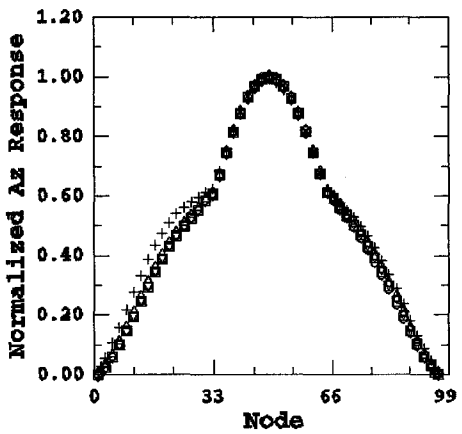

(b) Mode 2

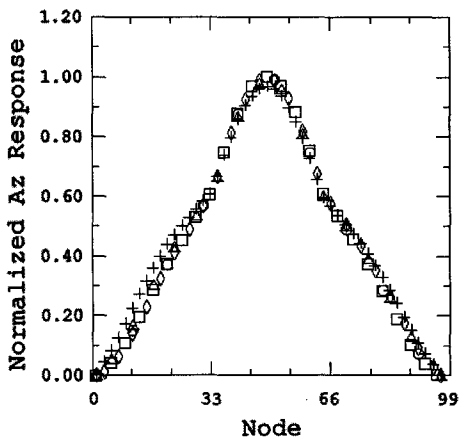

(c) Mode 5

Figure B.2: Normalized acceleration response of longitudinal #2 in the z- direction for damage cases #1 to #4: O: intact, □: case #1, ◇: case #2, △: case #3, +: case #4

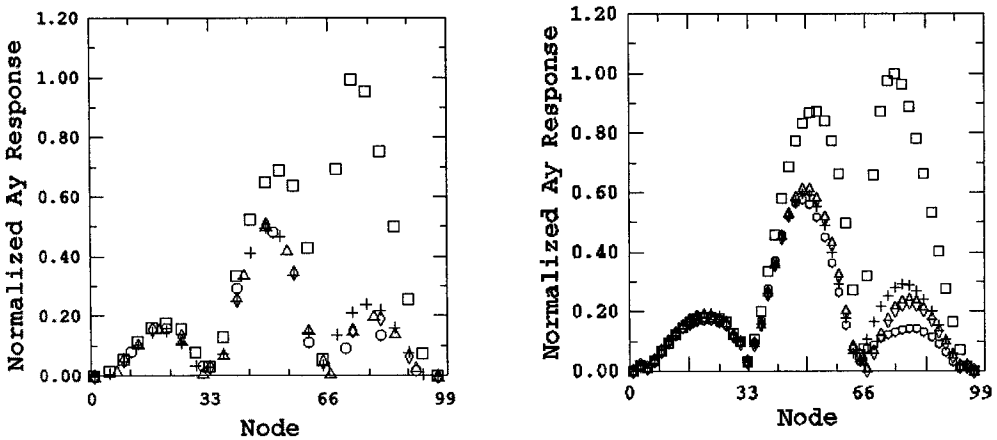

(a) Mode 1

(b) Mode 2

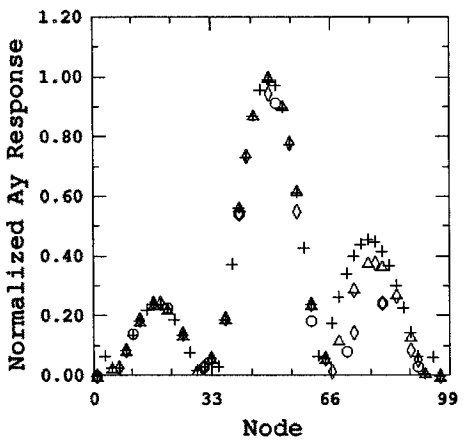

(c) Mode 5

Figure B.3: Normalized acceleration response of longitudinal #2 in the y- direction for damage cases #5 to #8: O: intact, □: case #5, ◇: case #6, △: case #7, +: case #8

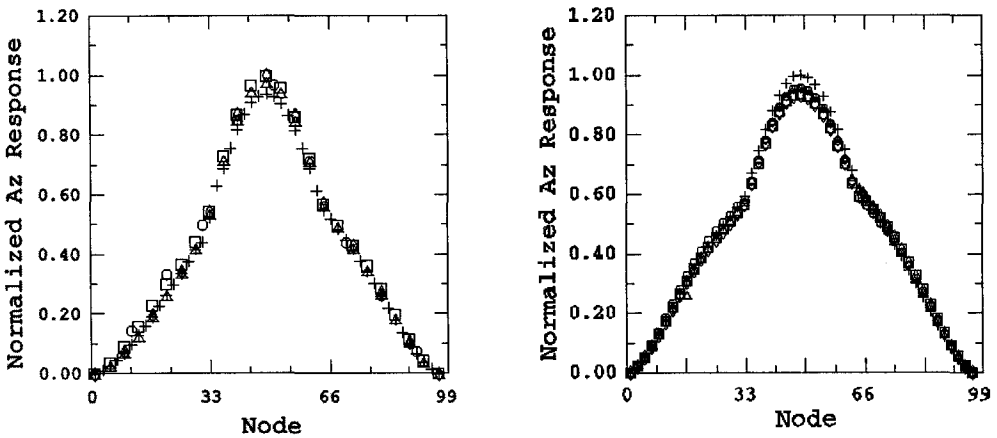

(a) Mode 1

(b) Mode 2

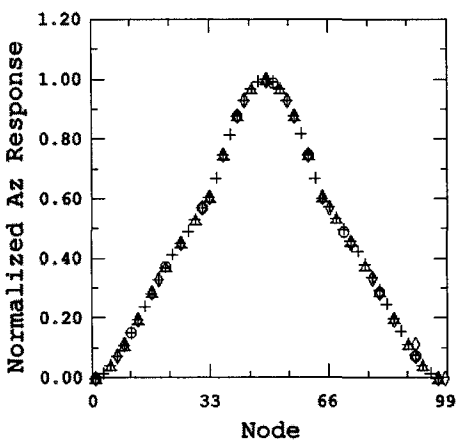

(c) Mode 5

Figure B.4: Normalized acceleration response of longitudinal #2 in the z- direction for damage cases #5 to #8: O: intact, □: case #5, ◇: case #6, △: case #7, +: case #8

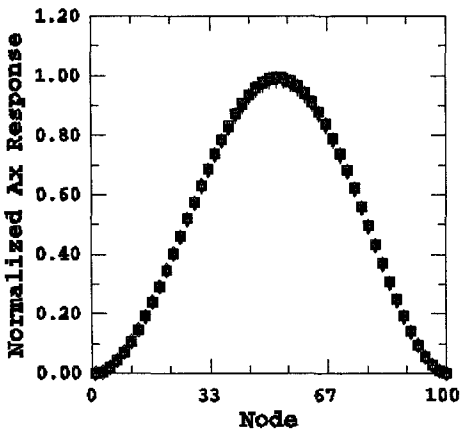

(a) Mode 1

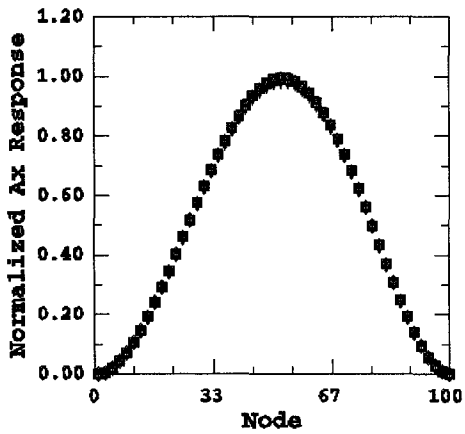

(b) Mode 2

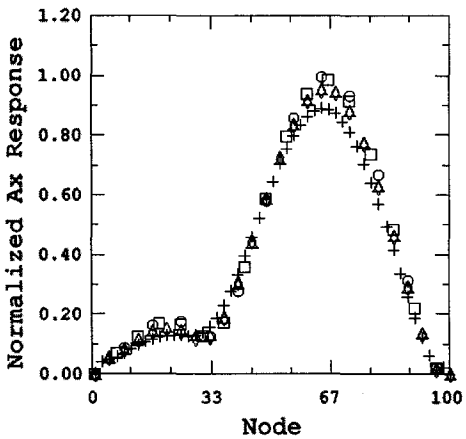

(c) Mode 5

Figure B.5: Normalized acceleration response of transverse web frame #1 in the x-direction for damage cases #1 to #4: O: intact, □: case #1, ◇: case #2, △: case #3, +: case #4

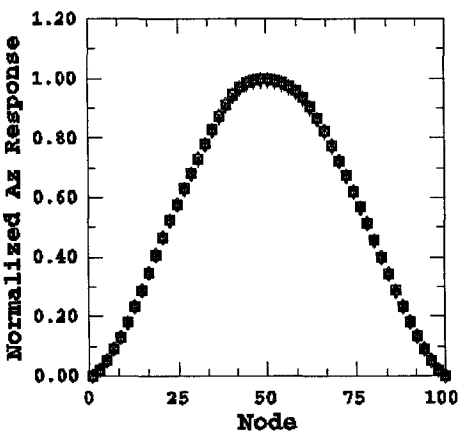

(a) Mode 1

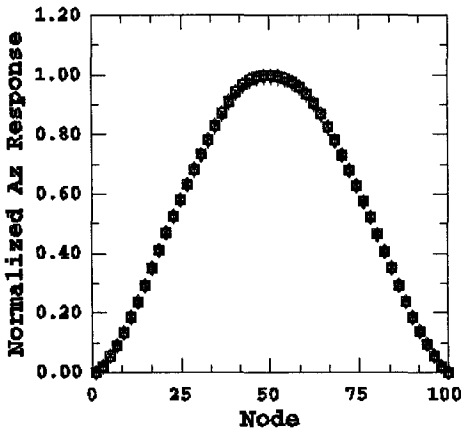

(b) Mode 2

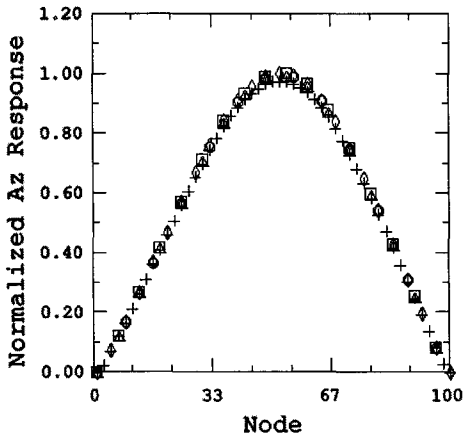

(c) Mode 5

Figure B.6: Normalized acceleration response of transverse web frame #1 in the z-direction for damage cases #1 to #4: O: intact, □: case #1, ◇: case #2, △: case #3, +: case #4

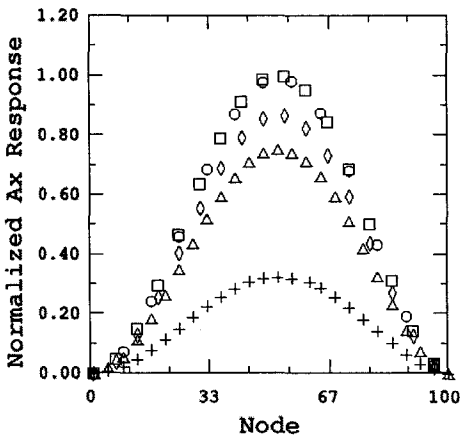

(a) Mode 1

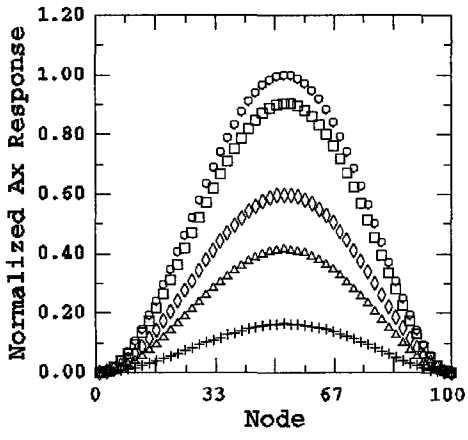

(b) Mode 2

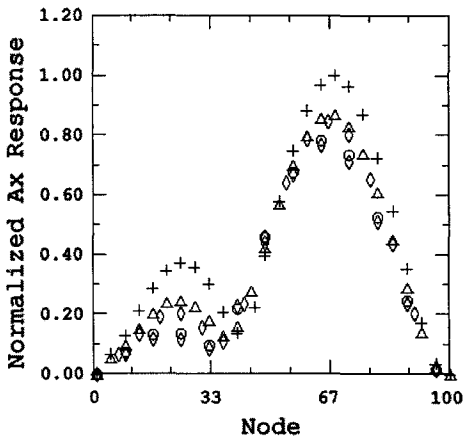

(c) Mode 5

Figure B.7: Normalized acceleration response of transverse web frame #1 in the x-direction for damage cases #5 to #8: O: intact, □: case #5, ◇: case #6, △: case #7, +: case #8

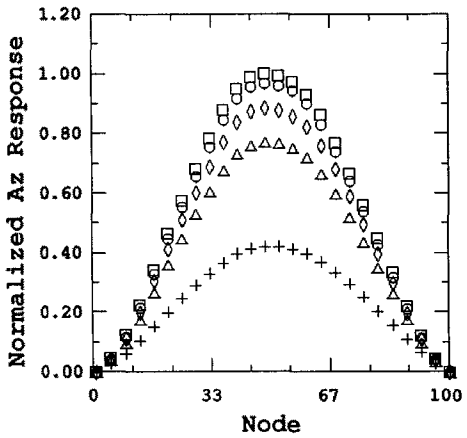

(a) Mode 1

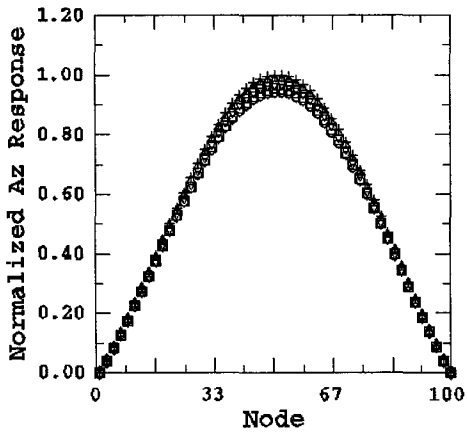

(b) Mode 2

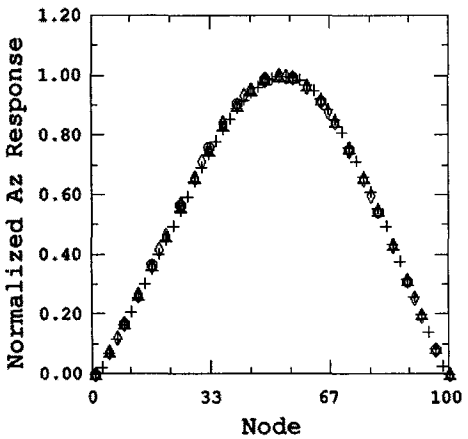

(c) Mode 5

Figure B.8: Normalized acceleration response of transverse web frame #1 in the z-direction for damage cases #5 to #8: O: intact, □: case #5, ◊: case #6, △: case #7, +: case #8

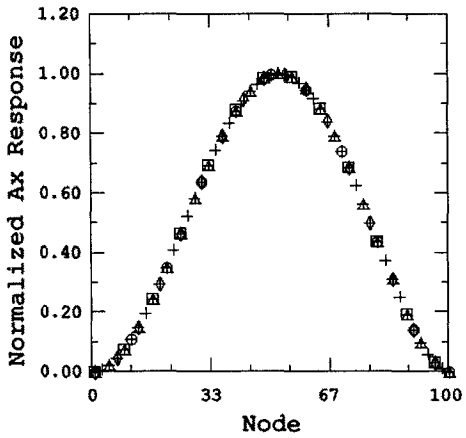

(a) Mode 1

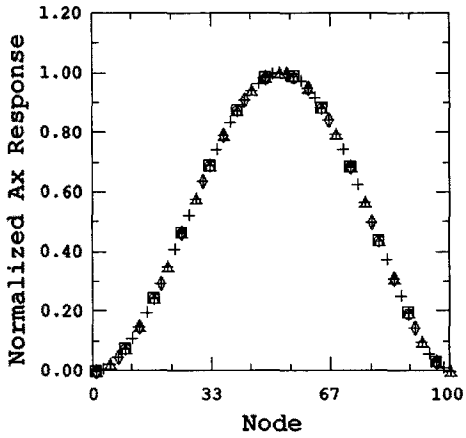

(b) Mode 2

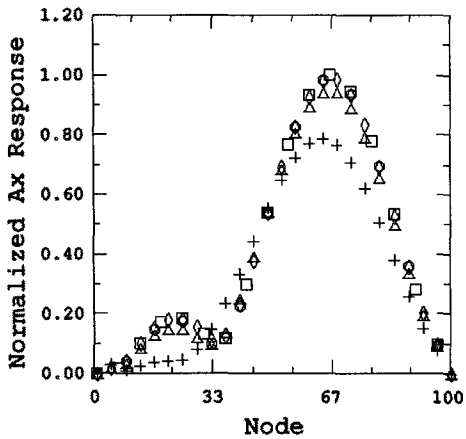

(c) Mode 5

Figure B.9: Normalized acceleration response of transverse web frame #2 in the x-direction for damage cases #1 to #4: O: intact, □: case #1, ◇: case #2, △: case #3, +: case #4

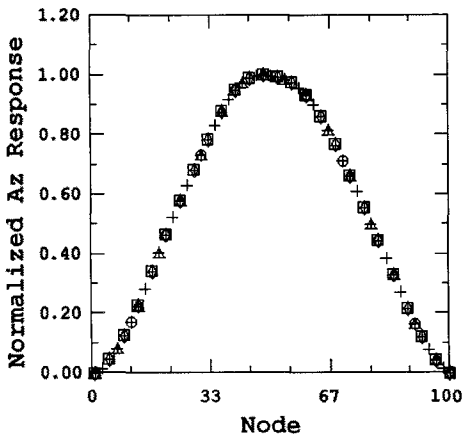

(a) Mode 1

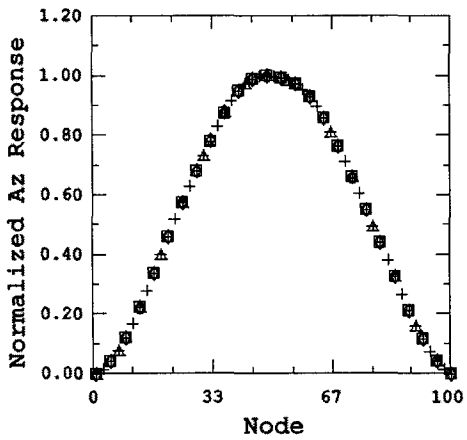

(b) Mode 2

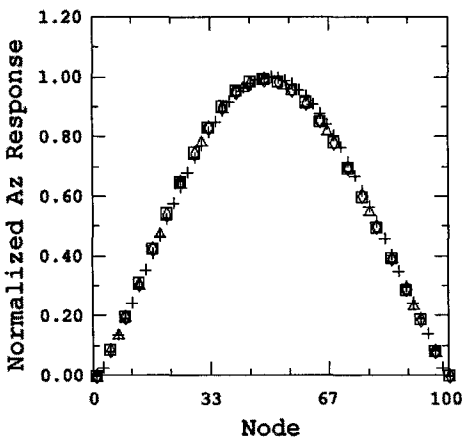

(c) Mode 5

Figure B.10: Normalized acceleration response of transverse web frame #2 in the z- direction for damage cases #1 to #4: O: intact, □: case #1, ◇: case #2, △: case #3, +: case #4

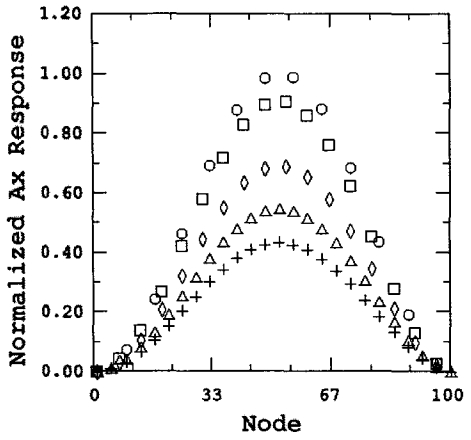

(a) Mode 1

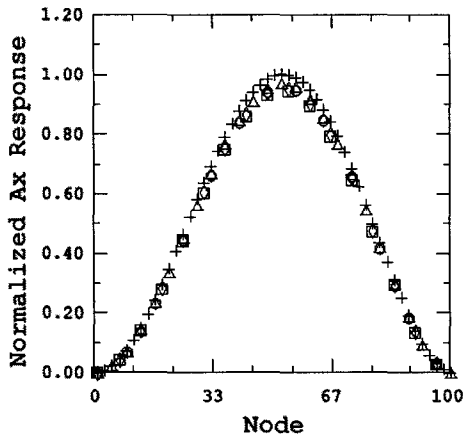

(b) Mode 2

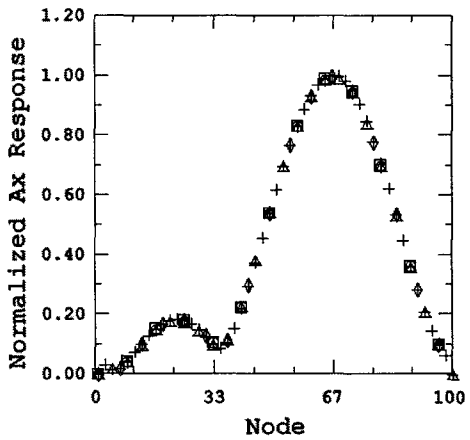

(c) Mode 5

Figure B.11: Normalized acceleration response of transverse web frame #2 in the x- direction for damage cases #5 to #8: O: intact, □: case #5, ◇: case #6, △: case #7, +: case #8

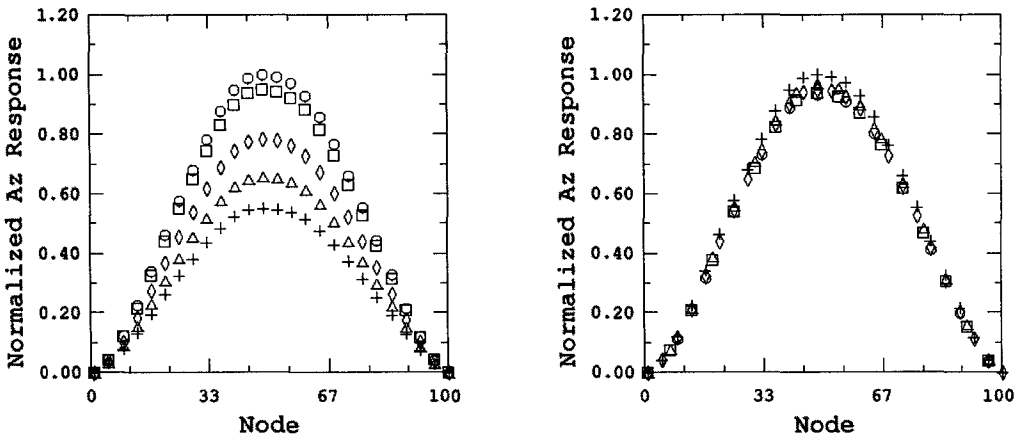

(a) Mode 1

(b) Mode 2

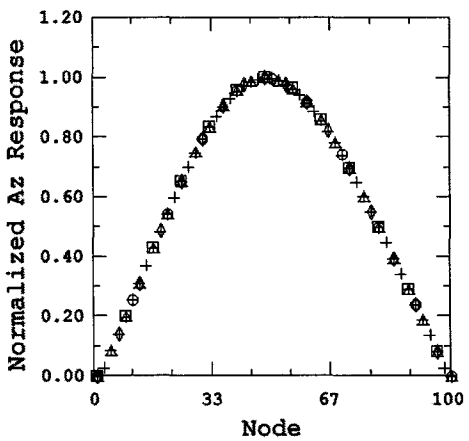

(c) Mode 5

Figure B.12: Normalized acceleration response of transverse web frame #2 in the z- direction for damage cases #5 to #8: O: intact, □: case #5, ◇: case #6, △: case #7, +: case #8

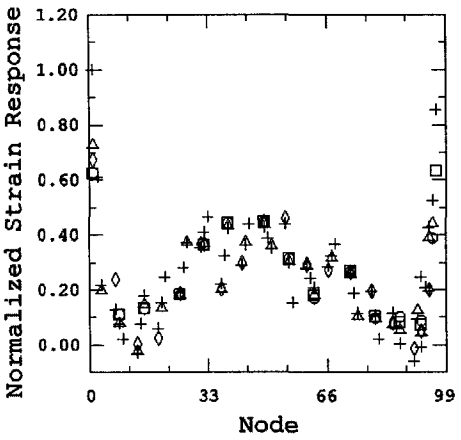

(a) Mode 1

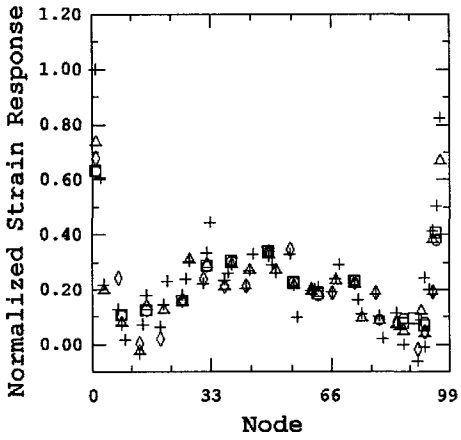

(b) Mode 2

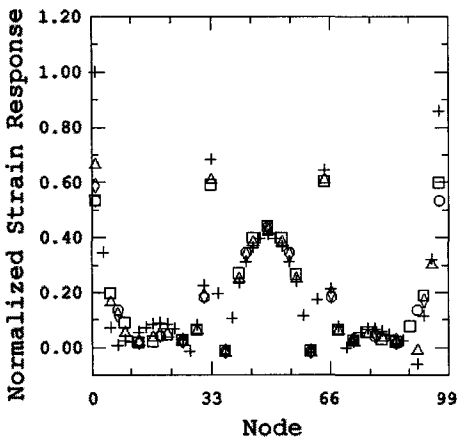

(c) Mode 5

Figure B.13: Normalized strain response of side shell plate along longitudinal #2 in the x- direction for damage cases #1 to #4: O: intact, □: case #1, ◊: case #2, △: case #3, +: case #4

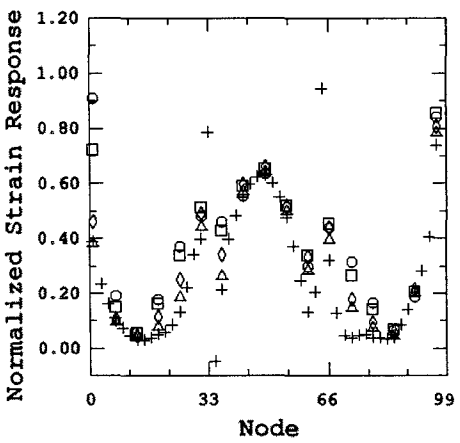

(a) Mode 1

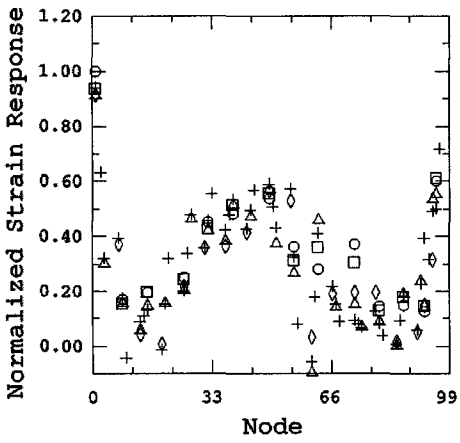

(b) Mode 2

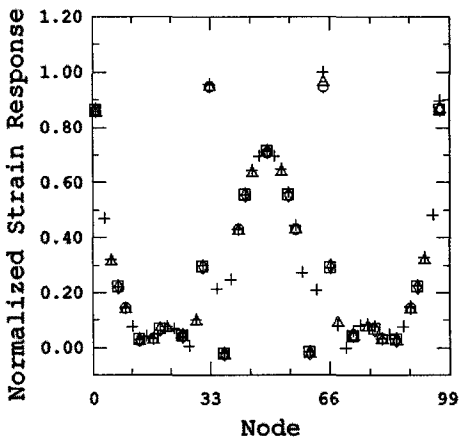

(c) Mode 5

Figure B.14: Normalized strain response of side shell plate along longitudinal #2 in the x- direction for damage cases #5 to #8: O: intact, □: case #5, ◊: case #6, △: case #7, +: case #8

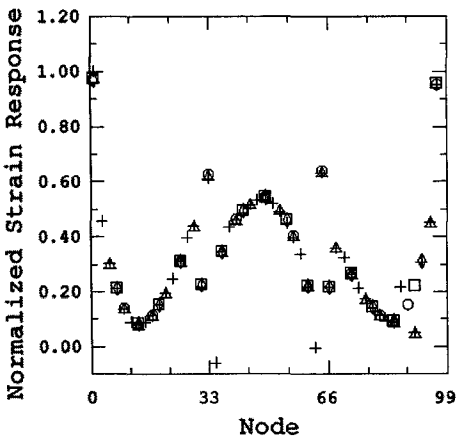

(a) Mode 1

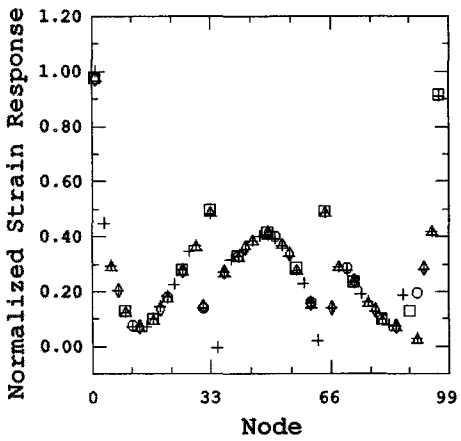

(b) Mode 2

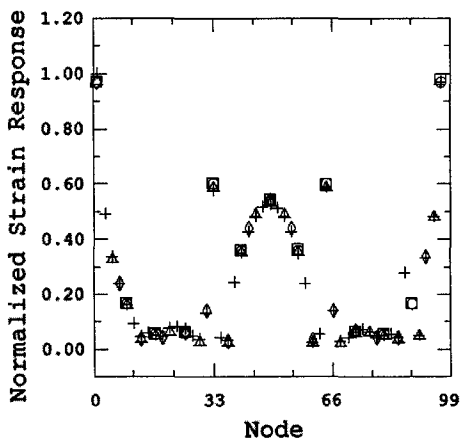

(c) Mode 5

Figure B.15: Normalized strain response of side shell plate along longitudinal # 3 in the x- direction for damage cases #1 to #4: O: intact, □: case #1, ◊: case #2, △: case #3, +: case #4

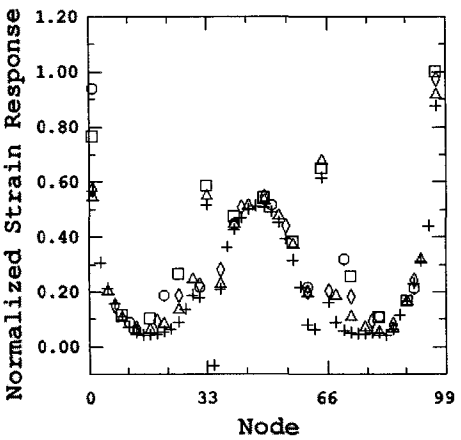

(a) Mode 1

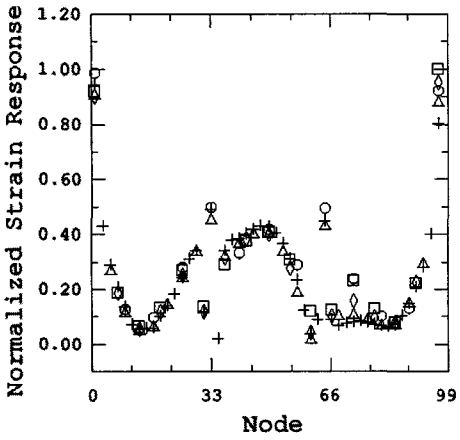

(b) Mode 2

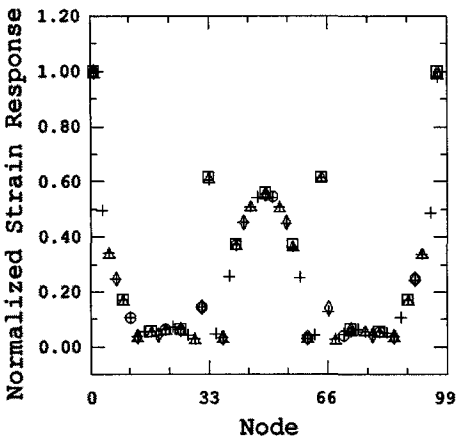

(c) Mode 5

Figure B.16: Normalized strain response of side shell plate along longitudinal #3 in the x- direction for damage cases #5 to #8: O: intact, □: case #5, ◊: case #6, △: case #7, +: case #8

Appendix C

Estimation of Excitation Frequency Range

A procedure for calculating wave load on the structure is presented in this appendix. The wave load on prototype was computed to determine the range of excitation frequencies to be used during the numerical and experimental investigation.

Wave force spectrum of the prototype was modeled to generate the typical dominant frequencies of the wave forces that would exist at the site. To predict wave force spectrum wave amplitude time history were generated, see Hughes (1988). The wave amplitudes were assumed to follow Pierson-Moskowitz (P.M.) spectrum as (Sorensen, 1997),

$$S_f = \frac{8.1\,10^{-3} g^2}{(2\pi)^4 f^5} e^{-0.74\left(\frac{g}{U 2\pi f}\right)^4} \tag{C.1}$$

where S_f is the wave spectrum at the wave frequency f, g is the acceleration due to gravity and U is the wind speed at 19.5 m above the sea surface. Two different wind speed values were used for this investigation purpose, i.e., 15.4 m/sec and 20.6 m/sec. A method presented by Haddara (1971) was utilized for estimating wave force for three wave angles of wave attack viz., 60°, 90° and 120°. Random wave force time history was obtained by summing wave force time histories at

random phases. Wave force spectrum (S_f) was then computed from the random force time history. For the wave force computation the ship characteristic data including ship's speed were taken from Taggart (1980). It was carried out in the MATLAB (1997) environment.

Figures C.1 to C.6 show the prototype P.M. wave amplitude spectra, wave amplitude and force time histories and wave force spectra computed using the above mentioned procedure. The wave force frequencies fell in the frequency range of 0 Hz to 0.3 Hz with a dominant frequency around 0.1 Hz. Therefore the one twentieth model was tested in a frequency range with a dominant wave frequency of 2 Hz.

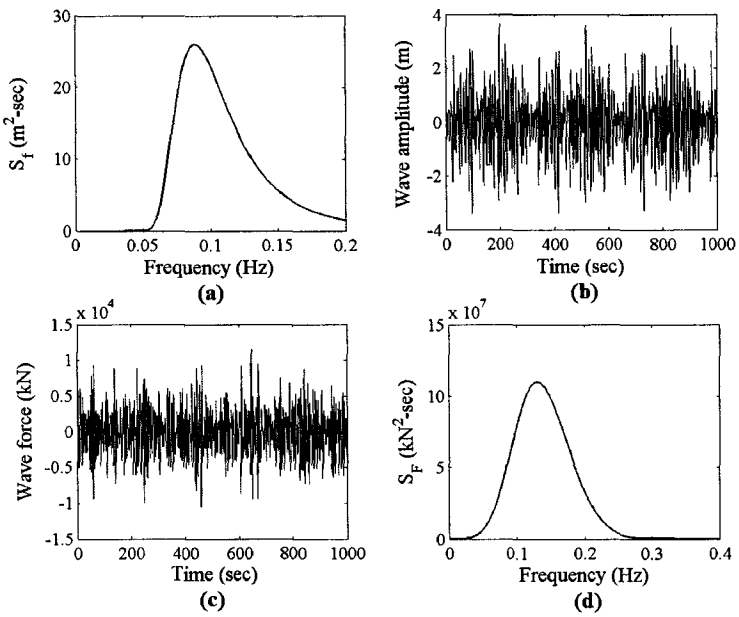

Figure C.1: Prototype random wave time history [(b) for wave amplitude and (c) wave force] and spectrum [(a) for wave amplitude and (d) for wave force] for wind speed = 15.4 m/sec and wave angle of attack = 60°

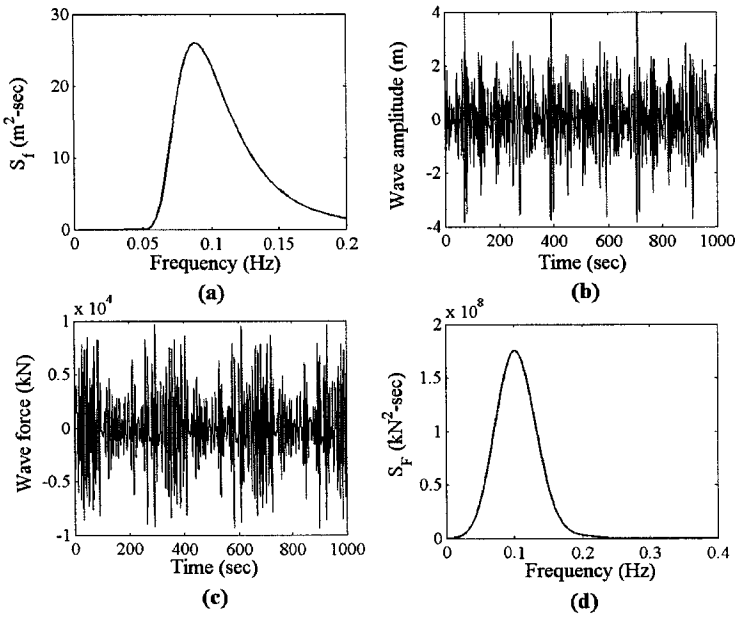

Figure C.2: Prototype random wave time history [(b) for wave amplitude and (c) for wave force] and spectrum [(a) for wave amplitude and (d) for wave force] for wind speed = 15.4 m/sec and wave angle of attack = 90°

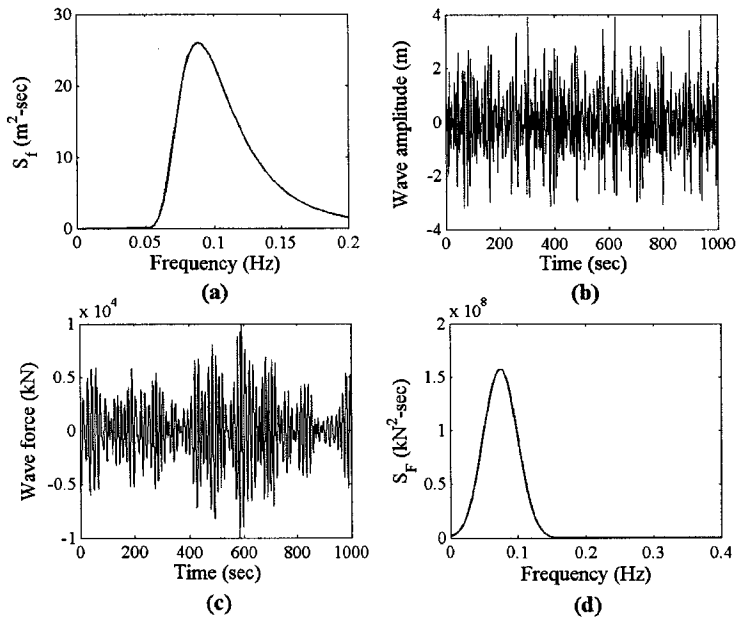

Figure C.3: Prototype random wave time history [(b) for wave amplitude and (c) for wave force] and spectrum [(a) for wave amplitude and (d) for wave force] for wind speed = 15.4 m/sec and wave angle of attack = 120°

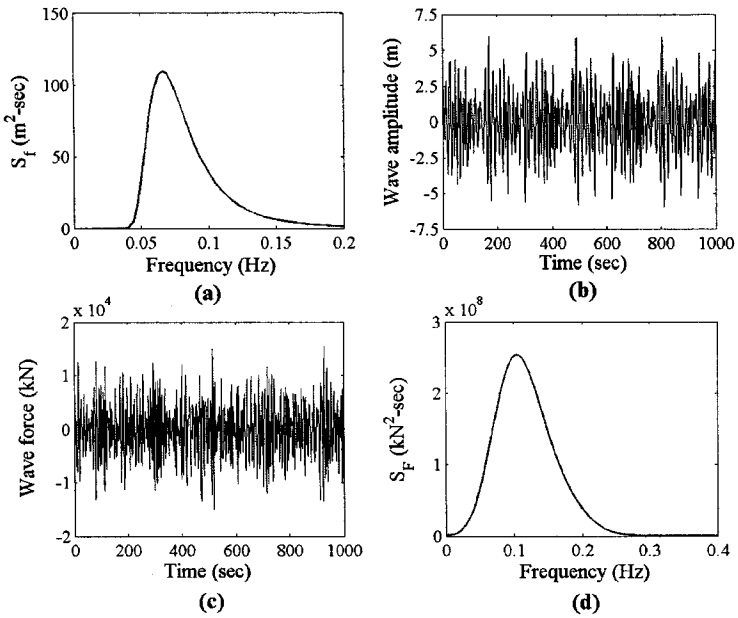

Figure C.4: Prototype random wave time history [(b) for wave amplitude and (c) for wave force] and spectrum [(a) for wave amplitude and (d) for wave force] for wind speed = 20.6 m/sec and wave angle of attack = 60°

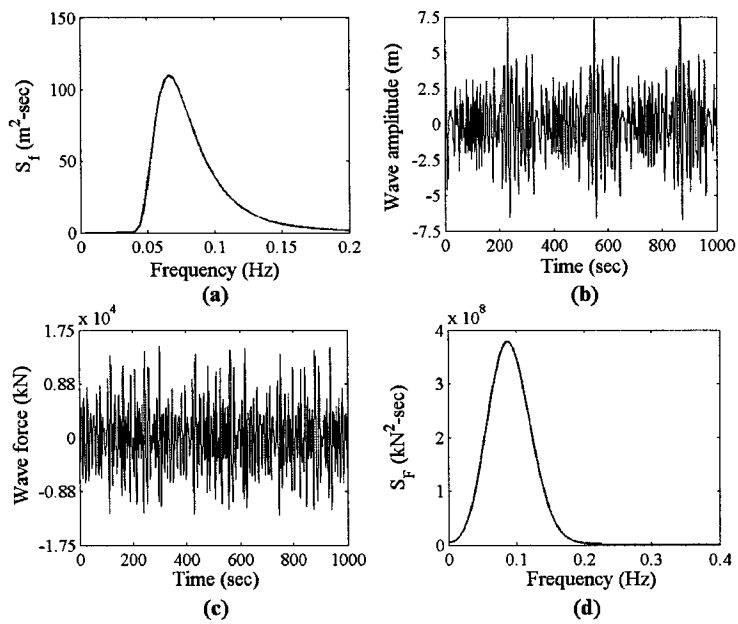

Figure C.5: Prototype random wave time history [(b) for wave amplitude and (c) for wave force] and spectrum [(a) for wave amplitude and (d) for wave force] for wind speed = 20.6 m/sec and wave angle of attack 90°

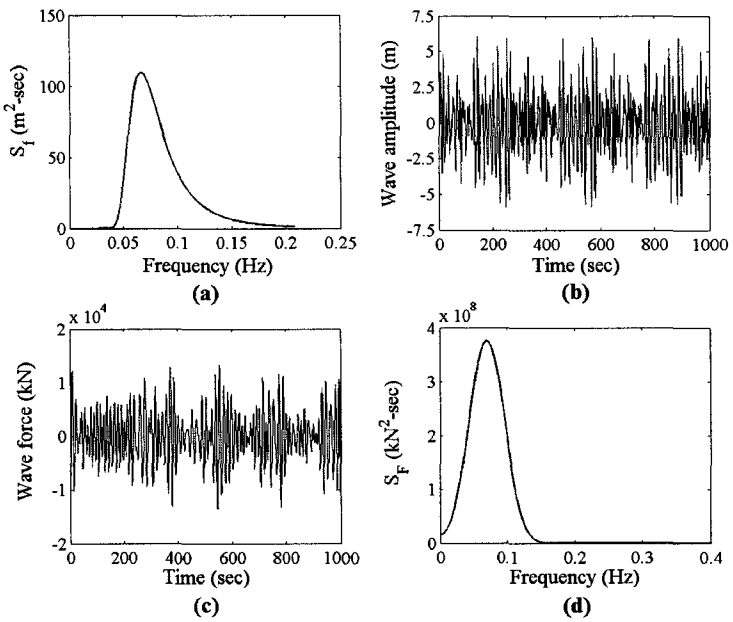

Figure C.6: Prototype random wave time history [(b) for wave amplitude and (c) for wave force] and spectrum [(a) for wave amplitude and (d) for wave force] for wind speed = 20.6 m/sec and wave angle of attack = 120°

Appendix D

Calibration Factors

Prior to carrying out experimental investigations, all sensors (accelerometers, strain gages and force transducer) were calibrated. Accelerometers were calibrated three times, viz., once prior to doing test for each model. Strain gages were calibrated two times for each model, i.e., once prior to carrying out experiments for intact and damage cases #1 to #4 and the other prior to carrying out experiments for undamaged condition (the condition after cracks at a locations 1 and 2 were welded) and damage cases #5 to #8. The strain gage calibration were performed twice to ensure that the strain gages worked properly after the welding. The force transducer (load cell) was calibrated once since forces applied to the modeled structures were not needed for the crack identification presented in this thesis. Accelerometers and strain gages calibration factors for models #1, #2 and #3 are presented in Tables D.1 to D.3. The relationship of force and voltage for the load cell used in the experimental investigations is shown in Figure D.1.

Table D.1: Accelerometer and strain gage calibration factors for model #1

Accelerometer calibration factor

Accelerometer #	The mean and standard deviation
1	1.726759 ± 0.005921
2	1.743422 ± 0.007685
3	1.590175 ± 0.006711
4	1.758471 ± 0.003650
5	1.514096 ± 0.011912
6	1.529398 ± 0.015335

Strain gage calibration factor

(a) Intact condition

Strain gage #	The mean and standard deviation
1	0.002600 ± 0.000086
2	0.002505 ± 0.000079
3	0.002535 ± 0.000056
4	0.002626 ± 0.000071
5	0.002590 ± 0.000086
6	0.002499 ± 0.000074

(b) Condition after the cracks at locations 1 and 2 were welded

Strain gage #	The mean and standard deviation
1	0.002366 ± 0.000078
2	0.002368 ± 0.000075
3	0.002337 ± 0.000084
4	0.002292 ± 0.000065
5	0.002300 ± 0.000079
6	0.002274 ± 0.000075

Table D.2: Accelerometer and strain gage calibration factors for model #2

Accelerometer calibration factor

Accelerometer #	The mean and standard deviation
1	1.469284 ± 0.002064
2	1.595644 ± 0.007619
3	1.471399 ± 0.001121
4	1.119709 ± 0.009070
5	1.387062 ± 0.001629
6	1.008344 ± 0.000876

Strain gage calibration factor

(a) Intact condition

Strain gage #	The mean and standard deviation
1	0.003740 ± 0.000012
2	0.003684 ± 0.000011
3	0.003719 ± 0.000008
4	0.003792 ± 0.000016
5	0.003736 ± 0.000009
6	0.003753 ± 0.000012

(b) Condition after cracks at locations 1 and 2 were welded

Strain gage #	The mean and standard deviation
1	0.003733 ± 0.000004
2	0.003670 ± 0.000097
3	0.003710 ± 0.000004
4	0.003737 ± 0.000087
5	0.003702 ± 0.000011
6	0.003721 ± 0.000011

Table D.3: Accelerometer and strain gage calibration factors for model #3

Accelerometer calibration factor

Accelerometer #	The mean and standard deviation
1	1.599352 ± 0.001212
2	1.648549 ± 0.001248
3	1.479119 ± 0.000954
4	1.141362 ± 0.002711
5	1.403732 ± 0.003986
6	1.167159 ± 0.000947

Strain gage calibration factor

(a) Intact condition

Strain gage #	The mean and standard deviation
1	0.003704 ± 0.000009
2	0.003723 ± 0.000007
3	0.003719 ± 0.000004
4	0.003714 ± 0.000010
5	0.003730 ± 0.000008
6	0.003687 ± 0.000011

(b) Condition after cracks at locations 1 and 2 were welded

Strain gage #	The mean and standard deviation
1	0.003715 ± 0.000011
2	0.003724 ± 0.000002
3	0.003744 ± 0.000004
4	0.003753 ± 0.000013
5	0.003732 ± 0.000007
6	0.003678 ± 0.000012

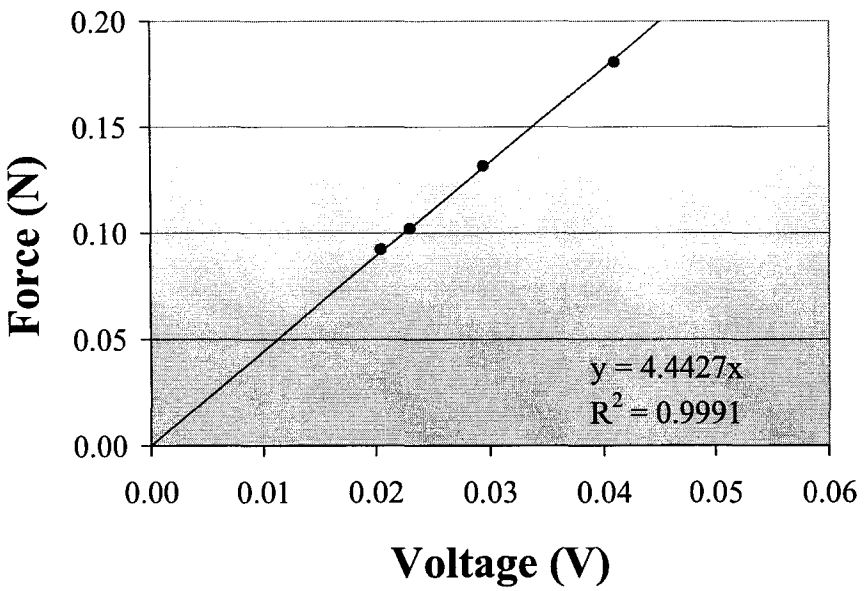

Figure D.1: Relationship of force and voltage used for load cell calibration

Appendix E

Comparisons of Numerical and Experimental Values

Comparisons of natural frequency, root mean square (rms) of acceleration and strain response obtained from numerical and experimental investigations for models #1, #2 and #3 are presented in this appendix. Comparison of numerical and experimental natural frequency of the models under intact and damaged conditions are shown in Figures E.1 to E.6. The rms of acceleration and strain response are shown in Figures E.7 to E.14.

Comparison of natural frequency measured from model #1 and that numerically computed using the finite element method for damage cases #1 to #8 are shown in Figures E.1 and E.2. Figures E.3 to E.4 and E.5 to E.6 show numerical and experimental natural frequency obtained from models #2 and #3, respectively.

Comparison of rms of acceleration and strain response obtained from numerical and experimental investigations of model #1 are shown in Figures E.7 to E.9. Figures E.10 to E.12 and Figures E.13 to E.15 show the rms of acceleration and strain response for models #2 and #3, respectively.

E.1 Numerical and Experimental Natural Frequency

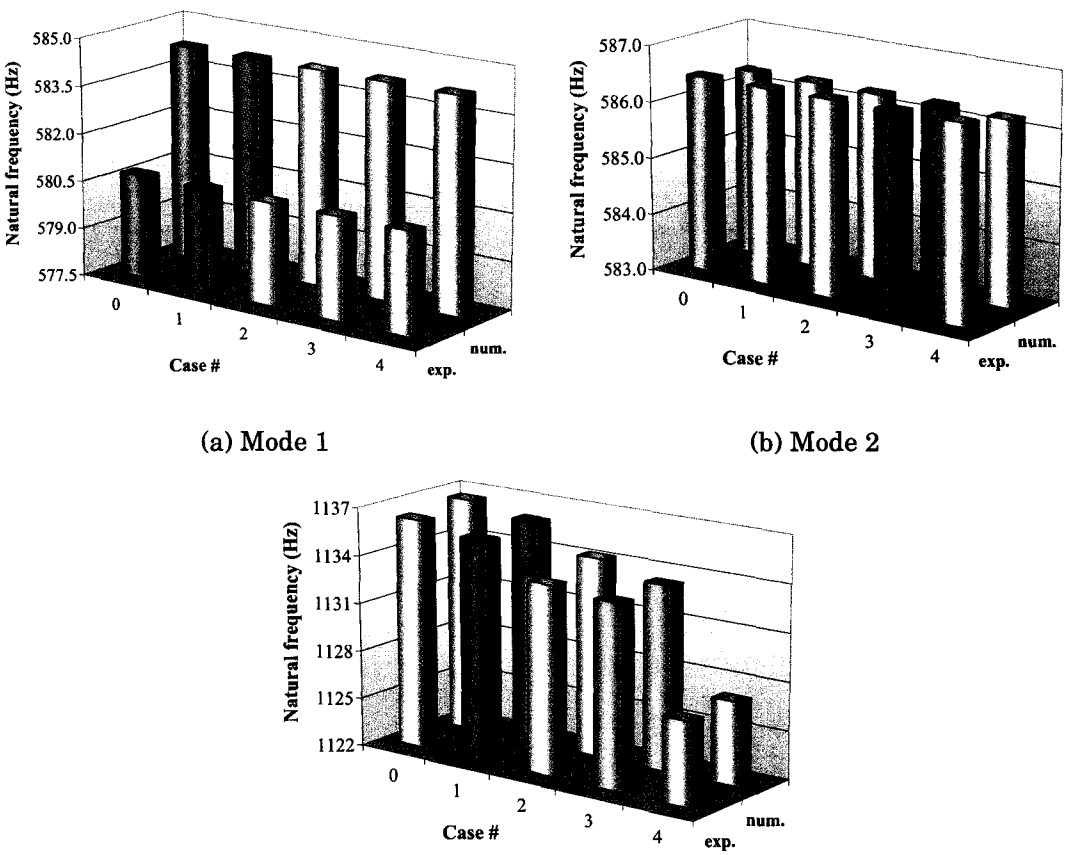

(a) Mode 1

(b) Mode 2

(c) Mode 5

Figure E.1: Comparison of numerical and experimental natural frequency for model #1 for damage cases #1 to #4

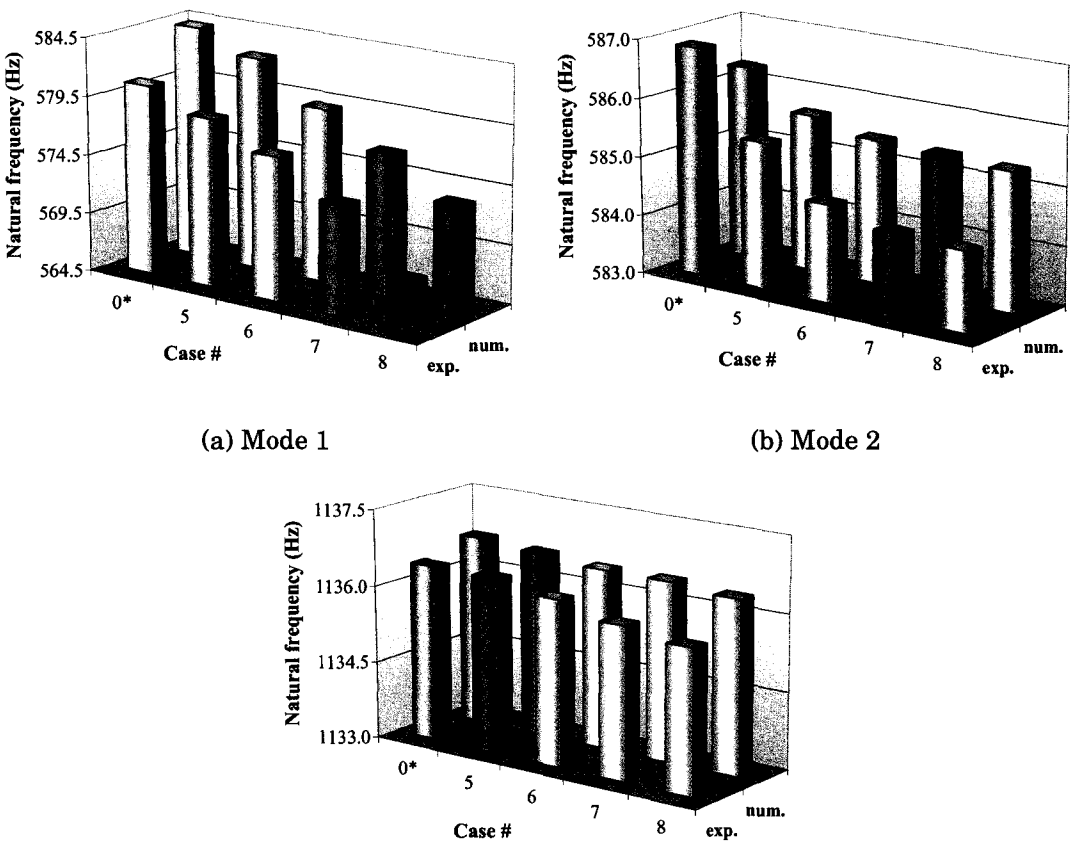

(a) Mode 1

(b) Mode 2

(c) Mode 5

Figure E.2: Comparison of numerical and experimental natural frequency for model #1 for damage cases #5 to #8

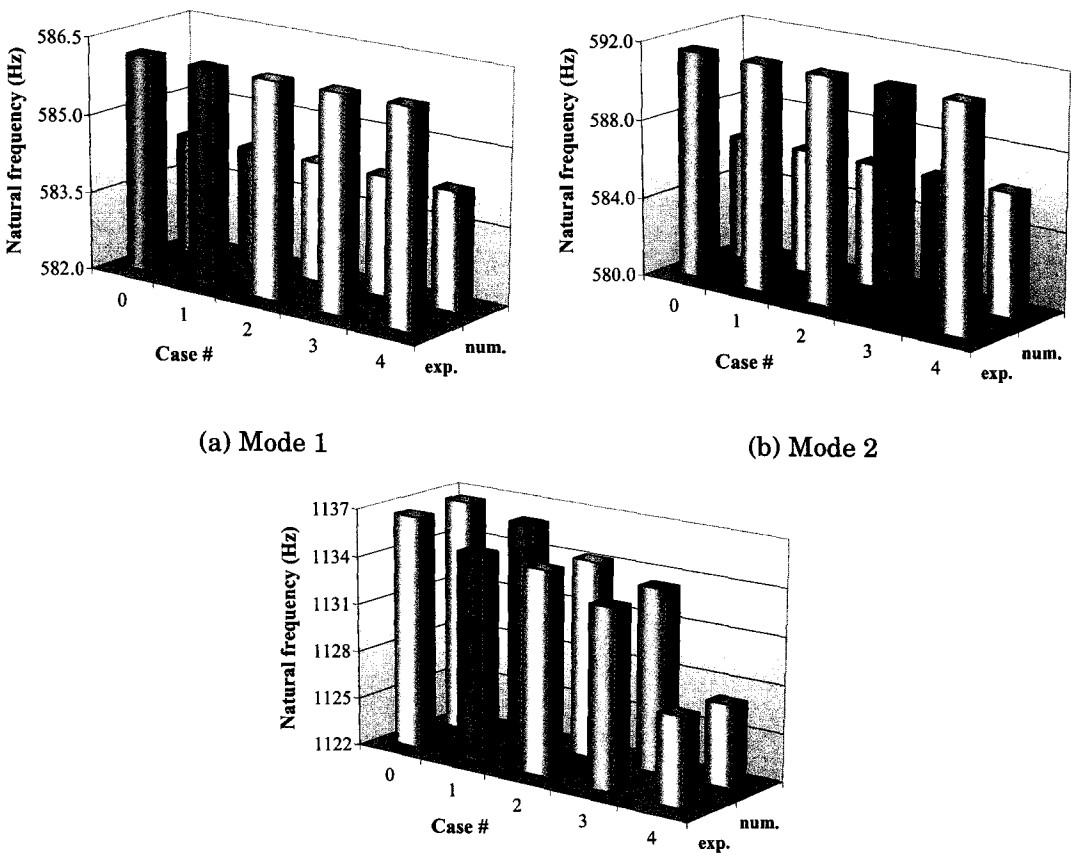

Figure E.3: Comparison of numerical and experimental natural frequency for model #2 for damage cases #1 to #4

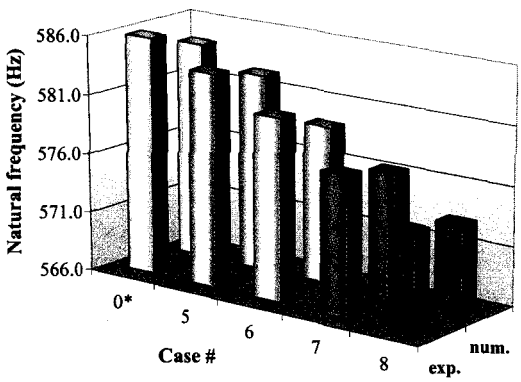

(a) Mode 1

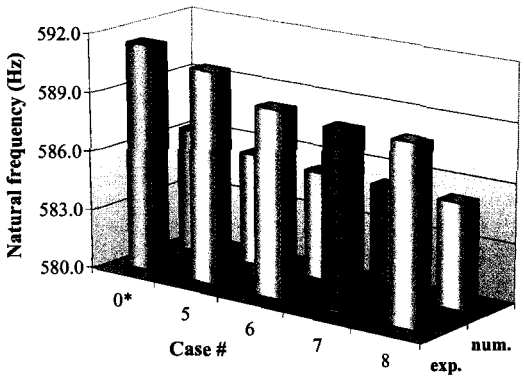

(b) Mode 2

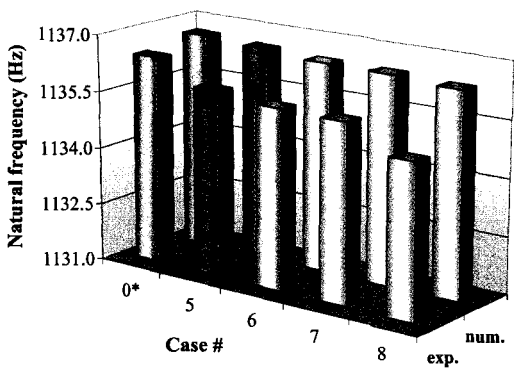

(c) Mode 5

Figure E.4: Comparison of numerical and experimental natural frequency for model #2 for damage cases #5 to #8

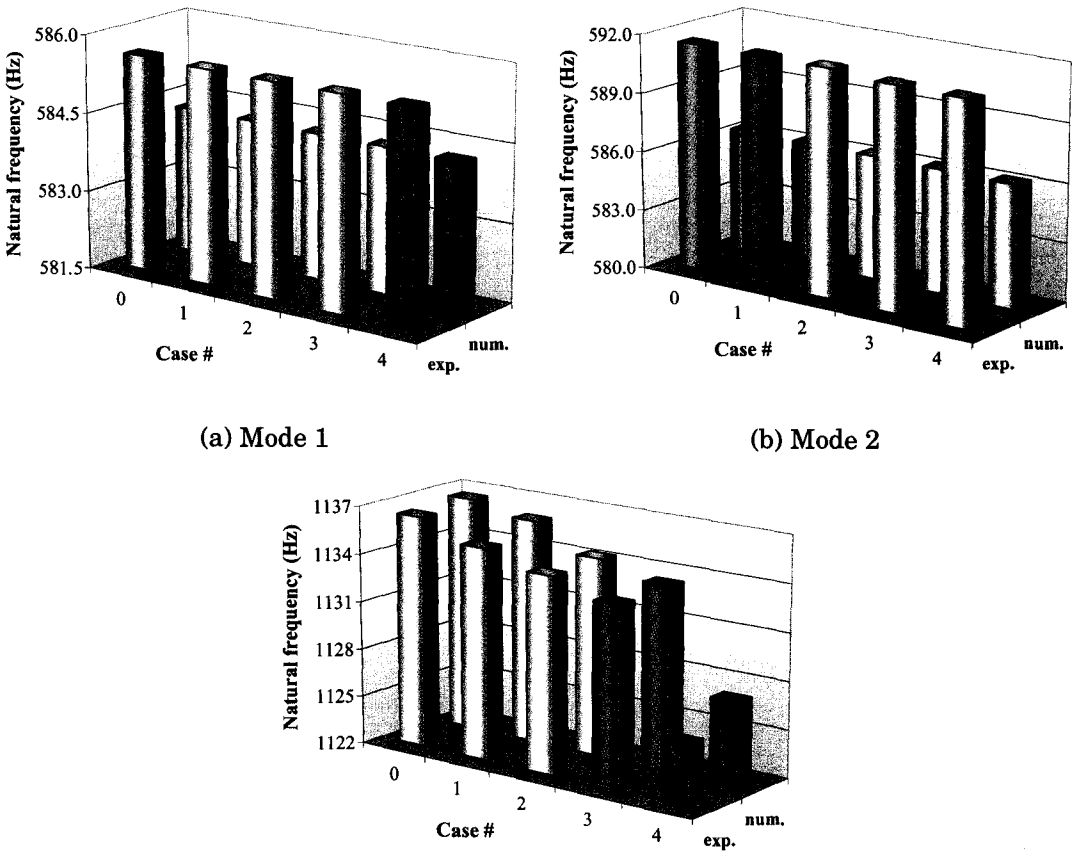

(a) Mode 1

(b) Mode 2

(c) Mode 5

Figure E.5: Comparison of numerical and experimental natural frequency for model #3 for damage cases #1 to #4

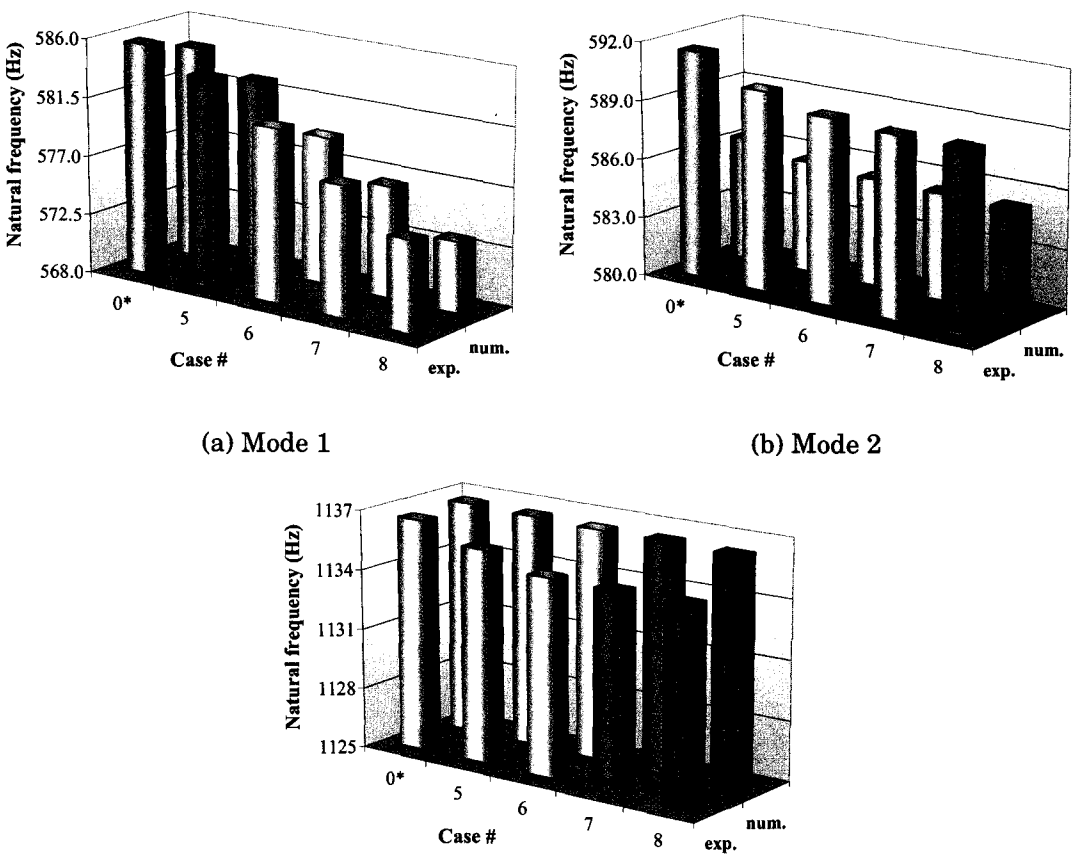

Figure E.6: Comparison of numerical and experimental natural frequency for model #3 for damage cases #5 to #8

E.2 Normalized Numerical and Experimental rms Response

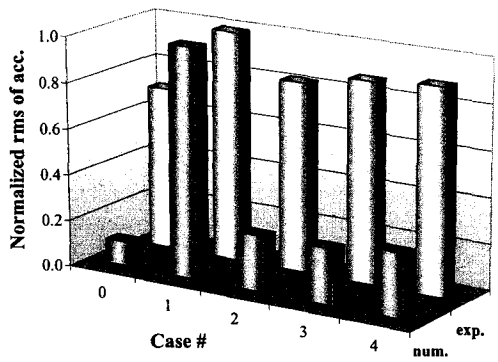

(a) accelerometer #1

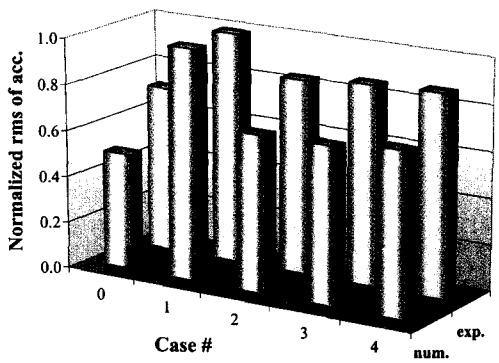

(b) accelerometer #2

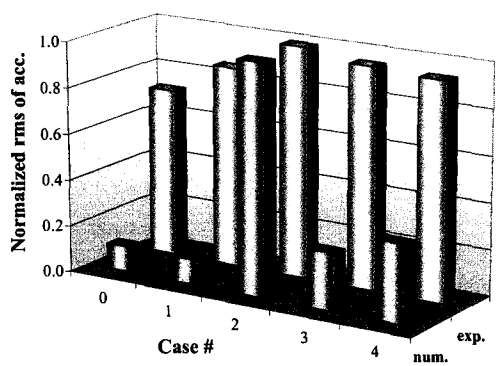

(c) accelerometer #3

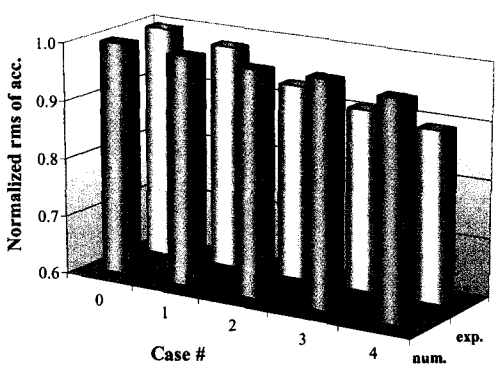

(d) accelerometer #4

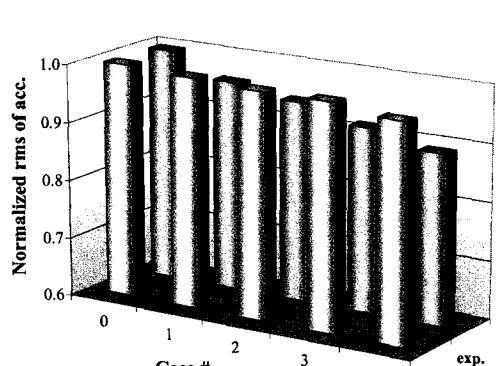

(e) accelerometer #5

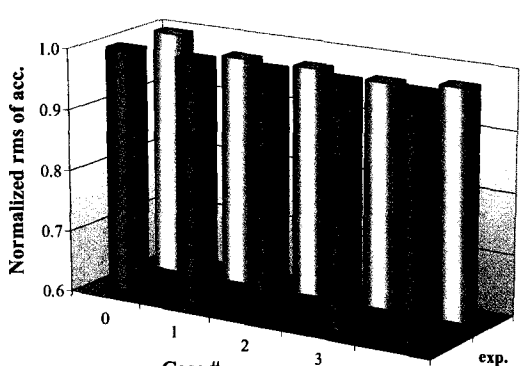

(f) accelerometer #6

Figure E.7: Normalized numerical and experimental rms of acceleration response of model #1 for damage cases #1 to #4

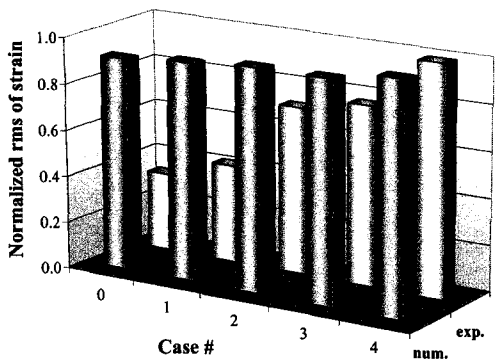

(a) strain gage #1

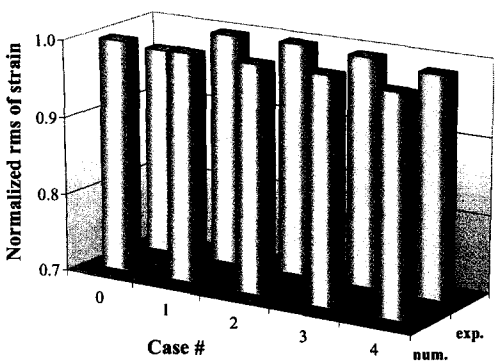

(b) strain gage #2

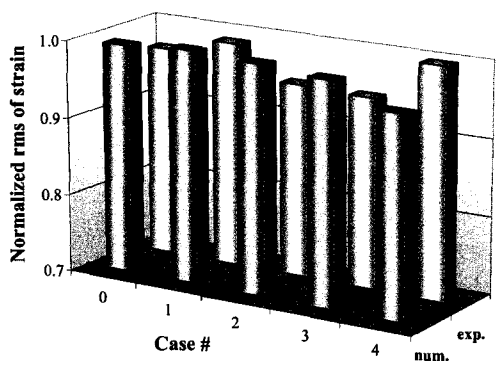

(c) strain gage #3

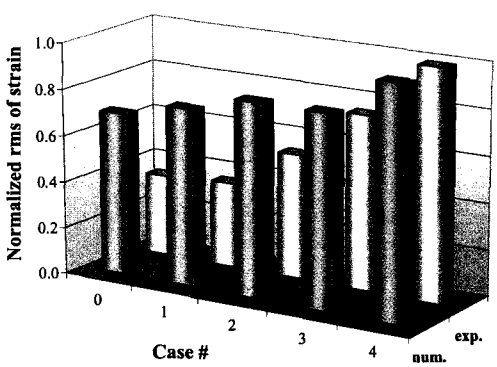

(d) strain gage #4

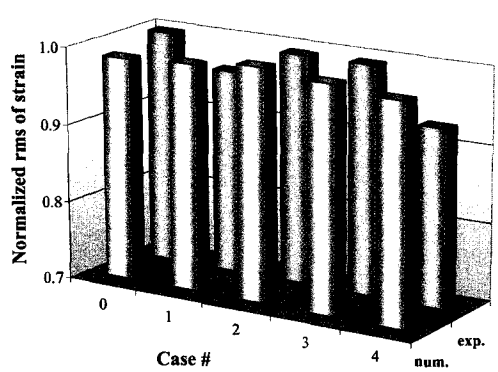

(e) strain gage #5

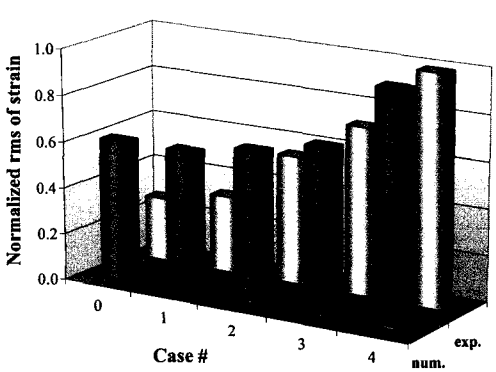

(f) strain gage #6

Figure E.8: Normalized numerical and experimental rms of strain response of model #1 for damage cases #1 to #4

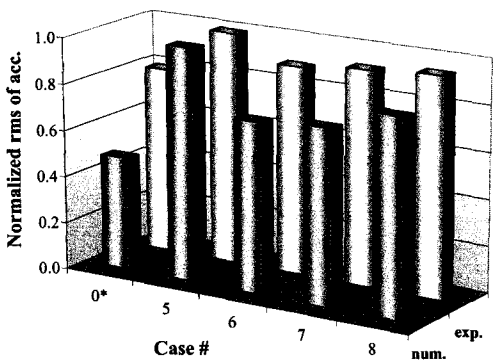

(a) accelerometer #1

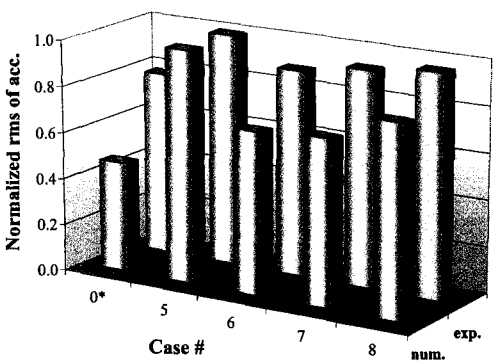

(b) accelerometer #2

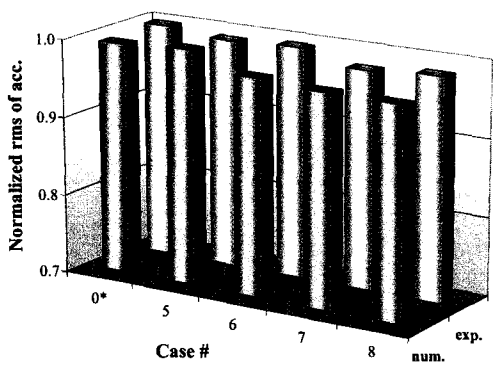

(c) accelerometer #3

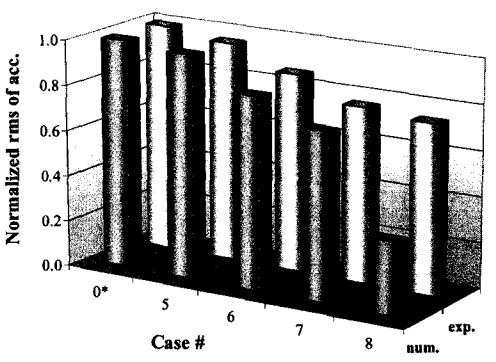

(d) accelerometer #4

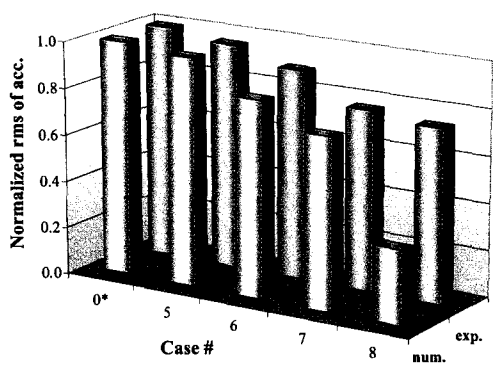

(e) accelerometer #5

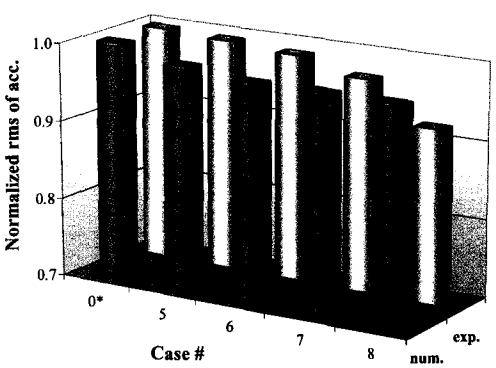

(f) accelerometer #6

Figure E.9: Normalized numerical and experimental rms of acceleration response of model #1 for damage cases #5 to #8

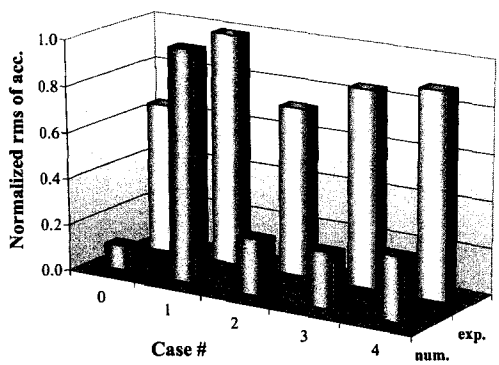

(a) accelerometer #1

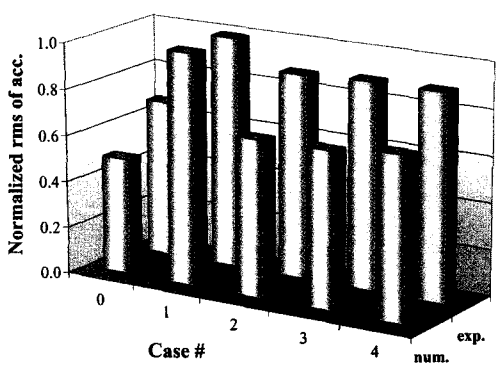

(b) accelerometer #2

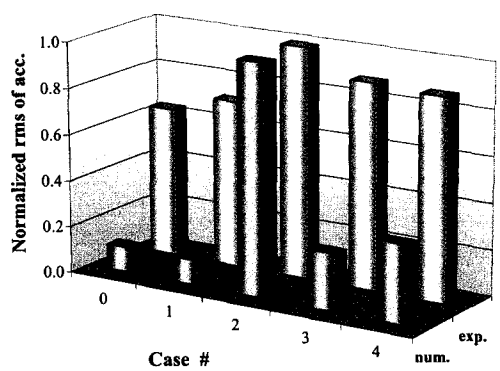

(c) accelerometer #3

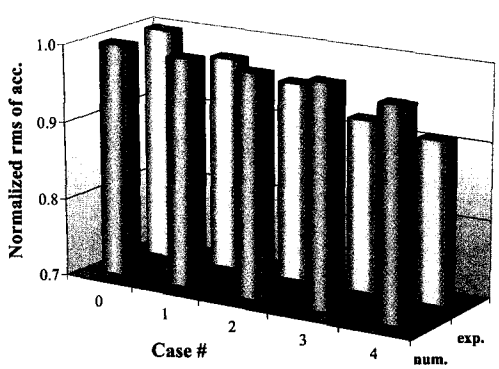

(d) accelerometer #4

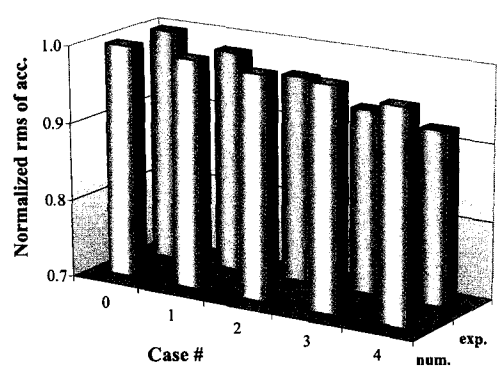

(e) accelerometer #5

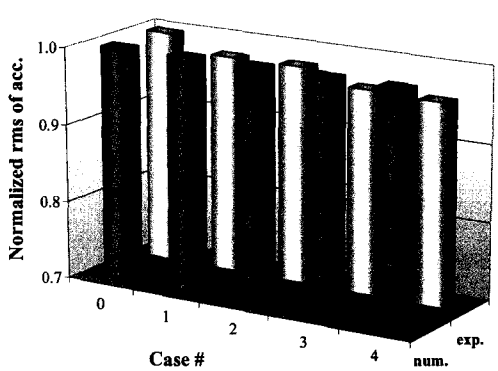

(f) accelerometer #6

Figure E.10: Normalized numerical and experimental rms of acceleration response of model #2 for damage cases #1 to #4

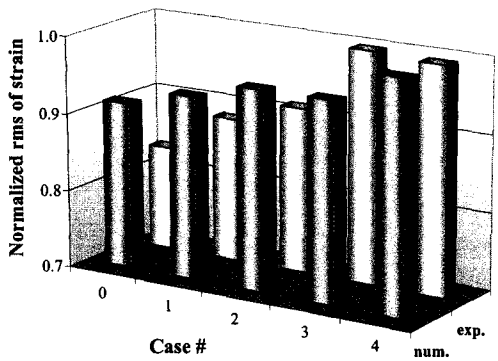

(a) strain gage #1

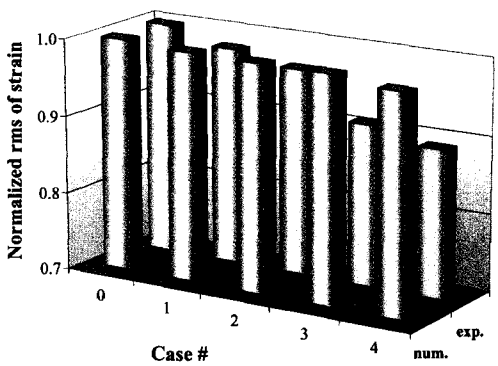

(b) strain gage #2

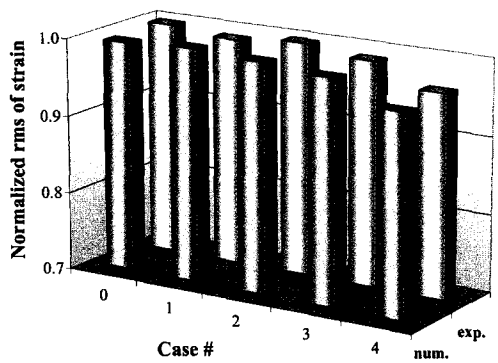

(c) strain gage #3

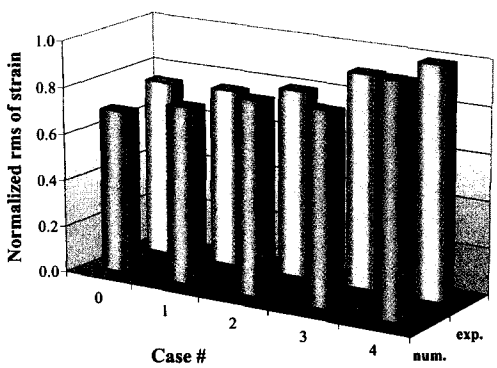

(d) strain gage #4

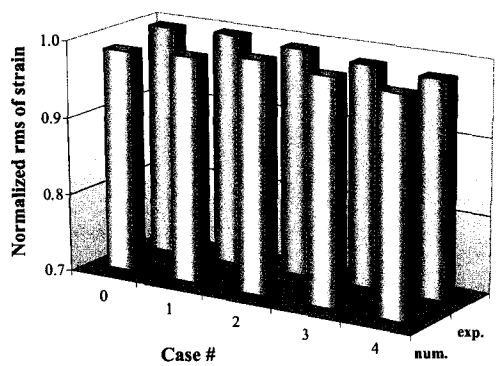

(e) strain gage #5

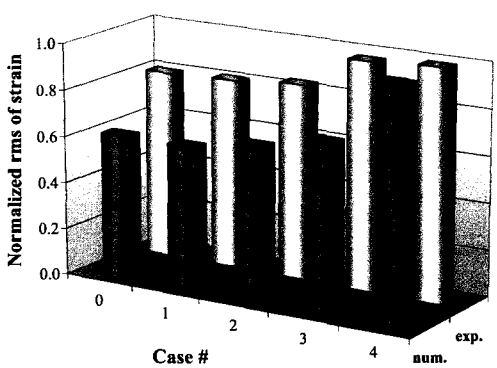

(f) strain gage #6

Figure E.11: Normalized numerical and experimental rms of strain response of model #2 for damage cases #1 to #4

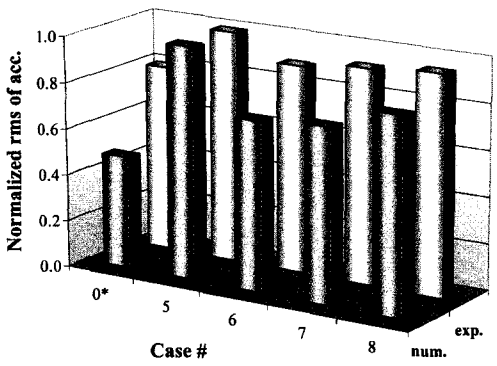

(a) accelerometer #1

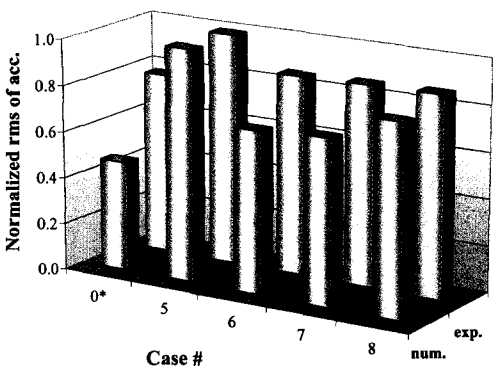

(b) accelerometer #2

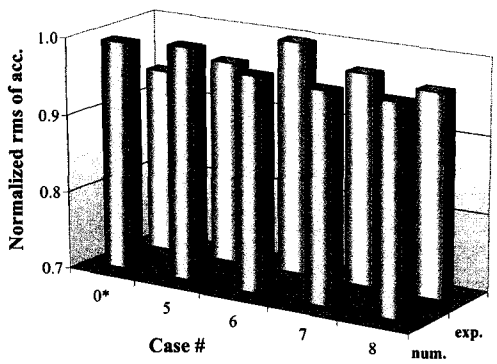

(c) accelerometer #3

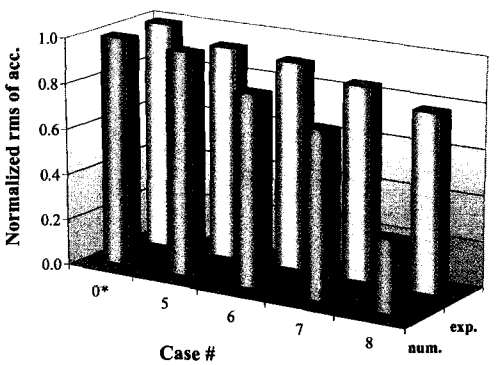

(d) accelerometer #4

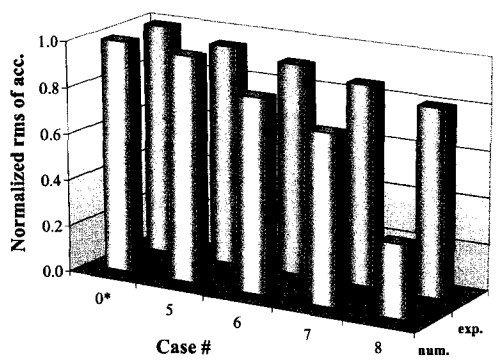

(e) accelerometer #5

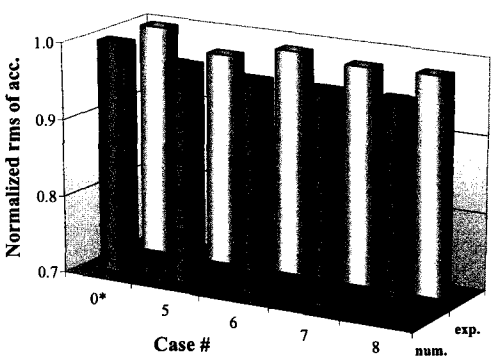

(f) accelerometer #6

Figure E.12: Normalized numerical and experimental rms of acceleration response of model #2 for damage cases #5 to #8

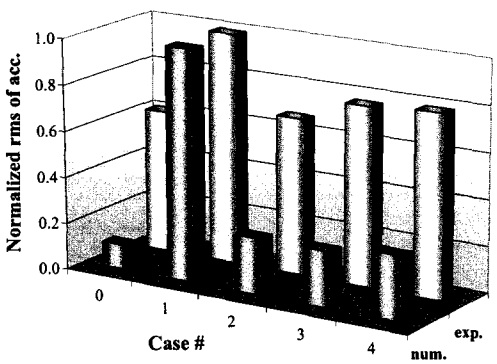

(a) accelerometer #1

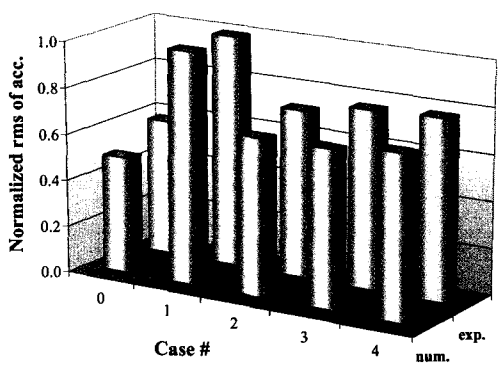

(b) accelerometer #2

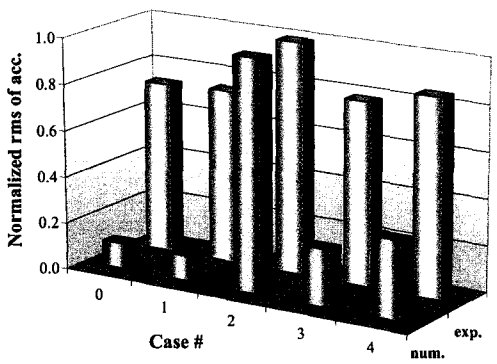

(c) accelerometer #3

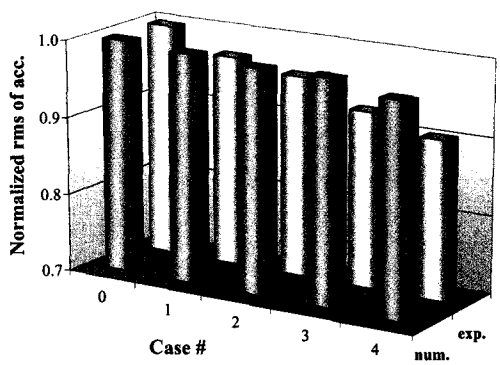

(d) accelerometer #4

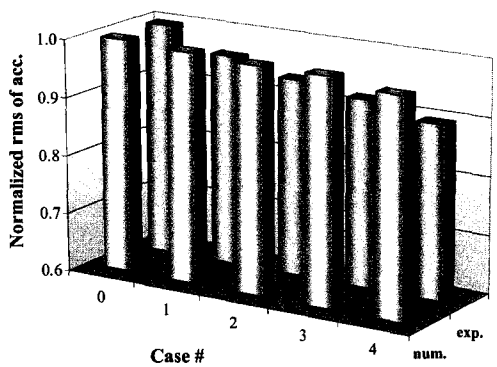

(e) accelerometer #5

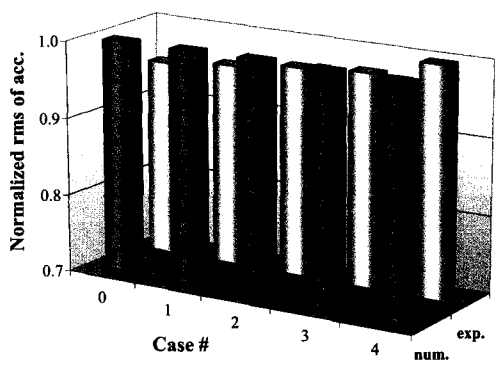

(f) accelerometer #6

Figure E.13: Normalized numerical and experimental rms of acceleration response of model #3 for damage cases #1 to #4

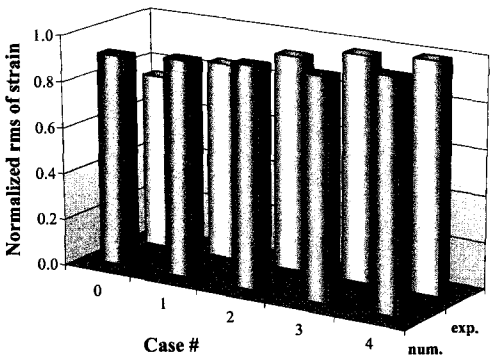

(a) strain gage #1

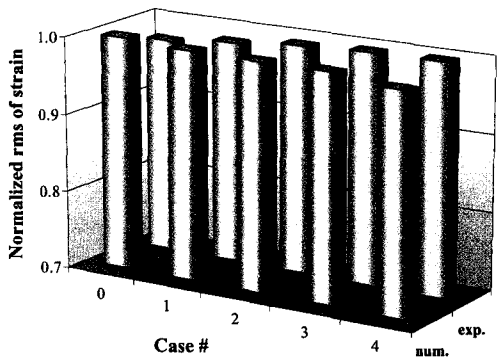

(b) strain gage #2

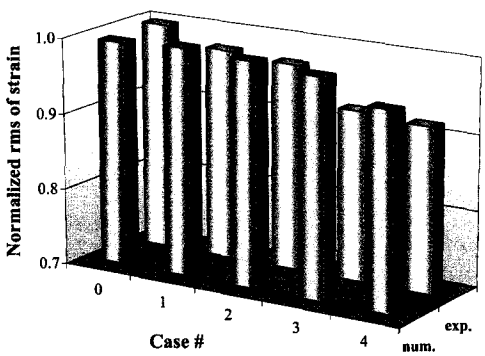

(c) strain gage #3

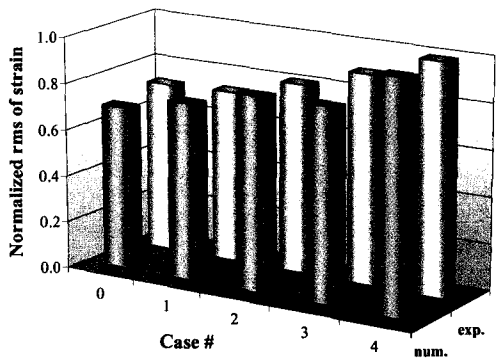

(d) strain gage #4

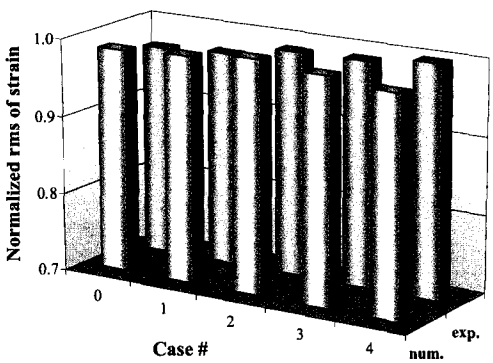

(e) strain gage #5

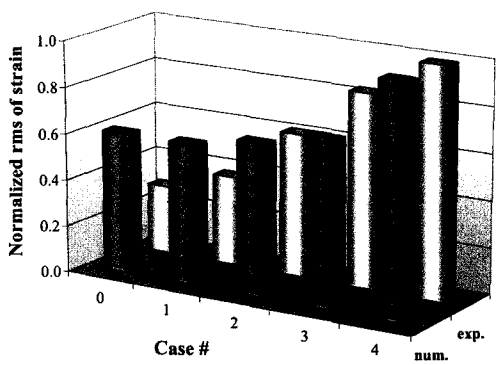

(f) strain gage #6

Figure E.14: Normalized numerical and experimental rms of strain response of model #3 for damage cases #1 to #4

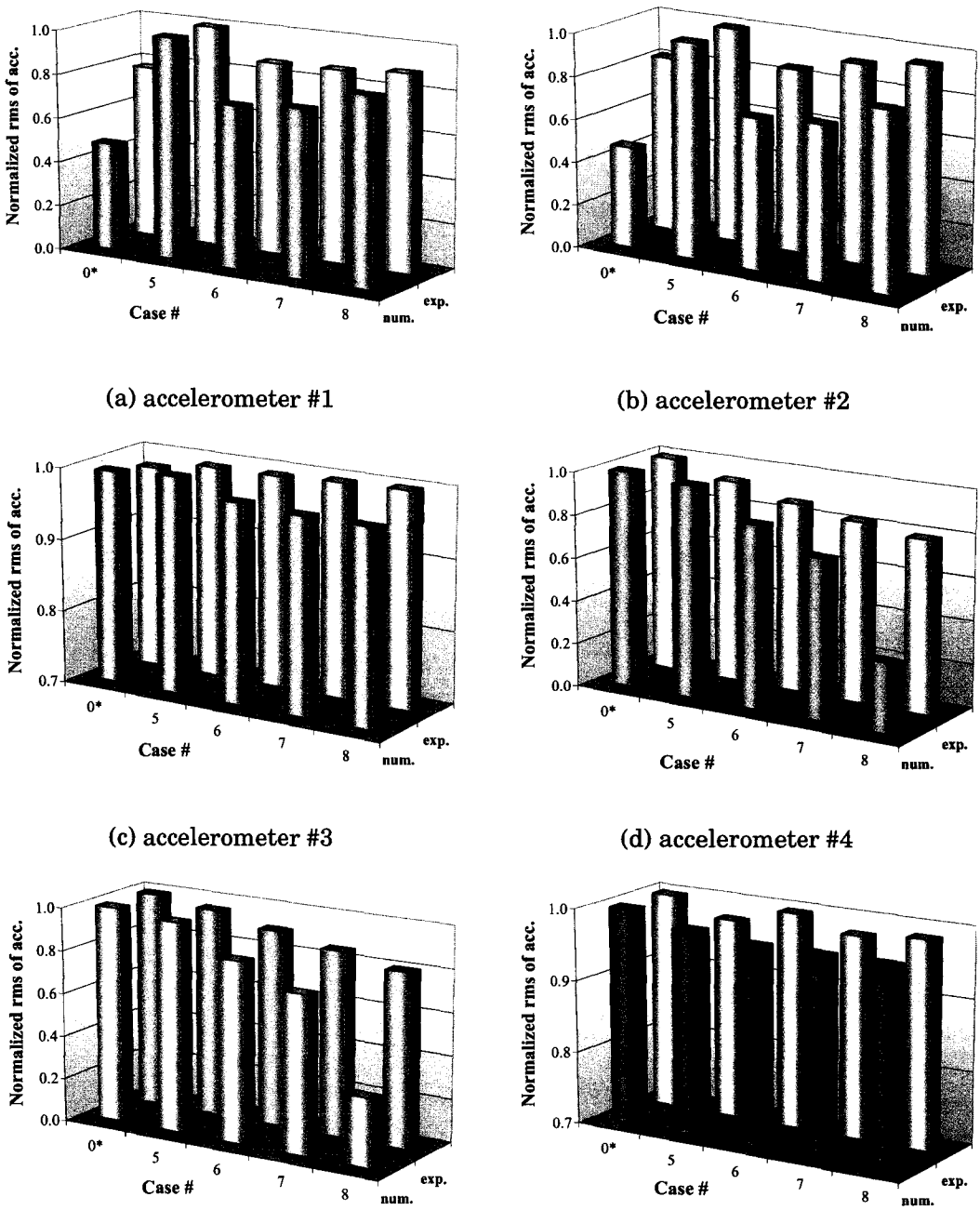

(a) accelerometer #1

(b) accelerometer #2

(c) accelerometer #3

(d) accelerometer #4

(e) accelerometer #5

(f) accelerometer #6

Figure E.15: Normalized numerical and experimental rms of acceleration response of model #3 for damage cases #5 to #8

Appendix F

The rms Response Obtained from Finite Element Analysis

Simulations using the finite element method were carried out to obtain root mean square (rms) acceleration and strain response of the modeled structure in two frequency ranges of 200 Hz to 600 Hz and 200 Hz to 1200 Hz, under intact and damaged conditions given Tables 6.6 and 6.7. The rms response values were normalized by the largest value. Using results of investigations presented in this appendix a damage indicator was calculated. The damage indicator values are presented in Appendix G.

In this appendix the simulation results for six accelerometers and six strain gages are presented in a tabular format. Tables F.1 to F.6 give the rms acceleration response for damage cases #1 to #4. The rms strain response for damage cases #1 to #4 are presented in Tables F.7 to F.12. The rms acceleration response for damage cases #5 to #8 are presented in Tables F.13 to F.18.

Table F.1: Normalized rms values of accelerometer #1 (cases #1 to #4)

(a) for frequency range of 200 Hz to 600 Hz				
Crack length at location 2 (mm)	Crack length at location 1 (mm)			
	0.0	10.0	20.0	25.4
0.0	0.105584	1.000000	0.245303	0.290959
10.0	0.104110	0.995261	0.242488	0.287847
20.0	0.104261	0.986744	0.242265	0.287413
30.8	0.100556	0.951480	0.233846	0.277608
(b) for frequency range of 200 Hz to 1200 Hz				
Crack length at location 2 (mm)	Crack length at location 1 (mm)			
	0.0	10.0	20.0	25.4
0.0	0.103818	1.000000	0.240596	0.283886
10.0	0.102187	0.993850	0.237445	0.280406
20.0	0.102185	0.983620	0.236847	0.279534
30.8	0.097625	0.940259	0.226511	0.267575

Table F.2: Normalized rms values of accelerometer #2 (cases #1 to #4)

(a) for frequency range of 200 Hz to 600 Hz				
Crack length at location 2 (mm)	Crack length at location 1 (mm)			
	0.0	10.0	20.0	25.4
0.0	0.501359	1.000000	0.688031	0.742983
10.0	0.494783	0.998037	0.679659	0.734324
20.0	0.495496	0.985786	0.679851	0.734278
30.8	0.478974	0.948753	0.656963	0.709952
(b) for frequency range of 200 Hz to 1200 Hz				
Crack length at location 2 (mm)	Crack length at location 1 (mm)			
	0.0	10.0	20.0	25.4
0.0	0.493067	1.000000	0.674730	0.722732
10.0	0.485648	0.996599	0.665294	0.713007
20.0	0.485625	0.982453	0.664436	0.711843
30.8	0.464667	0.937076	0.635707	0.681544

Table F.3: Normalized rms values of accelerometer #3 (cases #1 to #4)

(a) for frequency range of 200 Hz to 600 Hz				
Crack length at location 2 (mm)	Crack length at location 1 (mm)			
	0.0	10.0	20.0	25.4
0.0	0.108532	0.107533	0.108262	0.107722
10.0	0.999998	1.000000	0.997069	0.992589
20.0	0.247738	0.246054	0.247172	0.246075
30.8	0.340237	0.338401	0.339584	0.338307
(b) for frequency range of 200 Hz to 1200 Hz				
Crack length at location 2 (mm)	Crack length at location 1 (mm)			
	0.0	10.0	20.0	25.4
0.0	0.104520	0.103381	0.103974	0.103028
10.0	1.000000	0.998579	0.993914	0.984973
20.0	0.239582	0.237588	0.238345	0.236284
30.8	0.327259	0.325026	0.325698	0.323126

Table F.4: Normalized rms values of accelerometer #4(cases #1 to #4)

(a) for frequency range of 200 Hz to 600 Hz				
Crack length at location 2 (mm)	Crack length at location 1 (mm)			
	0.0	10.0	20.0	25.4
0.0	0.998752	0.993378	0.987731	0.972806
10.0	0.998768	0.993565	0.987920	0.972992
20.0	0.998972	0.993769	0.988121	0.973189
30.8	1.000000	0.994791	0.989137	0.974187
(b) for frequency range of 200 Hz to 1200 Hz				
Crack length at location 2 (mm)	Crack length at location 1 (mm)			
	0.0	10.0	20.0	25.4
0.0	1.000000	0.982223	0.948839	0.874970
10.0	0.999199	0.981353	0.947818	0.873754
20.0	0.999450	0.981499	0.947735	0.873329
30.8	0.994341	0.975746	0.940885	0.864989

Table F.5: Normalized rms values of accelerometer #5 (cases #1 to #4)

(a) for frequency range of 200 Hz to 600 Hz				
Crack length at location 2 (mm)	Crack length at location 1 (mm)			
	0.0	10.0	20.0	25.4
0.0	0.998756	0.993466	0.987873	0.973059
10.0	0.998819	0.993646	0.988054	0.973239
20.0	0.999016	0.993841	0.988249	0.973433
30.8	1.000000	0.994822	0.989228	0.974402
(b) for frequency range of 200 Hz to 1200 Hz				
Crack length at location 2 (mm)	Crack length at location 1 (mm)			
	0.0	10.0	20.0	25.4
0.0	0.900792	0.875832	0.824935	0.742101
10.0	0.910079	0.884695	0.832525	0.746748
20.0	0.924841	0.898820	0.844701	0.754140
30.8	1.000000	0.970999	0.908191	0.796481

Table F.6: Normalized rms values of accelerometer #6 (cases #1 to #4)

(a) for frequency range of 200 Hz to 600 Hz				
Crack length at location 2 (mm)	Crack length at location 1 (mm)			
	0.0	10.0	20.0	25.4
0.0	0.995553	0.995908	0.997076	1.000000
10.0	0.994204	0.995225	0.996401	0.999325
20.0	0.993503	0.994515	0.995692	0.998616
30.8	0.989974	0.990994	0.992171	0.995104
(b) for frequency range of 200 Hz to 1200 Hz				
Crack length at location 2 (mm)	Crack length at location 1 (mm)			
	0.0	10.0	20.0	25.4
0.0	0.987593	0.989973	0.992709	1.000000
10.0	0.983030	0.985633	0.988420	0.995829
20.0	0.977922	0.980567	0.983413	0.990973
30.8	0.953712	0.956498	0.959554	0.967599

Table F.7: Normalized rms values of strain gage #1 (cases #1 to #4)

(a) for frequency range of 200 Hz to 600 Hz				
Crack length at location 2 (mm)	Crack length at location 1 (mm)			
	0.0	10.0	20.0	25.4
0.0	0.887864	0.909369	0.934132	1.000000
10.0	0.885011	0.906423	0.931077	0.996664
20.0	0.881183	0.902468	0.926989	0.992221
30.8	0.863249	0.883930	0.907799	0.971292
(b) for frequency range of 200 Hz to 1200 Hz				
Crack length at location 2 (mm)	Crack length at location 1 (mm)			
	0.0	10.0	20.0	25.4
0.0	0.883589	0.905966	0.931717	1.000000
10.0	0.880583	0.902860	0.928495	0.996478
20.0	0.876638	0.898778	0.924277	0.991890
30.8	0.857836	0.879339	0.904150	0.969949

Table F.8: Normalized rms values of strain gage #2 (cases #1 to #4)

(a) for frequency range of 200 Hz to 600 Hz				
Crack length at location 2 (mm)	Crack length at location 1 (mm)			
	0.0	10.0	20.0	25.4
0.0	0.999643	0.995219	0.993745	0.984603
10.0	1.000000	0.995634	0.994204	0.985206
20.0	0.999362	0.995078	0.993707	0.984907
30.8	0.997716	0.993799	0.992707	0.984830
(b) for frequency range of 200 Hz to 1200 Hz				
Crack length at location 2 (mm)	Crack length at location 1 (mm)			
	0.0	10.0	20.0	25.4
0.0	0.999854	0.995023	0.993265	0.983039
10.0	1.000000	0.995230	0.993517	0.983433
20.0	0.998957	0.994268	0.992612	0.982734
30.8	0.995356	0.991053	0.989685	0.980802

Table F.9: Normalized rms values of strain gage #3 (cases #1 to #4)

(a) for frequency range of 200 Hz to 600 Hz				
Crack length at location 2 (mm)	Crack length at location 1 (mm)			
	0.0	10.0	20.0	25.4
0.0	0.977575	0.982329	0.987002	1.000000
10.0	0.968861	0.973629	0.978331	0.991395
20.0	0.962241	0.967014	0.971744	0.984856
30.8	0.920721	0.925541	0.930395	0.943791
(b) for frequency range of 200 Hz to 1200 Hz				
Crack length at location 2 (mm)	Crack length at location 1 (mm)			
	0.0	10.0	20.0	25.4
0.0	0.977826	0.982639	0.987209	1.000000
10.0	0.694068	0.698095	0.977905	0.990771
20.0	0.689144	0.693167	0.970745	0.983667
30.8	0.916370	0.656347	0.926020	0.939287

Table F.10: Normalized rms values of strain gage #4 (cases #1 to #4)

(a) for frequency range of 200 Hz to 600 Hz				
Crack length at location 2 (mm)	Crack length at location 1 (mm)			
	0.0	10.0	20.0	25.4
0.0	0.664398	0.723949	0.798541	1.000000
10.0	0.660406	0.719613	0.793781	0.994128
20.0	0.655260	0.714017	0.787655	0.986594
30.8	0.631249	0.687879	0.758956	0.951122
(b) for frequency range of 200 Hz to 1200 Hz				
Crack length at location 2 (mm)	Crack length at location 1 (mm)			
	0.0	10.0	20.0	25.4
0.0	0.669715	0.728618	0.802125	1.000000
10.0	0.665650	0.724205	0.797283	0.994039
20.0	0.660427	0.718529	0.791079	0.986428
30.8	0.635826	0.691786	0.761762	0.950337

Table F.11: Normalized rms of values strain gage #5 (cases #1 to #4)

(a) for frequency range of 200 Hz to 600 Hz				
Crack length at location 2 (mm)	Crack length at location 1 (mm)			
	0.0	10.0	20.0	25.4
0.0	0.955377	0.960025	0.974270	1.000000
10.0	0.949872	0.954533	0.968729	0.994424
20.0	0.942861	0.947535	0.961673	0.987324
30.8	0.909697	0.914424	0.928278	0.953680
(b) for frequency range of 200 Hz to 1200 Hz				
Crack length at location 2 (mm)	Crack length at location 1 (mm)			
	0.0	10.0	20.0	25.4
0.0	0.956067	0.960557	0.974704	1.000000
10.0	0.950451	0.954952	0.969053	0.994310
20.0	0.943302	0.947812	0.961860	0.987075
30.8	0.909392	0.913967	0.927730	0.952710

Table F.12: Normalized rms values of strain gage #6 (cases #1 to #4)

(a) for frequency range of 200 Hz to 600 Hz				
Crack length at location 2 (mm)	Crack length at location 1 (mm)			
	0.0	10.0	20.0	25.4
0.0	0.601089	0.600363	0.599114	0.596093
10.0	0.651472	0.650691	0.649346	0.646087
20.0	0.714067	0.713228	0.711790	0.708287
30.8	1.000000	0.998975	0.997182	0.992784
(b) for frequency range of 200 Hz to 1200 Hz				
Crack length at location 2 (mm)	Crack length at location 1 (mm)			
	0.0	10.0	20.0	25.4
0.0	0.606221	0.605423	0.604098	0.600812
10.0	0.656391	0.655533	0.654106	0.650567
20.0	0.718471	0.717548	0.716023	0.712218
30.8	1.000000	0.998857	0.996957	0.992183

Table F.13: Normalized rms values of accelerometer #1 (cases #5 to #8)

(a) for frequency range of 200 Hz to 600 Hz				
Crack length at location 4 (mm)	Crack length at location 3 (mm)			
	0.0	10.0	20.0	30.8
0.0	0.483036	1.000000	0.734159	0.816648
16.0	0.478977	0.909558	0.731732	0.815722
32.0	0.480675	0.871124	0.754886	0.841974
41.7	0.469188	0.719192	0.759070	0.848456
(b) for frequency range of 200 Hz to 1200 Hz				
Crack length at location 4 (mm)	Crack length at location 3 (mm)			
	0.0	10.0	20.0	30.8
0.0	0.582147	0.577807	0.885799	0.978960
16.0	0.575034	0.571568	0.876037	0.971673
32.0	0.590234	0.600039	0.902352	1.000000
41.7	0.591009	0.605092	0.900563	0.999717

Table F.14: Normalized rms values of accelerometer #2 (cases #5 to #8)

(a) for frequency range of 200 Hz to 600 Hz				
Crack length at location 4 (mm)	Crack length at location 3 (mm)			
	0.0	10.0	20.0	30.8
0.0	0.471210	1.000000	0.701730	0.803186
16.0	0.466431	0.919879	0.700682	0.803293
32.0	0.465378	0.869844	0.717328	0.823508
41.7	0.451394	0.717964	0.721247	0.829722
(b) for frequency range of 200 Hz to 1200 Hz				
Crack length at location 4 (mm)	Crack length at location 3 (mm)			
	0.0	10.0	20.0	30.8
0.0	0.573889	0.572178	0.863370	0.981734
16.0	0.570659	0.569801	0.857080	0.976894
32.0	0.580222	0.591724	0.876715	0.999100
41.7	0.582774	0.598627	0.876531	1.000000

Table F.15: Normalized rms values of accelerometer #3 (cases #5 to #8)

(a) for frequency range of 200 Hz to 600 Hz				
Crack length at location 4 (mm)	Crack length at location 3 (mm)			
	0.0	10.0	20.0	30.8
0.0	0.994704	1.000000	0.978300	0.975669
16.0	0.991627	0.997105	0.977343	0.975189
32.0	0.988251	0.991168	0.972736	0.970273
41.7	0.988679	0.990711	0.973879	0.971707
(b) for frequency range of 200 Hz to 1200 Hz				
Crack length at location 4 (mm)	Crack length at location 3 (mm)			
	0.0	10.0	20.0	30.8
0.0	0.999377	0.998133	0.985581	0.983141
16.0	1.000000	0.998727	0.986124	0.983307
32.0	0.994556	0.992207	0.979708	0.977116
41.7	0.994650	0.992895	0.980571	0.977911

Table F.16: Normalized rms values of accelerometer #4 (cases #5 to #8)

(a) for frequency range of 200 Hz to 600 Hz				
Crack length at location 4 (mm)	Crack length at location 3 (mm)			
	0.0	10.0	20.0	30.8
0.0	1.000000	0.978761	0.924088	0.719817
16.0	0.934999	0.904899	0.843783	0.631160
32.0	0.885427	0.803055	0.736945	0.515378
41.7	0.666299	0.617627	0.548360	0.319802
(b) for frequency range of 200 Hz to 1200 Hz				
Crack length at location 4 (mm)	Crack length at location 3 (mm)			
	0.0	10.0	20.0	30.8
0.0	0.786780	0.769185	0.823992	0.920877
16.0	0.817335	0.796920	0.848333	0.936817
32.0	0.836828	0.825072	0.875290	0.959432
41.7	0.902625	0.876868	0.923842	1.000000

Table F.17: Normalized rms values of accelerometer #5 (cases #5 to #8)

(a) for frequency range of 200 Hz to 600 Hz				
Crack length at location 4 (mm)	Crack length at location 3 (mm)			
	0.0	10.0	20.0	30.8
0.0	1.000000	0.974800	0.916927	0.712023
16.0	0.939864	0.906178	0.841904	0.627630
32.0	0.892199	0.806974	0.737811	0.513872
41.7	0.673362	0.622151	0.550412	0.319319
(b) for frequency range of 200 Hz to 1200 Hz				
Crack length at location 4 (mm)	Crack length at location 3 (mm)			
	0.0	10.0	20.0	30.8
0.0	0.559261	0.511594	0.513651	0.532161
16.0	0.697710	0.645623	0.650505	0.658460
32.0	0.762762	0.744012	0.757155	0.771367
41.7	1.000000	0.942071	0.955482	0.963631

Table F.18: Normalized rms values of accelerometer #6 (cases #5 to #8)

(a) for frequency range of 200 Hz to 600 Hz				
Crack length at location 4 (mm)	Crack length at location 3 (mm)			
	0.0	10.0	20.0	30.8
0.0	1.000000	0.982722	0.974557	0.968270
16.0	0.990626	0.979105	0.974635	0.973349
32.0	0.981696	0.975688	0.974835	0.977505
41.7	0.989765	0.987574	0.988044	0.991965
(b) for frequency range of 200 Hz to 1200 Hz				
Crack length at location 4 (mm)	Crack length at location 3 (mm)			
	0.0	10.0	20.0	30.8
0.0	0.996988	0.992431	0.989267	0.982583
16.0	0.996043	0.992782	0.990563	0.985171
32.0	0.995005	0.993755	0.992491	0.988137
41.7	1.000000	0.999271	0.998312	0.994211

Appendix G

e_{ij} Values for the rms Response Given in Appendix F

Normalized root mean square (rms) values presented in Appendix F were utilized to compute a damage indicator given in Equation 6.5 or 6.6. The damage indicator values obtained from accelerometer and strain response are presented in Tables G.1 to G.6 and Tables G.13 to G.18 for damage cases #1 to #4 and damage cases #5 to #8, respectively. The values obtained from strain response are presented in Tables G.7 to G.12.

Table G.1: The e_{ij} values of accelerometer #1 (cases #1 to #4)

(a) for frequency range of 200 Hz to 600 Hz				
Crack length at location 2 (mm)	Crack length at location 1 (mm)			
	1(0.0)	2(10.0)	3(20.0)	4(25.4)
1(0.0)	0.105584	1.000000	1.754697	1.800353
2(10.0)	0.104110	0.995261	1.748035	1.793394
3(20.0)	0.104261	0.986744	1.731223	1.776370
4(30.8)	0.100556	0.951480	1.669114	1.712876
(b) for frequency range of 200 Hz to 1200 Hz				
Crack length at location 2 (mm)	Crack length at location 1 (mm)			
	1(0.0)	2(10.00	3(20.0)	4(25.4)
1(0.0)	0.103818	1.000000	1.759404	1.802695
2(10.0)	0.102187	0.993850	1.750255	1.793215
3(20.0)	0.102185	0.983620	1.730393	1.773080
4(30.8)	0.097625	0.940259	1.654008	1.695071

Table G.2: The e_{ij} values of accelerometer #2 (cases #1 to #4)

(a) for frequency range of 200 Hz to 600 Hz				
Crack length at location 2 (mm)	Crack length at location 1 (mm)			
	1(0.0)	2(10.0)	3(20.0)	4(25.4)
1(0.0)	0.501359	1.000000	1.311969	1.366921
2(10.0)	0.494783	0.998037	1.316415	1.371080
3(20.0)	0.495496	0.985786	1.291721	1.346148
4(30.8)	0.478974	0.948753	1.240542	1.293531
(b) for frequency range of 200 Hz to 1200 Hz				
Crack length at location 2 (mm)	Crack length at location 1 (mm)			
	1(0.0)	2(10.0)	3(20.0)	4(25.4)
1(0.0)	0.493067	1.000000	1.325270	1.373272
2(10.0)	0.485648	0.996599	1.327905	1.375618
3(20.0)	0.485625	0.982453	1.300470	1.347877
4(30.8)	0.464667	0.937076	1.238444	1.284281

Table G.3: The e_{ij} values of accelerometer #3 (cases #1 to #4)

(a) for frequency range of 200 Hz to 600 Hz				
Crack length at location 2 (mm)	Crack length at location 1 (mm)			
	1(0.0)	2(10.0)	3(20.0)	4(25.4)
1(0.0)	0.108532	0.107533	0.108262	0.107722
2(10.0)	0.999998	1.000000	0.997069	0.992589
3(20.0)	1.752257	1.753946	1.746965	1.739103
4(30.8)	1.844756	1.846293	1.839377	1.831335
(b) for frequency range of 200 Hz to 1200 Hz				
Crack length at location 2 (mm)	Crack length at location 1 (mm)			
	1(0.0)	2(10.0)	3(20.0)	4(25.4)
1(0.0)	0.104520	0.103381	0.103974	0.103028
2(10.0)	1.000000	0.998579	0.993914	0.984973
3(20.0)	1.760418	1.759571	1.749483	1.733663
4(30.8)	1.848096	1.847009	1.836835	1.820506

Table G.4: The e_{ij} values of accelerometer #4 (cases #1 to #4)

(a) for frequency range of 200 Hz to 600 Hz				
Crack length at location 2 (mm)	Crack length at location 1 (mm)			
	1(0.0)	2(10.0)	3(20.0)	4(25.4)
1(0.0)	0.998752	0.993378	0.987731	0.972806
2(10.0)	0.998768	0.993565	0.987920	0.972992
3(20.0)	0.998972	0.993769	0.988121	0.973189
4(30.8)	1.000000	0.994791	0.989137	0.974187
(b) for frequency range of 200 Hz to 1200 Hz				
Crack length at location 2 (mm)	Crack length at location 1 (mm)			
	1(0.0)	2(10.0)	3(20.0)	4(25.4)
1(0.0)	1.000000	0.982223	0.948839	0.874970
2(10.0)	1.000801	0.983094	0.949859	0.876185
3(20.0)	1.001052	0.983240	0.949943	0.876610
4(30.8)	1.006160	0.988993	0.956792	0.884950

Table G.5: The e_{ij} values of accelerometer #5 (cases #1 to #4)

(a) for frequency range of 200 Hz to 600 Hz				
Crack length at location 2 (mm)	Crack length at location 1 (mm)			
	1(0.0)	2(10.0)	3(20.0)	4(25.4)
1(0.0)	0.998756	0.993466	0.987873	0.973059
2(10.0)	0.998819	0.993646	0.988054	0.973239
3(20.0)	0.999016	0.993841	0.988249	0.973433
4(30.8)	1.000000	0.994822	0.989228	0.974402
(b) for frequency range of 200 Hz to 1200 Hz				
Crack length at location 2 (mm)	Crack length at location 1 (mm)			
	1(0.0)	2(10.0)	3(20.0)	4(25.4)
1(0.0)	0.900792	0.875832	0.824935	0.742101
2(10.0)	0.910079	0.884695	0.832525	0.746748
3(20.0)	0.924841	0.898820	0.844701	0.754140
4(30.8)	1.000000	0.970999	0.908191	0.796481

Table G.6: The e_{ij} values of accelerometer #6 (cases #1 to #4)

(a) for frequency range of 200 Hz to 600 Hz				
Crack length at location 2 (mm)	Crack length at location 1 (mm)			
	1(0.0)	2(10.0)	3(20.0)	4(25.4)
1(0.0)	0.995553	0.995908	0.997076	1.000000
2(10.0)	0.994204	0.995225	0.996401	0.999325
3(20.0)	0.993503	0.994515	0.995692	0.998616
4(30.8)	0.989974	0.990994	0.992171	0.995104
(b) for frequency range of 200 Hz to 1200 Hz				
Crack length at location 2 (mm)	Crack length at location 1 (mm)			
	1(0.0)	2(10.0)	3(20.0)	4(25.4)
1(0.0)	0.987593	0.989973	0.992709	1.000000
2(10.0)	0.983030	0.985633	0.988420	0.995829
3(20.0)	0.977922	0.980567	0.983413	0.990973
4(30.8)	0.953712	0.956498	0.959554	0.967599

Table G.7: The e_{ij} values of strain gage #1 (cases #1 to #4)

(a) for frequency range of 200 Hz to 600 Hz				
Crack length at location 2 (mm)	Crack length at location 1 (mm)			
	1(0.0)	2(10.0)	3(20.0)	4(25.4)
1(0.0)	0.887864	0.909369	0.934132	1.000000
2(10.0)	0.890717	0.912315	0.937187	1.003336
3(20.0)	0.894544	0.916270	0.941274	1.007779
4(30.8)	0.912478	0.934808	0.960464	1.028708
(b) for frequency range of 200 Hz to 1200 Hz				
Crack length at location 2 (mm)	Crack length at location 1 (mm)			
	1(0.0)	2(10.0)	3(20.0)	4(25.4)
1(0.0)	0.883589	0.905966	0.931717	1.000000
2(10.0)	0.886595	0.909073	0.934939	1.003522
3(20.0)	0.890540	0.913154	0.939157	1.008110
4(30.8)	0.909342	0.932594	0.959284	1.030051

Table G.8: The e_{ij} values of strain gage #2 (cases #1 to #4)

(a) for frequency range of 200 Hz to 600 Hz				
Crack length at location 2 (mm)	Crack length at location 1 (mm)			
	1(0.0)	2(10.0)	3(20.0)	4(25.4)
1(0.0)	0.999643	0.995219	0.993745	0.984603
2(10.0)	1.000000	0.995634	0.994204	0.985206
3(20.0)	1.000638	0.996189	0.994702	0.985506
4(30.8)	1.002284	0.997469	0.995702	0.985583
(b) for frequency range of 200 Hz to 1200 Hz				
Crack length at location 2 (mm)	Crack length at location 1 (mm)			
	1(0.0)	2(10.0)	3(20.0)	4(25.4)
1(0.0)	0.999854	0.995023	0.993265	0.983039
2(10.0)	1.000000	0.995230	0.993517	0.983433
3(20.0)	1.001043	0.996192	0.994422	0.984131
4(30.8)	1.004644	0.999407	0.997349	0.986063

Table G.9: The e_{ij} values of strain gage #3 (cases #1 to #4)

(a) for frequency range of 200 Hz to 600 Hz				
Crack length at location 2 (mm)	Crack length at location 1 (mm)			
	1(0.0)	2(10.0)	3(20.0)	4(25.4)
1(0.0)	0.977575	0.982329	0.987002	1.000000
2(10.0)	0.986290	0.991029	0.995674	1.008605
3(20.0)	0.992910	0.997645	1.002260	1.015144
4(30.8)	1.034430	1.039117	1.043610	1.056209
(b) for frequency range of 200 Hz to 1200 Hz				
Crack length at location 2 (mm)	Crack length at location 1 (mm)			
	1(0.0)	2(10.0)	3(20.0)	4(25.4)
1(0.0)	0.977826	0.982639	0.987209	1.000000
2(10.0)	1.261583	1.267183	0.996513	1.009229
3(20.0)	1.266508	1.272111	1.003673	1.016333
4(30.8)	1.493734	1.308930	1.048399	1.060713

Table G.10: The e_{ij} values of strain gage #4 (cases #1 to #4)

(a) for frequency range of 200 Hz to 600 Hz				
Crack length at location 2 (mm)	Crack length at location 1 (mm)			
	1(0.0)	2(10.0)	3(20.0)	4(25.4)
1(0.0)	0.664398	0.723949	0.798541	1.000000
2(10.0)	0.668390	0.728285	0.803301	1.005872
3(20.0)	0.673535	0.733881	0.809427	1.013406
4(30.8)	0.697547	0.760019	0.838126	1.048878
(b) for frequency range of 200 Hz to 1200 Hz				
Crack length at location 2 (mm)	Crack length at location 1 (mm)			
	1(0.0)	2(10.0)	3(20.0)	4(25.4)
1(0.0)	0.669715	0.728618	0.802125	1.000000
2(10.0)	0.673780	0.733031	0.806967	1.005961
3(20.0)	0.679003	0.738707	0.813171	1.013572
4(30.8)	0.703603	0.765450	0.842488	1.049663

Table G.11: The e_{ij} values of strain gage #5 (cases #1 to #4)

(a) for frequency range of 200 Hz to 600 Hz				
Crack length at location 2 (mm)	Crack length at location 1 (mm)			
	1(0.0)	2(10.0)	3(20.0)	4(25.4)
1(0.0)	0.955377	0.960025	0.974270	1.000000
2(10.0)	0.960882	0.965516	0.979810	1.005576
3(20.0)	0.967894	0.972514	0.986866	1.012676
4(30.8)	1.001057	1.005625	1.020261	1.046320
(b) for frequency range of 200 Hz to 1200 Hz				
Crack length at location 2 (mm)	Crack length at location 1 (mm)			
	1(0.0)	2(10.0)	4(20.0)	5(25.4)
1(0.0)	0.956067	0.960557	0.974704	1.000000
2(10.0)	0.961682	0.966161	0.980355	1.005690
3(20.0)	0.968832	0.973301	0.987547	1.012925
4(30.8)	1.002742	1.007146	1.021677	1.047290

Table G.12: The e_{ij} values of strain gage #6 (cases #1 to #4)

(a) for frequency range of 200 Hz to 600 Hz				
Crack length at location 2 (mm)	Crack length at location 1 (mm)			
	1(0.0)	2(10.0)	3(20.0)	4(25.4)
1(0.0)	0.601089	0.601815	0.603065	0.606086
2(10.0)	0.651472	0.652254	0.653599	0.656858
3(20.0)	0.714067	0.714907	0.716345	0.719848
4(30.8)	1.000000	1.001025	1.002818	1.007216
(b) for frequency range of 200 Hz to 1200 Hz				
Crack length at location 2 (mm)	Crack length at location 1 (mm)			
	1(0.0)	2(10.0)	3(20.0)	4(25.4)
1(0.0)	0.606221	0.607019	0.608343	0.611630
2(10.0)	0.656391	0.657249	0.658676	0.662216
3(20.0)	0.718471	0.719394	0.720919	0.724724
4(30.8)	1.000000	1.001143	1.003043	1.007817

Table G.13: The e_{ij} values of accelerometer #1 (cases #5 to #8)

(a) for frequency range of 200 Hz to 600 Hz				
Crack length at location 4 (mm)	Crack length at location 3 (mm)			
	1(0.0)	2(10.0)	3(20.0)	4(30.8)
1(0.0)	0.483036	1.000000	1.265841	1.348331
2(16.0)	0.478977	0.909558	1.087385	1.171375
3(32.0)	0.480675	0.871124	0.987363	1.074451
4(41.7)	0.469188	0.719192	0.759070	0.848456
(b) for frequency range of 200 Hz to 1200 Hz				
Crack length at location 4 (mm)	Crack length at location 3 (mm)			
	1(0.0)	2(10.0)	3(20.0)	4(30.8)
1(0.0)	0.582147	0.577807	0.885799	0.978960
2(16.0)	0.589261	0.584047	0.895562	0.986247
3(32.0)	0.604461	0.612517	0.921877	1.014575
4(41.7)	0.605236	0.617570	0.923666	1.014857

Table G.14: The e_{ij} values of accelerometer #2 (cases #5 to #8)

(a) for frequency range of 200 Hz to 600 Hz				
Crack length at location 4 (mm)	Crack length at location 3 (mm)			
	1(0.0)	2(10.0)	3(20.0)	4(30.8)
1(0.0)	0.471210	1.000000	1.298270	1.399727
2(16.0)	0.466431	0.919879	1.139077	1.241688
3(32.0)	0.465378	0.869844	1.022361	1.128541
4(41.7)	0.451394	0.717964	0.721247	0.829722
(b) for frequency range of 200 Hz to 1200 Hz				
Crack length at location 4 (mm)	Crack length at location 3 (mm)			
	1(0.0)	2(10.0)	3(20.0)	4(30.8)
1(0.0)	0.573889	0.572178	0.863370	0.981734
2(16.0)	0.577119	0.574555	0.869661	0.986575
3(32.0)	0.586682	0.596479	0.889297	1.008781
4(41.7)	0.589234	0.603382	0.889481	1.009681

Table G.15: The e_{ij} values of accelerometer #3 (cases #5 to #8)

(a) for frequency range of 200 Hz to 600 Hz				
Crack length at location 4 (mm)	Crack length at location 3 (mm)			
	1(0.0)	2(10.0)	3(20.0)	4(30.8)
1(0.0)	0.994704	1.000000	1.021700	1.024331
2(16.0)	0.991627	0.997105	1.016868	1.019022
3(32.0)	0.988251	0.991168	1.009601	1.012064
4(41.7)	0.988679	0.990711	1.007543	1.009715
(b) for frequency range of 200 Hz to 1200 Hz				
Crack length at location 4 (mm)	Crack length at location 3 (mm)			
	1(0.0)	2(10.0)	3(20.0)	4(30.8)
1(0.0)	0.999377	0.998133	0.985581	0.983141
2(16.0)	1.000000	0.998727	0.986124	0.983307
3(32.0)	1.005444	1.005247	0.992540	0.989499
4(41.7)	1.005537	1.005935	0.993404	0.990294

Table G.16: The e_{ij} values of accelerometer #4 (cases #5 to #8)

(a) for frequency range of 200 Hz to 600 Hz				
Crack length at location 4 (mm)	Crack length at location 3 (mm)			
	1(0.0)	2(10.0)	3(20.0)	4(30.8)
1(0.0)	1.000000	1.021239	1.075912	1.280183
2(16.0)	0.934999	0.965098	1.026214	1.238837
3(32.0)	0.885427	0.967800	1.033909	1.255476
4(41.7)	0.666299	0.714972	0.784238	1.012796
(b) for frequency range of 200 Hz to 1200 Hz				
Crack length at location 4 (mm)	Crack length at location 3 (mm)			
	1(0.0)	2(10.0)	3(20.0)	4(30.8)
1(0.0)	0.786780	0.804375	0.859182	0.956067
2(16.0)	0.817335	0.837749	0.889161	0.977646
3(32.0)	0.836828	0.848585	0.898803	0.982945
4(41.7)	0.902625	0.928382	0.975355	1.051514

Table G.17: The e_{ij} values of accelerometer #5 (cases #5 to #8)

(a) for frequency range of 200 Hz to 600 Hz				
Crack length at location 4 (mm)	Crack length at location 3 (mm)			
	1(0.0)	2(10.0)	3(20.0)	4(30.8)
1(0.0)	1.000000	1.025200	1.083073	1.287977
2(16.0)	0.939864	0.973551	1.037825	1.252098
3(32.0)	0.892199	0.977425	1.046588	1.270527
4(41.7)	0.673362	0.724572	0.796311	1.027404
(b) for frequency range of 200 Hz to 1200 Hz				
Crack length at location 4 (mm)	Crack length at location 3 (mm)			
	1(0.0)	2(10.0)	3(20.0)	4(30.8)
1(0.0)	0.559261	0.606928	0.608985	0.627495
2(16.0)	0.697710	0.749798	0.754679	0.762635
3(32.0)	0.762762	0.781511	0.794654	0.808866
4(41.7)	1.000000	1.057929	1.071340	1.079489

Table G.18: The e_{ij} values of accelerometer #6 (cases #5 to #8)

(a) for frequency range of 200 Hz to 600 Hz				
Crack length at location 4 (mm)	Crack length at location 3 (mm)			
	1(0.0)	2(10.0)	3(20.0)	4(30.8)
1(0.0)	1.000000	0.982722	0.974557	0.968270
2(16.0)	1.009374	0.986339	0.974635	0.973349
3(32.0)	1.018304	0.989757	0.974835	0.977505
4(41.7)	1.026373	1.001643	0.988044	0.991965
(b) for frequency range of 200 Hz to 1200 Hz				
Crack length at location 4 (mm)	Crack length at location 3 (mm)			
	1(0.0)	2(10.0)	3(20.0)	4(30.8)
1(0.0)	0.996988	0.992431	0.989267	0.982583
2(16.0)	0.997934	0.992782	0.990563	0.985171
3(32.0)	0.998971	0.993755	0.992491	0.988137
4(41.7)	1.003967	0.999271	0.998312	0.994211

Appendix H

Three-dimensional Plots of the rms and e_{ij} Values

In this appendix, three-dimensional plots of normalized acceleration and strain rms response (given in Appendix F) and damage indicator values (presented in Appendix G) are presented.

Three dimensional plots of normalized rms acceleration response and damage indicator values for damage cases #1 to #4 are shown in Figures H.1 to H.6 and Figures H.13 to H.18 for damage cases #5 to #8. The plots of normalized strain response and the damage indicator are shown in Figures H.7 to H.12.

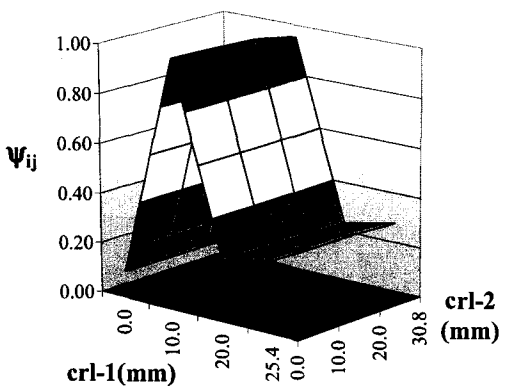

(a) the rms (200 Hz to 600 Hz)

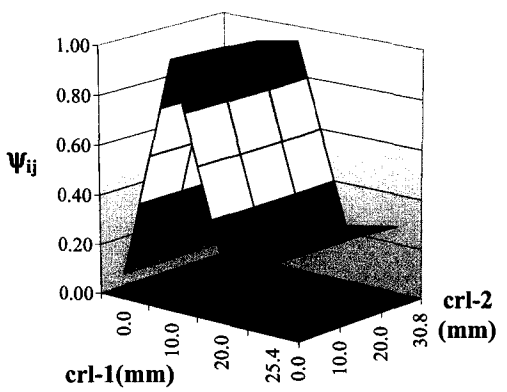

(b) the rms (200 Hz to 1200 Hz)

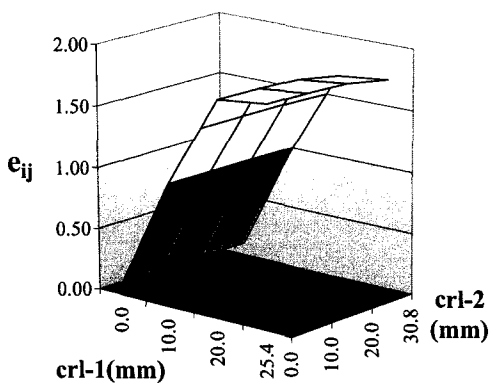

(a) e_{ij} values (200 Hz to 600 Hz)

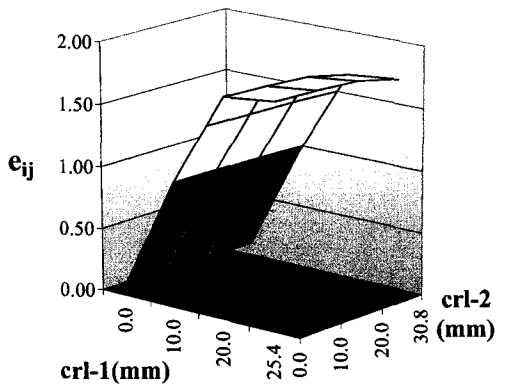

(b) e_{ij} values (200 Hz to 1200 Hz)

Figure H.1: Three-dimensional plot of the normalized rms and e_{ij} of acceleration #1 for frequency range of 200 Hz to 600 Hz and 200 Hz to 1200 Hz for damage cases #1 to #4

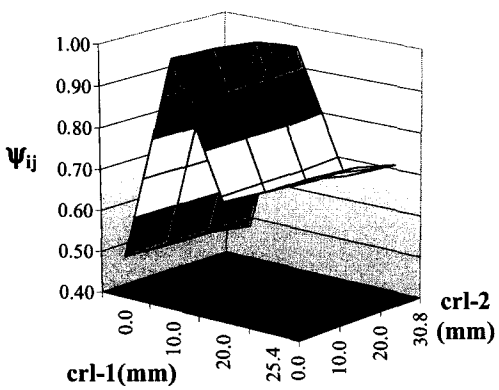

(a) the rms (200 Hz to 600 Hz)

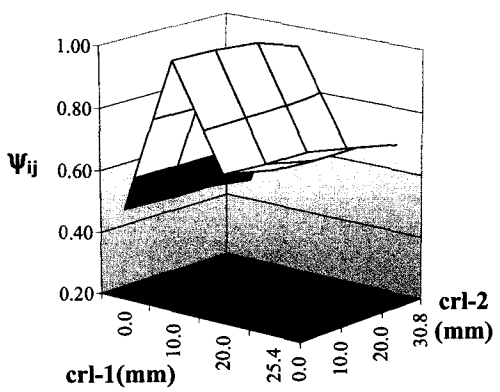

(b) the rms (200 Hz to 1200 Hz)

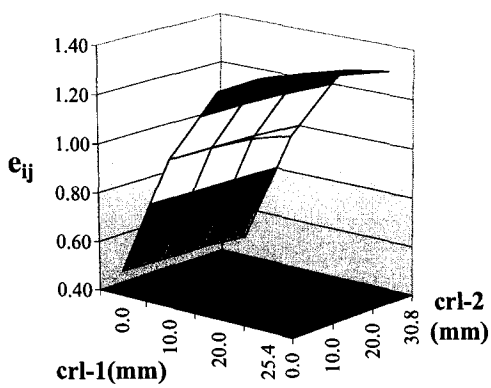

(a) e_{ij} values (200 Hz to 600 Hz)

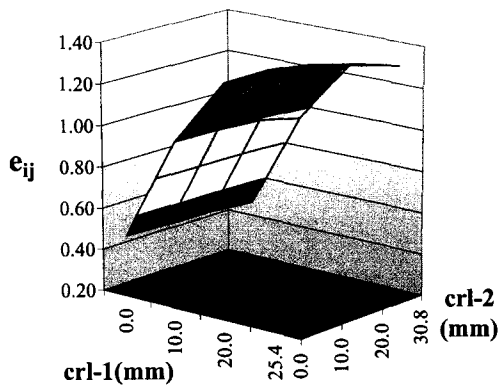

(b) e_{ij} values (200 Hz to 1200 Hz)

Figure H.2: Three-dimensional plot of the normalized rms and e_{ij} of acceleration #2 for frequency range of 200 Hz to 600 Hz and 200 Hz to 1200 Hz for damage cases #1 to #4

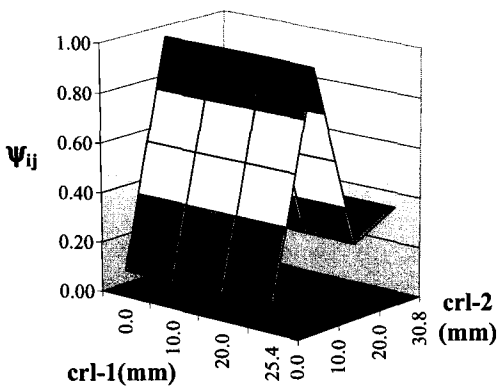

(a) the rms (200 Hz to 600 Hz)

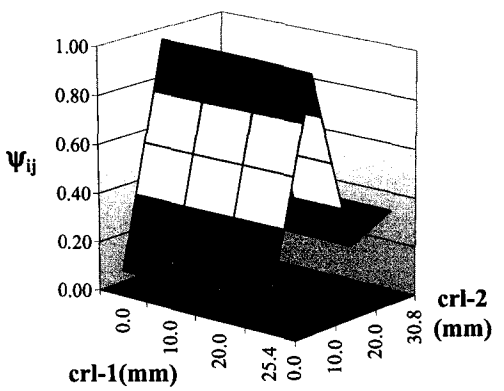

(b) the rms (200 Hz to 1200 Hz)

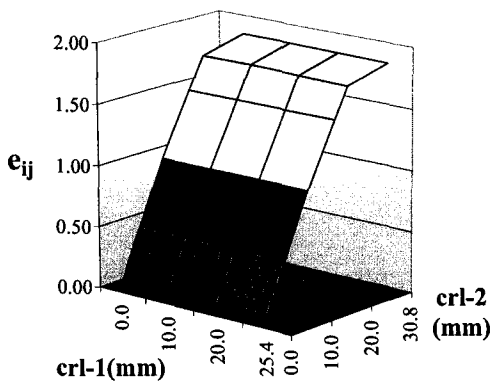

(a) e_{ij} values (200 Hz to 600 Hz)

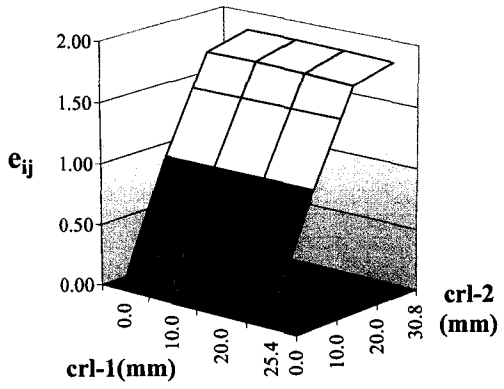

(b) e_{ij} values (200 Hz to 1200 Hz)

Figure H.3: Three-dimensional plot of the normalized rms and e_{ij} of acceleration #3 for frequency range of 200 Hz to 600 Hz and 200 Hz to 1200 Hz for damage cases #1 to #4

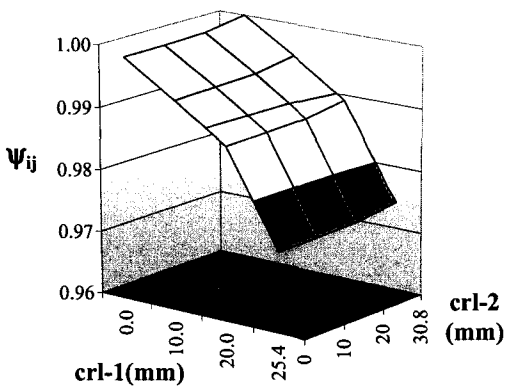

(a) the rms (200 Hz to 600 Hz)

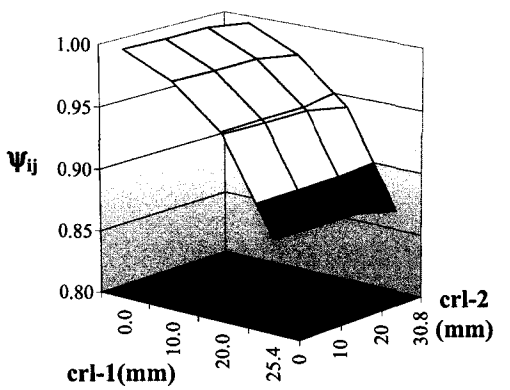

(b) the rms (200 Hz to 1200 Hz)

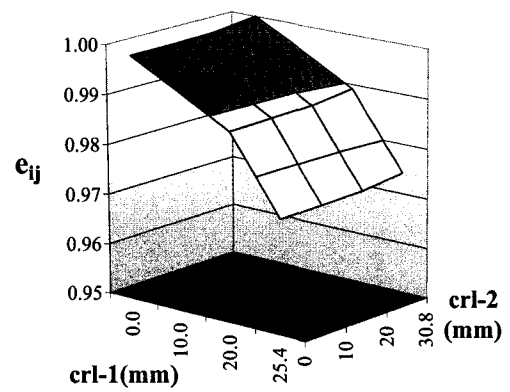

(a) e_{ij} values (200 Hz to 600 Hz)

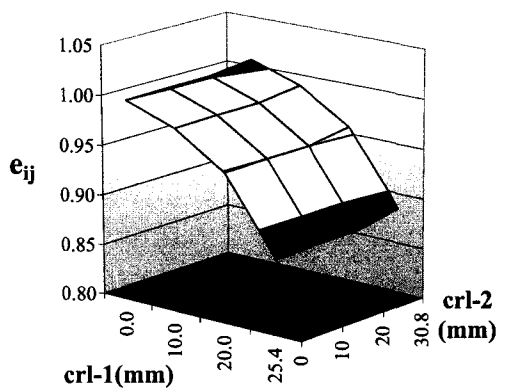

(b) e_{ij} values (200 Hz to 1200 Hz)

Figure H.4: Three-dimensional plot of the normalized rms and e_{ij} of acceleration #4 for frequency range of 200 Hz to 600 Hz and 200 Hz to 1200 Hz for damage cases #1 to #4

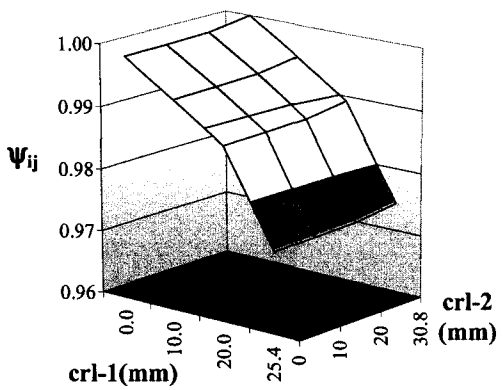

(a) the rms (200 Hz to 600 Hz)

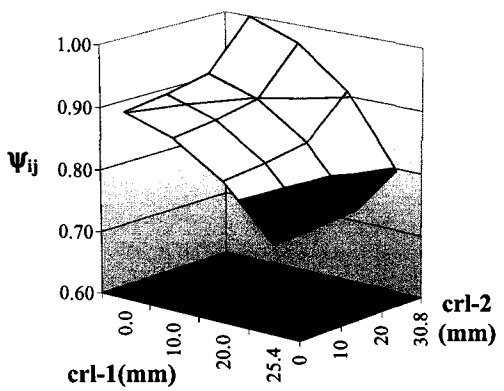

(b) the rms (200 Hz to 1200 Hz)

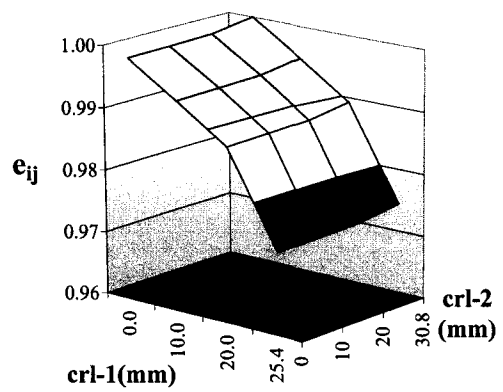

(a) e_{ij} values (200 Hz to 600 Hz)

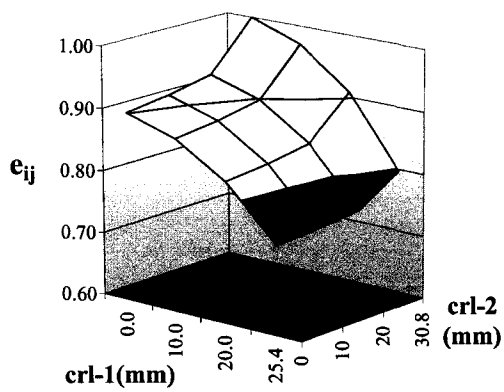

(b) e_{ij} values (200 Hz to 1200 Hz)

Figure H.5: Three-dimensional plot of the normalized rms and e_{ij} of acceleration #5 for frequency range of 200 Hz to 600 Hz and 200 Hz to 1200 Hz for damage cases #1 to #4

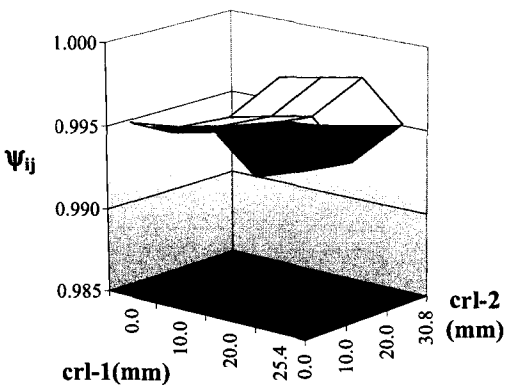

(a) the rms (200 Hz to 600 Hz)

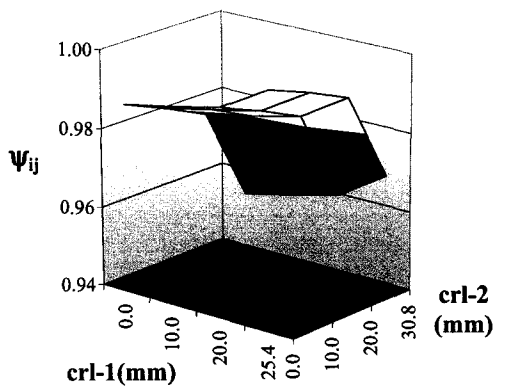

(b) the rms (200 Hz to 1200 Hz)

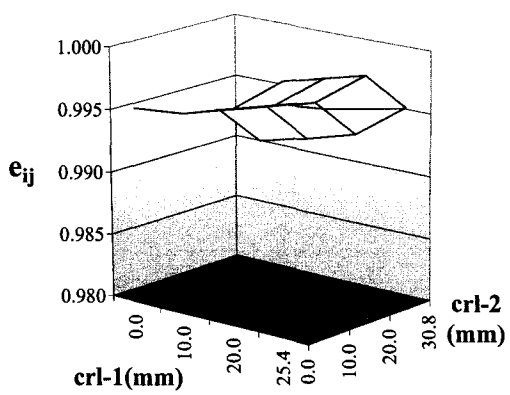

(a) e_{ij} values (200 Hz to 600 Hz)

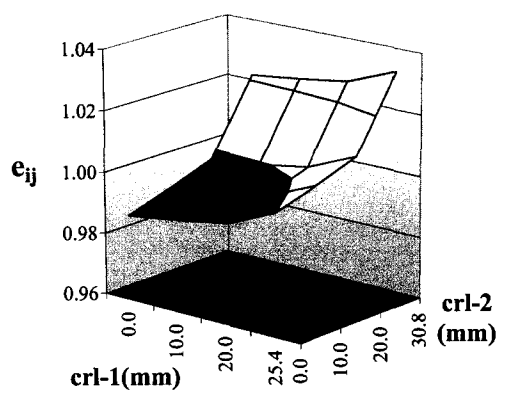

(b) e_{ij} values (200 Hz to 1200 Hz)

Figure H.6: Three-dimensional plot of the normalized rms and e_{ij} of acceleration #6 for frequency range of 200 Hz to 600 Hz and 200 Hz to 1200 Hz for damage cases #1 to #4

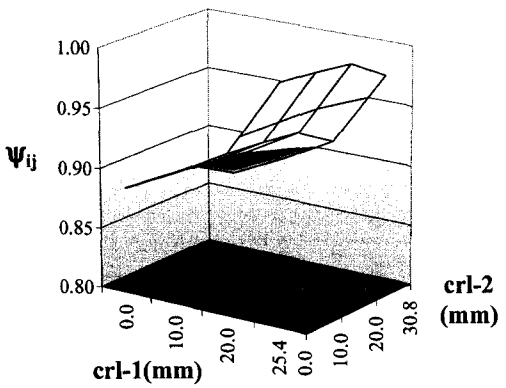

(a) the rms (200 Hz to 600 Hz)

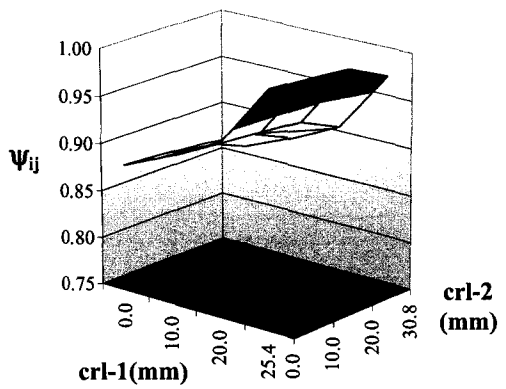

(b) the rms (200 Hz to 1200 Hz)

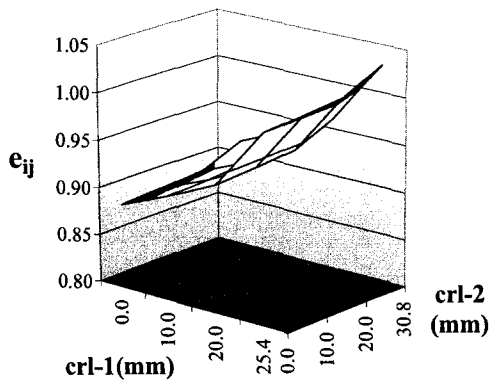

(a) e_{ij} values (200 Hz to 600 Hz)

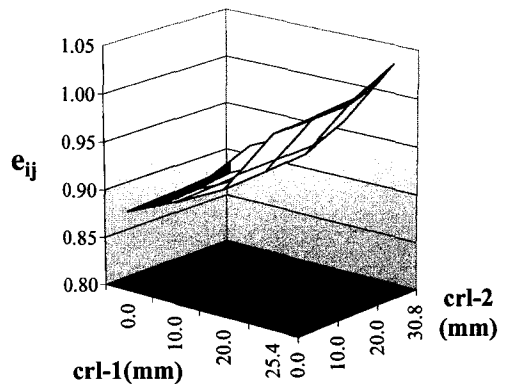

(b) e_{ij} values (200 Hz to 1200 Hz)

Figure H.7: Three-dimensional plot of the normalized rms and e_{ij} of strain gage #1 for frequency range of 200 Hz to 600 Hz and 200 Hz to 1200 Hz for damage cases #1 to #4

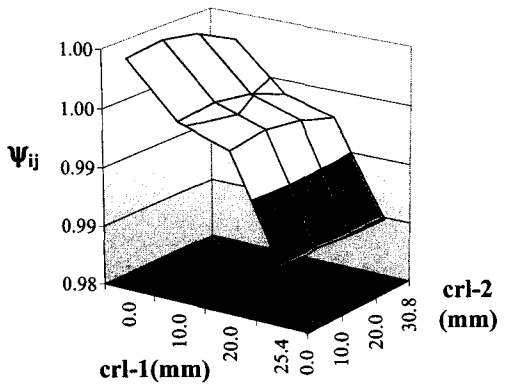

(a) the rms (200 Hz to 600 Hz)

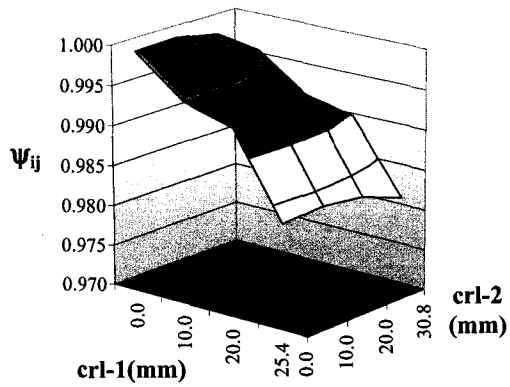

(b) the rms (200 Hz to 1200 Hz)

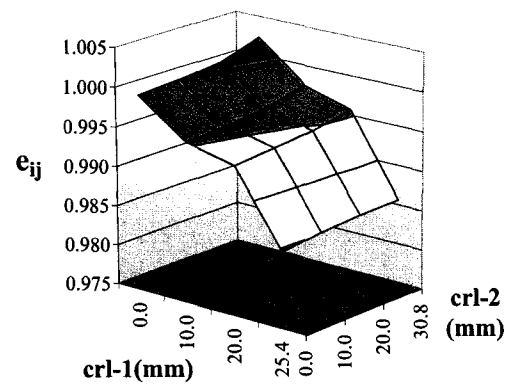

(a) e_{ij} values (200 Hz to 600 Hz)

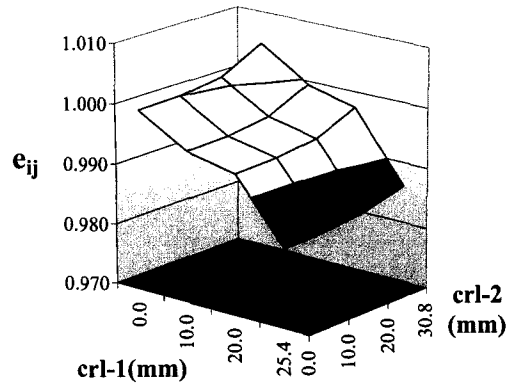

(b) e_{ij} values (200 Hz to 1200 Hz)

Figure H.8: Three-dimensional plot of the normalized rms and e_{ij} of strain gage #2 for frequency range of 200 Hz to 600 Hz and 200 Hz to 1200 Hz for damage cases #1 to #4

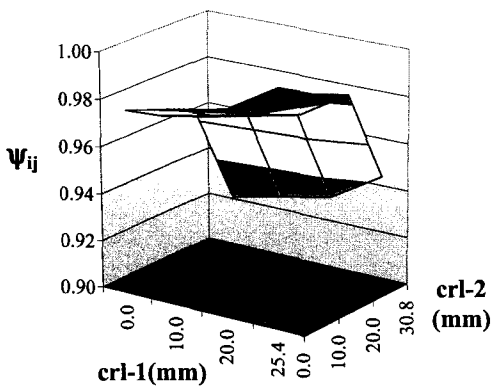

(a) the rms (200 Hz to 600 Hz)

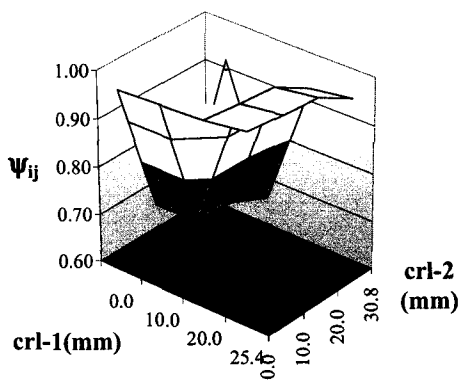

(b) the rms (200 Hz to 1200 Hz)

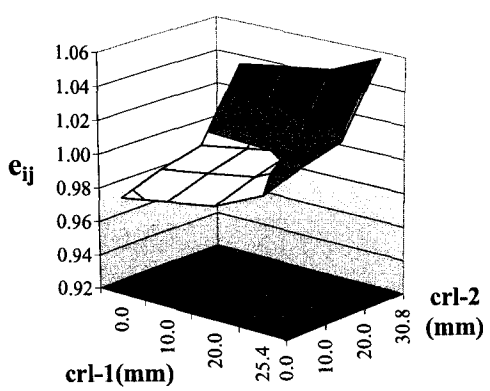

(a) e_{ij} values (200 Hz to 600 Hz)

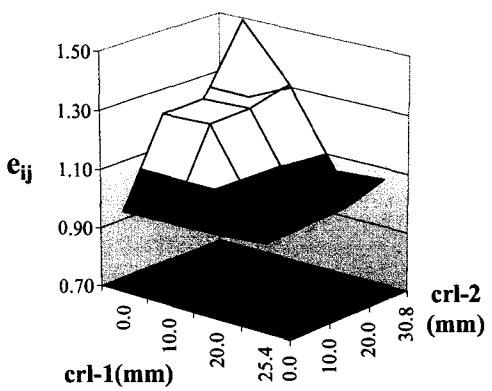

(b) e_{ij} values (200 Hz to 1200 Hz)

Figure H.9: Three-dimensional plot of the normalized rms and e_{ij} of strain gage #3 for frequency range of 200 Hz to 600 Hz and 200 Hz to 1200 Hz for damage cases #1 to #4

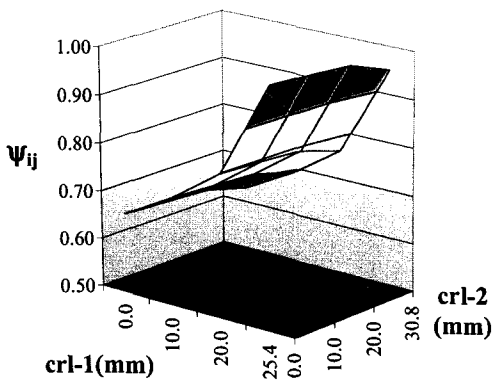

(a) the rms (200 Hz to 600 Hz)

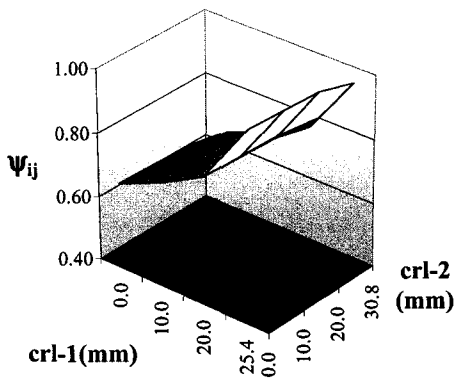

(b) the rms (200 Hz to 1200 Hz)

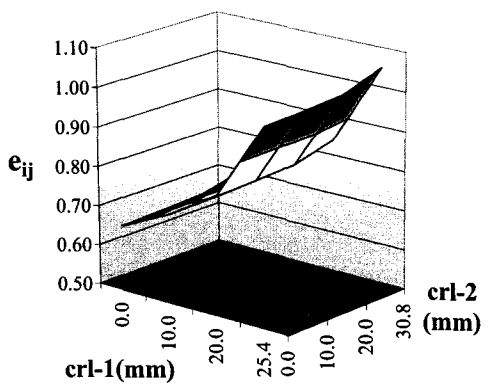

(a) e_{ij} values (200 Hz to 600 Hz)

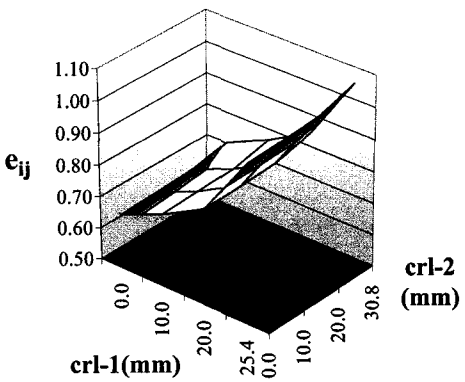

(b) e_{ij} values (200 Hz to 1200 Hz)

Figure H.10: Three-dimensional plot of the normalized rms and e_{ij} of strain gage #4 for frequency range of 200 Hz to 600 Hz and 200 Hz to 1200 Hz for damage cases #1 to #4

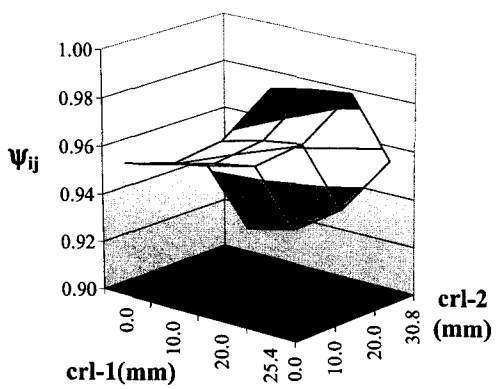

(a) the rms (200 Hz to 600 Hz)

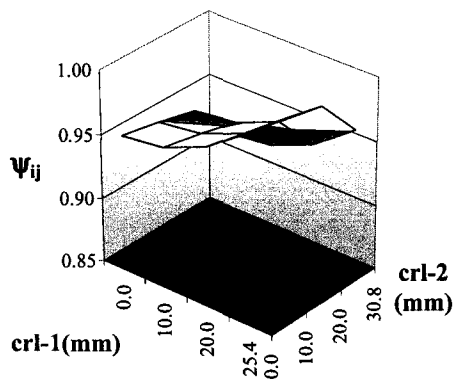

(b) the rms (200 Hz to 1200 Hz)

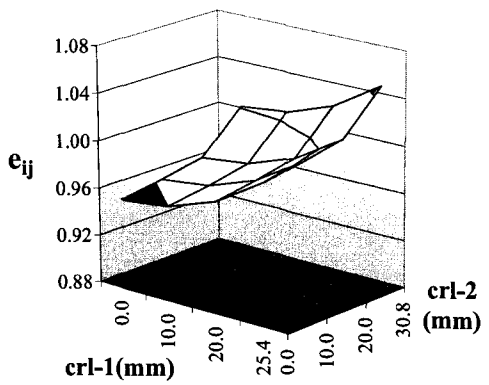

(a) e_{ij} values (200 Hz to 600 Hz)

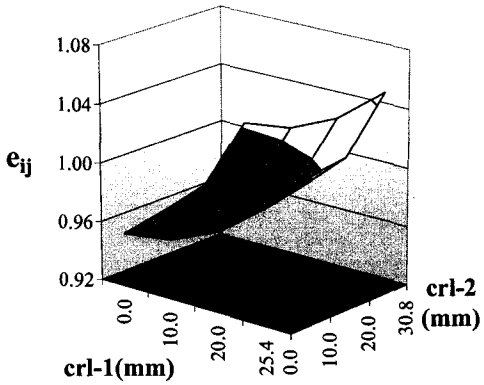

(b) e_{ij} values (200 Hz to 1200 Hz)

Figure H.11: Three-dimensional plot of the normalized rms and e_{ij} of strain gage #5 for frequency range of 200 Hz to 600 Hz and 200 Hz to 1200 Hz for damage cases #1 to #4

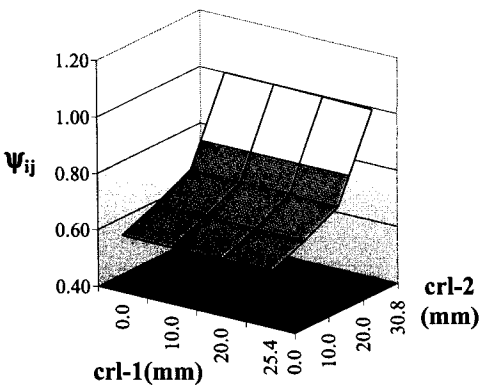

(a) the rms (200 Hz to 600 Hz)

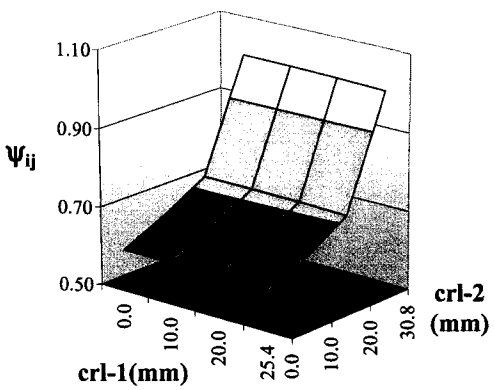

(b) the rms (200 Hz to 1200 Hz)

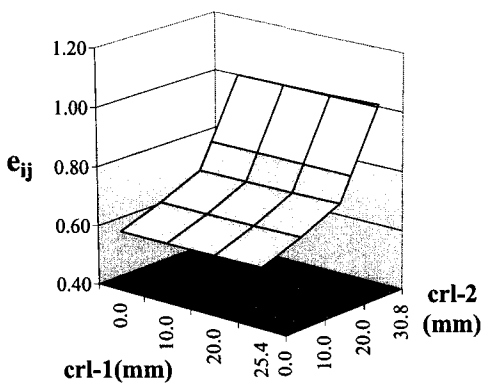

(a) e_{ij} values (200 Hz to 600 Hz)

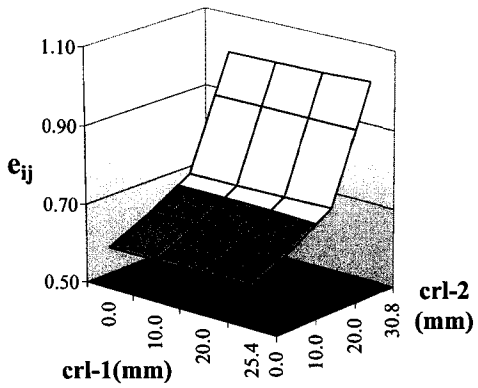

(b) e_{ij} values (200 Hz to 1200 Hz)

Figure H.12: Three-dimensional plot of the normalized rms and e_{ij} of strain gage #6 for frequency range of 200 Hz to 600 Hz and 200 Hz to 1200 Hz for damage cases #1 to #4

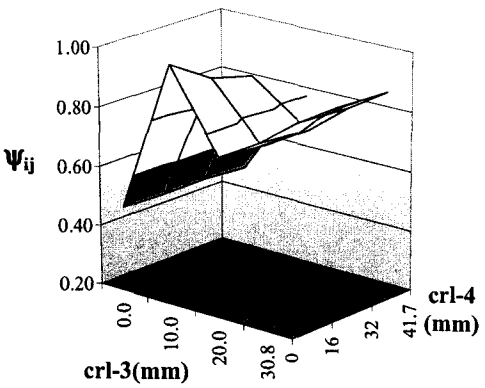

(a) the rms (200 Hz to 600 Hz)

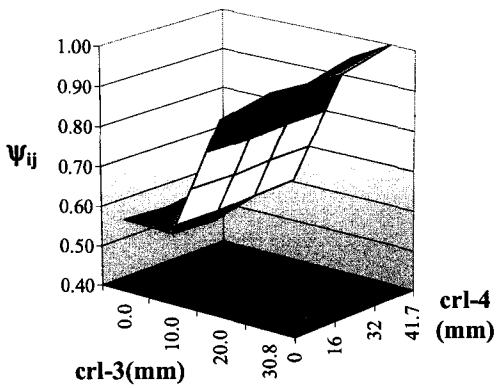

(b) the rms (200 Hz to 1200 Hz)

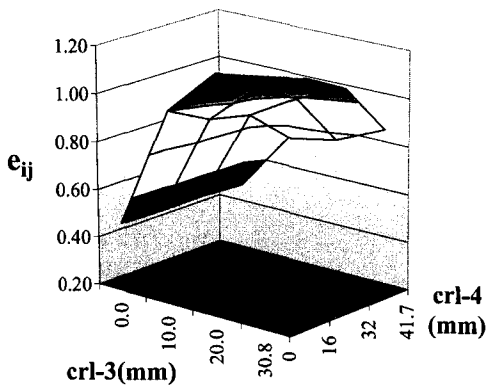

(a) e_{ij} values (200 Hz to 600 Hz)

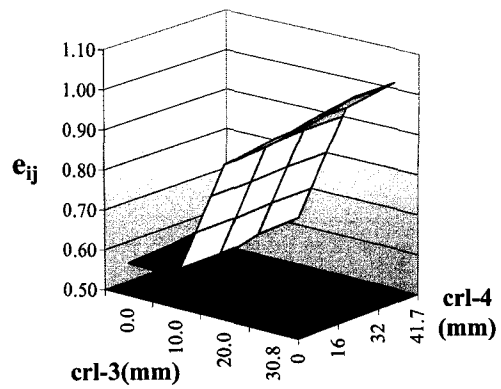

(b) e_{ij} values (200 Hz to 1200 Hz)

Figure H.13: Three-dimensional plot of the normalized rms and e_{ij} of acceleration #1 for frequency range of 200 Hz to 600 Hz and 200 Hz to 1200 Hz for damage cases #5 to #8

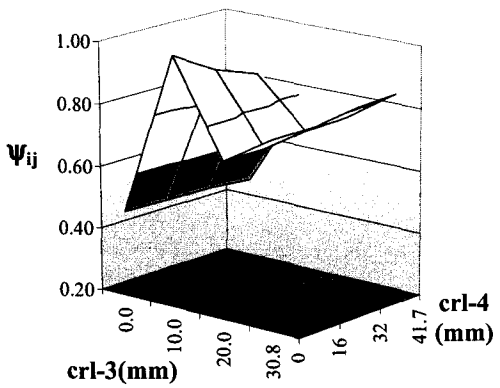

(a) the rms (200 Hz to 600 Hz)

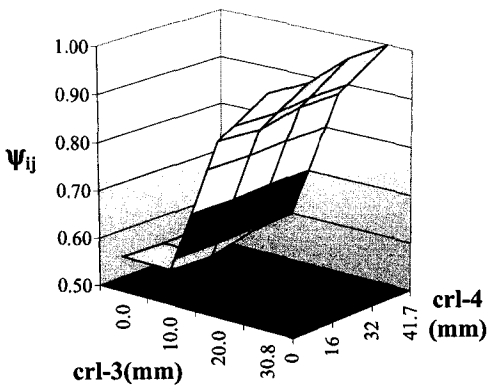

(b) the rms (200 Hz to 1200 Hz)

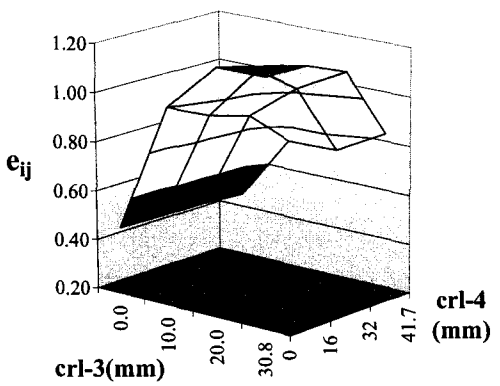

(a) e_{ij} values (200 Hz to 600 Hz)

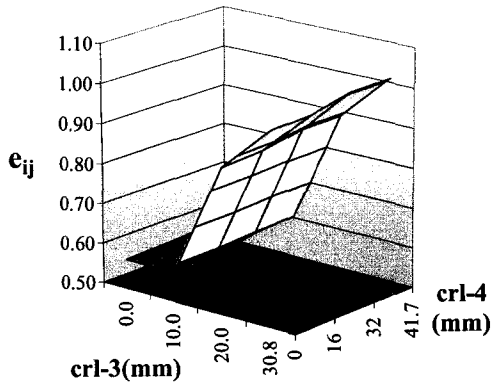

(b) e_{ij} values (200 Hz to 1200 Hz)

Figure H.14: Three-dimensional plot of the normalized rms and e_{ij} of acceleration #2 for frequency range of 200 Hz to 600 Hz and 200 Hz to 1200 Hz for damage cases #5 to #8

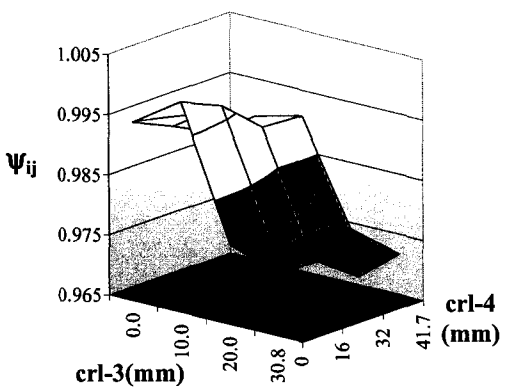

(a) the rms (200 Hz to 600 Hz)

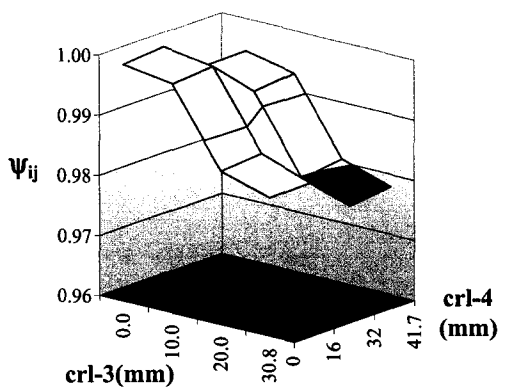

(b) the rms (200 Hz to 1200 Hz)

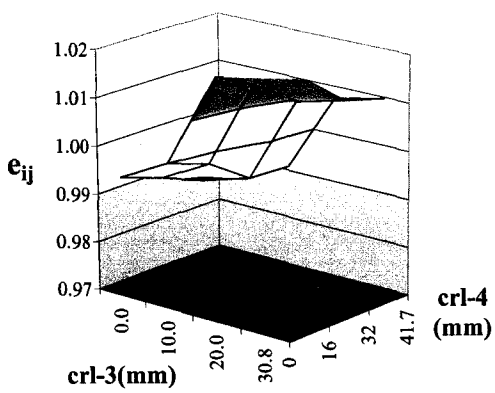

(a) e_{ij} values (200 Hz to 600 Hz)

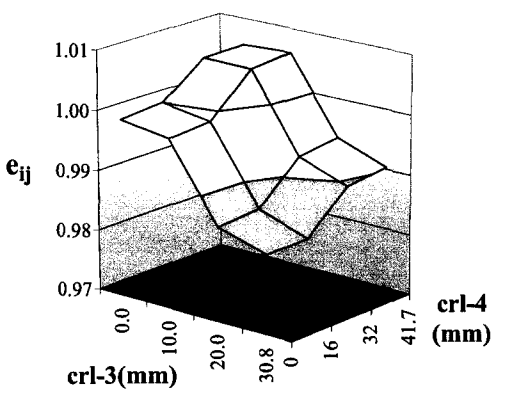

(b) e_{ij} values (200 Hz to 1200 Hz)

Figure H.15: Three-dimensional plot of the normalized rms and e_{ij} of acceleration #3 for frequency range of 200 Hz to 600 Hz and 200 Hz to 1200 Hz for damage cases #5 to #8

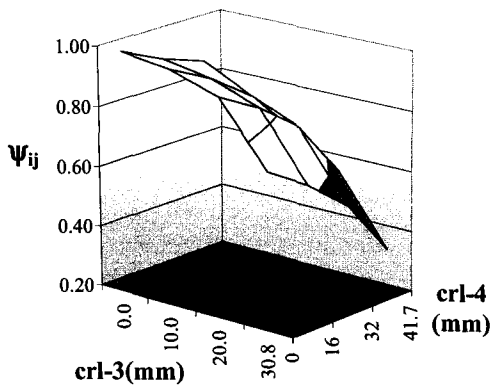

(a) the rms (200 Hz to 600 Hz)

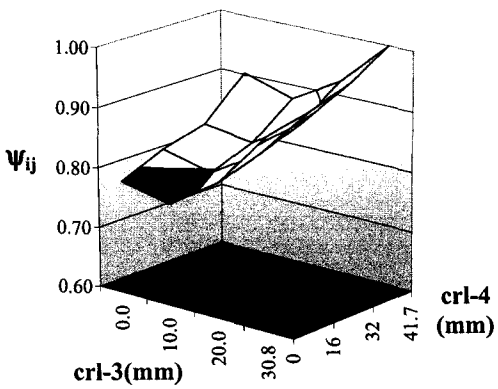

(b) the rms (200 Hz to 1200 Hz)

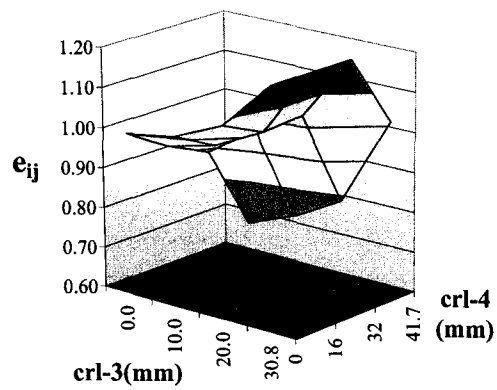

(a) e_{ij} values (200 Hz to 600 Hz)

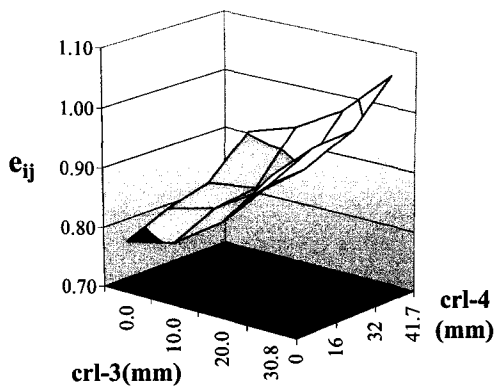

(b) e_{ij} values (200 Hz to 1200 Hz)

Figure H.16: Three-dimensional plot of the normalized rms and e_{ij} of acceleration #4 for frequency range of 200 Hz to 600 Hz and 200 Hz to 1200 Hz for damage cases #5 to #8

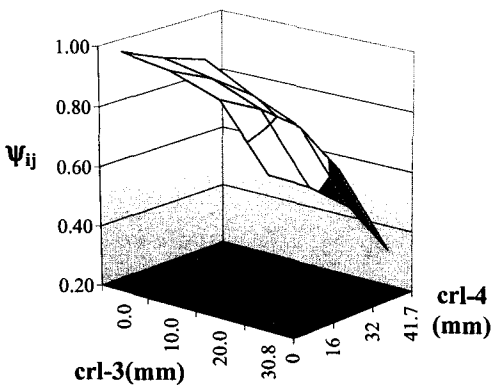

(a) the rms (200 Hz to 600 Hz)

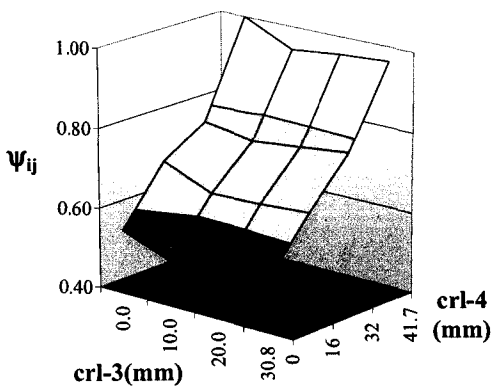

(b) the rms (200 Hz to 1200 Hz)

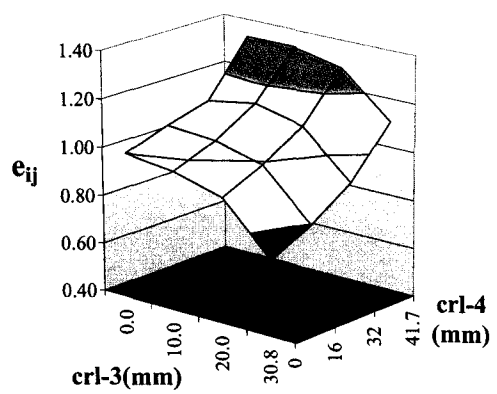

(a) e_{ij} values (200 Hz to 600 Hz)

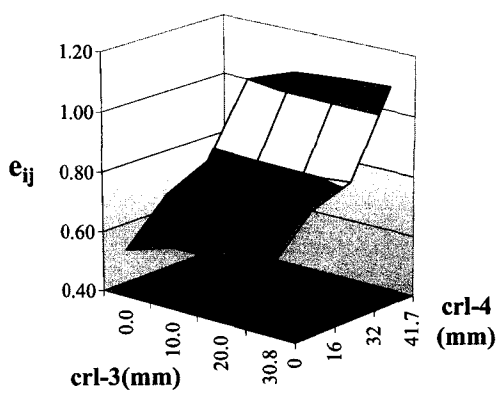

(b) e_{ij} values (200 Hz to 1200 Hz)

Figure H.17: Three-dimensional plot of the normalized rms and e_{ij} of acceleration #5 for frequency range of 200 Hz to 600 Hz and 200 Hz to 1200 Hz for damage cases #5 to #8

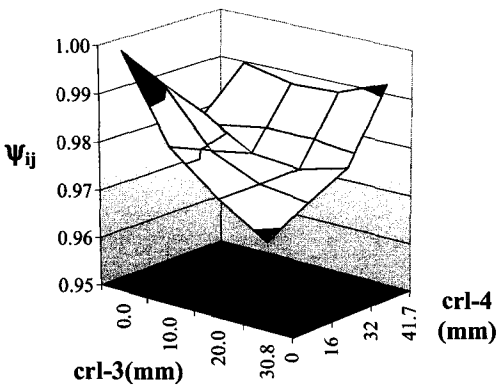

(a) the rms (200 Hz to 600 Hz)

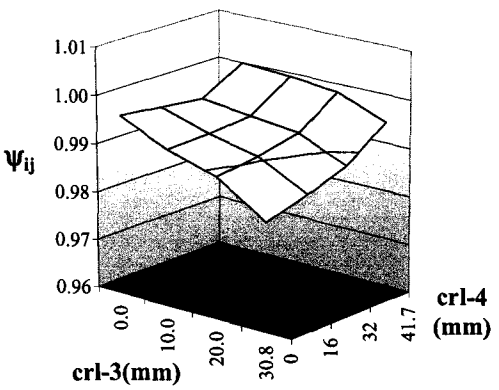

(b) the rms (200 Hz to 1200 Hz)

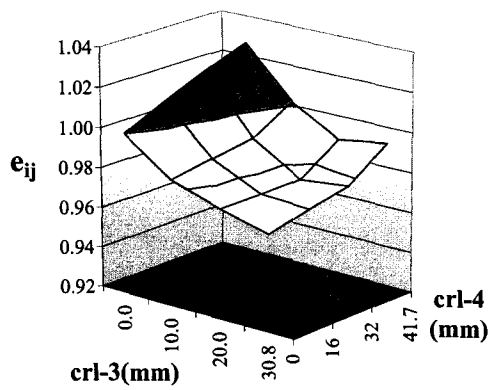

(a) e_{ij} values (200 Hz to 600 Hz)

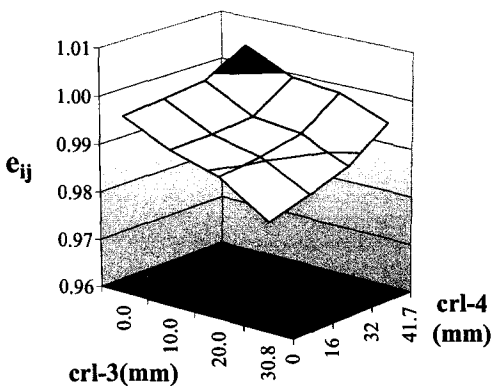

(b) e_{ij} values (200 Hz to 1200 Hz)

Figure H.18: Three-dimensional plot of the normalized rms and e_{ij} of acceleration #6 for frequency range of 200 Hz to 600 Hz and 200 Hz to 1200 Hz for damage cases #5 to #8